To the Graduate Council:
I am submitting herewith a thesis written by Devon Russell Goodspeed entitled "Integration of Magnetic Arc Oscillation into the Wire Arc Additive Manufacturing Workflow." I have examined the final paper copy of this thesis for form and content and recommend that it be accepted in partial fulfillment of the requirements for the degree of Doctor of Philosophy, with a major in Mechanical Engineering.

Dr. Bradley Jared, Major Professor

We have read this thesis
and recommend its acceptance:

Dr. Dustin Gilbert

Dr. Suresh Babu

Dr. Chad Duty

Accepted for the Council:

Dixie L. Thompson

Vice Provost and Dean of the Graduate School

To the Graduate Council:
I am submitting herewith a thesis written by Devon Russell Goodspeed entitled "Integration of Magnetic Arc Oscillation into the Wire Arc Additive Manufacturing Workflow." I have examined the final electronic copy of this thesis for form and content and recommend that it be accepted in partial fulfillment of the requirements for the degree of Doctor of Philosophy, with a major in Mechanical Engineering.

Dr. Bradley Jared, Major Professor

We have read this thesis
and recommend its acceptance:

Dr. Dustin Gilbert

Dr. Suresh Babu

Dr. Chad Duty

Accepted for the Council:

Dixie L. Thompson

Vice Provost and Dean of the Graduate School

(Original signatures are on file with official student records.)

Integration of Magnetic Arc Oscillation into the Wire Arc Additive Manufacturing Workflow

A Dissertation Presented for the

Doctor of Philosophy

Degree

The University of Tennessee, Knoxville

Devon Russell Goodspeed

August 2025

© by Devon Russell Goodspeed, 2025
All Rights Reserved.

This work is dedicated to my parents, for instilling in us the virtues of lifelong learning, teaching us that every endeavor worth doing is worth doing to the best of our abilities, and demonstrating to us that every educational experience carries with it inherent value.

This one's for you, dad.

Acknowledgements

I would like to thank...

- My brother, Travis Goodspeed, for providing moral and financial support, without which the pursuit of engineering would have been unobtainable.
- My best friend, Mila, for tolerating my late nights at the lab and being willing to accept bacon as bribery to make amends for it.
- Tiffany Quigley, for the late night experiments at the lab, garlic knots and regulating my V8 drink intake through thievery.
- Dylan Lewis, Steven Williams and Bennett Fowler for literally never saying "no" to any ridiculous research requests that I had.
- My coworkers, for being a sounding board to bounce ideas off of, and for being patient to my incessant ramblings about welding, magnets, and my dog.
- Dr. Bradley Jared, for being patient and open to my strange ideas, nurturing my curiosity, and for making me feel like a valued member of a team.

A human being should be able to change a diaper, plan an invasion, butcher a hog, conn a ship, design a building, write a sonnet, balance accounts, build a wall, set a bone, comfort the dying, take orders, give orders, cooperate, act alone, solve equations, analyze a new problem, pitch manure, program a computer, cook a tasty meal, fight efficiently, die gallantly.

Specialization is for insects.

-Robert A. Heinlein

Table of Contents

1 Introduction **1**

1.1 Intellectual Merit 2

1.2 Broader Impacts 2

2 Background **4**

2.1 The Gas Tungsten Arc Welding Process 4

2.2 The Gas Metal Arc Welding Process 8

2.2.1 Short Circuit Gas Metal Arc Welding Process 9

2.2.2 Globular Transfer Gas Metal Arc Welding Process 11

2.2.3 Spray Transfer Gas Metal Arc Welding Process 11

2.2.4 Pulsed Spray Transfer Gas Metal Arc Welding Process 11

2.2.5 Specialty Gas Metal Arc Welding Processes 12

2.3 Wire Arc Additive Manufacturing 12

2.4 Magnetic Arc Oscillation 17

2.5 Magnetic Arc Oscillation with the GMAW Process 20

3 Proposed Solution **24**

3.1 Experimental Test Stands 26

3.1.1 Off-Robot 26

3.1.2 On-Robot 26

3.2 System Development 26

3.2.1 Task 1: Hardware Development 26

3.2.2 Task 2: Control System Development . . . 29
3.2.3 Task 3: Weave Adaptation and Corner Negotiation . . . 29
3.2.4 Task 4: Exploration of Process Limitations . . . 29
3.3 Success Criteria . . . 30
3.3.1 Paired Analysis . . . 30
3.4 Potential Challenges . . . 31
3.4.1 Hardware-Based Challenges . . . 31
3.4.2 Controls-Based Challenges . . . 32
3.4.3 Process-Based Challenges . . . 34
3.5 Potential Risks . . . 34

4 System Requirements **36**
4.1 Functional/Performance Requirements . . . 36
4.2 Trade-offs . . . 36
4.3 Material and Tooling Selection . . . 37
4.3.1 Substrates and Feedstocks . . . 37
4.3.2 Design, Modeling and Controls Tools . . . 38

5 Modeling **39**
5.1 Initial Mathematical Modeling . . . 39
5.2 Data-Driven Modeling . . . 43

6 Electromagnet Design, Manufacturing and Calibration **45**
6.1 Initial Proof of Concept . . . 45
6.2 Electromagnet Modeling, Manufacturing and Calibration . . . 47
6.2.1 Electromagnet Modeling . . . 47
6.2.2 Three-Dimensional Design . . . 48
6.2.3 Manufacturing . . . 48
6.2.4 Testing . . . 51
6.2.5 Calibration . . . 51

7 Off-Robot Hardware **55**

7.1 Torch Fixture Design and Fabrication . . . 55
7.2 Motion Platform . . . 60
7.3 Alignment Procedure . . . 60
7.4 Data Collection . . . 67
7.4.1 Procedure . . . 67
7.4.2 Limitations . . . 67
7.5 Trailing Gas . . . 71
7.6 Imaging . . . 71

8 On-Robot Hardware **77**

8.1 Fabrication Process . . . 77
8.1.1 Design Considerations . . . 77
8.1.2 Fabrication . . . 78
8.2 Alignment Procedure . . . 91
8.3 Data Collection . . . 91
8.4 Trailing Gas . . . 91

9 Control System **99**

9.1 Objectives . . . 99
9.2 Control Hardware . . . 100
9.2.1 Magnet Control Hardware . . . 100
9.2.2 Onboard Sensing . . . 103
9.2.3 Onboard Sensing Limitations . . . 103
9.2.4 Signal Routing . . . 107
9.3 Control Logic . . . 107
9.3.1 Microcontrollers . . . 111
9.3.2 Signal Modeling and Development . . . 111
9.3.3 Signal Transition Smoothing . . . 112
9.3.4 Weave Rotation . . . 117

9.3.5 Weld Simulation . . . 120
9.3.6 Signal Conditioning . . . 120
9.3.7 Programmatic Approach . . . 122
9.4 GTAW to GMAW Transition . . . 127
9.5 Magnetic Field Strength . . . 127

10 Testing, Validation and Results **130**
10.1 Procedures . . . 130
10.1.1 Alignment with Standards . . . 130
10.1.2 +/-100 Percent Offset . . . 132
10.1.3 Elongated Weave . . . 132
10.1.4 Destructive Testing . . . 132
10.1.5 Macro-Etching . . . 147
10.1.6 Dye Penetrant Testing . . . 157
10.2 Final Corner Negotiation Geometry . . . 162
10.3 Paired Analysis . . . 162
10.3.1 Destructive Testing Results . . . 162
10.3.2 Dye Penetrant Results . . . 170
10.3.3 Macro-Etching Results . . . 170
10.3.4 Geometric Comparison . . . 181
10.3.5 Comparison with Data-Driven Model . . . 183
10.3.6 Waveform and Frequency Domain Analysis . . . 189
10.3.7 Exploration of Out-of-Scope Processes . . . 201

11 Discussion **208**
11.1 Interpretation of Test Results . . . 208
11.2 Performance Related To Design Goals . . . 209
11.3 Performance Related to Proposed Challenges and Risks . . . 210
11.3.1 Hardware-Focused . . . 210
11.3.2 Controls-Focused . . . 211

11.3.3 Process-Focused . . . 212
11.4 Limitations of Current Design . . . 212
11.4.1 Hardware Limitations . . . 213
11.4.2 Materials Limitations . . . 213
11.4.3 Model and Controls Limitations . . . 216
11.5 Best Practices for MAO in WAAM . . . 216
11.5.1 Substrates and Feedstocks . . . 217
11.5.2 Hardware . . . 217
11.5.3 Process . . . 217

12 Conclusions and Future Work **218**
12.1 Contributions to Field . . . 218
12.2 Recommendations for Future Development . . . 219

Bibliography **220**

Appendix **228**

A Block Diagrams **228**

B Matlab Scripts **232**
B.1 Predictive Bead Deflection Model . . . 232
B.2 Wire Turn Estimation Script . . . 236
B.3 Data Plotting . . . 239

C Supplementary 316L Welding Waveform Data - Fronius CMT4000 Power Supply **250**
C.1 220ipm 14.3V case . . . 250
C.2 300ipm 24V case . . . 258

D Supplementary 316L Welding Waveform Data - Miller Pipeworx 400 **268**
D.1 200ipm 20.2V Case on Miller Pipeworx400 Power Supply . . . 268

D.2 220ipm 14.3V Case on Miller Pipeworx400 Power Supply 280
D.3 300ipm 24V Case on Miller Pipeworx400 Power Supply 292

E Supplementary 2319AL Welding Waveform Data **304**
E.1 360ipm 20.9V Pulse 2319AL 304
E.2 360ipm 18.3V GMAW 2319AL 313
E.3 360ipm 21V Spray Transfer 2319AL 320

Vita **327**

List of Tables

10.1 Welding Process Parameters - 316L 131
10.2 Tensile Testing Results 168
10.3 Measured Width and Depth of Weld Penetration 181
10.4 Predicted vs Actual Weld Deflections 190
10.5 Recorded Heat Inputs - 316L Fronius Power Supply 202
10.6 Welding Process Parameters - 316L Miller Pipeworx 400 Power Supply . . . 202
10.7 Welding Process Parameters - 316L - Spray Transfer 202
10.8 Welding Process Parameters - 2319AL 206

List of Figures

2.1 Component Diagram of GTAW Torch 4
2.2 Example of GTAW Pulse Waveform (1) 5
2.3 Arc Efficiencies in GMAW and SAW (2) 7
2.4 Heat Source Efficiencies in Various Welding Processes (2) 7
2.5 Droplet Size vs Speed for 7A52AL GMAW Process (3) 8
2.6 Short Circuit Welding Cycle (4) 10
2.7 Example CMT Waveform (5) 13
2.8 CMT Wire Electrode Movement (4) 13
2.9 Tandem GMAW Torch Assembly 15
2.10 GTAW WAAM Torch and Wire Feed Orientation (6) 15
2.11 Non-Gravity Alignment due to Narrow Groove 16
2.12 Illustration of Forces Acting on a Charged Particle in a Magnetic Field (7) . 18
2.13 Diagrammatic Illustration of Arc Deflection (7) 19
2.14 Illustration of MAO in Narrow Groove Geometry (8) 21
2.15 MAO Electromagnetic Field Produced vs Voltage (7) 21
2.16 Arc Column Images for Various Magnetic Oscillation Field Strengths During Narrow Groove Welding (9) 22

3.1 Layout of Research Tasks 25
3.2 University of Tennessee Wire Arc Additive Manufacturing Cell 27
3.3 Illustration of MIL-STD-1913 Mounting Solution 28

4.1 Lincoln Electric Blue Max 316L Wire 37

5.1 Lorentz Force Illustration on GMAW Welding Process 41
5.2 Initial Testing of Mathematical Model 44
5.3 Data Driven Model Output Plot Example 44

6.1 Initial Proof of Concept Electromagnetic Coil 46
6.2 Initial Proof of Concept Experimental Setup 46
6.3 3-Dimensional Model of Electromagnetic Coil Bobbin 49
6.4 Magnetic Coil Winding on Logan 1442 Lathe 49
6.5 Coil Winding Experimental Setup 50
6.6 Pole Piece Torch Forming Fixture 50
6.7 Finished Pole Pieces - 45 and 90 Degree Poles Shown 52
6.8 Assembled Electromagnetic Coil 52
6.9 3d Model of Magnet Characterization Fixture 53
6.10 Comparison of Magnetic Field Strength at Operating Distance 53
6.11 Comparison of Magnetic Field Linear Region with 2.5% Correction Factor . 54

7.1 Off-Robot Full Experimental Setup 56
7.2 Test Fixture 3d Model 56
7.3 Computer Modeled Flat Pattern 57
7.4 Resulting CNC Plasma Cut Components 58
7.5 Final Folded Component from Flat Pattern 59
7.6 Assembled Test Fixture with FDM Printed Alignment Fixture Shown 61
7.7 PWM Controlled Motion Platform 62
7.8 Custom Developed Motion Platform Controller 63
7.9 Motion Platform Process Map 64
7.10 PWM Velocity Profile 65
7.11 Off-Robot Alignment Fixture 65
7.12 GMAW Alignment in Off-Robot Setup 66

7.13 GTAW Alignment in Off-Robot Setup 66
7.14 Arduino-Based Data Collection System 68
7.15 Transparent Model of Arduino-Based Data Collection System 69
7.16 Example Off-Robot Collected Current and Voltage Data 70
7.17 Example Off-Robot FFTs from Current and Voltage Data 70
7.18 CK Worldwide TS300 Trailing Gas Shield 72
7.19 CK Worldwide Trailing Gas Shield Installed on GMAW Torch 72
7.20 Custom Manufactured Trailing Gas Controller 73
7.21 Trailing Gas Process Map 74
7.22 Visible Weld Camera 75
7.23 Nikon D5100 Imaging Setup 75
7.24 Example Captured Image Using Nikon D5100 76

8.1 Torch-based Hardware Mounting Solution for Kuka KR6-2 79
8.2 Raw Material for Torch Mounting Solution on Kuka KR6-2 80
8.3 In-Process Machining for Kuka KR6-2 MAO Mounting Solution 81
8.4 In-Process Thread Cutting for Kuka KR6-2 MAO Mounting Solution 82
8.5 LSM9-DS1 Accelerometer Torch Mounting Bracket 3d Model 83
8.6 LSM9-DS1 Accelerometer Torch Mounting Bracket 84
8.7 LSM9-DS1 Accelerometer Mounting Bracket Maximum (+) Adjustment . . . 85
8.8 LSM9-DS1 Accelerometer Mounting Bracket Maximum (-) Adjustment . . . 85
8.9 LSM9-DS1 Accelerometer Mounted on Kr6-2 86
8.10 LSM9-DS1 Accelerometer Bracket Heat Damage 87
8.11 CNC Plasma Cut Path for Kuka KR6-2 Magnet Mounting 88
8.12 Complete Magnet Mounting Solution for Kuka KR6-2 89
8.13 Total Weight of KR6-2 Torch Mounted Components 90
8.14 Bosch GLL2 Self Correcting Line Laser 92
8.15 Laser Cross-line Layout 93
8.16 Laser Alignment of Wire Electrode, Magnetic Pole Piece and Accelerometer 94

8.17 Miller LEM Data Acquisition System 95
8.18 Omnidirectional Trailing Gas Shield 96
8.19 Triple Nozzle Trailing Gas Configuration 98

9.1 Example PWM Signal 100
9.2 Relay-Based Initial Breadboarding 102
9.3 BTS7960 H-Bridge Motor Driver 102
9.4 B0B389WHM6 Photodiode Sensor Module 104
9.5 LSM9DS1 IMU 104
9.6 135 Degree Path X (blue) and Y (yellow) Acceleration 105
9.7 45 Degree Path X (blue) and Y (yellow) Acceleration 105
9.8 90 Degree Path X (blue) and Y (yellow) Acceleration 106
9.9 90 Degree Path Signal During Conditioning 106
9.10 Moving Standard Deviations of 90 Degree Path Acceleration Signals 106
9.11 90 Degree Corner Path Conditioned Signal Angular Output 108
9.12 Initial Breadboard Iteration 108
9.13 PCB Wiring Schematic 109
9.14 PCB Signal Routing Layout 110
9.15 Current PCB Iteration 110
9.16 Trigonometric Relationship Between Sines and Cosines 113
9.17 Circular Path Stationary Overhead Visualization 113
9.18 Signal Flow Chart 114
9.19 Stationary Figure 8 Weld Simulation Example 115
9.20 Spiral Weave Example 115
9.21 Triangular Weave Example 116
9.22 Figure-8 Weave Example 116
9.23 Simulated Angle Changes with PID Control 118
9.24 Simulated Random Angle Changes with PID Control 118
9.25 EPA US06 Emissions Drive Cycle (10) 119

9.26 Three Weld Weave Patterns with PID Controlled Transition 119
9.27 Three Weld Weave Patterns with PID Controlled Autogenous GTAW Weld . 119
9.28 Stationary 45-Degree Rotated Figure-8 Weave Example 119
9.29 Velocity-Incorporated Figure 8 Weld Simulation Example 121
9.30 Figure 8 Weaving Profile with Split Signals 121
9.31 Figure 8 Weaving Profile PWM Output Signals 123
9.32 Final Geometry Layout 124
9.33 Time vs Angle Final Geometry Path Plan 125
9.34 Final Geometry X-Deflection Output Pre PWM Conversion 125
9.35 Final Geometry Y-Deflection Output Pre PWM Conversion 126
9.36 Arc Length Differences in GMAW vs GTAW 128
9.37 External Magnetic Field Strength Differences in GMAW vs GTAW-based MAO Experiments 128

10.1 100 Percent Offset Deflection Path 133
10.2 Keyence VR-5000 134
10.3 100 Percent Offset Scanned Weld Bead 135
10.4 Elongated Weave Samples As Deposited 135
10.5 WAAM Produced 316L Destructive Testing Sample Wall 136
10.6 Destructive Testing Sample Wall Cut Profile 136
10.7 Substrate Removal and Machining 138
10.8 Waterjet Workholding Backing Plate 139
10.9 Waterjet Workholding Backing Plate with Welding Samples 140
10.10OMAX 2626 Waterjet 141
10.11Waterjet Cut Tensile Test Samples Pre-Machining 142
10.12Tensile Test Sample Rough Machining 143
10.13FDM Manufactured Machining Soft Vise Jaws 143
10.14Tensile Test Sample in FDM Manufactured Vise Soft Jaw 144
10.15Tensile Test Samples Pre vs Post Machining 145

10.16Tensile Testing Experimental Setup 146
10.17Insize HDT-RW160 Hardness Tester 148
10.18Material Being Hardness Tested 149
10.19AWS D1.6 Guidance on Bend Test Specimens (11) 149
10.20AWS D1.6 Guidance on Bend Test Fixture Dimensions (11) 150
10.21Bend Test Samples for Kinematic and MAO Material 151
10.22Bend Testing Experimental Setup (Pre-Sample Deformation) 152
10.23Bend Testing Experimental Setup (Post-Sample Deformation) 153
10.24Sampled Elongated Weave Testing Material (Post Dye-Penetrant Machining) 154
10.25EDM-Cut Sample Sections for Macro Etching 155
10.26Final Etch Sample Polish 156
10.27Dye Penetrant Sample Machining 158
10.28Machined Dye Penetrant Sample 159
10.29Example Area of Concern for Dye Penetrant Removal Process 160
10.30Aerosol Dye Penetrant Testing Material 161
10.31Dye Penetrant Experimental Setup 161
10.32Final Geometry Path Layout 163
10.33Final Geometry as Deposited 164
10.34Final Geometry After Wire-brushing 165
10.35Tensile Testing Results 166
10.36Diffuse Necking Along Gage Length 167
10.37Hardness Testing Results 169
10.38MAO-based Exterior Bend Test Results 171
10.39Kinematically Woven Exterior Bend Test Results 171
10.40Bend Test Interior Face Results (MAO shown above) 172
10.41Dye Penetrant Tested Sample 173
10.42Dye Penetrant Tested Sample 174
10.43Dye Penetrant Tested Traditionally Deposited Material 175
10.44Dye Penetrant Tested MAO Deposited Material 176

10.45Macro Etching Results for Traditional and MAO Cases 177
10.46Wall Samples Prior to Etching (MAO on left) 178
10.47Macro Etched Wall Samples (MAO on right) 179
10.48Macro Etching Example Layout 180
10.49CSWIP 3.1 Guidance on Gas Composition Effect on Weld Bead Profile (12) 182
10.50Deflection Magnitude Evaluation Method 182
10.51Deflected Weld Bead Profiles 182
10.52Parameter Set 4 Symmetry Evaluation 184
10.53Parameter Set 3 Symmetry Evaluation 184
10.54Sectioned Samples for Wall Thickness Deviation Examination 185
10.55Perimeter Sketch for Wall Thickness Deviation Examination 186
10.56Evaluation Method for Wall Thickness Deviation (kinematic example shown) 187
10.57Evaluation Method for Straightness Deviation (kinematic example shown) . 188
10.58Predictive Model Output Plot for Parameter Set 5 190
10.59Predictive Model Output for Parameter Set 5 190
10.60Parameter Set 5 Width Measurement Locations 191
10.61Measured Values for Parameter Set 5 Width 191
10.62Voltage vs Time (Area of Interest Highlighted) for 200ipm/20.1V Case . . . 192
10.63Current vs Time (Area of Interest Highlighted) for 200ipm/20.1V Case . . . 192
10.64MATLAB Average Current and Voltage Output for 200ipm/20.1V Case . . . 193
10.65MATLAB Current Output for 200ipm/20.1V Case in Interval 1 193
10.66MATLAB Voltage Output for 200ipm/20.1V Case in Interval 1 194
10.67MATLAB Current Output for 200ipm/20.1V Case in Interval 2 194
10.68MATLAB Voltage Output for 200ipm/20.1V Case in Interval 2 195
10.69MATLAB Overlaid Voltage Output for 200ipm/20.1V Case 195
10.70MATLAB Overlaid Current Output for 200ipm/20.1V Case 196
10.71MATLAB FFT Plot for Interval 1 in 200ipm/20.1V Case 197
10.72MATLAB FFT Plot for Interval 2 in 200ipm/20.1V Case 198
10.73MATLAB Voltage FFT Overlaid for 200ipm/20.1V Case 198

10.74MATLAB Current FFT Overlaid for 200ipm/20.1V Case 199
10.75MATLAB Voltage FFT Overlaid for Entire Range of 200ipm/20.1V Case . . 199
10.76MATLAB Current FFT Overlaid for Entire Range of 200ipm/20.1V Case . . 200
10.77Stationary Spray Transfer Welding Arc 203
10.78Deflected Spray Transfer Welding Arc 203
10.79Test GTAW-MAO Weld (left) vs Traditional Weld (right) on A36/1018 Substrate 204
10.80Spray Transfer Test Weld on A36/1018 Substrate 206
10.812319Al Test Welds (Left to right: Spray Transfer, GMAW, CMT, GMAW-P shown) 207

11.1 Demonstration of Substrate to Magnetic Pole Clearance 214
11.2 Comparison of Potential Magnetic Pole Redesign (Left) vs Current Geometry (Right) for Improved Substrate Clearance 215

A.1 Simulink Signal Input Block Diagrams 229
A.2 X and Y Signal Development Block Diagram 229
A.3 Travel Direction Adaptation Block Diagram 230
A.4 Response Tuning Block Diagram 230
A.5 Signal Visualization Block Diagram 231
A.6 Simulink Signal Output Block Diagram 231

C.1 Voltage vs Time (Area of Interest Highlighted) for 220ipm/14.3V Case . . . 251
C.2 Current vs Time (Area of Interest Highlighted) for 220ipm/14.3V Case . . . 251
C.3 MATLAB Current Output for 220ipm/14.3V Case in Interval 1 252
C.4 MATLAB Voltage Output for 220ipm/14.3V Case in Interval 1 252
C.5 MATLAB Current Output for 220ipm/14.3V Case in Interval 2 253
C.6 MATLAB Voltage Output for 220ipm/14.3V Case in Interval 2 253
C.7 MATLAB Overlaid Current Output for 220ipm/14.3V Case 254
C.8 MATLAB Overlaid Voltage Output for 220ipm/14.3V Case 254

C.9 MATLAB FFT Plot for Interval 1 in 220ipm/14.3V Case 255
C.10 MATLAB FFT Plot for Interval 2 in 220ipm/14.3V Case 255
C.11 MATLAB Voltage FFT Overlaid for 220ipm/14.3V Case 256
C.12 MATLAB Current FFT Overlaid for 220ipm/14.3V Case 256
C.13 MATLAB Voltage FFT Overlaid for Entire Range of 220ipm/14.3V Case . . 257
C.14 MATLAB Current FFT Overlaid for Entire Range of 220ipm/14.3V Case . . 257
C.15 Voltage vs Time (Area of Interest Highlighted) for 300ipm/24V Case 259
C.16 Current vs Time (Area of Interest Highlighted) for 300ipm/24V Case 259
C.17 Average Current and Voltage for Areas of Interest for 300ipm/24V Case . . . 260
C.18 MATLAB Current Output for 300ipm/24V Case in Interval 1 260
C.19 MATLAB Voltage Output for 300ipm/24V Case in Interval 1 261
C.20 MATLAB Current Output for 300ipm/24V Case in Interval 2 261
C.21 MATLAB Voltage Output for 300ipm/24V Case in Interval 2 262
C.22 MATLAB Overlaid Current Output for 300ipm/24V Case 262
C.23 MATLAB Overlaid Voltage Output for 300ipm/24V Case 263
C.24 MATLAB FFT Plot for Interval 1 in 300ipm/24V Case 263
C.25 MATLAB FFT Plot for Interval 2 in 300ipm/24V Case 264
C.26 MATLAB Voltage FFT Overlaid for 300ipm/24V Case 265
C.27 MATLAB Current FFT Overlaid for 300ipm/24V Case 266
C.28 MATLAB Voltage FFT Overlaid for Entire Range of 300ipm/24V Case . . . 267
C.29 MATLAB Current FFT Overlaid for Entire Range of 300ipm/24V Case . . . 267

D.1 Voltage vs Time for 200ipm/20.2V Case on Miller Pipeworx400 Power Supply 269
D.2 Current vs Time for 200ipm/20.2V Case on Miller Pipeworx400 Power Supply 269
D.3 MATLAB Current Output for 200ipm/20.2V Case on Miller Pipeworx400 Power Supply 270
D.4 MATLAB Voltage Output for 200ipm/20.2V Case on Miller Pipeworx400 Power Supply 271

D.5 MATLAB Current Output for 200ipm/20.2V Case on Miller Pipeworx400 Power Supply 272
D.6 MATLAB Voltage Output for 200ipm/20.2V Case on Miller Pipeworx400 Power Supply 273
D.7 MATLAB Overlaid Current Output for 200ipm/20.2V Case on Miller Pipeworx400 Power Supply 274
D.8 MATLAB Overlaid Voltage Output for 200ipm/20.2V Case on Miller Pipeworx400 Power Supply 275
D.9 MATLAB FFT Plot for Interval 1 in 200ipm/20.2V Case on Miller Pipeworx400 Power Supply 276
D.10 MATLAB FFT Plot for Interval 2 in 200ipm/20.2V Case on Miller Pipeworx400 Power Supply 277
D.11 MATLAB Voltage FFT Overlaid for 200ipm/20.2V Case on Miller Pipeworx400 Power Supply 278
D.12 MATLAB Current FFT Overlaid for 200ipm/20.2V Case on Miller Pipeworx400 Power Supply 279
D.13 Voltage vs Time for 220ipm/14.3V Case on Miller Pipeworx400 Power Supply 281
D.14 Current vs Time for 220ipm/14.3V Case on Miller Pipeworx400 Power Supply 281
D.15 MATLAB Current Output for 220ipm/14.3V Case on Miller Pipeworx400 Power Supply 282
D.16 MATLAB Voltage Output for 220ipm/14.3V Case on Miller Pipeworx400 Power Supply 283
D.17 MATLAB Current Output for 220ipm/14.3V Case on Miller Pipeworx400 Power Supply 284
D.18 MATLAB Voltage Output for 220ipm/14.3V Case on Miller Pipeworx400 Power Supply 285
D.19 MATLAB Overlaid Current Output for 220ipm/14.3V Case on Miller Pipeworx400 Power Supply 286

D.20 MATLAB Overlaid Voltage Output for 220ipm/14.3V Case on Miller Pipeworx400 Power Supply 287
D.21 MATLAB FFT Plot for Interval 1 in 220ipm/14.3V Case on Miller Pipeworx400 Power Supply 288
D.22 MATLAB FFT Plot for Interval 2 in 220ipm/14.3V Case on Miller Pipeworx400 Power Supply 289
D.23 MATLAB Voltage FFT Overlaid for 220ipm/14.3V Case on Miller Pipeworx400 Power Supply 290
D.24 MATLAB Current FFT Overlaid for 220ipm/14.3V Case on Miller Pipeworx400 Power Supply 291
D.25 Voltage vs Time for 300ipm/24V Case on Miller Pipeworx400 Power Supply 293
D.26 Current vs Time for 300ipm/24V Case on Miller Pipeworx400 Power Supply 293
D.27 MATLAB Current Output for 300ipm/24V Case on Miller Pipeworx400 Power Supply 294
D.28 MATLAB Voltage Output for 300ipm/24V Case on Miller Pipeworx400 Power Supply 295
D.29 MATLAB Current Output for 300ipm/24V Case on Miller Pipeworx400 Power Supply 296
D.30 MATLAB Voltage Output for 300ipm/24V Case on Miller Pipeworx400 Power Supply 297
D.31 MATLAB Overlaid Current Output for 300ipm/24V Case on Miller Pipeworx400 Power Supply 298
D.32 MATLAB Overlaid Voltage Output for 300ipm/24V Case on Miller Pipeworx400 Power Supply 299
D.33 MATLAB FFT Plot for Interval 1 in 300ipm/24V Case on Miller Pipeworx400 Power Supply 300
D.34 MATLAB FFT Plot for Interval 2 in 300ipm/24V Case on Miller Pipeworx400 Power Supply 301

D.35 MATLAB Voltage FFT Overlaid for 300ipm/24V Case on Miller Pipeworx400 Power Supply 302
D.36 MATLAB Current FFT Overlaid for 300ipm/24V Case on Miller Pipeworx400 Power Supply 303

E.1 Voltage vs Time for 360ipm/20.9V Pulsed Transfer Case 305
E.2 Current vs Time for 360ipm/20.9V Pulsed Transfer Case 305
E.3 MATLAB Current Output for 360ipm/20.9V Pulsed Transfer Case in Interval 1 306
E.4 MATLAB Voltage Output for 360ipm/20.9V Pulsed Transfer Case in Interval 1 307
E.5 MATLAB Current Output for 360ipm/20.9V Pulsed Transfer Case in Interval 2 308
E.6 MATLAB Voltage Output for 360ipm/20.9V Pulsed Transfer Case in Interval 2 309
E.7 MATLAB Overlaid Current Output for 360ipm/20.9V Pulsed Transfer Case 309
E.8 MATLAB Overlaid Voltage Output for 360ipm/20.9V Pulsed Transfer Case . 310
E.9 MATLAB FFT Plot for Interval 1 in 360ipm/20.9V Pulsed Transfer Case . . 310
E.10 MATLAB FFT Plot for Interval 2 in 360ipm/20.9V Pulsed Transfer Case . . 311
E.11 MATLAB Voltage FFT Overlaid for 360ipm/20.9V Pulsed Transfer Case . . 311
E.12 MATLAB Current FFT Overlaid for 360ipm/20.9V Pulsed Transfer Case . . 312
E.13 Voltage vs Time for 360ipm/18.3V GMAW Case 314
E.14 Current vs Time for 360ipm/18.3V GMAW Case 314
E.15 MATLAB Current Output for 360ipm/18.3V GMAW Case in Interval 1 . . . 315
E.16 MATLAB Voltage Output for 360ipm/18.3V GMAW Case in Interval 1 . . . 315
E.17 MATLAB Current Output for 360ipm/18.3V GMAW Case in Interval 2 . . . 316
E.18 MATLAB Voltage Output for 360ipm/18.3V GMAW Case in Interval 2 . . . 316
E.19 MATLAB Overlaid Voltage Output for 360ipm/18.3V GMAW Case 317
E.20 MATLAB Overlaid Current Output for 360ipm/18.3V GMAW Case 317
E.21 MATLAB FFT Plot for Interval 1 in 360ipm/18.3V GMAW Case 318
E.22 MATLAB FFT Plot for Interval 2 in 360ipm/18.3V GMAW Case 318
E.23 MATLAB Voltage FFT Overlaid for 360ipm/18.3V GMAW Case 319
E.24 MATLAB Current FFT Overlaid for 360ipm/18.3V GMAW Case 319

E.25 Voltage vs Time for 360ipm/21V Spray Transfer Case 321
E.26 Current vs Time for 360ipm/21V Spray Transfer Case 321
E.27 MATLAB Current Output for 360ipm/21V Spray Transfer Case in Interval 1 322
E.28 MATLAB Voltage Output for 360ipm/21V Spray Transfer Case in Interval 1 322
E.29 MATLAB Current Output for 360ipm/21V Spray Transfer Case in Interval 2 323
E.30 MATLAB Voltage Output for 360ipm/21V Spray Transfer Case in Interval 2 323
E.31 MATLAB Overlaid Voltage Output for 360ipm/21V Spray Transfer Case . . 324
E.32 MATLAB Overlaid Current Output for 360ipm/21V Spray Transfer Case . . 324
E.33 MATLAB FFT Plot for Interval 1 in 360ipm/21V Spray Transfer Case . . . 325
E.34 MATLAB FFT Plot for Interval 2 in 360ipm/21V Spray Transfer Case . . . 325
E.35 MATLAB Voltage FFT Overlaid for 360ipm/21V Spray Transfer Case 326
E.36 MATLAB Current FFT Overlaid for 360ipm/21V Spray Transfer Case . . . 326

Chapter 1

Introduction

The current state of the art in the Wire Arc Additive Manufacturing (WAAM) industry involves adjusting a robot's kinematic programming to deflect from the centerline of the direction of travel, creating certain weaving patterns. This approach, however, can lead to shutdown conditions in certain circumstances when the direction of travel changes, stemming from errors in the robot's kinematic system which currently cannot be predicted nor recovered from. Moving this weaving profile external to the motion kinematics of the system by deflecting the welding arc through the influence of external magnetic fields could resolve this issue, as well as provide the ability to better tailor the process to the desired final product.

While the utilization of external magnetic fields within various welding processes is not a contemporary concept, very seldom is it seen integrated into the wire arc additive manufacturing architecture (6; 13). Additionally, it is also rarely used in Gas Metal Arc Welding (GMAW) applications outside of narrow-groove welding processes in which current commercially available solutions are analog devices that have limited application due to a lack of programmability and control. Historically used as a process aid in long-run industrial welding applications, such as power piping, or to tailor grain structure in research applications, Magnetic Arc Oscillation (MAO) involves the use of electromagnets to influence the position of an electric welding arc by varying the field strength output by electromagnets to create a desired amount of deflection due to the Lorentz force imparted on a charged

particle, in this case the arc itself, within a magnetic field. By utilizing this process within the additive manufacturing space, robotic kinematic input requirements could be dramatically reduced, allowing for a combination of decreased overall build times, comparable quality and increased equipment maintenance windows, all while resolving the aforementioned kinematic programming errors seen in current systems.

This research aims to design and prototype a low-cost, modular engineered solution to this problem, capable of being retrofit in a configuration that expands upon existing welding hardware.

1.1 Intellectual Merit

This work will advance the capabilities of WAAM by leveraging legacy welding techniques and combining them with modern controllability meant for integration into a WAAM framework. Currently there is little published work on the use of magnetic arc oscillation techniques in WAAM, with much of it being GTAW-based (6; 13), and this work aims to close that gap. Further, this work will also generate new knowledge in the GMAW-based magnetic arc oscillation space by serving as a critical resource for those who wish to incorporate MAO into a larger WAAM framework by detailing the hardware, control systems, and challenges faced throughout the development process.

1.2 Broader Impacts

When compared to traditional subtractive manufacturing techniques, WAAM aids in both reducing lead times and optimizing material usage to reduce waste. This can contribute to reduced overall manufacturing cost, particularly on small-batch parts, as well as potentially providing a cost-effective solution to supply chain shortages. By leveraging WAAM as part of a larger hybrid-manufacturing framework, where additive and subtractive manufacturing techniques are combined, long lead times for raw billets could be circumvented, reducing national dependency on foreign suppliers and helping to bolster supply chain security. To

support this, advanced control techniques must be established to reduce frequency of failed parts, as well as increase throughput. By using magnetic arc oscillation technology, the final part could reach the end user with comparable quality and improved process efficiency.

Chapter 2

Background

2.1 The Gas Tungsten Arc Welding Process

First patented in 1941 by Russell Meredith (Figure 2.1) and based off an earlier 1890 patent by C.L. Coffin (14; 15), Gas Tungsten Arc Welding (GTAW), also referred to as Tungsten Inert Gas (TIG) welding was developed when a need to weld magnesium arose for the aircraft industry. In GTAW welding, the arc is maintained between the workpiece and a tungsten-alloy non-consumable electrode and is shielded and sustained by being enveloped by an inert gas, such as argon, helium, or a mixture thereof.

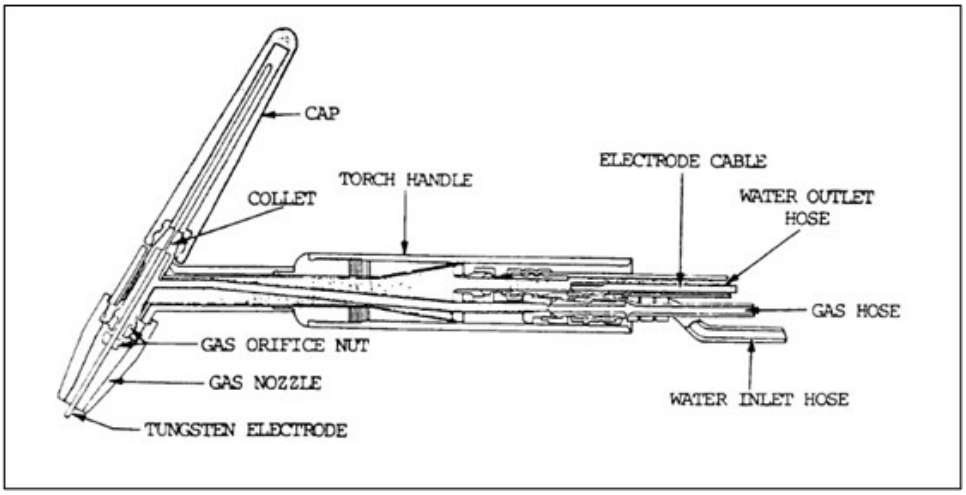


Figure 2.1: Component Diagram of GTAW Torch

Several types of GTAW welding modes are available in modern power supplies. These include direct-current-electrode-negative (DCEN), direct-current-electrode-positive (DCEP), and alternating-current (AC) modes. While the latter has cleaning properties due to the arc balancing characteristics of the AC welding architecture and is ideally suited to aluminum joining, DCEN-configured GTAW is the most common due to increased tungsten wear with DCEP, and is well-suited to mild steel, stainless steels, and titanium welding. In a DCEN configuration, the substrate acts as the anode and the tungsten electrode acts as the cathode. As a result of this configuration, a single, localized cathode spot is formed at the tip of the tungsten electrode and is both stationary and highly constrained (16). While beneficial for the deep, concentrated heat that this polarity provides, the arc can become unstable if the cathode spot is disrupted by wear or contamination and cleanliness is of utmost importance during this process. Each of these processes can be combined with a pulsing strategy, whereby the welding operator specifies a maximum current, minimum current, usually in a percentage of the maximum value, and desired number of pulses per second. With this, the power supply will alternate between the chosen maximum and minimum current in conformance to a specific waveform, seen in Figure 2.2.

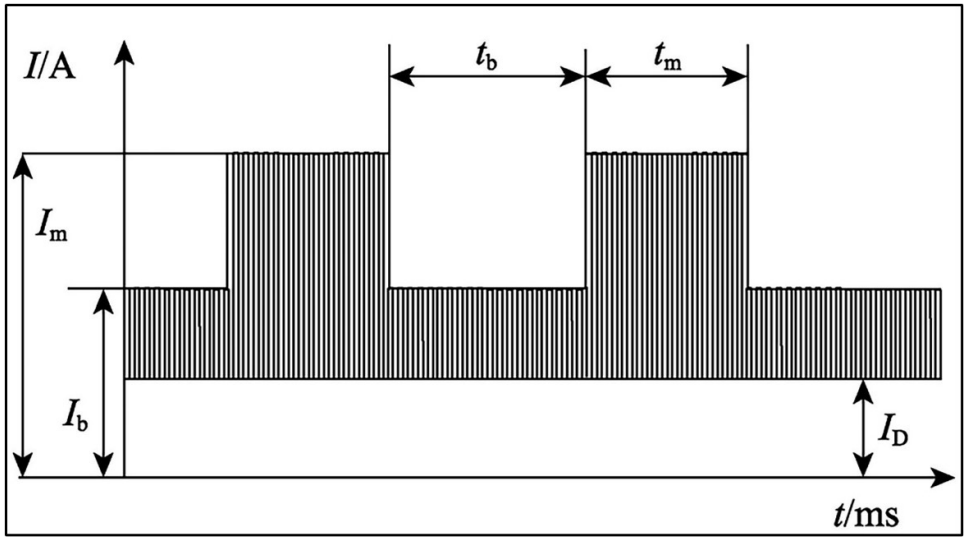


Figure 2.2: Example of GTAW Pulse Waveform (1)

GTAW produces high quality welds with low distortion, no spatter, can weld dissimilar materials and offers improved welding heat control when compared to GMAW processes. Since the arc is concentrated, the Heat-Affected Zone (HAZ) of a GTAW weld is also much narrower than comparable processes, but these advantages come at the cost of lower material deposition rates and traditionally steeper learning curves for manual weld operators to master the process. Current GTAW research is focused on mathematically modeling the melt pool physics (17), improving process stability (6), and continuing research into novel materials (18).

Welding heat input can be calculated for GTAW and other welding processes by using Equation 2.1 below, where U is welding voltage, I is welding current, and V is the welding travel speed. Welding efficiency, η, is calculated in equation 2.2, where H* is the heat absorbed by the substrate, and E_{weld} is the calculated welding energy, shown in equation 2.1 by omitting η. (19; 20). Industry accepted estimated efficiency values for various welding processes are referenced in Figures 2.3 and 2.4.

$$H = \frac{UI}{V}\eta \tag{2.1}$$

$$\eta = \frac{H^*}{E_{weld}} \tag{2.2}$$

Due to the decoupling of heat input and material deposition processes, GTAW welding has many observational benefits within the research space, since the welding arc can be observed without the spatter-producing mass transfer required of consumable electrode processes, such as GMAW, outlined in section 2.2.

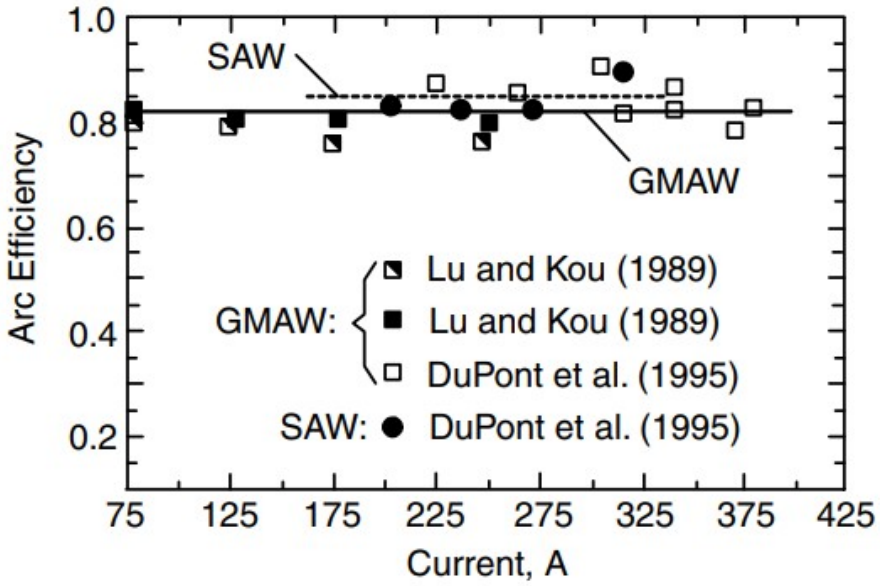


Figure 2.3: Arc Efficiencies in GMAW and SAW (2)

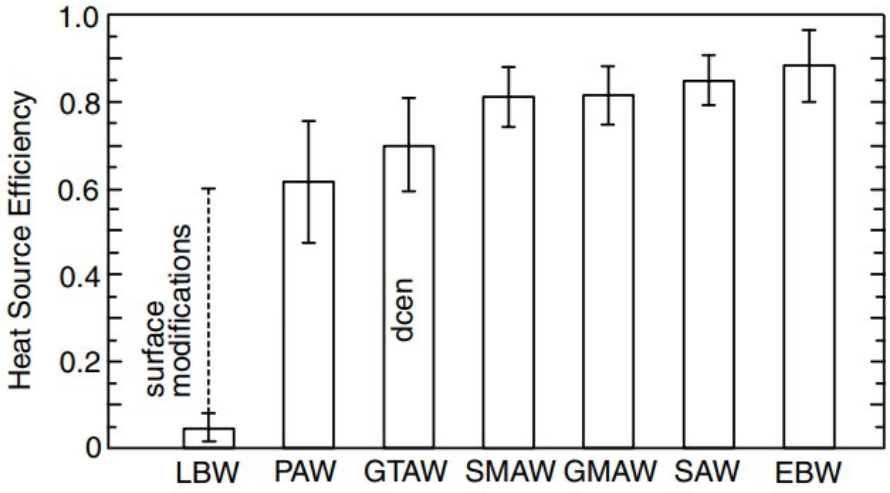


Figure 2.4: Heat Source Efficiencies in Various Welding Processes (2)

2.2 The Gas Metal Arc Welding Process

Widely favored for its versatility, ease of use, and efficiency in many industrial applications, Gas Metal Arc Welding (GMAW) is similar to GTAW in that an electric arc is employed to melt and join metals, aided by an inert or semi-inert shielding gas environment. In contrast to GTAW, however, GMAW utilizes a consumable wire electrode and coupled heat and mass inputs, which allows for high travel speeds, reduced production times, shallower learning curve for operators, minimal post-weld cleanup, enhanced productivity and consistency in production environments, such as automotive production and shipbuilding applications. GMAW welding can be broken primarily into five different categories: Short Circuit GMAW, Globular Transfer, Spray Transfer, Pulsed Spray Transfer, and specialty GMAW processes. Example droplet size related to velocity for a 200A, 20V GMAW process on 7A52AL alloy can be seen in Figure 2.5.

In contrast to the GTAW welding process, outlined in Section 2.1, the GMAW welding process employs a direct-current-electrode-positive polarity, whereby the substrate acts as

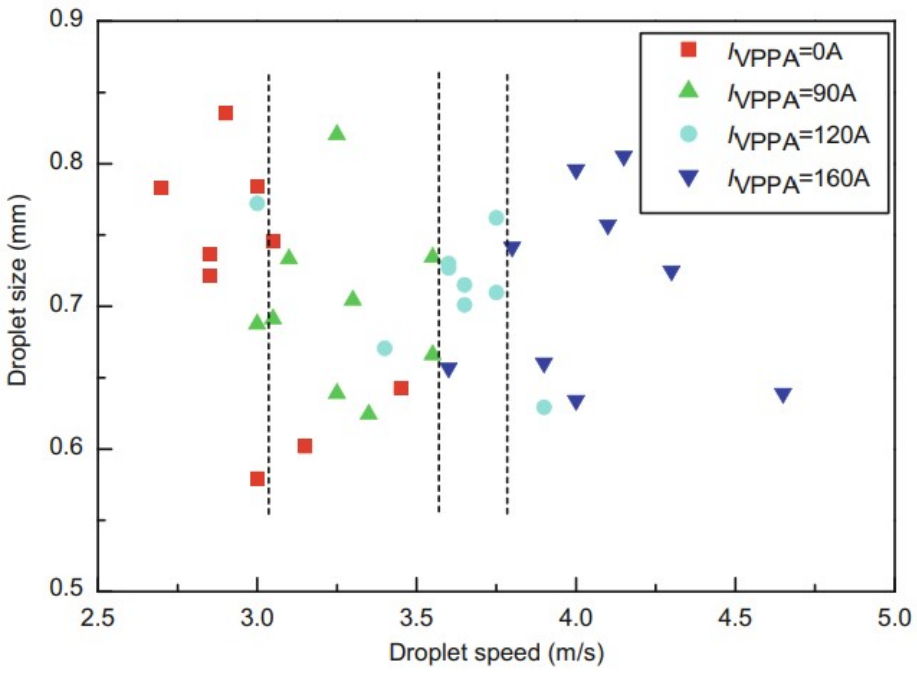


Figure 2.5: Droplet Size vs Speed for 7A52AL GMAW Process (3)

the cathode and the consumable electrode acts as the anode. Because of this orientation, the cathode spot forms on the surface of the base metal and not the electrode, as seen in the GTAW case. Current research efforts into the cathode location in the GMAW welding process (2; 21) indicate that, rather than a single fixed point, there are multiple micro cathode spots that traverse the surface of the substrate dynamically and localized heating is observed due to this. As these spots travel across the surface of the substrate, they also aid in distributing thermal fluxes across the melt pool, which aid in droplet detachment, disrupt oxide layer formation and increase melt pool fluidity, which are beneficial characteristics of the GMAW heat transfer process.

2.2.1 Short Circuit Gas Metal Arc Welding Process

Often referred to as dip-transfer, short-circuit GMAW is characterized by low current input. In this process, a continuously fed consumable wire electrode contacts the workpiece, creating a short circuit that generates heat through electrical resistance to melt the electrode and deposit material onto the substrate. Due to its low-current input, this process is ideally suited for thinner materials and more intricate welding. This process also produces minimal spatter and is preferred in non-gravity-aligned welds.

Shown in Figure 2.6a, during the short circuit GMAW process, the filler material physically contacts the workpiece, shorting the circuit. This causes the filler to melt and "neck down" due to increased resistance in the wire (2.6b), where it isolates from the substrate, causing an arc (2.6c), setting down a small droplet of the filler material and creating a melt pool. The heat of the arc then smoothes the melt pool (2.6d), where the advancing wire feed extinguishes the arc (2.6e), and the filler material is advanced towards the substrate once again, causing the process to repeat (2.6f). This process repeats $\sim 20-200$ times per second, with higher frequencies generally corresponding to a more stable process. (4).

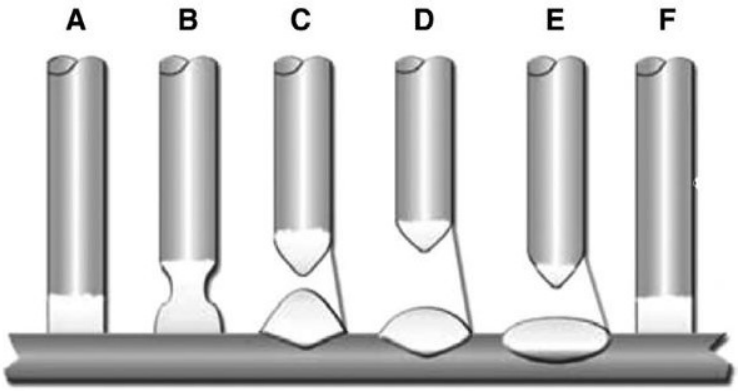


Figure 2.6: Short Circuit Welding Cycle (4)

2.2.2 Globular Transfer Gas Metal Arc Welding Process

In the globular transfer GMAW process, larger droplets (> electrode diameter) are transferred from the consumable electrode to the melt pool at higher current when compared to the short-circuit process outlined in Section 2.2.1, creating a more robust welding arc. In this process, the consumable electrode forms larger droplets that detach and are deposited into the melt pool, resulting in deeper penetration, making it particularly suitable for thicker material welding in gravity-aligned positions, at the expense of increased spatter and a more robust, but less stable, arc generated.

2.2.3 Spray Transfer Gas Metal Arc Welding Process

Usually employed at welding parameters above 30 volts and 200 amps, spray transfer GMAW produces a transfer of fine droplets of material from the consumable electrode to the melt pool, producing a smooth, stable arc and high quality welds. The finer droplets provide improved penetration and minimal spatter, but limited to thicker materials and gravity-aligned applications. Spray transfer is seldom utilized in WAAM applications due to its increased heat input characteristics.

2.2.4 Pulsed Spray Transfer Gas Metal Arc Welding Process

Similar to pulsed GTAW, outlined in Section 2.1, pulsed spray transfer GMAW is a more advanced welding process that involves alternating welding current levels between high and low set points to better control droplet transfer from the consumable welding electrode to the melt pool. This pulsing process provides a better atomization of filler metal droplets that provides optimized penetration characteristics while minimizing heat input when compared to traditional spray transfer, making it ideal for thinner materials and more complex geometries. This process is ideally suited for applications where precise parameter control is available and quality and precision are critical.

2.2.5 Specialty Gas Metal Arc Welding Processes

Cold Metal Transfer

The Cold Metal Transfer (CMT) GMAW-based process, pioneered by Fronius of Austria in 2004 (4), utilizes a reciprocating wire electrode (22) that produces a lower material deposition rate (2-3 kg/hr vs 3-4 kg/hr with traditional GMAW) but is considered to be a significantly reduced heat input process with little to no weld spatter at various welding positions, an example waveform of which can be seen in figure 2.7. During this process, an alternating current servo is added to the filler deposition mechanism such that the wire is retracted at $\sim 0-70Hz$, aiding in droplet detachment. The droplet then gets transferred to the melt pool by electromagnetic force and the retraction force of the melt pool (4). The wire electrode movement during this process is illustrated in Figure 2.8.

2.3 Wire Arc Additive Manufacturing

Wire Arc Additive Manufacturing (WAAM) is a 3D printing technology that uses an electric arc to melt metallic filler wire material and deposit it layerwise to create a three-dimensional object. This technology has gained popularity in recent years due to its ability to create large-scale parts with a low-cost and high-speed production process when compared to that of other metal additive manufacturing processes, such as laser powder bed fusion, where metallic powder is melted in successive layers contained within an inert environment until the final geometry is realized. WAAM has several advantages over traditional manufacturing methods, including reduced material waste, improved design flexibility, the ability to create complex geometries not possible through traditional casting and forging methods, and reduced costs for small manufacturing runs. (23) While WAAM offers many advantages when compared to more traditional processes, there are some design constraints, most notable of which is that the produced pieces may have altered mechanical properties than their traditional counterparts due to high heat input and rapid cooling rates during the process. These produced parts are also susceptible to distortion due to material contraction while cooling.

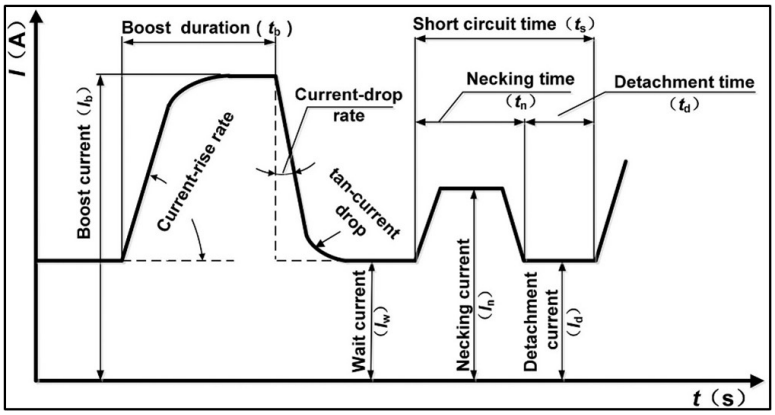


Figure 2.7: Example CMT Waveform (5)

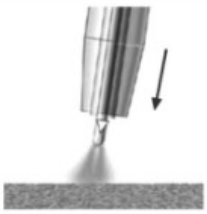
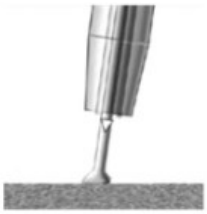
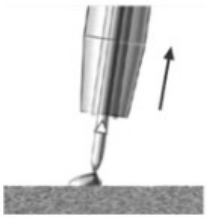
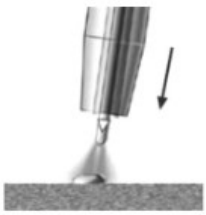
S. No.	The succession of the wire electrode movement	Description
1.		The wire electrode moves toward the weld puddle during the weld arc initiation.
2.		The welding arc extinguishes when the filler wire descends into the melted weld puddle. The current drops.
3.		A back-drawing force acts upon the wire electrode for reverse movement leading to the droplet separation amid the short circuit. The current and voltage values are lowered.
4.		The movement of the wire electrode is reversed for the commencement of the next cycle.

Figure 2.8: CMT Wire Electrode Movement (4)

There are currently three primary methods of material deposition for WAAM; Gas Metal Arc Welding (GMAW), Gas Tungsten Arc Welding (GTAW), and Plasma Arc Welding (PAW) (24; 25). Traditional GMAW-based WAAM utilizes a constant velocity consumable wire electrode, and benefits from higher material deposition rates (26) and low equipment cost at the expense of poor arc stability and the presence of weld spatter.

Last of the GMAW WAAM processes is Tandem GMAW, whereby a WAAM system utilizes two consumable wire electrodes fed into a melt pool simultaneously, the torch assembly of which can be seen in Figure 2.9. (27) In this configuration, higher deposition rates are achieved (6-8 kg/hr). It is also easier to tailor material composition with this process, at the expense of higher heat input and the possibility of increased distortion in the final part. Figure 2.9 shows a welding torch with this configuration mounted.

PAW and GTAW-based WAAM both utilize a non-consumable electrode with a separate wire feed process, seen in figure 2.10 below, where wire feeder and torch rotation are required to maintain proper wire alignment with the leading edge of the melt pool, taking into account travel direction of the motion platform. Because of this, more degrees-of-freedom and coordinated motion between them is required (6). While this process has a reduced deposition rate when compared to GMAW-based processes, the concentrated heat input and cleanliness of the process can be an ideal solution to certain design problems.

Challenges exist with all WAAM processes, such as undesirable microstructures, residual stress and distortion (13), as well as challenges with geometric access, which can be seen in Figure 2.11, where gravity alignment is unable to be achieved due to a narrow-groove restricting torch gas nozzle access. Different welding parameter sets also must be developed when welding in Non-Gravity Aligned (NGA) configurations, to take weld droop due to gravitational forces into account, adding further complexity to the overall fabrication strategy.



Figure 2.9: Tandem GMAW Torch Assembly

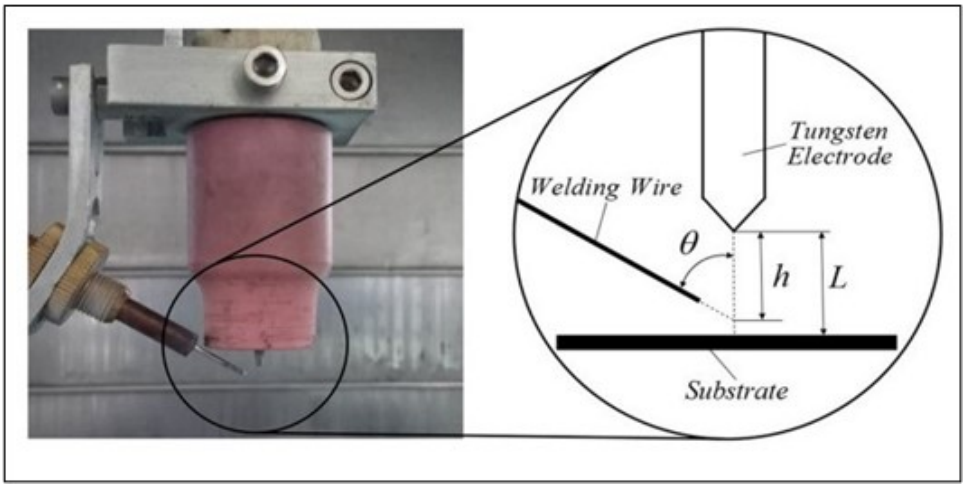


Figure 2.10: GTAW WAAM Torch and Wire Feed Orientation (6)

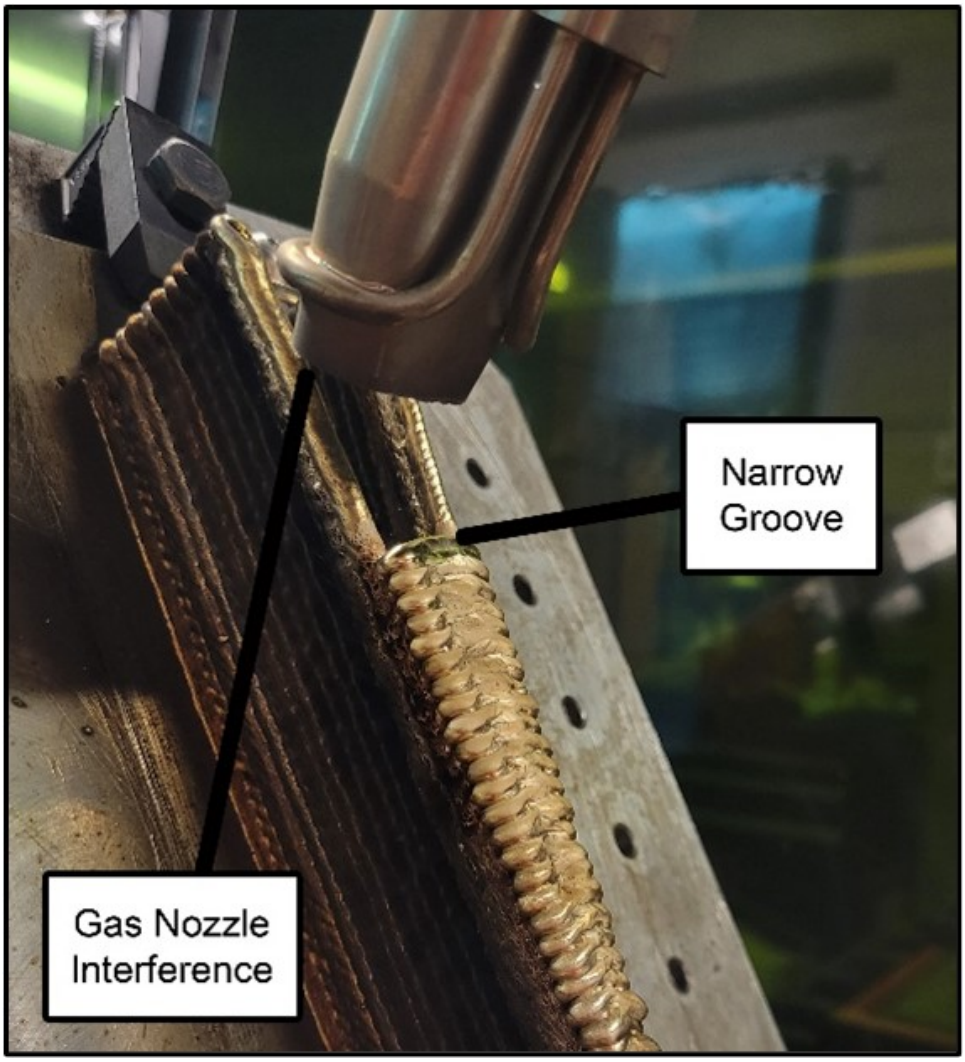


Figure 2.11: Non-Gravity Alignment due to Narrow Groove

2.4 Magnetic Arc Oscillation

Shown in Figures 2.12 and 2.13, when a charged particle, in the GTAW case a welding arc plasma, travels through an external magnetic field, it is subjected to a magnetic force of magnitude proportional to its velocity and the strength of the magnetic field. The force is determined using Equation 2.3 below, where F is the force generated in Newtons (N), E is the electric field generated by the welding process in Volts per meter (V/m), q is the electric charge in Coulombs (C), V is the velocity of the charge in meters per second (m/s), and B is the magnetic field strength in Teslas (T). (7; 28; 8; 29) The electric field generated during the welding process can be estimated through Equation 2.4, where E is the electric field in Volts per meter (V/m), V is the voltage across the arc in volts (V), and d is the distance between the electrode and the workpiece in meters (m). Due to the dynamic nature of the welding process, the electric field may not be uniform due to changes in arc length or changes in gas flow characteristics.

$$F = q(E + VxB) \tag{2.3}$$

$$E = \frac{V}{d} \tag{2.4}$$

Magnetic Arc Oscillation (MAO) takes advantage of this phenomenon to control the motion of the welding arc. This process lends itself well to the GTAW welding process, because it involves a non-consumable electrode, which creates a static magnetic field that can interact with the arc plasma. This contrasts with the GMAW process, where the electrode is consumable and has a more dynamic magnetic field due to this. MAO is traditionally accomplished at a frequency of $< 10Hz$, although higher frequencies have been investigated in literature. (30; 31) Yu, et al, investigated hot cracking in weld overlays with this process and found 7Hz to be ideal, which resulted in grain size refinement and a significant reduction in cracking. (32)

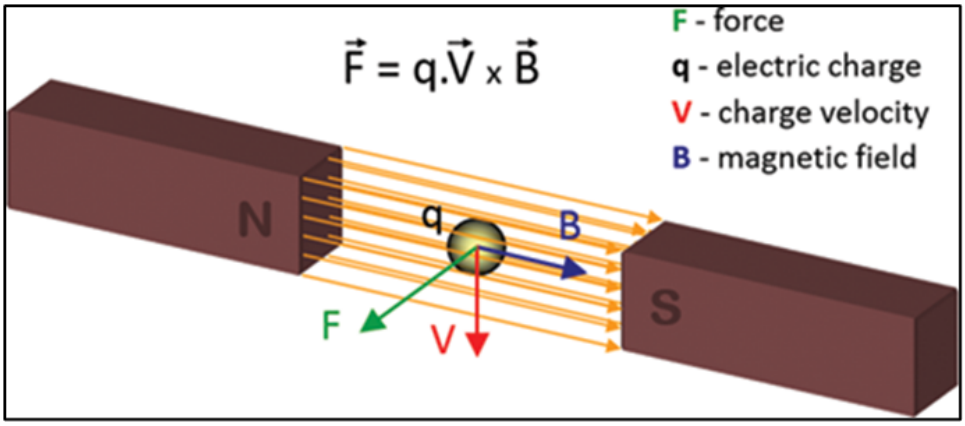


Figure 2.12: Illustration of Forces Acting on a Charged Particle in a Magnetic Field (7)

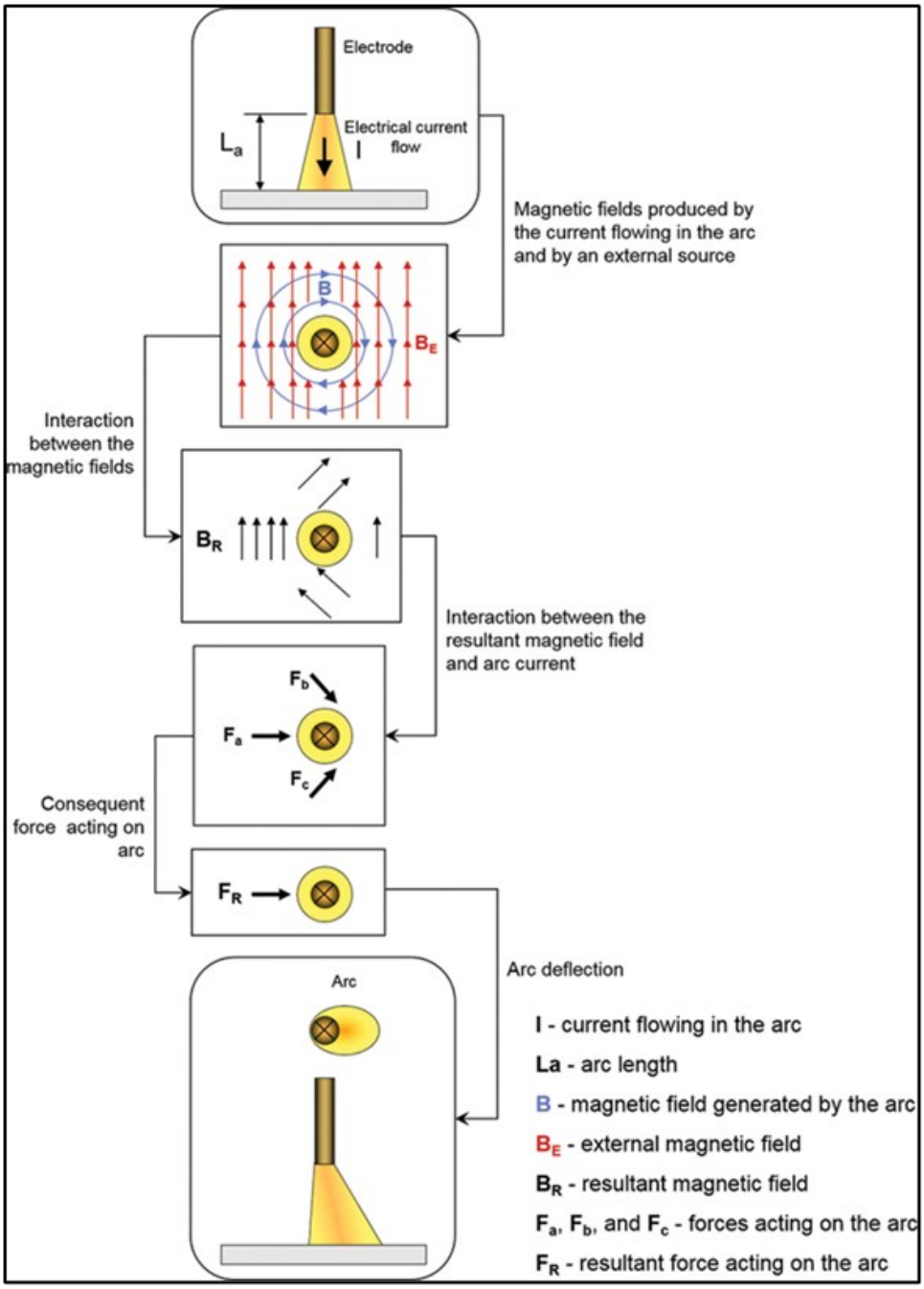


Figure 2.13: Diagrammatic Illustration of Arc Deflection (7)

The technique has been implemented in industry for narrow-groove GTAW process', shown in Figure 2.14, as well as joining of thick plates in the marine and transport industries. (8; 33; 34; 35)

Much research has been done on the tailoring of microstructures using MAO (22; 30; 32; 36; 37; 38; 39), as well as control process development. Kumar, Shailesh and Sundarrajan found that the influence of an external magnetic field to deflect a welding arc in AL 5456, which is non-heat treatable, contributed to grain refinement and resulted in finer grain structure when compared to continuous and pulsed welds, contributing to increased mechanical properties. (40)

Current limitations of the process are the bulkiness, cost and complexity of the equipment, the steeper learning-curve for welding professionals as well as the possibility of extinguishing the welding arc due to the strength of the external magnetic field, which is typically limited to $<$ 60 Gauss ($0.006T$) and proportional to the welding arc current, seen in Figure 2.15, where lower arc currents have weaker magnetic fields that are more easily manipulated.(7; 8)

2.5 Magnetic Arc Oscillation with the GMAW Process

While a vast range of data is available in the individual research spaces of wire arc additive manufacturing, welding, and GTAW-based magnetic arc oscillation, few resources are available for the utilization of MAO within a GMAW-based joining or additive manufacturing architecture. Kang and Na (9) investigated producing parameter sets for ideal groove face penetration in a narrow-groove MAO-assisted GMAW process and produced uniform and sufficient penetration to both wall faces with $< 70Gauss$ ($0.007T$) of external magnetic field strength, as shown in Figure 2.16.

Juliana et al (41) explored the influence of shielding gas composition on a magnetically oscillated GMAW process with $< 120Gauss$ ($0.012T$) maximum external field strength and observed strong indications that, while limited effect was observed on weld bead shape in a short-circuit transfer process, it could be leveraged to reduce the heat concentration transferred to the workpiece, which would be beneficial to possibly reduce distortion from

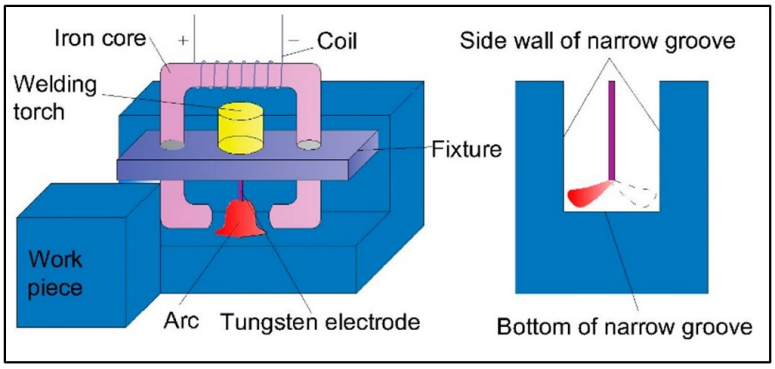


Figure 2.14: Illustration of MAO in Narrow Groove Geometry (8)

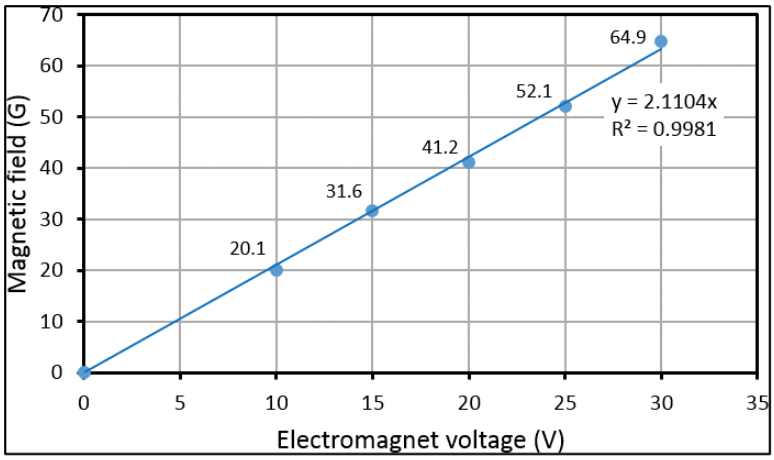


Figure 2.15: MAO Electromagnetic Field Produced vs Voltage (7)

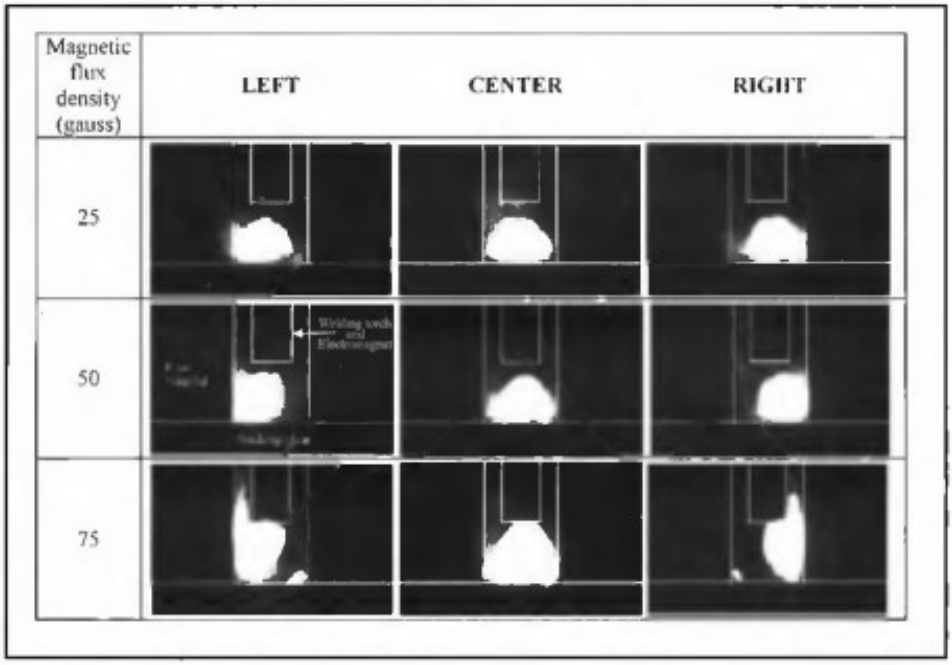


Figure 2.16: Arc Column Images for Various Magnetic Oscillation Field Strengths During Narrow Groove Welding (9)

thermal effects within a WAAM architecture. Chang et al (42) showed that the introduction of external magnetic fields can have a significant effect on the frequency and shape of droplet transfer, causing an increase in droplet frequency observed in relation to increasing external magnetic field strength, as well as a transition from a spherical to an elliptical droplet shape. Jiang et al (43) found that short-circuit transition frequency was "uniform and faster, has smaller droplet size and the welding process is more stability than welding without adscititious magnetic field." Furthermore, improved penetration was observed (44) due to arc constriction and reduced cathode spot mobility as a result of the utilization of external magnetic fields.

Additionally, the influence of external magnetic fields has been shown to improve the weld bead shape (45), refine the overall grain structure (46; 47), aid in preventing weld defects and improve joint performance (48; 49), all of which would be beneficial in a WAAM framework. This presents a unique opportunity for the development of an MAO-influenced and GMAW-based WAAM system to capitalize on the additional control MAO provides.

Chapter 3

Proposed Solution

The aim of this research is to design and prototype a system capable of negotiating historically difficult geometries, such as right-angle corners, in programmatic weave patterns with the aid of magnetic arc oscillation in a gas metal arc welding process utilizing 3XX series stainless steels. Preparation for this began with designing and manufacturing an experimental test stand for the work, followed by the sequence of work seen in Figure 3.1. Work will continue to build on Tasks **1** and **2**, shown in blue and red, respectively, where functional and iterable hardware and control logic is in place for further development. Weave adaptation and corner negotiation, task **3** shown in purple, will work in tandem with task **4**, shown in gray, where the exploration of process limitations will aid in the refinement of the initial mathematical model, outlined in green. This work will culminate in a series of paired characterization experiments, where the process and the produced material will be compared against traditional wire arc additively manufactured examples.

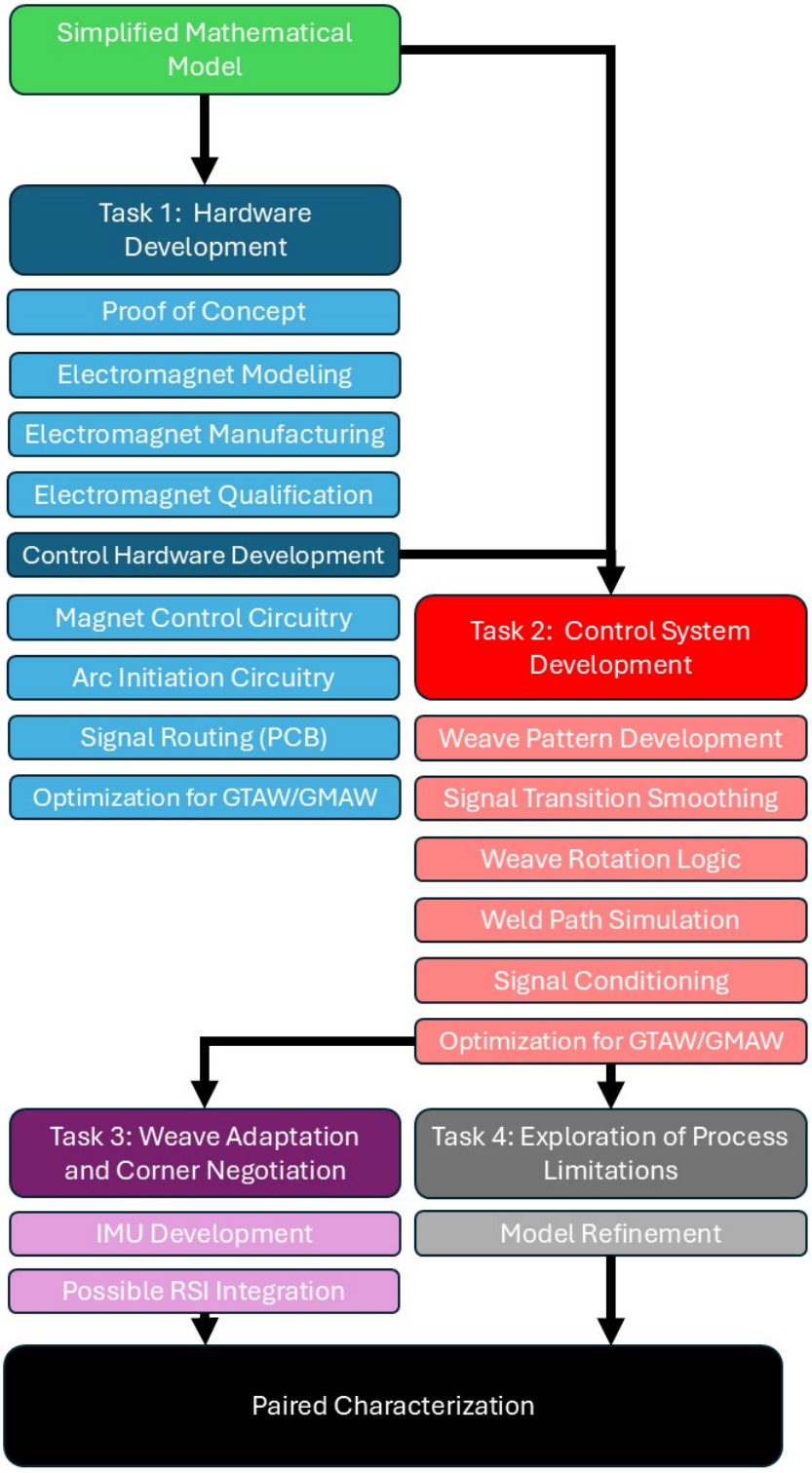


Figure 3.1: Layout of Research Tasks

3.1 Experimental Test Stands

3.1.1 Off-Robot

To streamline and expedite the development process, a test stand decoupled from the University of Tennessee's robotic weld cell will be developed. This fixture will be flexible in configuration and optimized for the manufacturing processes currently available. It will include a rigid arm to locate a welding torch and arc deflection apparatus, as well as a motion platform with user selectable velocity control in a minimum of one travel axis. Additional functionality, such as a trailing-type shielding gas capability, or imaging capabilities will be added on an as-needed basis.

3.1.2 On-Robot

During later stages, work will be transitioned to the robotic weld cells at the University of Tennessee, utilizing a KUKA KR6 robotic positioner coupled with a Fronius CMT Advanced 4000 power supply, utilizing a Fronius VR7000-CMT wire feeder, shown in Figure 3.2. Hardware mounting solutions will be developed by leveraging a modular kinematic mounting solution based on MIL-STD-1913 profile extrusion, shown in Figure 3.3 below.

3.2 System Development

3.2.1 Task 1: Hardware Development

During the hardware development phase, electromagnetic hardware is designed and implemented based on mathematical modeling and design-for-manufacturing techniques. While the bulk of available knowledge in the MAO space is directed towards the GTAW process space, the assumption is that stronger external magnetic field influences will be required to create suitable deflection and, thus, hardware will be manufactured with sufficient design margin to accommodate.

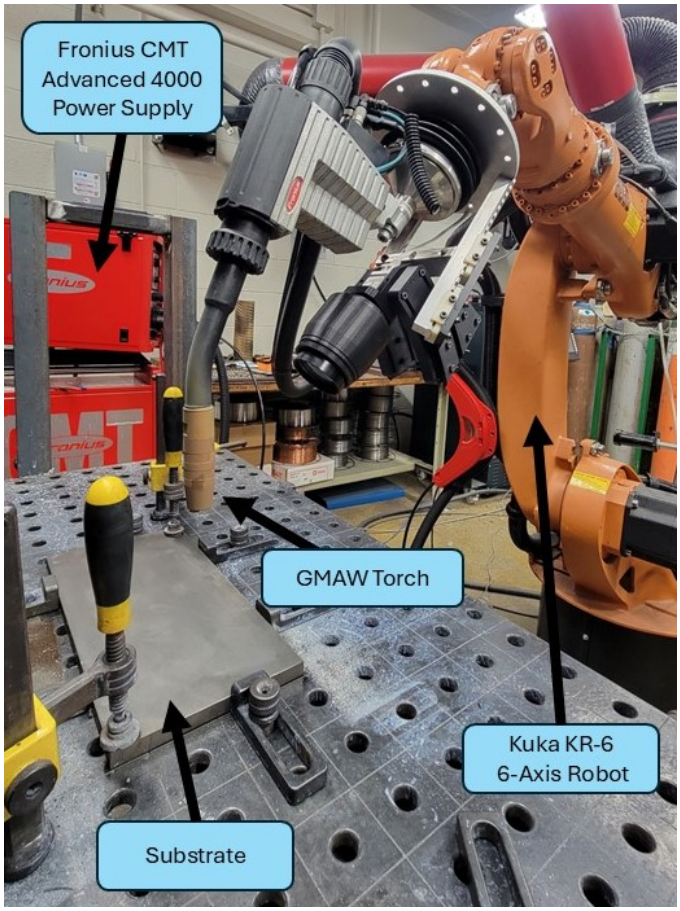


Figure 3.2: University of Tennessee Wire Arc Additive Manufacturing Cell

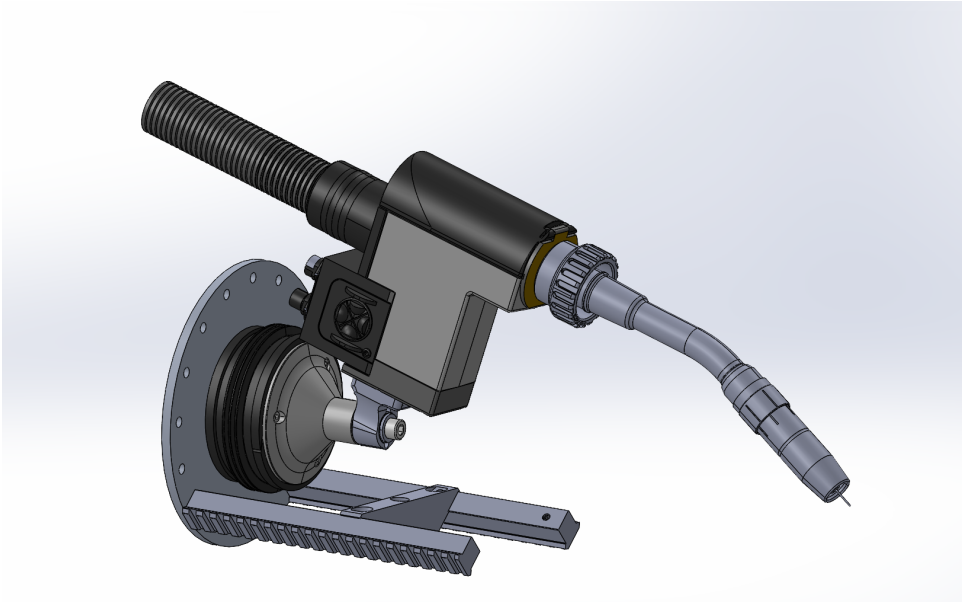


Figure 3.3: Illustration of MIL-STD-1913 Mounting Solution

3.2.2 Task 2: Control System Development

In conjunction with Task 1, a suitable control system has been developed, utilizing gas tungsten arc welding (GTAW) for initial development stages due to its decoupled mass and heat inputs, before being transitioned to gas metal arc welding (GMAW). During this transition, it is expected that differences in arc-length, charged particle variations, and welding power supply configurations will all influence control system design iterations. To accomplish this, a combination of MATLAB and SIMULINK software was leveraged to create a control structure that allows for the simulation of welding weave profiles prior to hardware deployment. Logic has also been introduced to field-balance the respective electromagnets to each other within the overall control scheme and is designed for deployment as a stand-alone system.

3.2.3 Task 3: Weave Adaptation and Corner Negotiation

Once the overall hardware and control system architecture is in place, focus will transition to adaptation to process changes regarding in-situ weld weaving profile control, as well as in-situ weave direction control. To accomplish the former, it is anticipated that logic will be integrated to damp the system's response and provide a smoother transition from the initial to the final trajectory. The latter will require the integration of robot-direction information being introduced into the control logic, either by external sensing, communication with the robot's internal control system, or a combination thereof.

3.2.4 Task 4: Exploration of Process Limitations

Finally, Task 4 will involve the exploration of process limitations in the attainable magnitude of deflection, practically attainable weaving patterns, and welding parameter spaces based on input current to both the external magnetic and welding systems. A predictive deflection model will be developed based on the physical system and comparison to a mathematical representation will be demonstrated, with the end goal being a tool that is deployable by an operator without extensive development or testing.

3.3 Success Criteria

3.3.1 Paired Analysis

The efficacy of the system will be demonstrated through a combination of process and material-based testing, where a statistically relevant number of samples with and without MAO will be compared side by side to evaluate process equivalency, material composition, and overall time efficiency.

Process-Based

To demonstrate process performance, experimental geometries with and without MAO technology will be produced, and comparisons will be drawn based on geometric accuracy and appearance of the produced welds, as well as overall process time. To evaluate the functionality of weave adaptation and corner negotiation logic, geometries incorporating right angles will be tested and evaluated for initial and final weave orientation, as well as corner geometry and weave orientation settling time. This work will be performed using the on-robot test fixture outlined in Section 3.1.2 using 316L stainless steel filler wire on 304 stainless steel substrates. Current and voltage data will also be recorded and analyzed to determine the material deposition frequency and estimate the droplet transfer mode.

Material-Based

To benchmark produced weld material, comparisons will be made in the material-composition space between traditionally produced and MAO-produced welds. This will be accomplished mechanically via tensile testing of ~ 20 layer wall-type structures, non-destructively through dye penetrant testing, and destructive metallography sectioning and macro-etching to identify structural defects and heat affected zones (HAZ), as well as macro-hardness of both the deposited material and the substrate.

3.4 Potential Challenges

Identification of possible challenges is key to every engineering project because it affords the opportunity to anticipate and analyze risk, as well as to develop mitigation strategies and optimize solutions to potential issues before they arise. In this research, potential challenges are hardware, controls and processed-based.

3.4.1 Hardware-Based Challenges

Thermal Effects

As with every welding process, managing heat to minimize distortion will be critical, as well as to ensure hardware integrity. This is especially true in the case of magnetic processes, where elevated temperatures will result in a material losing its magnetic properties and transitioning from a ferromagnetic to a paramagnetic state, known as the Curie point. Therefore, careful management of heat through thermal isolation and shielding will be employed, with the possibility of liquid cooling of the electromagnets, or tailoring of magnetic materials to those with higher Curie Temperatures. When compared to the Curie temperature of soft iron (770C), cobalt (1130C) may be a suitable replacement if required.

Weld Spatter

Weld spatter consists of small, molten droplets of material ejected from a melt pool during some welding processes. While this is not a concern with GTAW welding, in GMAW the magnetic poles could attract particles due to their charge. Thus, non-ferrous protective sleeves may be necessary over the pole pieces as a level of protection. Otherwise, increased magnet strength may be suppled from an increased distance. Due to the inverse square relationship between magnetic field strength and distance from the source, however, this may not be an ideal solution.

Packaging

Since this research aims to design a system capable of integrating with currently existing robotic weld cells, the overall hardware footprint is a critical design parameter due to its limiting overall welding torch access and, thus, the ability to produce some geometries. While not a concern in initial iterations, future work could be focused on streamlining the packaging to nest around the existing welding torch and leverage under-utilized space.

Manufacturing

Minimizing part count, designing for ease of assembly, and minimizing complex assemblies are all key concepts in the Design for Manufacturing (DFM) practice, and will all be considered during this research. In addition, component modularity will be considered to reduce the overall number of fabricated assemblies required during the life of the project, as well as careful consideration will be placed on standardizing material and process requirements to align with available manufacturing hardware and techniques, with an emphasis placed on cost-effectiveness of each manufacturing solution.

3.4.2 Controls-Based Challenges

Model Fidelity

Due to the highly complex nature of the physics of an electric welding arc and in an effort to reduce on-board hardware computational expense, streamlined models will be employed based on industry-accepted assumptions to estimate the magnitude of weld deflection. Qualitative data acquired during experimentation will be used to calibrate the model to reflect experimental results on the physical system.

Magnet Control

Since simple on/off circuitry will not be a practical solution in the context of controlling the magnetic field strength output of an electromagnet, hardware and/or control logic will need

to be developed to be able to vary the current input to the magnetic coil to achieve the desired results. Emphasis will be placed on cost-effective and serviceable solutions during this effort. Current design directions involve microcontroller-driven potentiometers or transistor-related solutions.

Processor Speed

As previously mentioned, due to model complexity and the number of processes required, the ability of off-the-shelf micro-controllers to provide the necessary processing speed may come into question. To mitigate this, Arduino microcontrollers ($\sim 19mhz$) may be substituted in favor of Raspberry Pi Single Board Computers (SBC) due to their increased processing power ($\sim 1.5GHz$). If further computing power is required above this, a dedicated personal computer (PC) will be leveraged if needed.

Signal Sensitivity

The influence of external magnetic fields on solid-state electronic hardware can cause a myriad of interference issues, such as inductive coupling, where an external magnetic field generates currents in adjacent circuits, or signal distortion leading to noise in both digital and analog circuits. Due to the magnetic field strength required in this research ($\sim 0.007T$), special consideration should be made to isolate sensitive circuitry either through electromagnetic interference (EMI) hardening techniques, such as shielding, or by distance isolation.

Signal Smoothing

To ease the transition between one respective welding weave and another, the current assumption is that signal smoothing will be required to effectively damp the signal and provide a gradual transition while maintaining a reasonable settling time ($\sim 1s$), also factoring in welding velocity. This hypothesis may be incorrect in the GMAW space, however, due to the nature of the welding process detaching droplets in series and not in continuous

deposition. The same logic structure may be leveraged for the transition zones between an initial and final travel direction.

3.4.3 Process-Based Challenges

Ferrous and Non-Ferrous Substrates

When compared to non-ferrous alloys, ferrous substrates, such as carbon steel, will interact with the external magnetic fields produced in this research and, thus, can become magnetized and exhibit magnetic hysteresis, whereby magnetization can remain even after the external magnetic field is removed. While the scope of this research is limited to 3XX-series stainless steel alloys, special consideration should be taken as to the effects of differing materials on the overall system efficacy related to both the substrate and the materials used for hardware manufacturing.

Process Transition

With the current approach to leverage the GTAW process space for primary controls development, fixture design should be optimized to be utilized for both the GTAW and GMAW processes. In addition, with the assumption that increased magnetic field strength, and thus increased input currents, will be required for the GMAW process, control logic and hardware should be developed that is adaptable to both processes and provides sufficient headroom for further iterations if necessary.

3.5 Potential Risks

As with potential challenges, potential risks that hinder the success of this research are outlined below:

- Thermal effects could reduce device effectiveness after extended use or damage electromagnet hardware.

- Weld spatter could damage components due to their charged nature.
- Model fidelity required for control system may not be manageable by computational capabilities.
- Noise from electromagnetic interference could hinder arc control efforts.
- Directional information hardware sensitivity may be too low for implementation.
- Electromagnet control techniques, such as pulse-width-modulation, may negatively impact weld process.

Chapter 4

System Requirements

4.1 Functional/Performance Requirements

The following bullet points were identified as primary design goals for this research:

- Modular design for multiple experimental setups.
- Leverage off-the-shelf hardware when applicable.
- Design for manufacturability and serviceability, where components can be iterated upon when necessary without the need for a complete overhaul
- Operate in a robot-agnostic configuration, where hardware is not limited to a specific robotic manipulator.
- Utilize non-ferrous materials where applicable to limit magnetic interactions in the hardware.

4.2 Trade-offs

While integrating with the systems of a robotic manipulator could potentially produce a more robust end product, the decision to operate in a robot-agnostic manner was motivated

by the ability to leverage the hardware developed in this research across multiple models and manufacturers. Furthermore, the low-cost and reduced time to implementation approach taken during this research was driven by the ability to successively iterate the design to realize a potentially more technically superior end product at the expense of possibly increased cost due to increased number of design iterations.

4.3 Material and Tooling Selection

4.3.1 Substrates and Feedstocks

This work was completed using Lincoln Electric Blue Max 316L stainless steel 0.045" diameter wire electrode material deposited on 6"x12"x0.25" 304H stainless steel substrates, with the notable exception of the out-of-scope processes outlined in Section 10.3.7. Material lot numbers can be seen in Figure 4.1.



Figure 4.1: Lincoln Electric Blue Max 316L Wire

Shielding Gases

Primary shielding gas for this work was 98/2 industrial Argon/Oxygen, with 100% industrial grade Argon as a trailing gas, where applicable, all sourced from Airgas Inc.

4.3.2 Design, Modeling and Controls Tools

Autodesk Fusion

Chosen for its cloud-based architecture that integrates well with available computer numerical contorolled (CNC) fabrication equipment, Autodesk Fusion was used as the primary 3D modeling suite for this work. It was also leveraged for geometric comparison efforts outlined in Section 10.3.4.

Matlab

Mathworks Matlab r2022a and its accompanying Simulink simulation suite was used throughout this research for simulation, control logic development, data collection and data interpretation and visualization efforts.

Arduino IDE

The Arduino Integrated Development Environment (IDE) was used exclusively for off-robot data collection efforts outlined in Section 7.4.

Chapter 5

Modeling

5.1 Initial Mathematical Modeling

To develop a simplified mathematical model for calculating magnitude of deflection based on chosen welding parameters, and taking the influence of the external magnetic field into consideration, the welding arc was initially modeled as a current-carrying wire to determine the magnitude of the internally produced magnetic field. Using Ampere's law, shown in Equation 5.1 below, the magnetic field can be estimated, where $\mathbf{B}$ is the magnetic field in Tesla, μ_0 is the permeability of free space ($4\pi * 10^{-}7\ \frac{N}{A^2}$), $\mathbf{I}$ is the current flowing through the wire in Amperes, and r is the distance from the wire in meters.

$$\mathbf{B} = \frac{\mu_0 \mathbf{I}}{2\pi r} \tag{5.1}$$

The charge on the droplet can be estimated by examining the current and the time spent in the magnetic field. The time in field (T_{Field}) is estimated in Equation 5.2 below, where L_{Arc} is the length of the electric welding arc in meters, and $\mathbf{V}_{Droplet}$ is the velocity of the droplet, estimated at $\sim 0.5 - 8\frac{m}{s}$, for the GMAW process, based on the sub-process used.(50; 3) The charge in coulombs, q, can then be estimated in Equation 5.3, where $\mathbf{I}$ is the welding current in Amperes and T_{Field} is the estimated time spent in the arc from Equation 5.2.

$$T_{Field} = \frac{L_{Arc}}{\mathbf{V}_{Droplet}} \tag{5.2}$$

$$q = \mathbf{I} * T_{Field} \tag{5.3}$$

The electric field can be calculated in Equation 5.4, where $\mathbf{E}_{Field}$ is the electric field produced by the welding process, V_{Arc} is the arc voltage as a chosen weld parameter and, as seen in Equation 5.2, L_{Arc} is the length of the welding arc in meters.

$$\mathbf{E} = \frac{V_{Arc}}{L_{Arc}} \tag{5.4}$$

Leveraging values from above, the Lorentz force can then be calculated in Equation 5.5 below, where $\mathbf{F}_B$ is the magnetic force in Newtons, q is the charge of the particle in Coulombs, $\mathbf{E}_{Field}$ is the produced electric field from the welding process, $\mathbf{V}_{Droplet}$ is the velocity of the particle in meters per second, and $\mathbf{B}$ is the magnetic field in Tesla.

$$\mathbf{F}_B = q(\mathbf{E}_{Field} + \mathbf{V}_{Droplet} X \mathbf{B}) \tag{5.5}$$

Due to the perpendicular relationship between the velocity and magnetic force in Equation 5.5, the magnetic force does not contribute much work but rather causes the particle to form a circular path. This also assumes a uniform magnetic field. Due to this, the radius of the path of the particle can be estimated by Equation 5.6, where R_{Path} is the radius of the path in meters, $M_{Droplet}$ is the mass of the droplet in kilograms, $V_{Droplet}$ is the velocity of the droplet in meters per second, q is the charge of the droplet, calculated in Equation 5.3, and $\mathbf{B}$ is the magnetic field strength in Tesla, estimated in Equation 5.1. This is illustrated in Figure 5.1, where the external magnetic field strength, B, is shown in green, the welding current, I, is shown in blue, the Lorentz force, F_B, imparted on the GMAW weld droplet is shown in white, and the radius of the particle, R_{Path}, is shown in yellow.

$$R_{Path} = \frac{M_{Droplet} V_{Droplet}}{|q|\mathbf{B}} \tag{5.6}$$

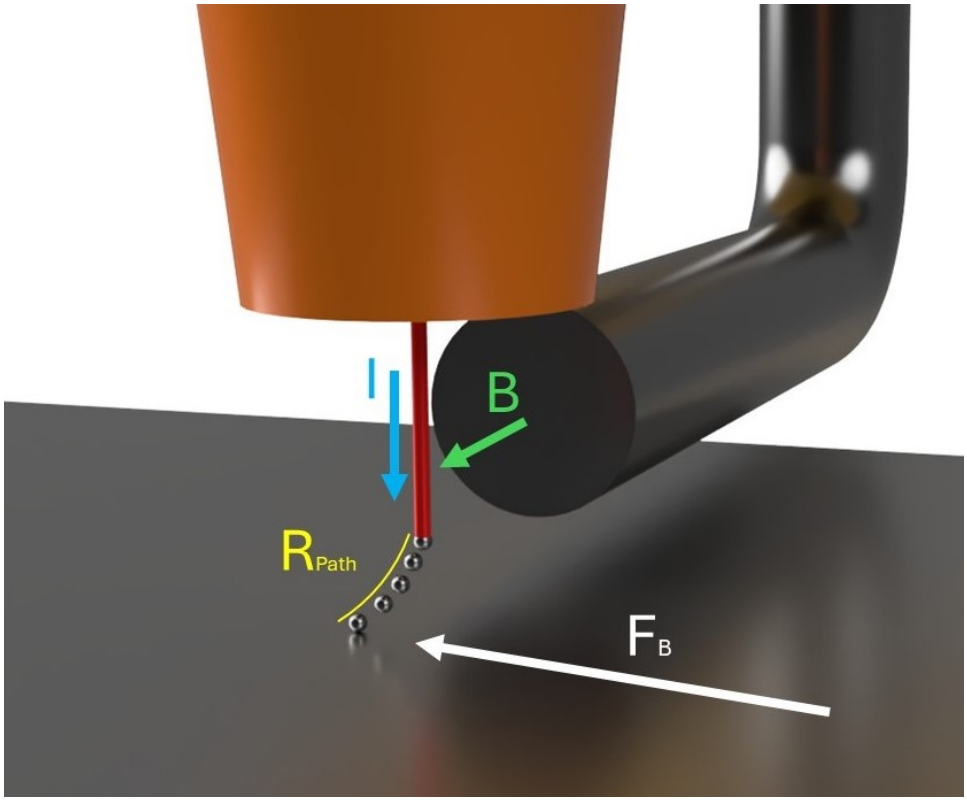


Figure 5.1: Lorentz Force Illustration on GMAW Welding Process

The angle of deflection of the weld droplet due to the influence of external magnetic fields is estimated by using the estimated time period required for the particle to complete one circular motion, illustrated in Equation 5.7, where $T_{Rotation}$ is the time it takes to travel a full revolution in seconds, R_{Path} is the radius of the path calculated in 5.6, and $V_{Droplet}$ is the velocity of the droplet in meters per second.

$$T_{Rotation} = \frac{2\pi R_{Path}}{V_{Droplet}} \tag{5.7}$$

Substituting Equation 5.6 for R_{Path} gives the following...

$$T_{Rotation} = \frac{2\pi M_{Droplet}}{|q|\mathbf{B}} \tag{5.8}$$

The angular velocity of the weld droplet can then be estimated by Equation 5.9, where ω is the angular velocity in radians per second, q is the charge in coulombs, $\mathbf{B}$ is the magnetic field in Tesla, and $M_{Droplet}$ is the estimated mass of the droplet in kg. The change in angle is then calculated in Equation 5.10, where θ is the angle of deflection in radians, ω is the angular velocity calculated in Equation 5.9, and T_{Field} is the amount of time in seconds that the droplet is in the arc field.

$$\omega = \frac{|q|\mathbf{B}}{M_{Droplet}} \tag{5.9}$$

$$\Delta\theta = \omega T_{Field} \tag{5.10}$$

Lastly, this angle change is then related to the length of the welding arc to arrive at a magnitude of deflection in mm, shown in Equation 5.11 below, where $L_{Deflection}$ is the normal distance of deflection from centerline of weld travel in meters, L_{Arc} is the length of the welding arc in meters, and θ is the angle of deflection in radians.

$$L_{Deflection} = L_{Arc} \tan(\Delta\theta) \tag{5.11}$$

These equations were then leveraged and developed into a Matlab script to estimate arc deflections for GMAW. Response curves are seen in Figure 5.2, where, for initial calculations, L_{Arc} was estimated at 0.004m, the welding input current and voltage, I and V_{Arc}, were set at 100A and 18V, respectively. Velocity of the weld droplet, $V_{Droplet}$, was estimated at 4 m/s based on values found in literature (3) illustrated in Figure 2.5 in Section 2.2, and the mass of the droplet, $M_{Droplet}$, was estimated at $4.1 * 10^{-6}$kg, chosen based on diametral measurements found in literature (51; 52; 53). With these values and a sinusoidal magnetic field input from 0-7mT, a maximum total deflection of $\sim$ 1.38mm was initially calculated for the GMAW case. This model was discontinued with the development of a data-driven option, outlined below.

5.2 Data-Driven Modeling

Leveraging data from three-dimensionally scanned 100 percent offset welds, outlined in section 10.1.2, an interpolative model was developed in Matlab that accepts welding power and oscillation frequency as inputs and outputs a predicted weld deflection from centerline, giving the operator the ability to more accurately tailor weld parameters to a desired deflection (Figure 5.3). This model is currently limited to 1/2in contact-tip-to-workpiece distance and 12 in/min travel speed, but could be iterated upon to include multiple parameter sets. The complete MATLAB model script can be found in B.1, along with validation results in section 10.3.5.

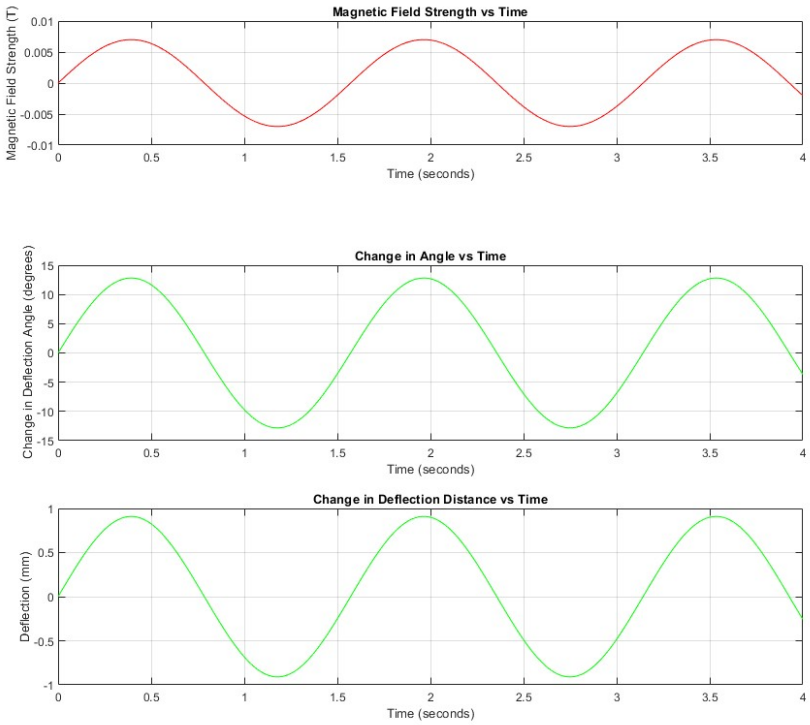


Figure 5.2: Initial Testing of Mathematical Model

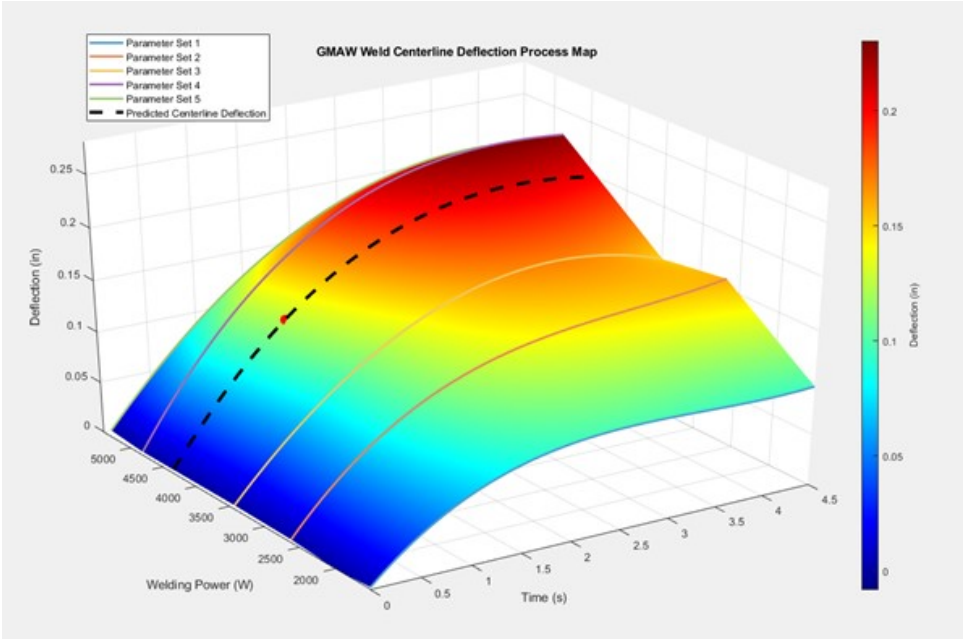


Figure 5.3: Data Driven Model Output Plot Example

Chapter 6

Electromagnet Design, Manufacturing and Calibration

6.1 Initial Proof of Concept

Desiring a low barrier-to-entry and short time-to-implementation proof of concept, an electromagnetic coil, shown in Figure 6.1, initially meant for classroom demonstration was leveraged in conjunction with soft iron rod machined on a Logan 1442 toolroom metal lathe. This was then packaged in a custom-machined aluminum housing designed to interface with an off-the-shelf 18 series water-cooled GTAW torch and powered by an existing laboratory power supply (Figure 6.2). Insights from initial experimentation with this proof of concept, where it was observed that reversing the polarity of the magnetic coil produced an opposite reaction and that a sufficient wire diameter would be needed to manage the heat generated from electrical resistance in the coil, were an integral part in the identification of a path forward and applied to further iterations.



Figure 6.1: Initial Proof of Concept Electromagnetic Coil

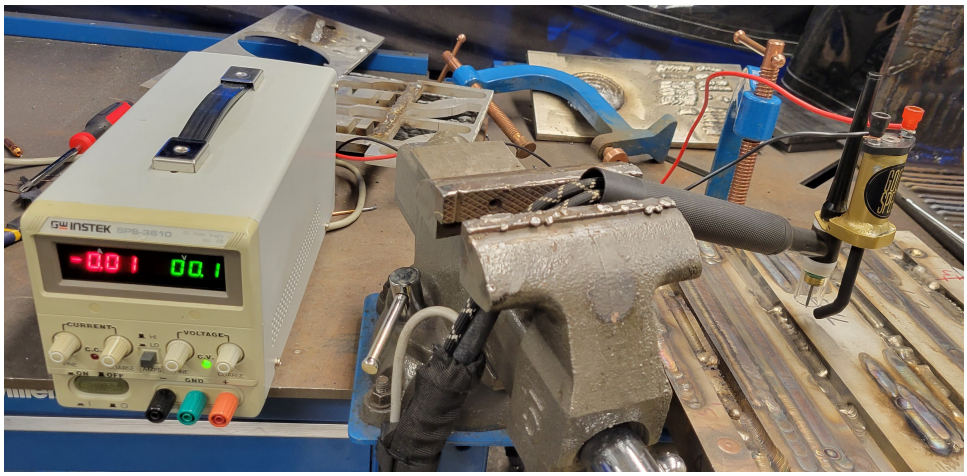


Figure 6.2: Initial Proof of Concept Experimental Setup

6.2 Electromagnet Modeling, Manufacturing and Calibration

Hardware development began with a thorough review of current magnet technology, with emphasis placed on the cost effectiveness of potential solutions in both raw materials and manufacturing. Using findings from the initial proof-of-concept phase in conjunction with mathematical modeling and both additive and subtractive manufacturing techniques, electromagnets were then manufactured in a modular fashion intended to explore multiple configurations and testing environments.

6.2.1 Electromagnet Modeling

Shown in Equation 6.1 below, the number of turns of wire required in a solenoid to produce a prescribed magnetic field can be estimated, with N being the number of turns, I being the input current, $F_{strength}$ being the magnetic field strength in Tesla, identified through literature review outlined in Section 2.5, L_{core} being the length of the core in meters, L_{gap} being the distance from the magnetic pole in meters, μ_0 being a permeability constant for air, $4\pi * 10^{-7}\frac{N}{A^2}$, and μ being a permeability constant for iron, $2.5 * 10^{-1}\frac{N}{A^2}$. It should be noted that, while the diameter of the wire is not defined in this equation, it is a critical design constraint because it is directly related to the heat generated from electrical resistance in the coil and was taken into consideration by choosing material with a rated ampacity above the design requirements.

$$NI = F_{strength}\ (\frac{L_{core}}{\mu} + \frac{L_{gap}}{\mu_0}\ ) \tag{6.1}$$

Using the above equation in conjunction with previously established magnetic field strength values shown in Chapter 2, as well as manufacturer-specified ampacity ratings for readily-available magnet wire, a minimum of 575 turns of 16awg wire was identified to meet the design objective below the manufacturer's rated ampacity of 5.2A.

6.2.2 Three-Dimensional Design

Having defined the minimum number of wire turns and wire diameter as design constraints, a three dimensional solid model was developed in Autodesk Fusion360, being driven by Equation 6.2, where x is the outside diameter in inches, ID is the inside diameter in inches, L is the length of the coil in inches, D_{copper} is the density of copper, and W_{copper} is the weight of the copper in pounds. Using Equation 6.3, a packing density of (0.48) for a custom-wound coil was assumed to arrive at a corrected outside diameter, which is reflected in the final bobbin model, shown in Figure 6.3.

$$\left[\left(\pi\frac{x^2}{2}\right) - \left(\pi\frac{ID^2}{2}\right)\right] \; L = \left(D_{copper}\frac{lb}{in^3}\right)^{-1} * W_{copper} \tag{6.2}$$

$$\left(OD * \frac{1}{packing\ density}\right) = OD_{Corrected} \tag{6.3}$$

6.2.3 Manufacturing

Acrylonitrile Butadiene Styrene (ABS) was chosen as the bobbin material due to its higher heat resistance when compared to Polylactic Acid (PLA), availability at low cost, and insulating properties. A quantity of two bobbins were manufactured using a Fused Deposition Modeling (FDM) additive manufacturing process, integrating a sacrificial work-holding stanchion for coil winding and machining operations.

A Logan 1442 tool-room metal lathe was retrofit with a hall-effect counter and leveraged as a winding mechanism, shown in Figure 6.4 and 6.5, ensuring that both manufactured coils had matching turns of wire. Each completed magnet was wound with 662 turns of 16 AWG magnet wire to provide design margin above the 575 turn initially calculated requirement, as well as to maximize the available commercially sourced wire length per spool.

Soft iron rod was lathe-turned from 13mm to 12.54mm in diameter for the magnet cores. A fixture (Figure 6.6) was machined so both cores could then be oxy-acetylene torch formed to a 90-degree angle. The leg heights were machined in parallel on an Excello 602 milling

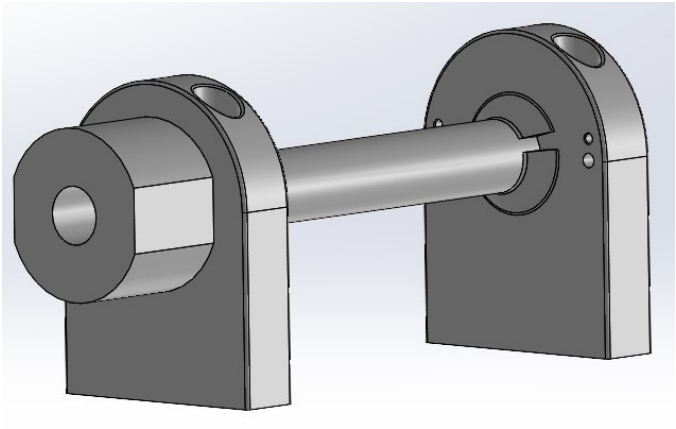


Figure 6.3: 3-Dimensional Model of Electromagnetic Coil Bobbin

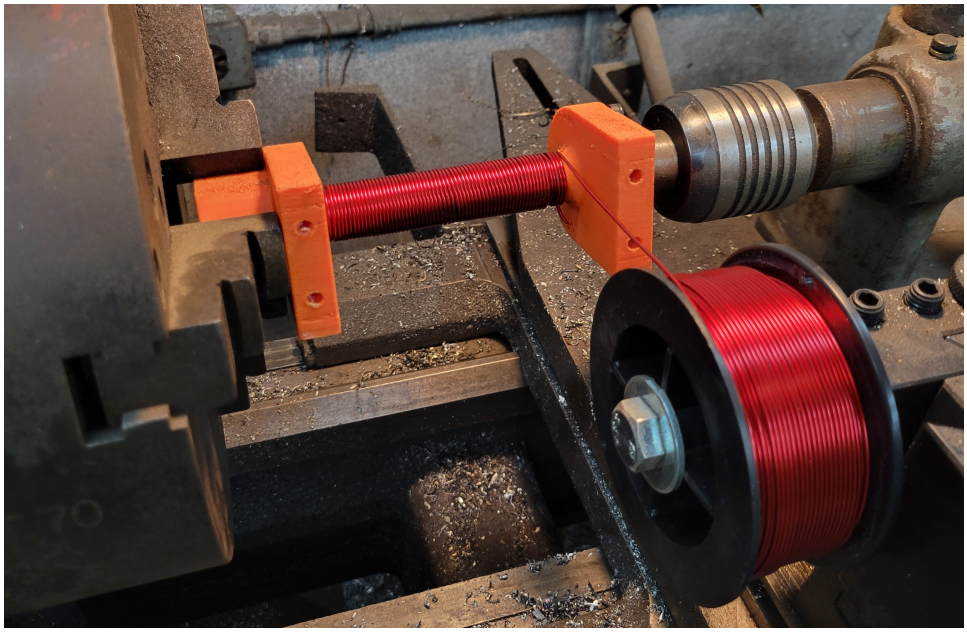


Figure 6.4: Magnetic Coil Winding on Logan 1442 Lathe

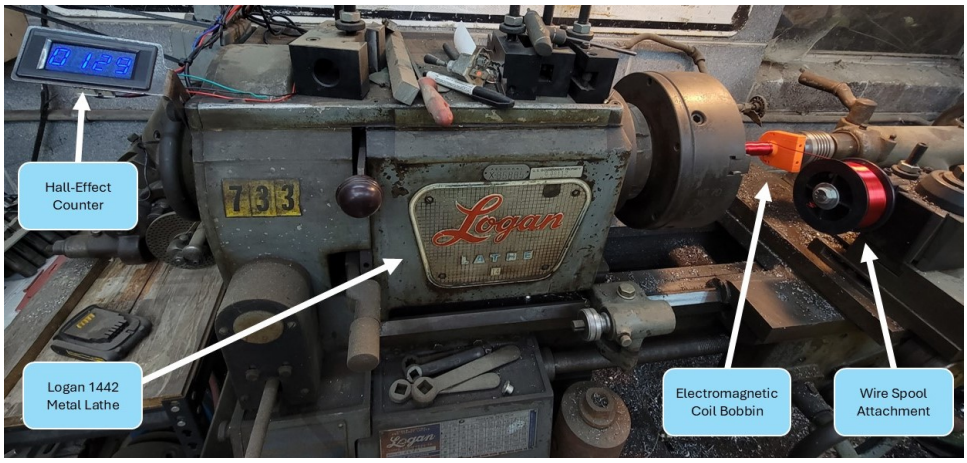


Figure 6.5: Coil Winding Experimental Setup

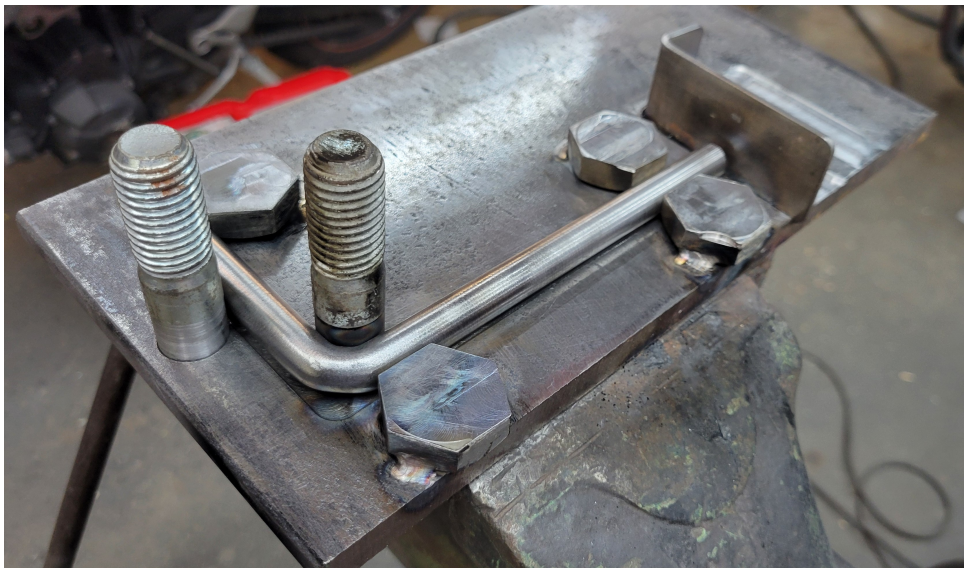


Figure 6.6: Pole Piece Torch Forming Fixture

machine to provide reasonable dimensional symmetry. The final pole pieces in both 45 and 90-degree configurations for setup flexibility can be seen in Figure 6.7. The final wound magnetic coil (45-degree configuration shown) can be seen in Figure 6.8.

6.2.4 Testing

To maintain parallelism between the machined face of the electro-magnet's pole piece and a Sypris 5170 Gauss/Tesla meter, a combination of an FDM additively manufactured fixture and a 6061 aluminum CNC plasma cut and brake-formed fixture were employed for both magnets, shown in Figure 6.9. Magnetic field strength was measured at the operating distance between the pole piece and the welding electrode in 0.1A current increments from 0-6A in a total of six trials with a minimum of 24 hours elapsed between each trial. Figure 6.10 illustrates average measured magnetic field strength values for each magnet with both 45 and 90-degree magnetic pole orientations.

6.2.5 Calibration

Due to the custom fabricated nature of the aforementioned electromagnetic coils, differences in the strength of each coil are expected due to variations in manufacturing, ex. inconsistencies in the packing density of the coils. Taking this into consideration, the operating, linear region of each coil was examined, Figure 6.11. Linear regression was used to arrive at a correction factor ($\sim 2.5\%$) that would later be integrated into the system's control logic, outlined in Section 9.3, to provide similar magnetic field strength in both the X and Y axes.



Figure 6.7: Finished Pole Pieces - 45 and 90 Degree Poles Shown



Figure 6.8: Assembled Electromagnetic Coil



Figure 6.9: 3d Model of Magnet Characterization Fixture

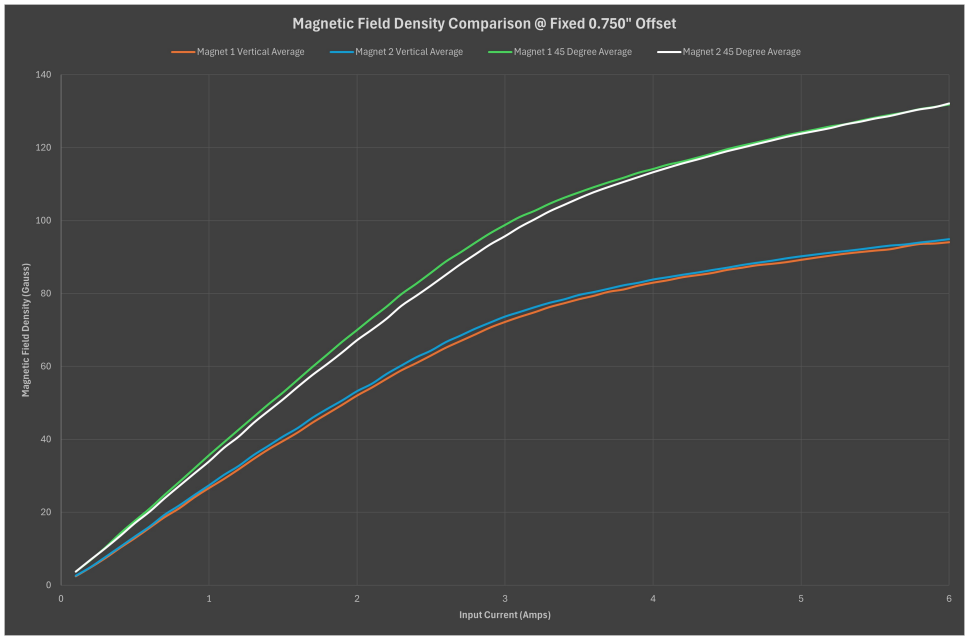


Figure 6.10: Comparison of Magnetic Field Strength at Operating Distance

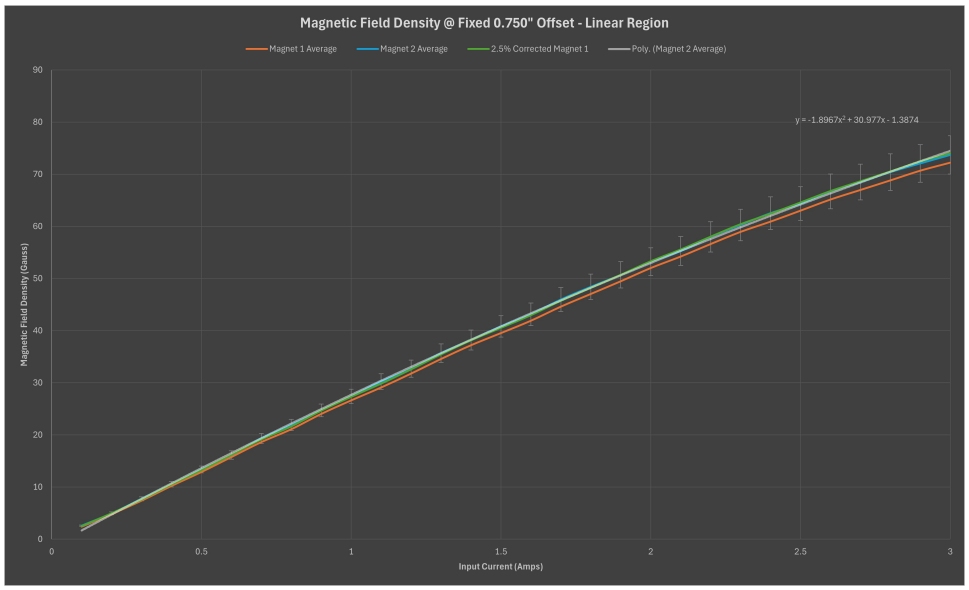


Figure 6.11: Comparison of Magnetic Field Linear Region with 2.5% Correction Factor

Chapter 7

Off-Robot Hardware

To limit the amount of development time required on The University of Tennessee's robotic weld cells, testing hardware (Figure 7.1) was developed using pulse width modulated-velocity controlled linear stages and configured to utilize both Tweco-style GMAW and 18-series pencil-type GTAW welding torches. This test stand was designed to be modular, leverage aluminum components in areas where magnetic interaction could be detrimental, as well as to incorporate an additional trailing-style shielding gas capability if needed. This test fixture has a horizontal reach of $\sim 19in$, ± 15 deg of rotation to accomodate leading or trailing configurations, and a maximum travel velocity of $17\frac{in}{min}$. A three-dimensional model of the developed test fixture can be seen on Figure 7.2.

7.1 Torch Fixture Design and Fabrication

Leveraging design-for-manufacturability concepts, the aforementioned test stand was optimized for available tooling and manufacturing techniques by designing flat assemblies to be plasma cut on a Langmuir Crossfire Pro CNC plasma table. Structural components were fabricated from 0.125" ($\sim 3mm$) 1018 mild steel plate with added relief cuts to aid in successive forming operations to arrive at a final product. Figures 7.3, 7.4 and 7.5 show a flat cut pattern, a resulting component cut from flat plate and the final product, respectively. All assemblies were designed for reduced out-of-plane stiffness to allow for accidental collisions.

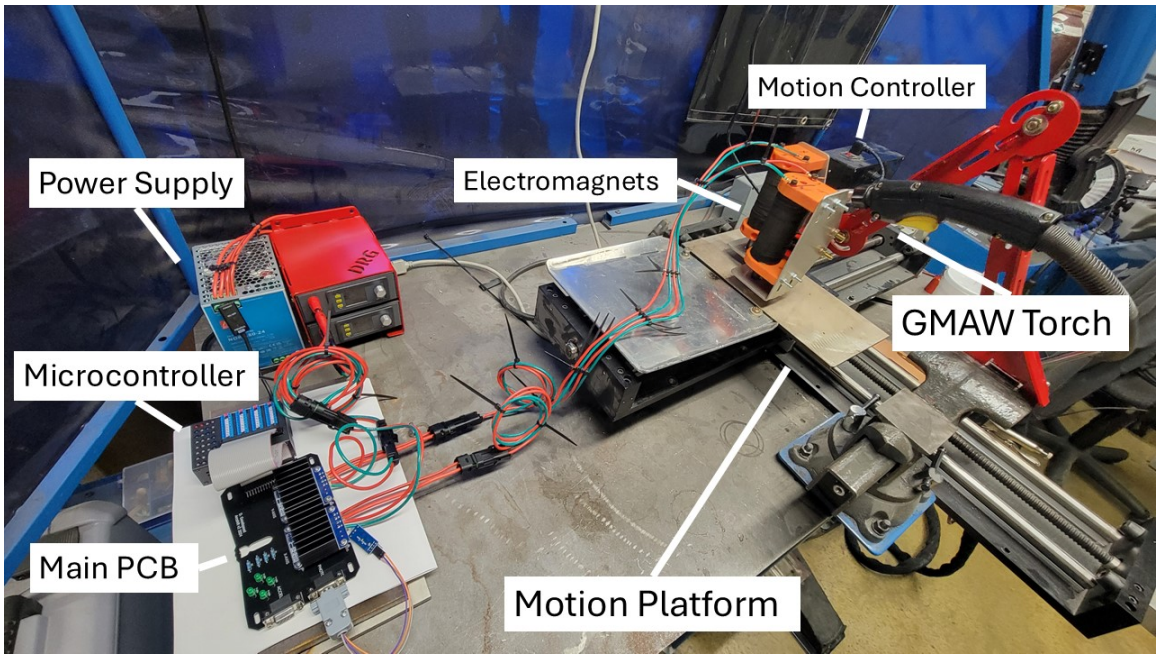


Figure 7.1: Off-Robot Full Experimental Setup

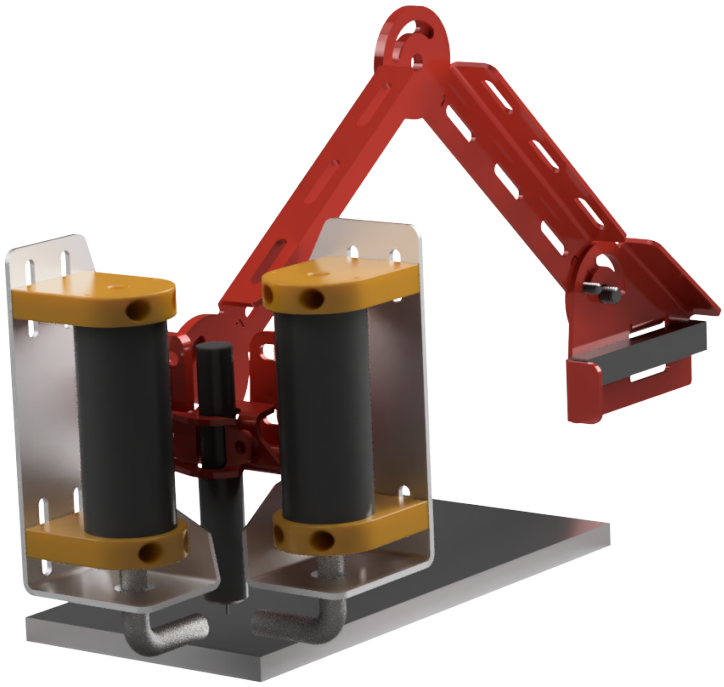


Figure 7.2: Test Fixture 3d Model

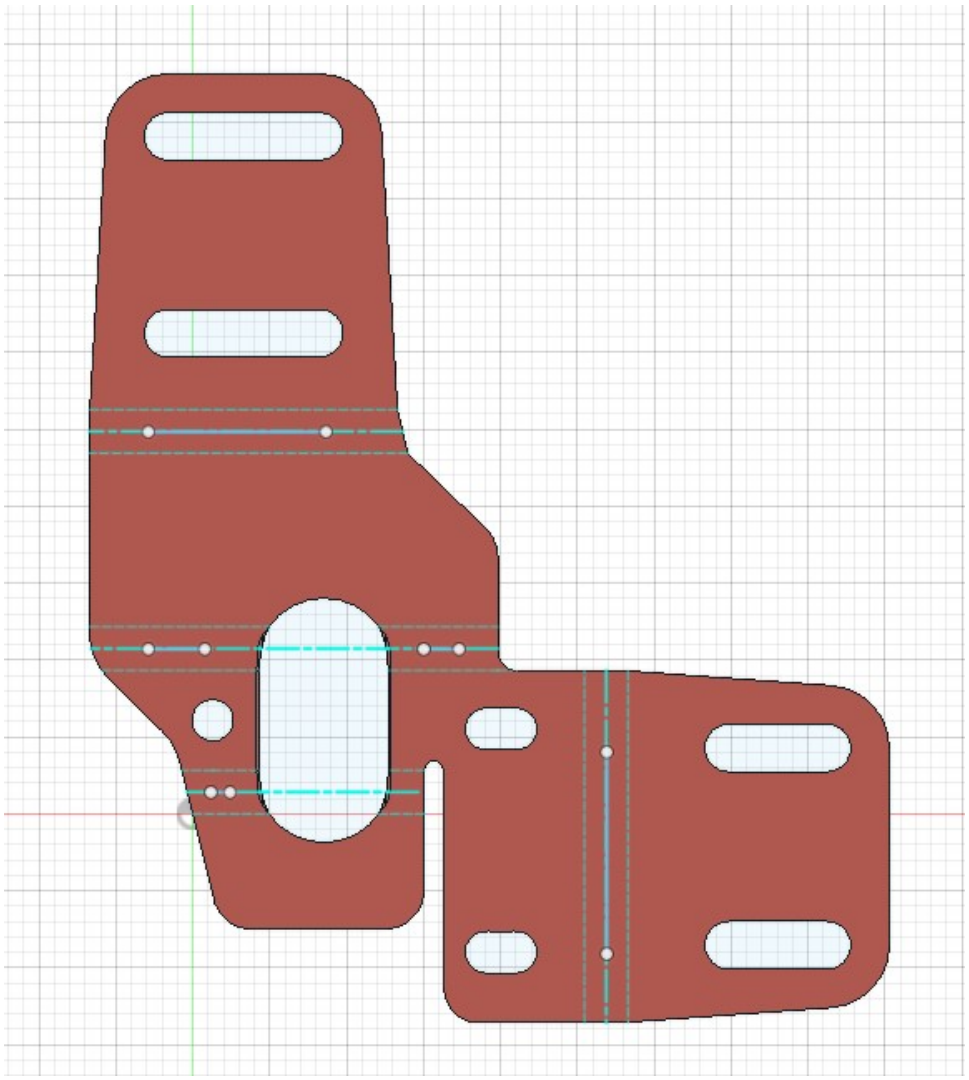


Figure 7.3: Computer Modeled Flat Pattern



Figure 7.4: Resulting CNC Plasma Cut Components



Figure 7.5: Final Folded Component from Flat Pattern

They were also designed with sufficient adjustment room for reconfiguration to adapt to differing testing requirements. The final assembled torch fixture can be seen in Figure 7.6.

7.2 Motion Platform

Shown in Figures 7.7-7.9, a PWM controlled X-axis linear stage for weld travel direction was coupled with a manually controlled Y-axis stage, allowing for multiple weld tests with limited material handling by applying a prescribed offset to successive welds. A velocity profile was developed to determine the appropriate PWM percentage for a chosen weld velocity, as seen in Figure 7.10.

7.3 Alignment Procedure

To aid in alignment of both the torch to a desired contact-tip-to-workpiece distance, as well as to align the magnetic poles ~ 90 degrees apart in relation to the travel axis of the weld, an FDM printed alignment fixture was developed, as seen in Figures 7.11, 7.12, and 7.13. This fixture was produced in two components to aid in removal around the electromagnets, and optimized to work in both the GMAW and GTAW cases. Each respective magnet can be repositioned in the X, Y, and Z axes to achieve a coarse position, where a Starrett 0.001in dial indicator on a magnetic base was used in conjunction with the motion platform, described in Section 7.2 to fine-tune magnetic pole position.

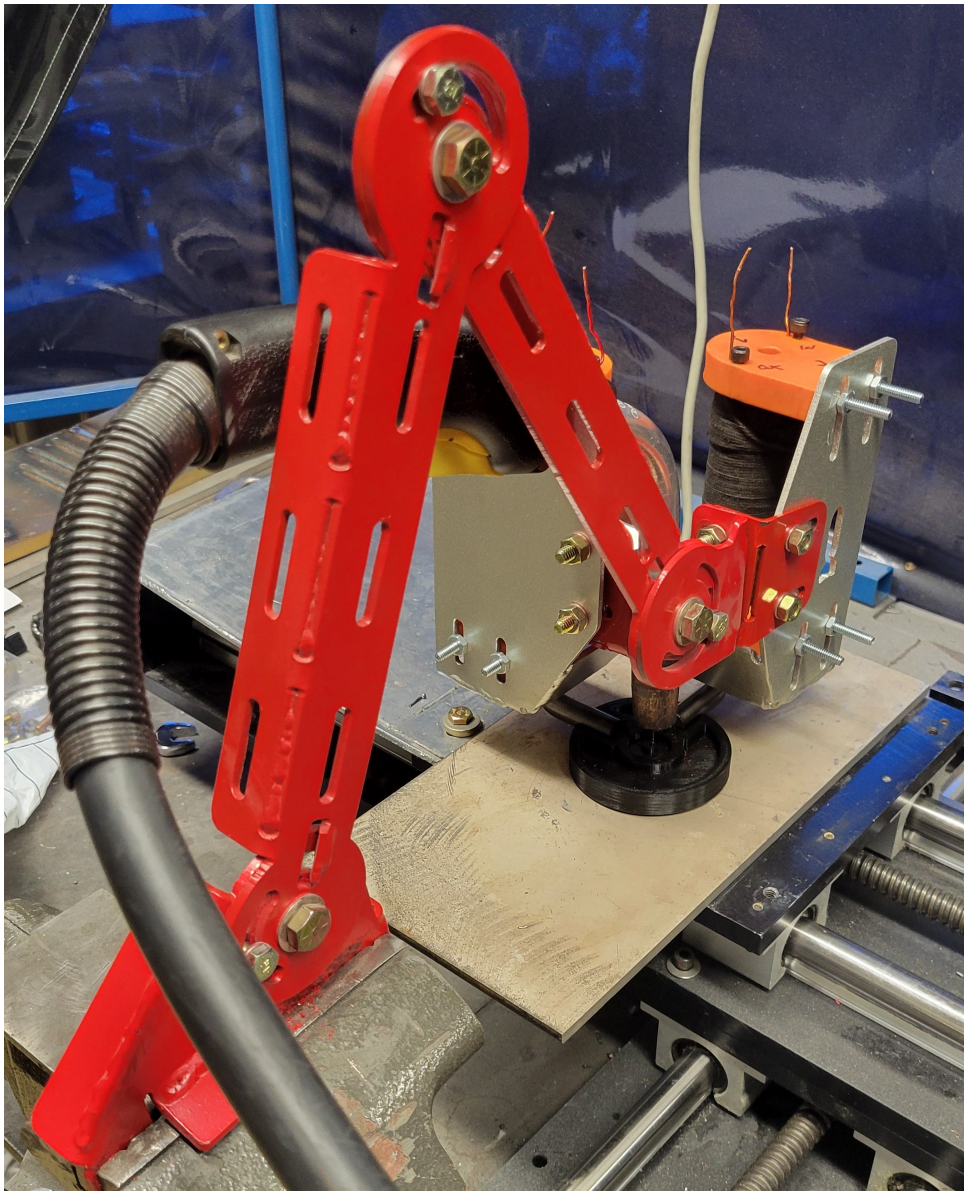


Figure 7.6: Assembled Test Fixture with FDM Printed Alignment Fixture Shown

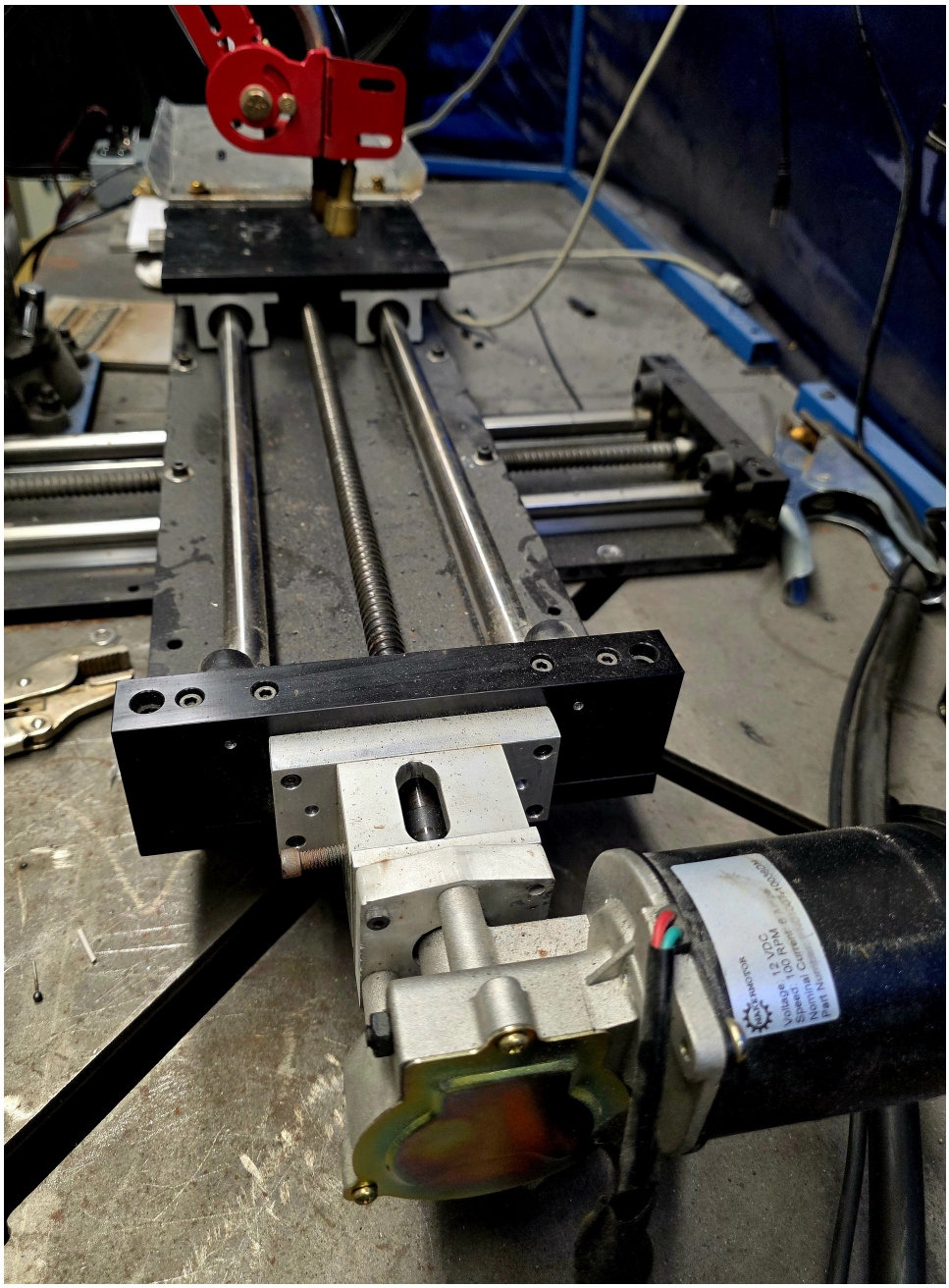


Figure 7.7: PWM Controlled Motion Platform

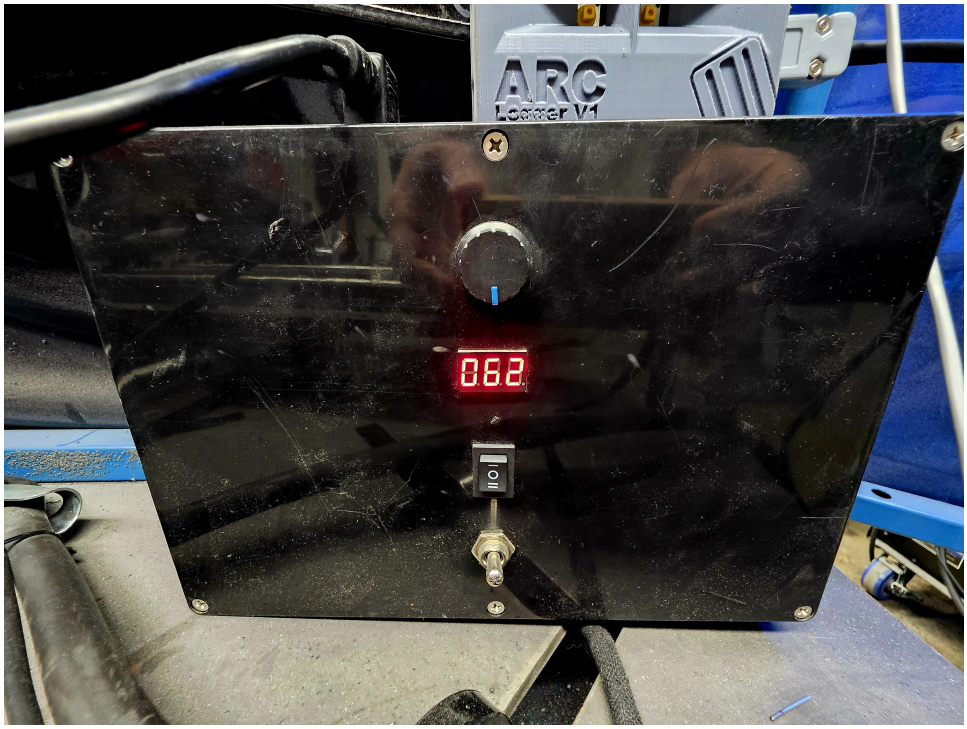


Figure 7.8: Custom Developed Motion Platform Controller

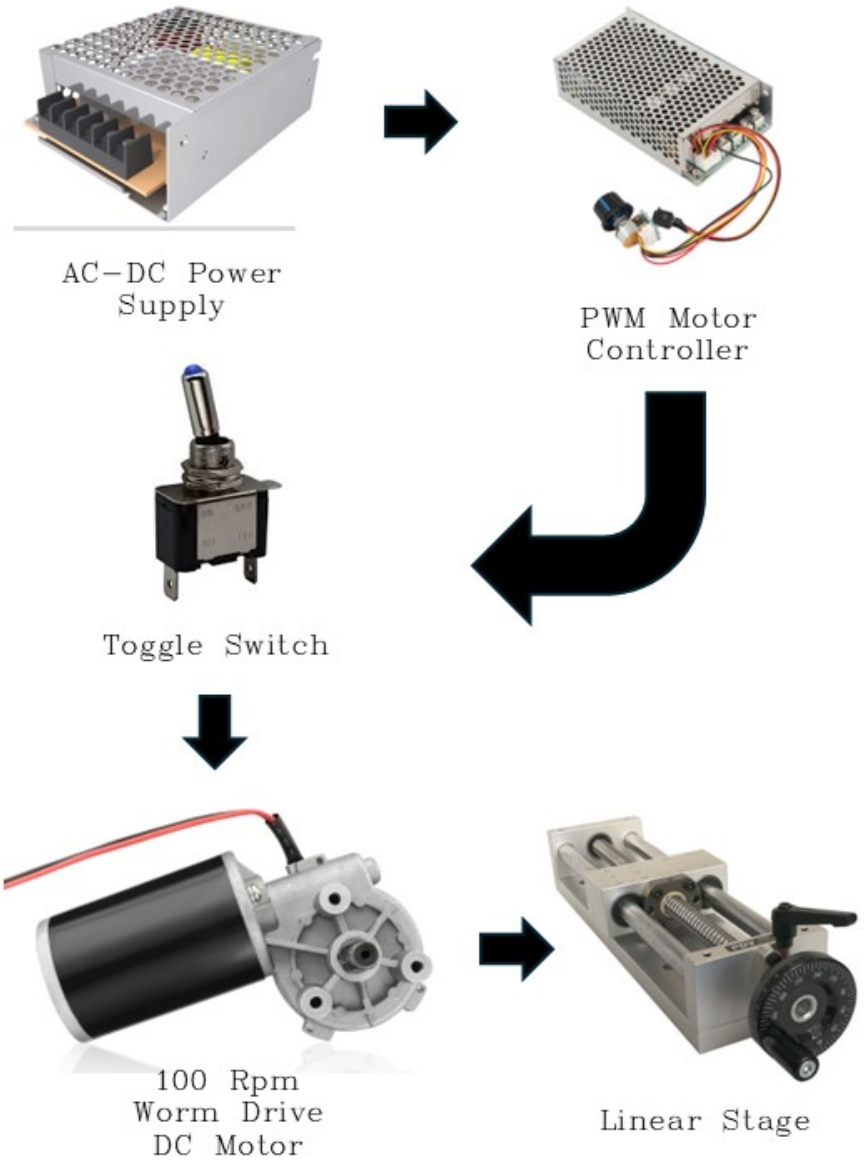


Figure 7.9: Motion Platform Process Map

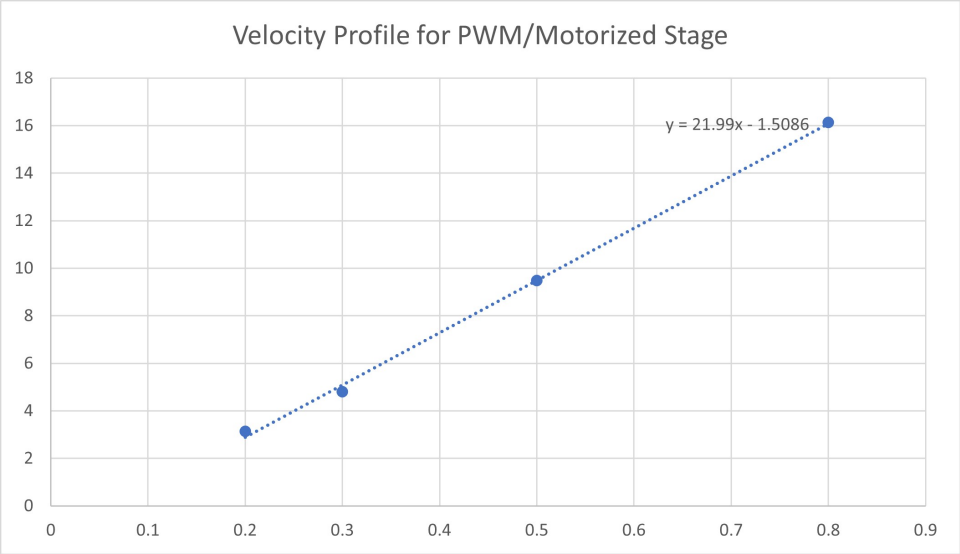


Figure 7.10: PWM Velocity Profile

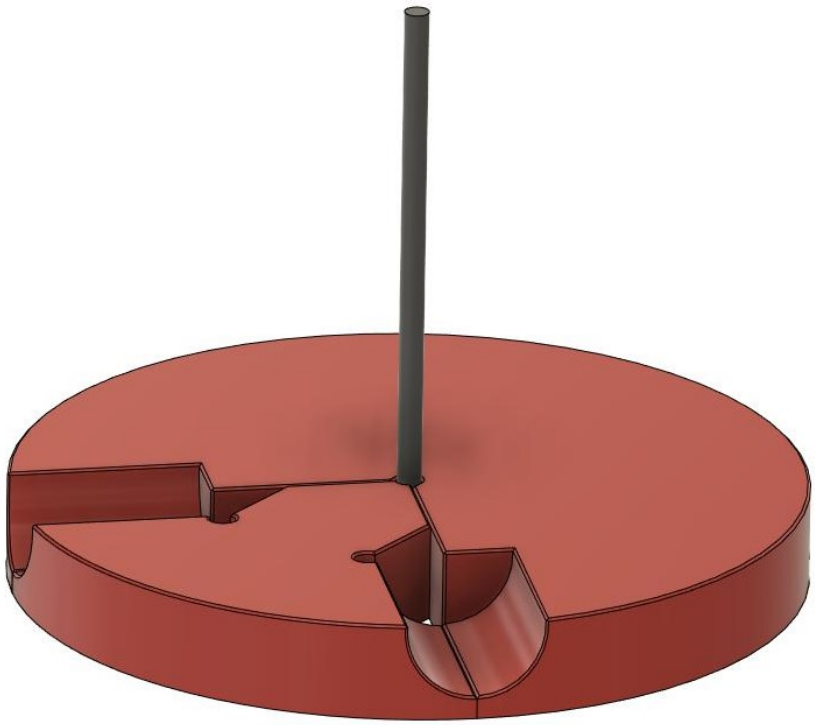


Figure 7.11: Off-Robot Alignment Fixture



Figure 7.12: GMAW Alignment in Off-Robot Setup

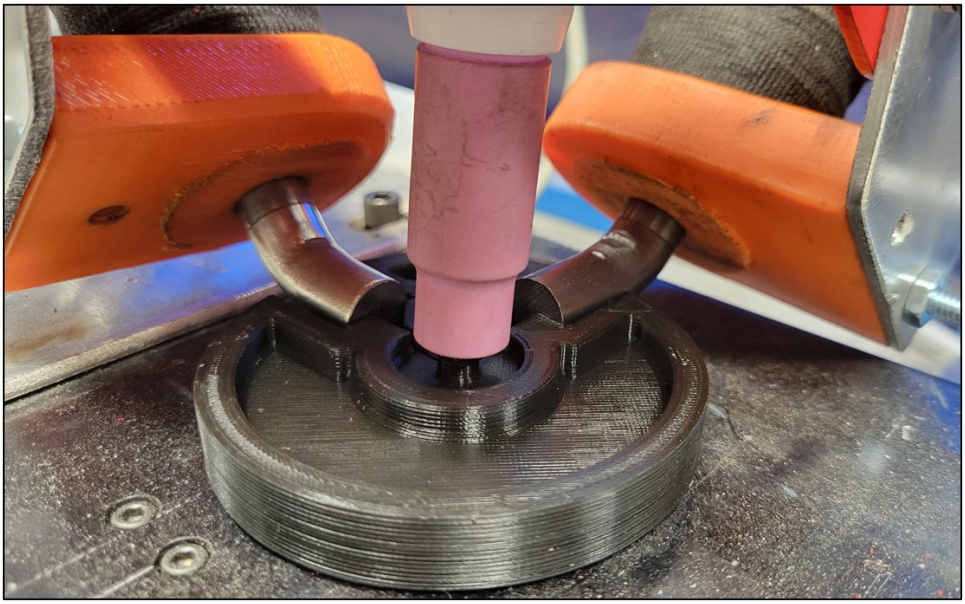


Figure 7.13: GTAW Alignment in Off-Robot Setup

7.4 Data Collection

To record current and voltage data in the off-robot test configuration, an Arduino microcontroller based data collection system was developed (Figures 7.14, 7.15) around a custom manufactured printed circuit board. This hardware interfaces with the wire feeder voltage sensing port and ground circuitry on the Miller Pipeworx 400 welding power supply and utilizes an onboard voltage divider to reduce the welding voltage to a 0-5V input signal in 1024 steps, providing a usable resolution of ∼0.5V at ∼1kHz sampling rate. Current data is captured via a Hall-effect current sensor in 200A and 500A maximum current ranges, respectively. Post processing was done via a Matlab script, seen in Appendix B.3. Example voltage, current and resulting fast-fourier-transform (FFT) plots can be seen in Figures 7.16 and 7.17.

7.4.1 Procedure

To operate the data collection system, a Hall-effect current sensor with the appropriate range is chosen and installed along the ground clamp circuitry of the welding power supply. Voltage sensing leads are placed in their corresponding locations at the wire feeding mechanism. Following this initial setup, a micro SD card is installed and initialized by the operator by depressing the reset button on the right-hand side of the controller. When data is to be collected, the operator depresses the start/stop button on the left-hand side of the controller to start the recording, and again to stop it. Upon successful recording, the unit will display the file name on the LCD screen, where up to 10 successive files can be recorded.

7.4.2 Limitations

With any analog voltage recording device, noise is minimized through the utilization of proper grounding, shielding cable runs and twisted wire pairs, as well as the placement of the circuitry as far from the welding arc as is conveniently possible. This is made more difficult through the high currents and rapidly changing voltages seen in welding power supplies,



Figure 7.14: Arduino-Based Data Collection System

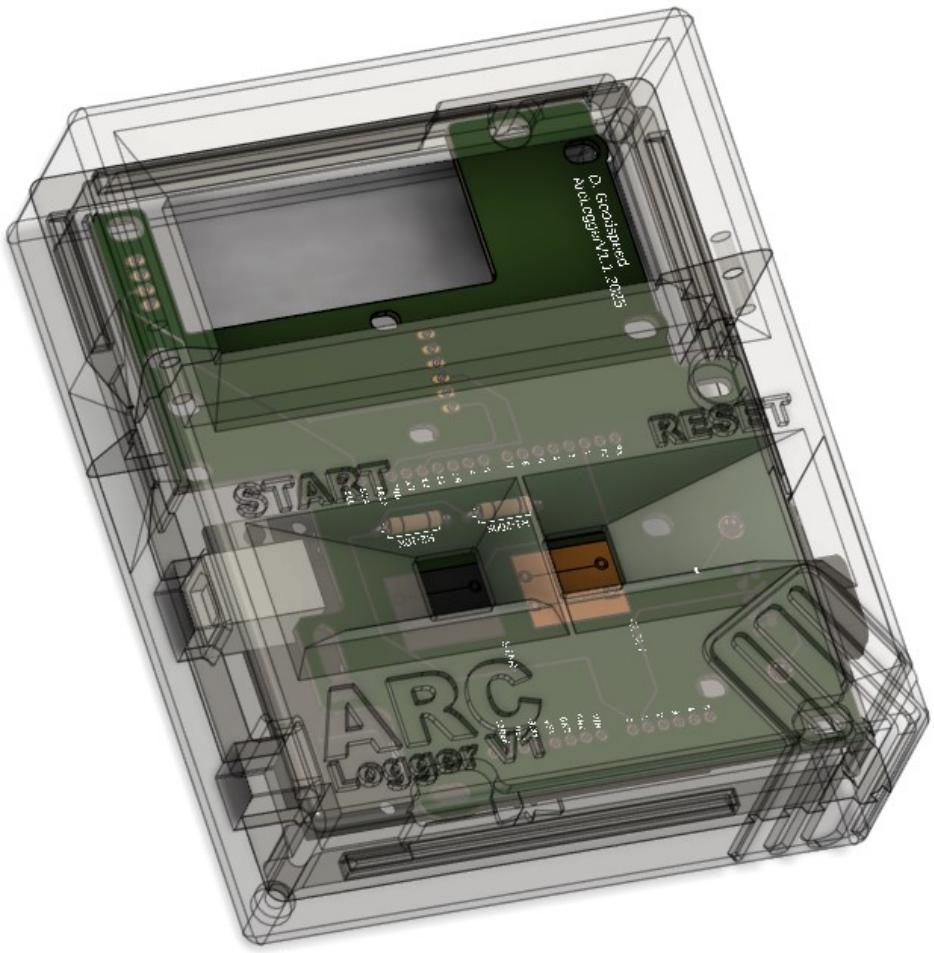


Figure 7.15: Transparent Model of Arduino-Based Data Collection System

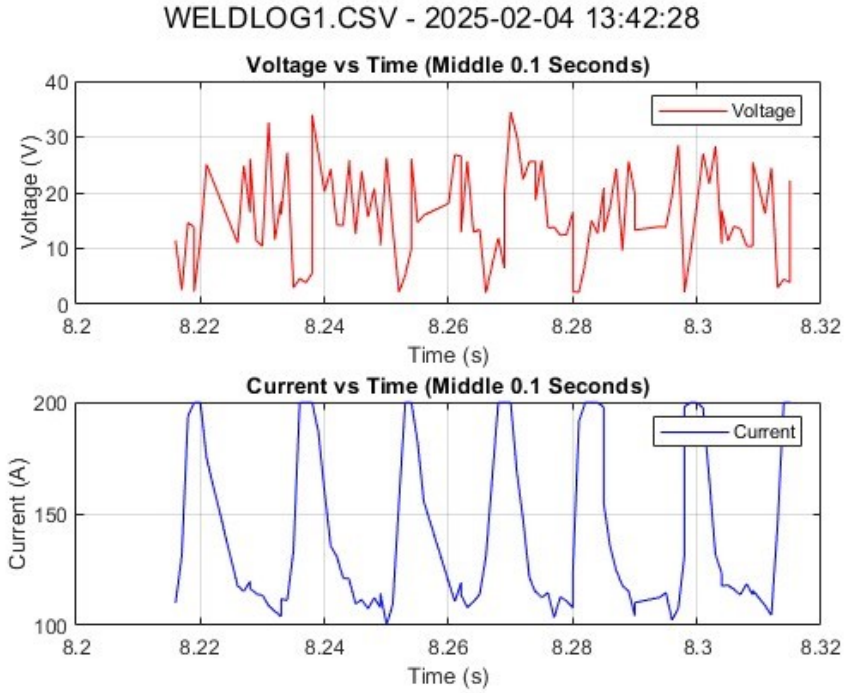


Figure 7.16: Example Off-Robot Collected Current and Voltage Data

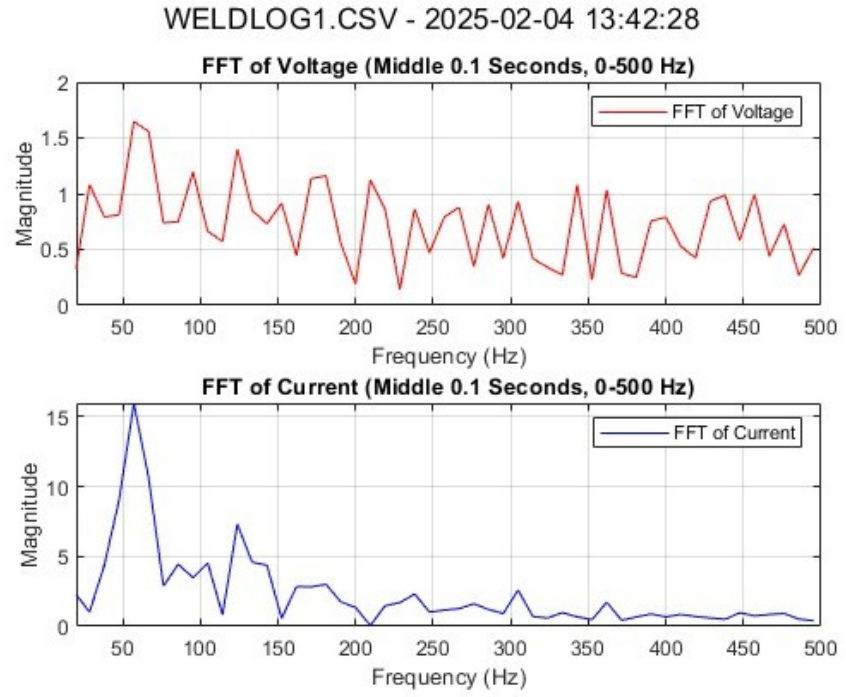


Figure 7.17: Example Off-Robot FFTs from Current and Voltage Data

which produce strong electromagnetic fields and can induce unwanted voltage signals within the data collection system, as was seen by the amount of noise in the collected data. This could potentially be mitigated by utilizing analog to digital data conversion circuitry at the sampling site before transmission to the data collection device and is an area for future work. For on-robot testing, a different approach was taken, as outlined in Section 8.3.

7.5 Trailing Gas

While a 98% Argon/ 2%Oxygen mix was used for primary shielding gas, 100 percent industrial-grade Argon, also sourced from Airgas Inc, was employed as a trailing gas using a CK Worldwide TS300 trailing shield (Figures 7.18-7.19). This was utilized in a secondary gas lens configuration to provide additional inert gas coverage to the weld as it cools. To accomplish this, a gas control solenoid was placed inline with the flow and controlled via a custom developed and manually operated controller (Figure 7.20). This controller and process (Figure 7.21) was utilized in both off-robot, as well as on-robot experimental setups, as outlined in Section 8.4.

7.6 Imaging

A Visible Welding camera, coupled with proprietary WeldWatch software, was utilized for video-based welding image capture, as seen in Figure 7.22. For still welding images, a Nikon D5100 digital single-lens-reflex (DSLR) camera (Figure 7.23) was used with either an 18-55mm f3.5 or 55-200 f4.0 lens in conjunction with stacked ND2, ND4, ND8 and ND16 neutral density filters in a continuous shutter control mode at an aperture of f10, ISO of 6400 and 1/4000s shutter speed, respectively. A total of 725 images were collected during this research, an un-retouched example of which can be seen in Figure 7.24.



Figure 7.18: CK Worldwide TS300 Trailing Gas Shield

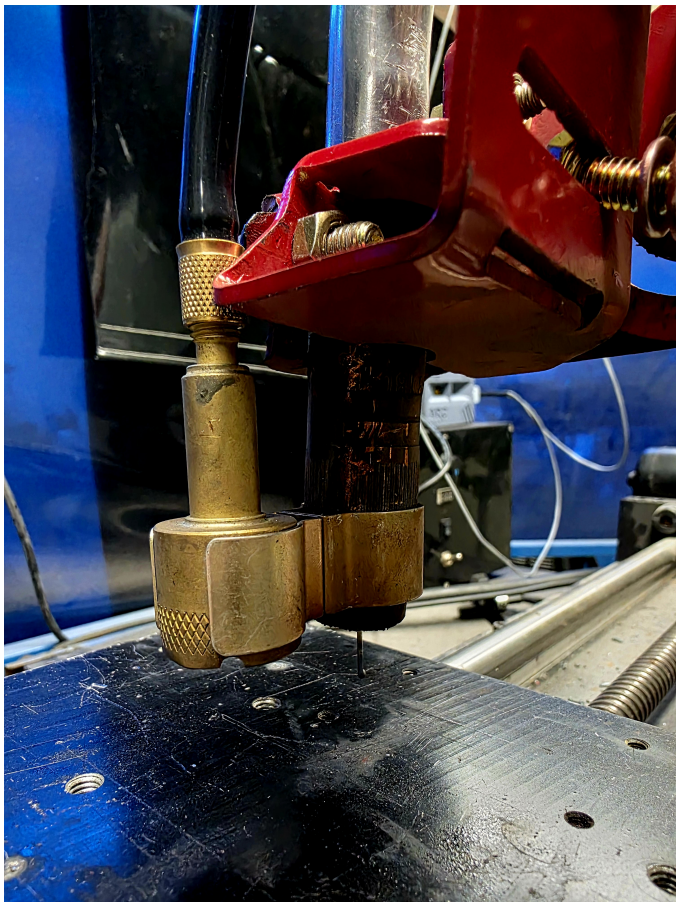


Figure 7.19: CK Worldwide Trailing Gas Shield Installed on GMAW Torch

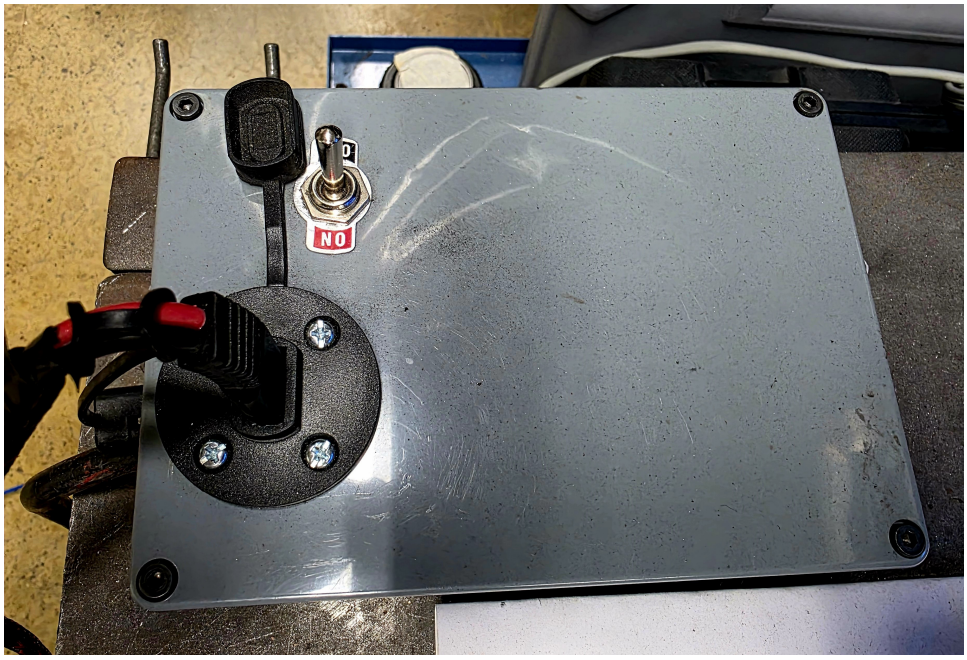


Figure 7.20: Custom Manufactured Trailing Gas Controller



Figure 7.21: Trailing Gas Process Map

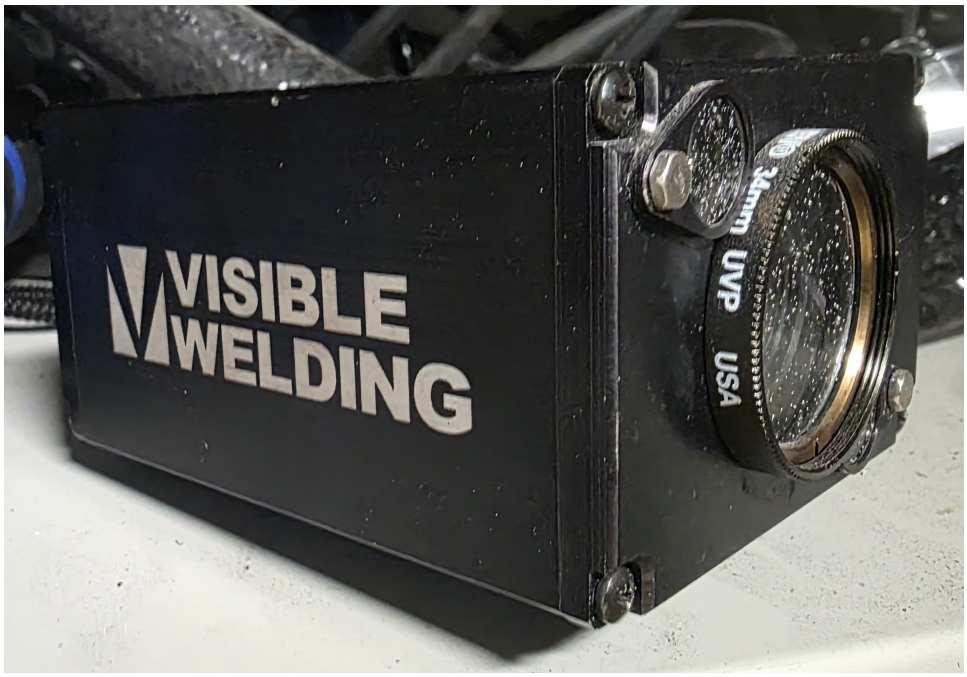


Figure 7.22: Visible Weld Camera



Figure 7.23: Nikon D5100 Imaging Setup



Figure 7.24: Example Captured Image Using Nikon D5100

Chapter 8

On-Robot Hardware

8.1 Fabrication Process

8.1.1 Design Considerations

The following design constraints were identified as critical during development:

- Overall weight of torch mounted hardware <6 lbs (∼2.72kg). With a 13.23lb (6kg) overall robot payload inclusive of the welding torch and supporting hardware, it was imperative to not exceed this limit and ensure robot movement at its full range of motion.
- To limit magnetic interactions within the hardware, materials will be chosen for the purpose of low magnetic permeability where required, such as areas in close proximity to the magnetic coils and poles.
- Hardware should be reconfigurable and serviceable for differing experimental setups.
- Minimize outsourced custom-fabricated components, such as powder-based additively manufactured components.
- Hardware should leverage as many components as feasible from the off-robot hardware outlined in Chapter 7.

8.1.2 Fabrication

Machined Components

Components machined from billet, such as the hardware mounting base shown in Figure 8.1 were fabricated using a Logan 14"x40 toolroom metal lathe for turning operations, coupled with an Excello 602 toolroom milling machine for milling operations. The main mounting component shown in Figures 8.1-8.4 was produced from 2in 6061 aluminum round bar, bored to size, allowing clearance for welding gas nozzles and contact tip removal for servicing, then machined with 90-degree sides and 4x 1/4"-20 UNC threaded holes on each face for flexibility in future work.

Additively Manufactured Components

In addition to the electromagnet bobbins, discussed in 6.2.3, carbon fiber reinforced FDM-printed components were utilized for low-load mounting solutions, such as accelerometry hardware mounting (Figures 8.5-8.9). This was done for increased design flexibility and reduced time to implementation, but limited to non-critical applications since heat damage, shown in Figure 8.10, was seen after $\sim$ 2hrs of weld time in areas closest in proximity to the welding arc.

Cut/Formed Components

As a preferred method of fabrication due to low cost and reduced time to implementation, mounting components for this research stage were either leveraged from the previous off-robot experiments, or CNC plasma cut using a Langmuir Crossfire Pro from 0.125in 1018/A36 cold rolled mild steel or 0.125in 6061 aluminum. An example cut path is shown in Figure 8.11.

Weight Considerations

To align with design goals, the torch assembly, shown installed in Figure 8.12, was weighed, including both electromagnets, assorted mounting hardware and bracketry, and the welding torch itself. At 5lbs 11.9oz, the design target of $< 6lbs$ was realized, as seen in Figure 8.13.

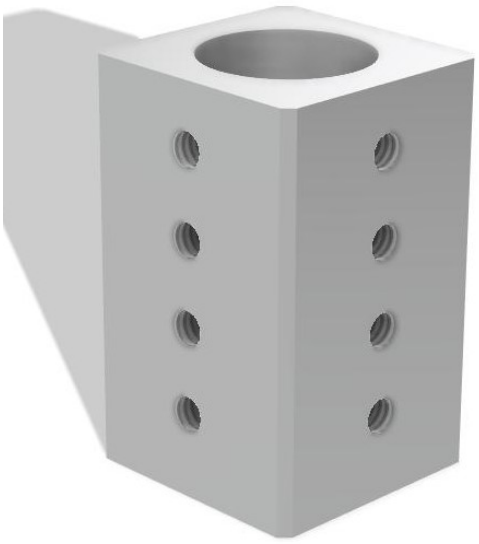


Figure 8.1: Torch-based Hardware Mounting Solution for Kuka KR6-2



Figure 8.2: Raw Material for Torch Mounting Solution on Kuka KR6-2



Figure 8.3: In-Process Machining for Kuka KR6-2 MAO Mounting Solution



Figure 8.4: In-Process Thread Cutting for Kuka KR6-2 MAO Mounting Solution

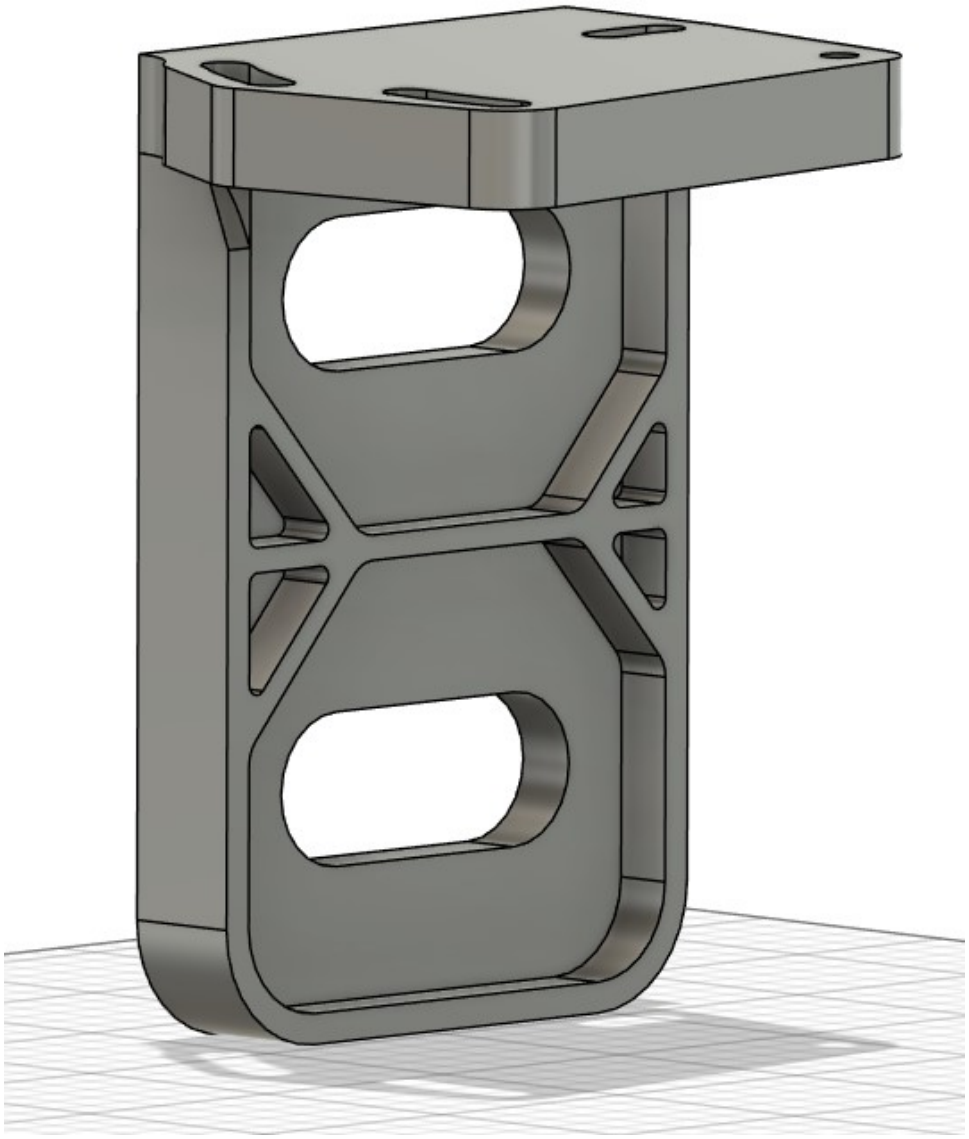


Figure 8.5: LSM9-DS1 Accelerometer Torch Mounting Bracket 3d Model



Figure 8.6: LSM9-DS1 Accelerometer Torch Mounting Bracket

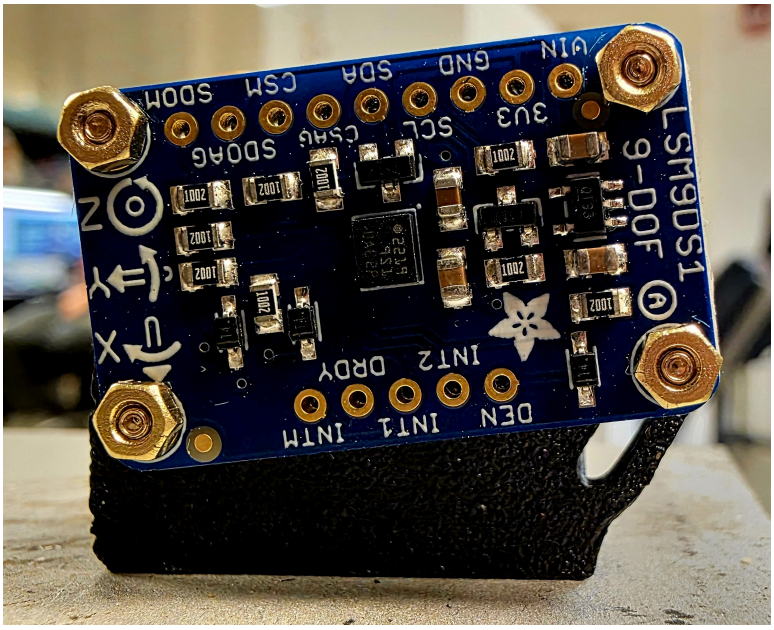


Figure 8.7: LSM9-DS1 Accelerometer Mounting Bracket Maximum (+) Adjustment

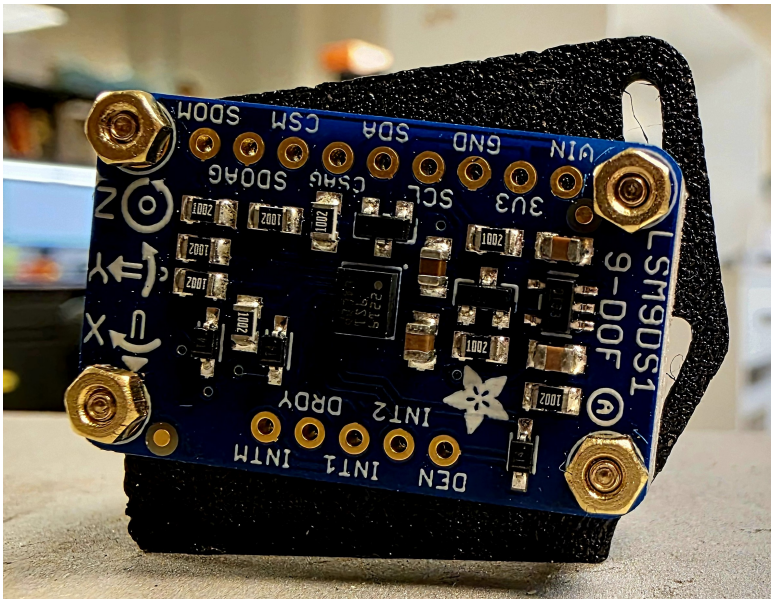


Figure 8.8: LSM9-DS1 Accelerometer Mounting Bracket Maximum (-) Adjustment

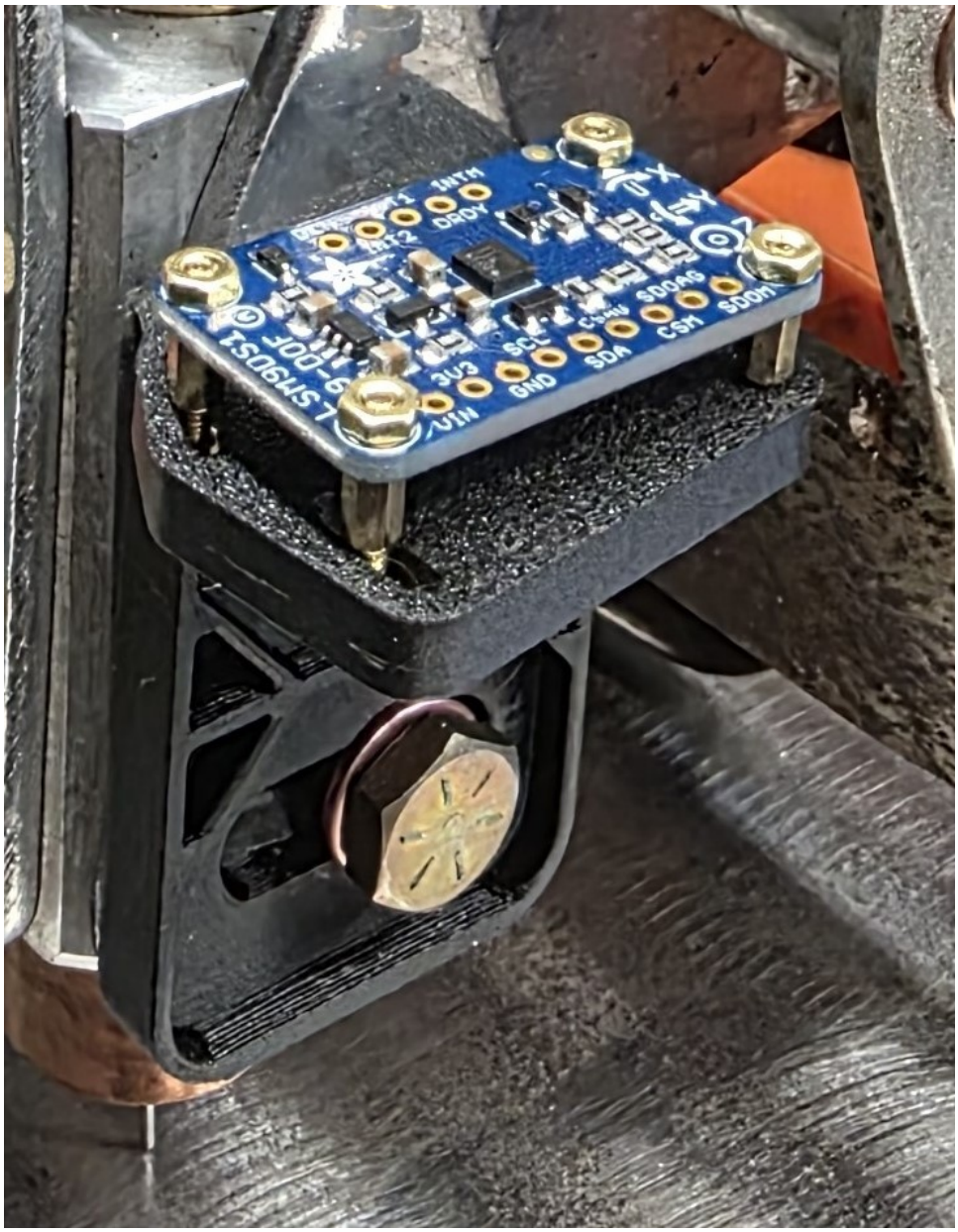


Figure 8.9: LSM9-DS1 Accelerometer Mounted on Kr6-2



Figure 8.10: LSM9-DS1 Accelerometer Bracket Heat Damage

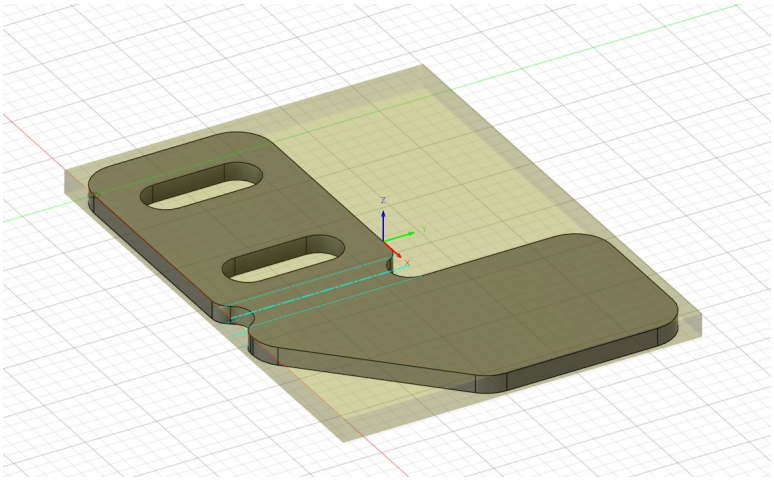


Figure 8.11: CNC Plasma Cut Path for Kuka KR6-2 Magnet Mounting

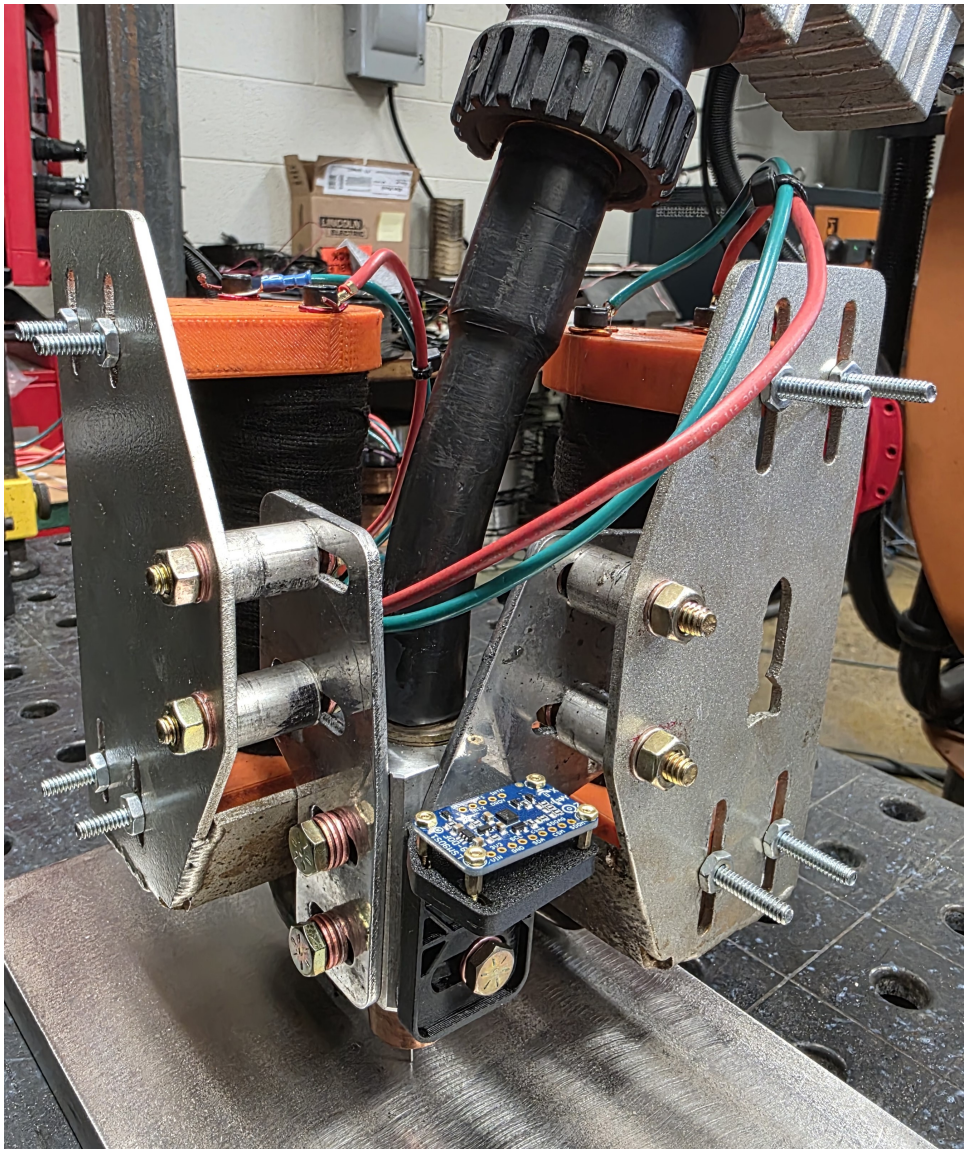


Figure 8.12: Complete Magnet Mounting Solution for Kuka KR6-2

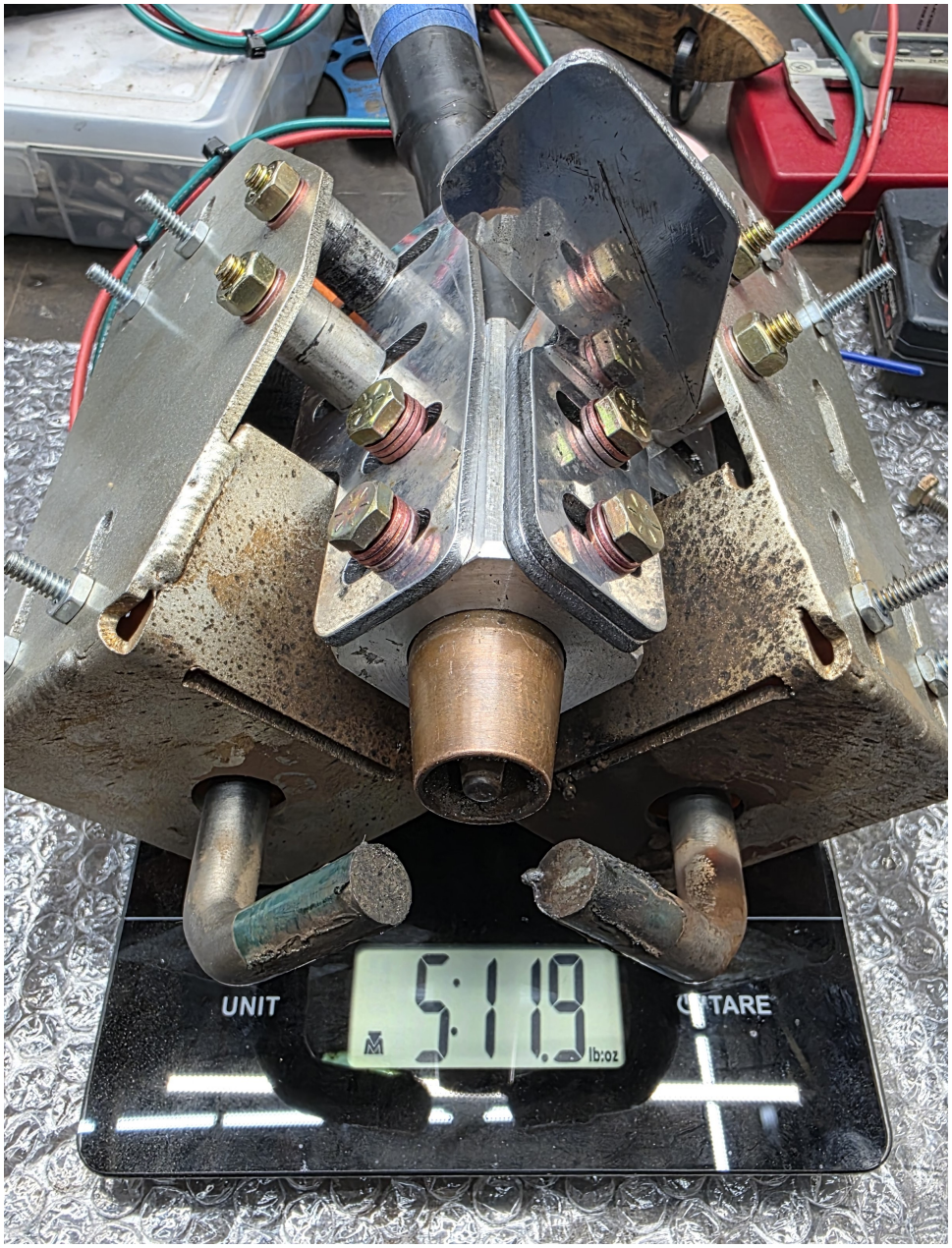


Figure 8.13: Total Weight of KR6-2 Torch Mounted Components

8.2 Alignment Procedure

To aid in alignment in the on-robot case, the same FDM-printed alignment fixture discussed in Section 7.3 was utilized for coarse alignment, followed by a laser-based alignment strategy, where a line was laid out using the wire electrode as a datum and its path traced as the robotic manipulator was jogged inline with the X-axis. A Bosch self-correcting GLL2 cross-line laser (Figure 8.14) was aligned with the established line, providing a means of establishing a second line normal to the first (Figure 8.15). After the electromagnets were aligned using this process, focus was shifted to aligning the accelerometer onboard sensing hardware outlined in Section 9.2.2 with the X and Y axes. To do this, the edge of the LSM9DS1 circuit board was chosen as an alignment datum and aligned using the previously established laser grid (Figure 8.16).

8.3 Data Collection

On-robot data collection was accomplished using a purpose manufactured acquisition system by Miller Electric Inc (Figure 8.17) with a custom-developed Python script sampling up to ~20kHz. While the KUKA KR6 weld cell has capabilities to record audio and IR video, the focus here was narrowed to just welding current and voltage. The data collected with this hardware is outlined in Section 10.3.6.

8.4 Trailing Gas

Leveraging work and control hardware described in Section 7.5, trailing gas was utilized during the on-robot testing phase using one of the three configurations outlined below:

- The CK TS300 configuration outlined in Section 7.5.
- Additively-manufactured omnidirectional trailing gas shield (Figure 8.18): A laser powderbed fusion additively manufactured built-for-purpose gas nozzle was designed



Figure 8.14: Bosch GLL2 Self Correcting Line Laser

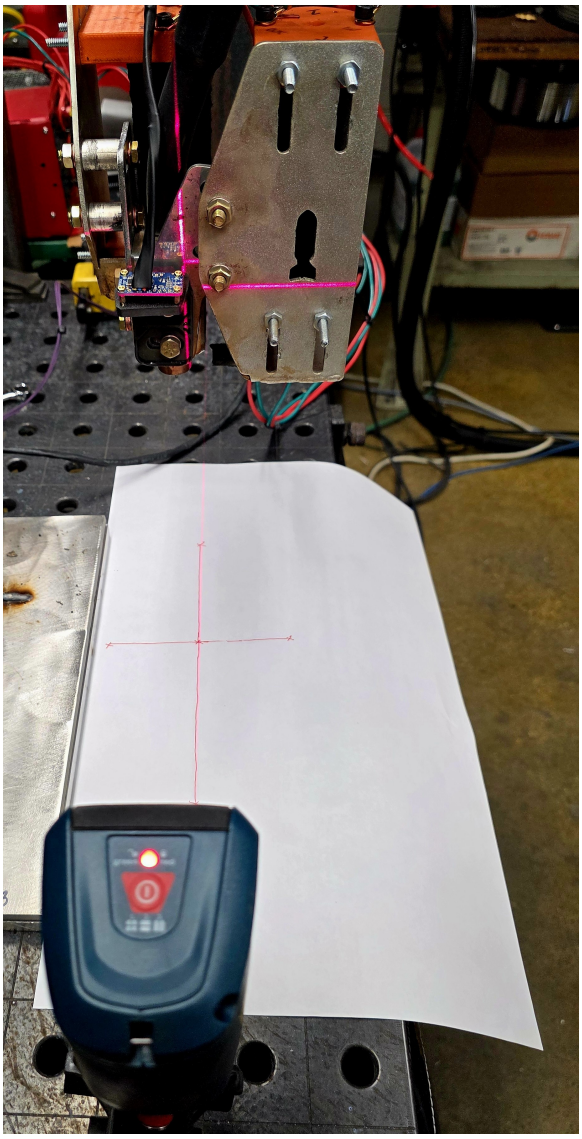


Figure 8.15: Laser Cross-line Layout

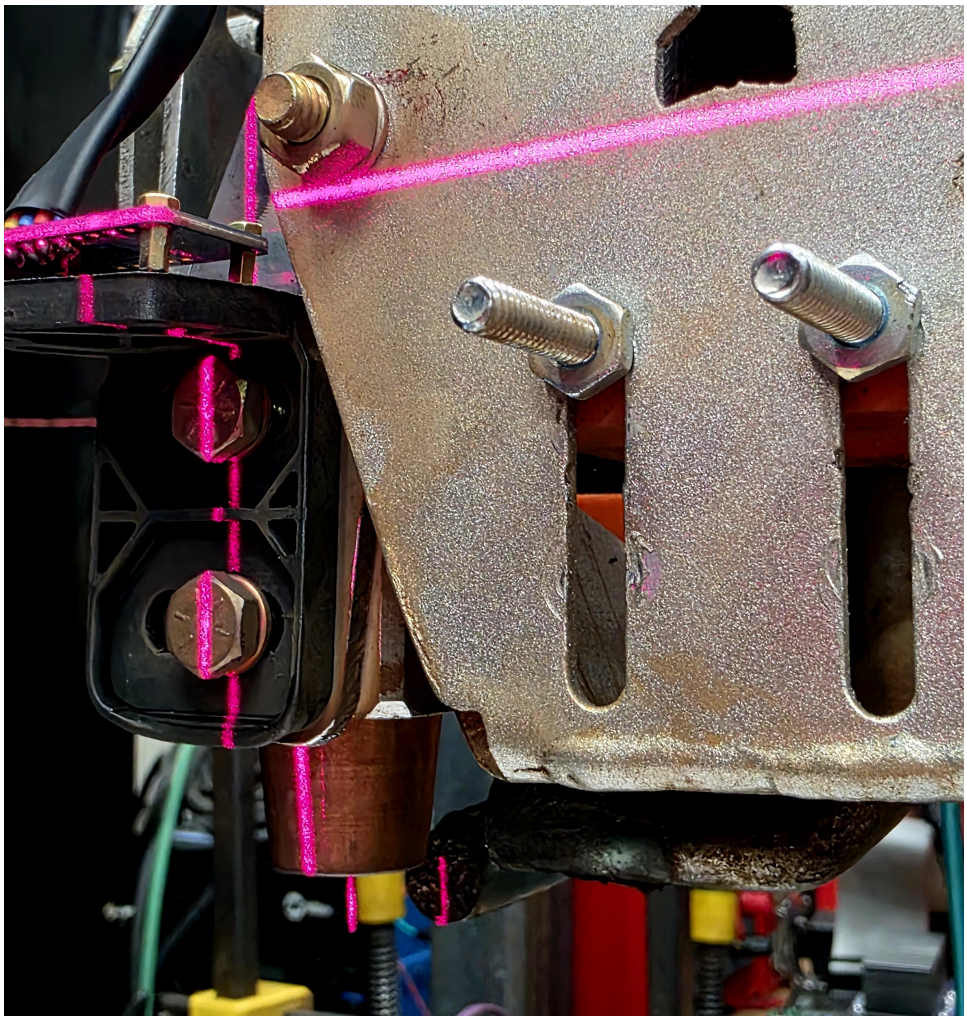


Figure 8.16: Laser Alignment of Wire Electrode, Magnetic Pole Piece and Accelerometer



Figure 8.17: Miller LEM Data Acquisition System



Figure 8.18: Omnidirectional Trailing Gas Shield

to surround the existing GMAW gas nozzle with an additional layer of 100 percent Argon shielding as the weld cools. This experimental setup was discontinued due to its inability to maintain an inert environment long enough for the weld to cool.

- Triple-nozzle trailing shield (Figure 8.19): Leveraging spare components from the Fronius CMT 4000 welding power supply, additional welding torch assemblies were mounted on either side of the deposition torch and plumbed to 100 percent argon with a valve to adjust the flow and accommodate different travel directions. While this was the most user friendly setup, access with the magnet assembly proved impractical.

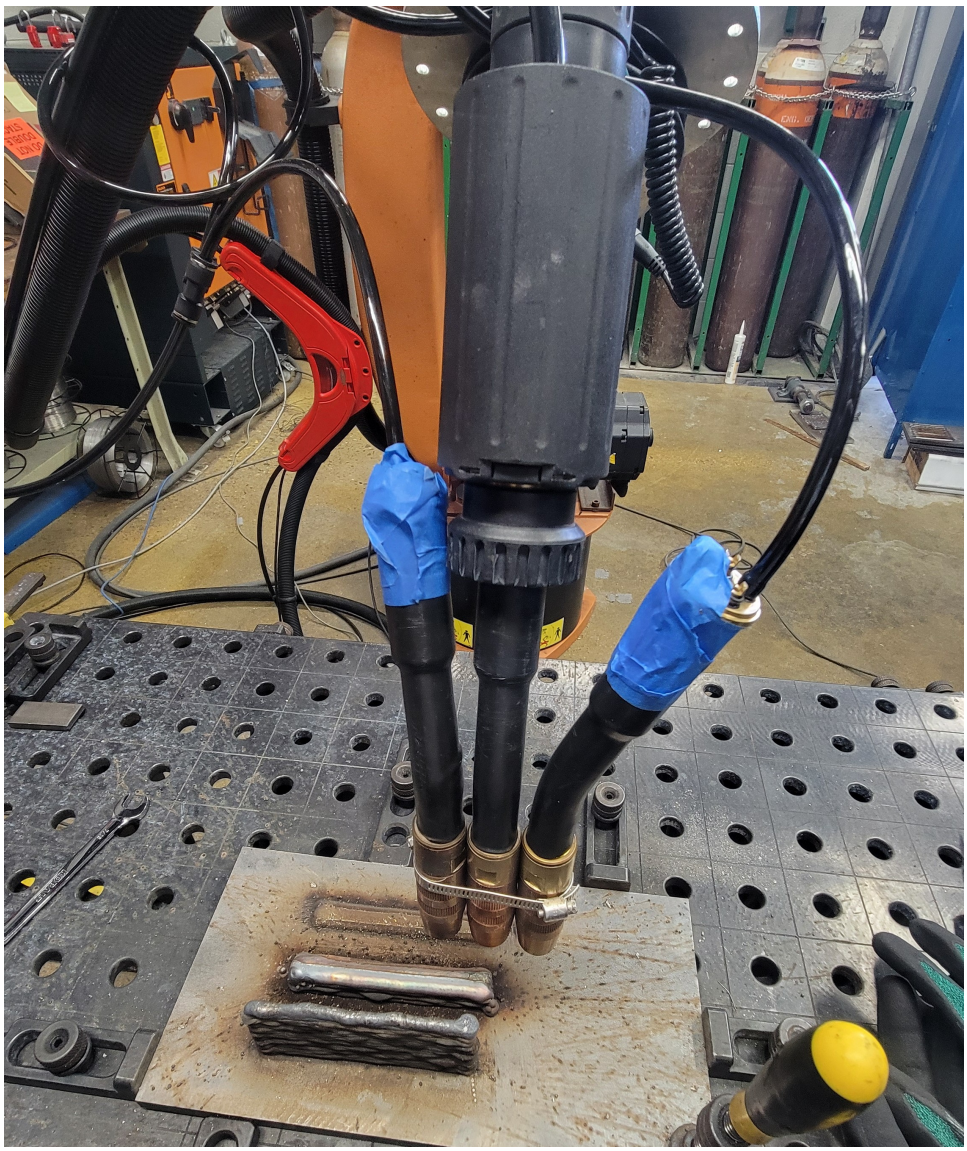


Figure 8.19: Triple Nozzle Trailing Gas Configuration

Chapter 9

Control System

9.1 Objectives

The following control system design objectives were identified as critical for the success of this project:

- Standalone Operation: Operate in a standalone configuration, where weaving logic is automatically deployed upon recognition of welding arc initiation.
- Fast Transient Response: Respond to positive arc detection signals within the dwell time of the robotic manipulator after arc initiation ($\leq 0.1s$).
- Safe Over-current Protection: Limit or shutdown hardware in an overheating or over-current event.
- PWM-Based Current Control: Regulate current supplied to electromagnets via pulse-width-modulation.
- Fine Tuning: Allow for fine tuning to account for variations in electromagnet field strength outputs.
- Simulation: Allow the operator to visualize a potential weld bead deflection path before hardware deployment.

- User Interface for Parameter Adjustment: Provide an interface to allow operators to adjust weld velocity, deflection amplitude and weave profile before hardware deployment.

9.2 Control Hardware

9.2.1 Magnet Control Hardware

In keeping with a driving principle of high performance at reduced cost, commercially available hardware was re-imagined to suit a contemporary solution by capitalizing on existing solutions within the do-it-yourself CNC community. To achieve a controlled magnetic field output, varying input current to the electromagnets via pulse-width-modulation (PWM) was chosen. Primarily used for light-emitting-diode (LED) or direct-current (DC) motor control, PWM operates by varying the width of input pulses to a device, usually in the 20-25 kHz range, as a means of varying input power. An example is shown in Figure 9.1 where a sine wave, in blue, has been converted to all positive PWM values. By doing so, the input power supply remains fixed at the maximum safe input current allowable in the system and average output current is varied via pulse width modulation.

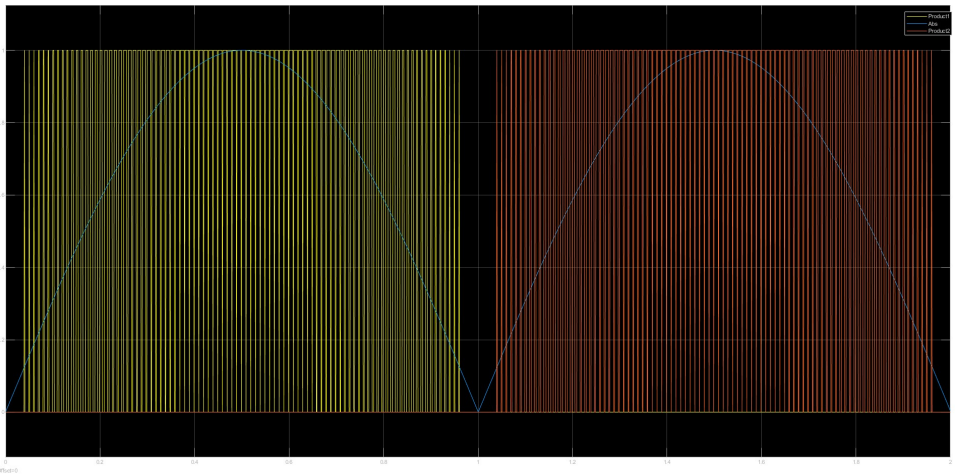


Figure 9.1: Example PWM Signal

Electromagnetic Relays

Due to availability and the requirement to have a polarity-reversing capability, electromagnetic relays were initially explored for the earliest control logic iterations, where PWM had yet to be implemented, Figure 9.2. To test this control hardware, light emitting diodes (LED) were oriented in a parallel configuration with one wired in a traditional-polarity configuration and one oriented in a reversed-polarity configuration. Due to their ability to only conduct electricity in one direction, this configuration allowed only one polarity direction to illuminate at a time, simulating the polarity of the electromagnet. This setup was also used to implement and test logic initiation methods, such as the momentary switch-based configuration shown in Figure 9.2. This electromagnetic hardware, however, was quickly iterated upon due to their inability to maintain control at the frequencies required by PWM circuitry ($\sim 20 - 25kHz$), and the logic/wiring complexity necessary for polarity reversing.

Motor Drivers

Available in a low-cost and self-contained package optimized for high-current DC motor applications, a pair of BTS7960 H-bridge motor drivers, shown in Figure 9.3, were utilized for current iterations of magnet control hardware. Rated at 42A input current, as well as reversing output polarity made this the logical choice due to being pre-optimized for the operating parameters and providing significant operating headroom over the $\sim 6A$ maximum input current required of the electromagnetic coils. It also utilizes a pin-header control input configuration that was later leveraged for streamlined signal routing. By moving forward with a modular component design, serviceability is greatly improved, where failed individual components can be replaced with a minimum of downtime.

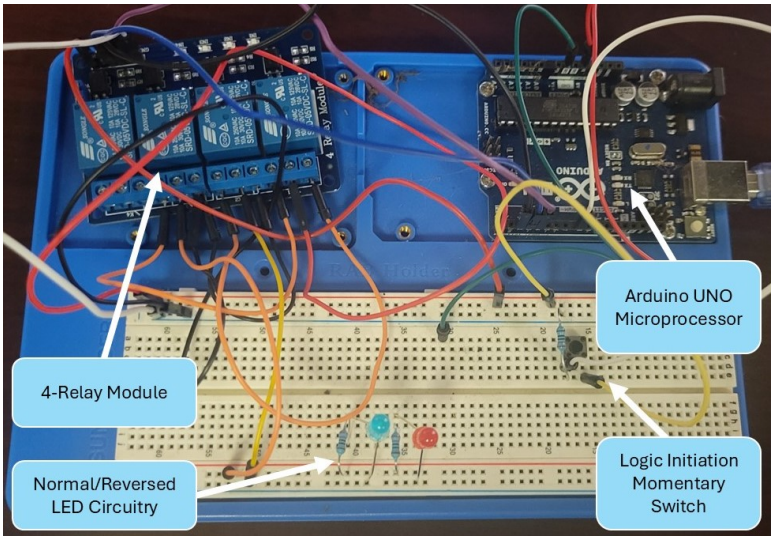


Figure 9.2: Relay-Based Initial Breadboarding

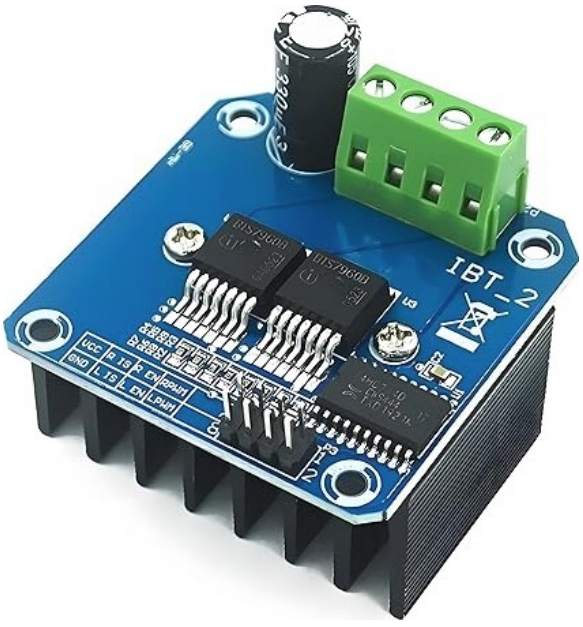


Figure 9.3: BTS7960 H-Bridge Motor Driver

9.2.2 Onboard Sensing

Arc Light Initiation

By automating initial logic control based on the light emitted by the welding arc, errors in start time, especially in the case of multi-pass welding or WAAM, can be kept to a minimum. To do this, a B0B389WHM6 photodiode sensor module (Figure 9.4) was chosen for its adjustable sensitivity, ease of integration and $\sim 20ms$ response time. Utilizing this, weave initiation is directly linked to arc-on time, therefore the weaving profile will restart with every arc-off cycle. This is further discussed in section 9.3.2.

Accelerometry

Combining a 3-axis accelerometer, gyroscope, and magnetometer in a single package, an LSM9DS1, shown in Figure 9.5, is a compact inertial measurement unit (IMU) commonly used in robotics, drone, and wearable device applications. This was chosen to provide directional travel information to the control logic due to its ability to communicate with microcontrollers via I2C or SPI interfaces. The device also provides versatility by combining multiple types of information within a single package. This data was provided to the control logic with the intent of informing the weave direction, discussed in section 9.3.4.

9.2.3 Onboard Sensing Limitations

To test the efficacy of onboard accelerometry as a possible input to control weave direction in a WAAM application, 45, 90, and 135-degree corner paths (Figures 9.6, 9.7, 9.8) were programmed for the on-robot test configuration outlined in Chapter 8 in a hardware-in-the-loop (HIL) configuration using an Arduino micro-controller as the PC interfacing hardware. The output data was then conditioned by utilizing PID control to amplify the signal, sectioning it into positive (+) and negative (-) portions, respectively (Figure 9.9), then a moving standard deviation across 100 samples was calculated (Figure 9.10) and a boolean comparison was made to inform the control logic of a 0 or 90-degree angularity on each

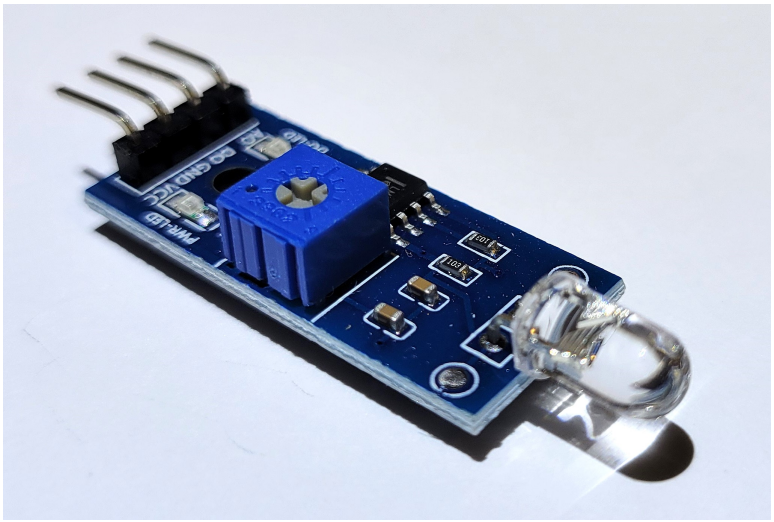


Figure 9.4: B0B389WHM6 Photodiode Sensor Module

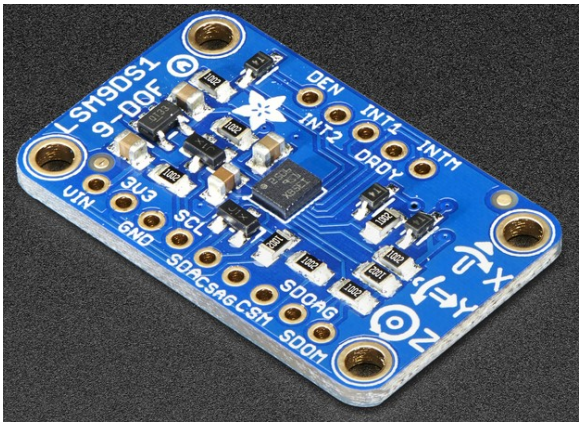


Figure 9.5: LSM9DS1 IMU

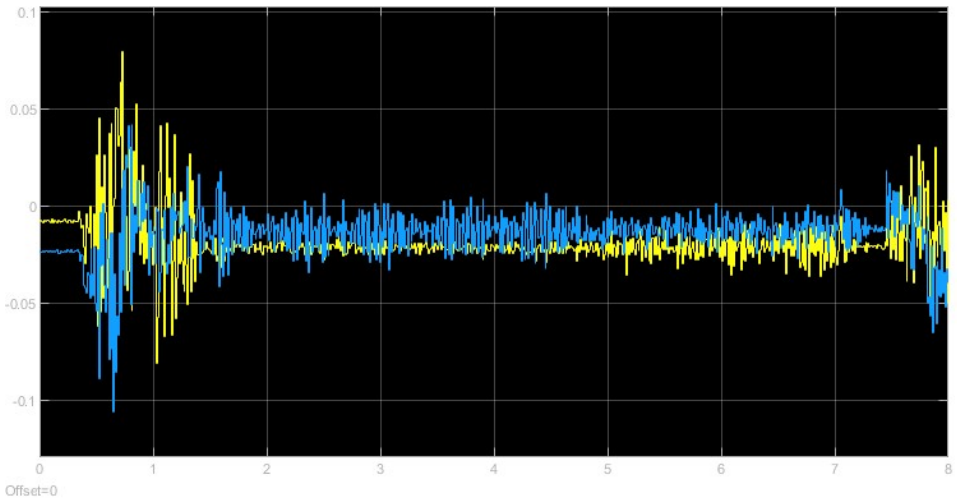


Figure 9.6: 135 Degree Path X (blue) and Y (yellow) Acceleration

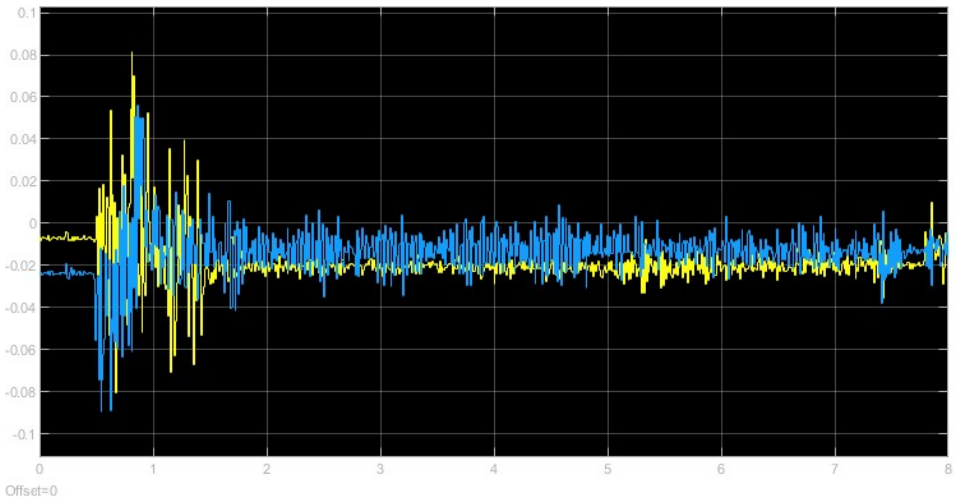


Figure 9.7: 45 Degree Path X (blue) and Y (yellow) Acceleration

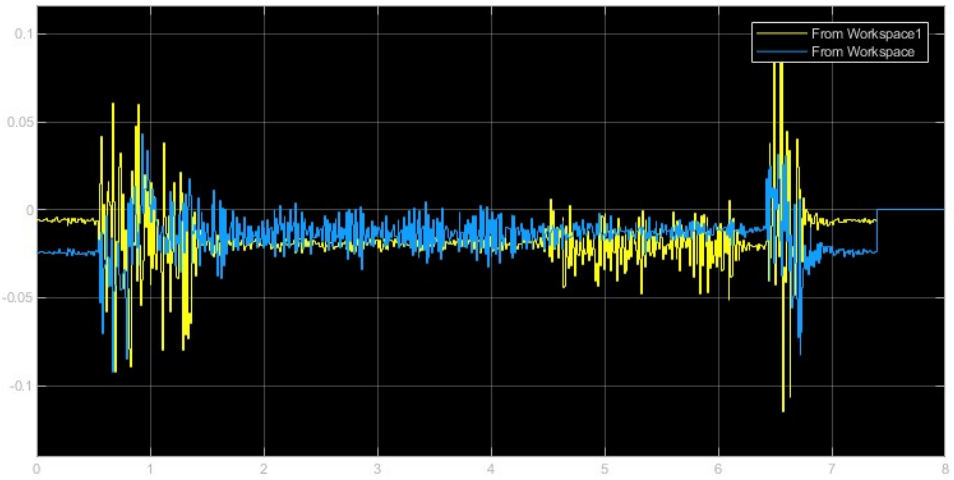


Figure 9.8: 90 Degree Path X (blue) and Y (yellow) Acceleration

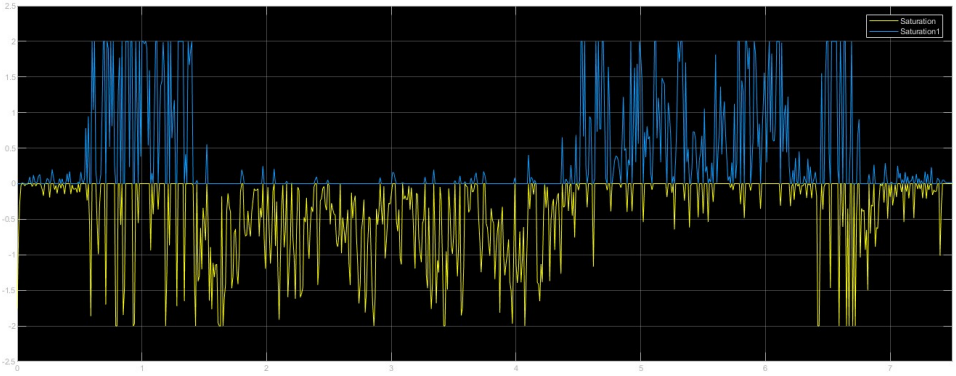


Figure 9.9: 90 Degree Path Signal During Conditioning

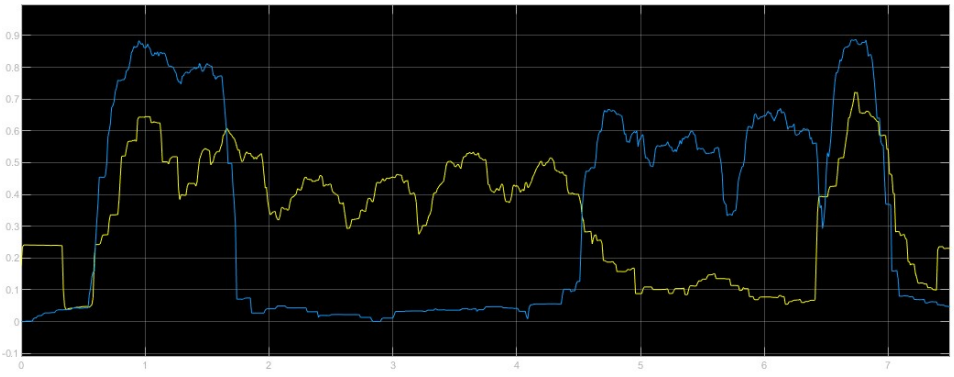


Figure 9.10: Moving Standard Deviations of 90 Degree Path Acceleration Signals

axis resulting in a 0 or 1 boolean value, corresponding with a 0 or 100 percent deflection magnitude on that axis' respective magnet, shown in Figure 9.11. Because of this comparison, a 0-degree or 90-degree weave rotation would be possible, along with 45-degree orientation if both axes calculated a boolean comparison value of 1. While initial success was realized with this control strategy, it proved unreliable primarily due to the level of noise in the signals and was replaced with the programmatic approach outlined in 9.3.7. This approach, however, has potential for future work dedicated towards the utilization of an accelerometry signal as a means of validation for other control strategies.

9.2.4 Signal Routing

By utilizing rapid prototyped breadboards, signal routing was vetted for initial iterations, as shown in Figure 9.12. This was used to develop a wiring schematic, Figure 9.13, after which Autodesk Fusion360 was employed to design a final signal layout (Figure 9.14), which was then utilized to develop and manufacture a printed-circuit-board (PCB), shown in Figure 9.15, for signal routing. This was also optimized for hardware servicing by installing primary components on pin-header type interfaces, as well as giving the ability to communicate with the chosen microcontroller in an external configuration.

9.3 Control Logic

During the initial phase of control logic development, Matlab Simulink software was used to develop and visualize signal routing to reduce time to implementation. The ability to simulate signal outputs in a software-in-the-loop (SIL) environment prior to HIL deployment was also invaluable during the development process. Individual system block diagrams are available in Appendix A.

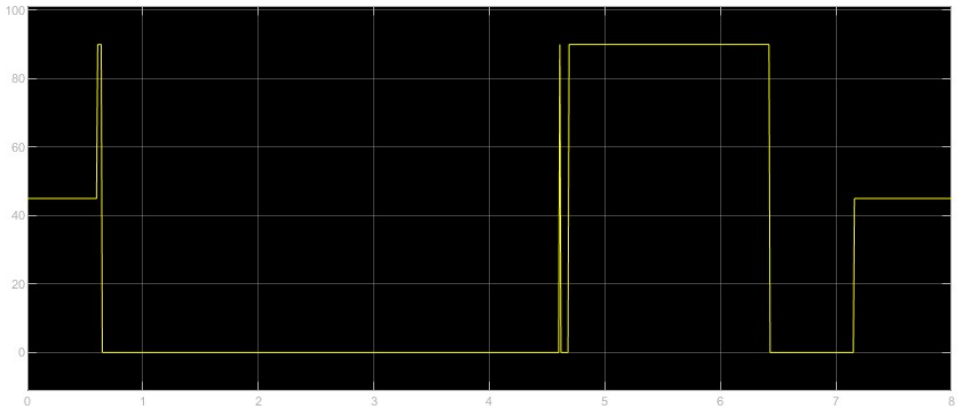


Figure 9.11: 90 Degree Corner Path Conditioned Signal Angular Output

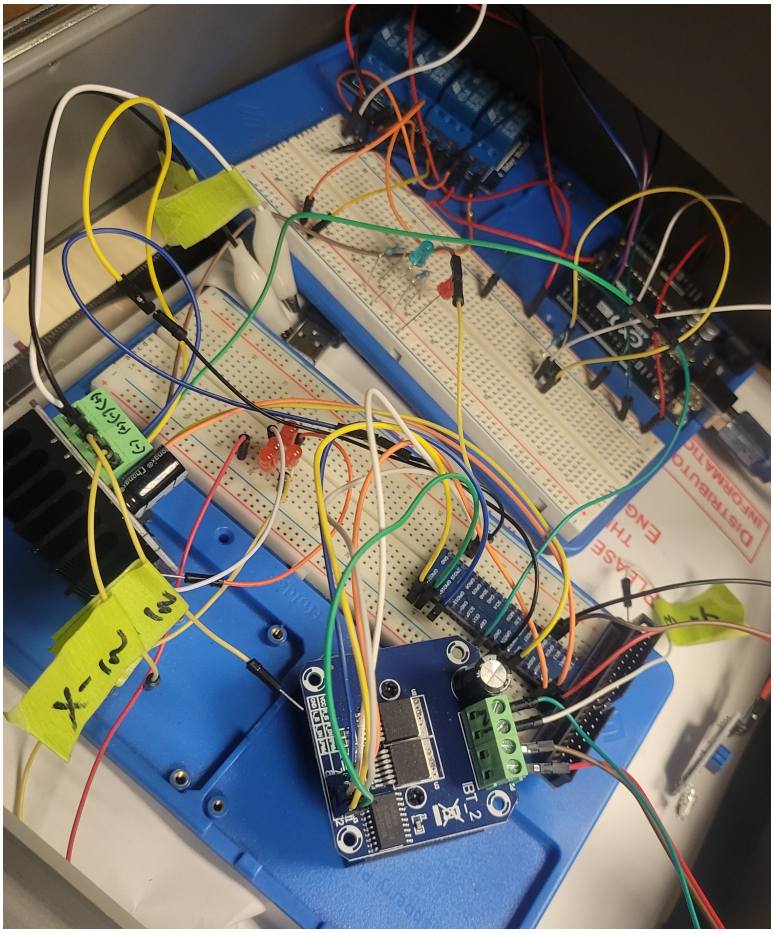


Figure 9.12: Initial Breadboard Iteration

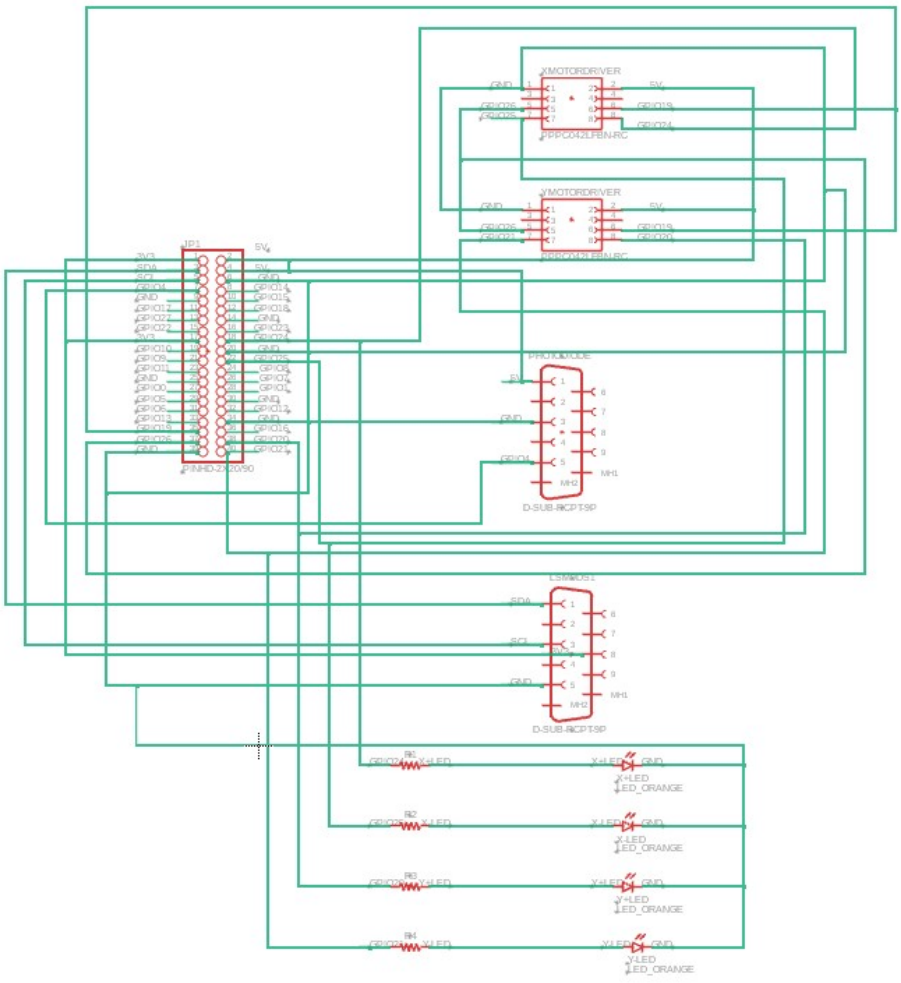


Figure 9.13: PCB Wiring Schematic

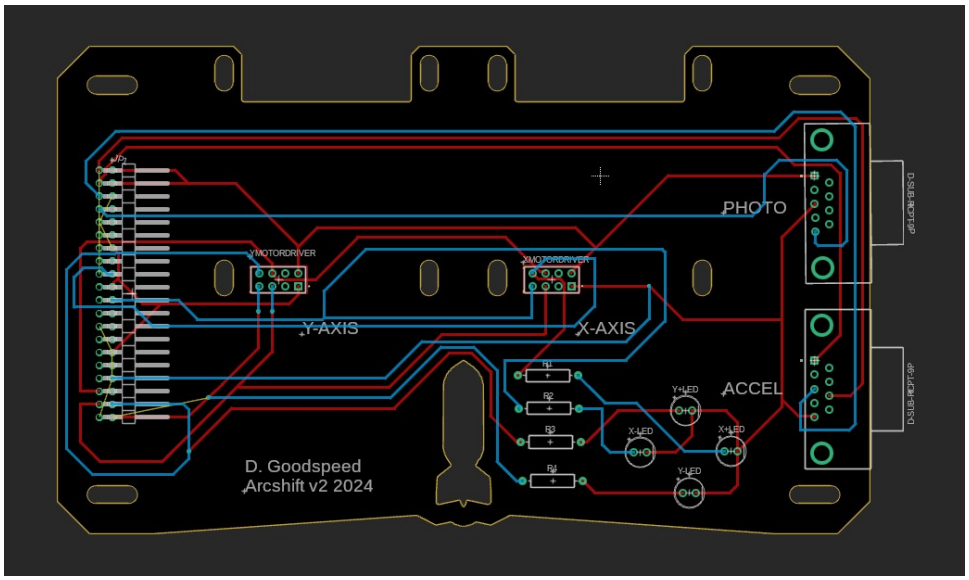


Figure 9.14: PCB Signal Routing Layout



Figure 9.15: Current PCB Iteration

9.3.1 Microcontrollers

More often than not, microcontrollers such as Arduino and Raspberry Pi serve as the building blocks for electronics prototyping. Arduino is a popular microcontroller board renowned for its simplicity, featuring a straightforward programming environment ideal for beginners, and also offers Simulink compatability. It excels in controlling sensors and actuators for projects in the do-it-yourself robotics and home automation fields. Raspberry Pi, on the other hand, is a full-fledged single-board computer capable of running an operating system if the end use requires it. It offers greater processing power, multimedia capabilities, and expanded connectivity options, making it suitable for complex applications such as media centers, Internet-of-Things (IoT) devices, and data processing tasks.

Arduino UNO

Initially used for development due to their low barrier to entry, Arduino UNO-based microcontrollers, while useful for logic development, proved to be inadequate from a performance perspective in later iterations due to their greatly reduced processing speed (19 Mhz) and limited input and output support when compared to other options, which resulted in reduced magnetic arc oscillation frequency ($< 25\%$).

Raspberry Pi

A RaspberryPi4 was eventually chosen due to its higher processing speed (1.5 GHz), development flexibility, and ability to integrate with Simulink nearly seamlessly with already developed models previously optimized for Arduino hardware. In addition, the ability to expand storage capacity and massive aftermarket and technical support offered made it a clear winner for the purposes of meeting the outlined research objectives.

9.3.2 Signal Modeling and Development

Initial signal development work was focused on creating a spiral weave pattern. A spiral weave's path is built upon a simple circle that can be described in a 2-dimensional coordinate

system using sine and cosine functions, shown in Figure 9.16. The X component of a point on the circle is given by Equation 9.1, and the Y component along the same circular path is represented as Equation 9.2, where r is the amplitude of the path's radius and θ is the angle in radians, with the X-plane being zero. By varying θ from zero to 2π, a circular path is created, illustrated in Figure 9.17. An integrator, shown in orange on 9.18, is used in lieu of an internal clock at this stage, providing the ability to restart the weave pattern, ensuring that the weave always starts in the same direction and with zero amplitude.

$$X = r * cos(\theta) \tag{9.1}$$

$$Y = r * sin(\theta) \tag{9.2}$$

Similarly, if the amplitude of the X or Y component is altered, an ellipse is created, or by doubling the frequency of a particular component, a figure 8 pattern, demonstrated in Figure 9.19, can be achieved. By leveraging these trigonometric relationships, multiple weaving patterns can be created, such as spiral weaves (Figure 9.20), triangular weaves (Figure 9.21), or figure-8 patterned weaves (Figure 9.22). Amplitudes can also be tailored to match weave patterns to the velocity of the welding torch, for example to ensure a spiral weave instead of an elliptical weave is produced.

9.3.3 Signal Transition Smoothing

To smooth the transition between one respective weave profile or angle and another, a proportional-integral-derivative (PID) control strategy was employed, shown in green on Figure 9.18, to manage the system's response. The gains of the controller are experimentally tailored via Simulink simulation to a desired settling time or smoothness, as shown in Equation 9.3 below, where $u(t)$ is the output from the controller at time t, $e(t)$ is the error at time t, and K_p, K_i and K_d are the proportional, integral and derivative gains, respectively. The proportional gain, K_p, responds to the amplitude of the current error,

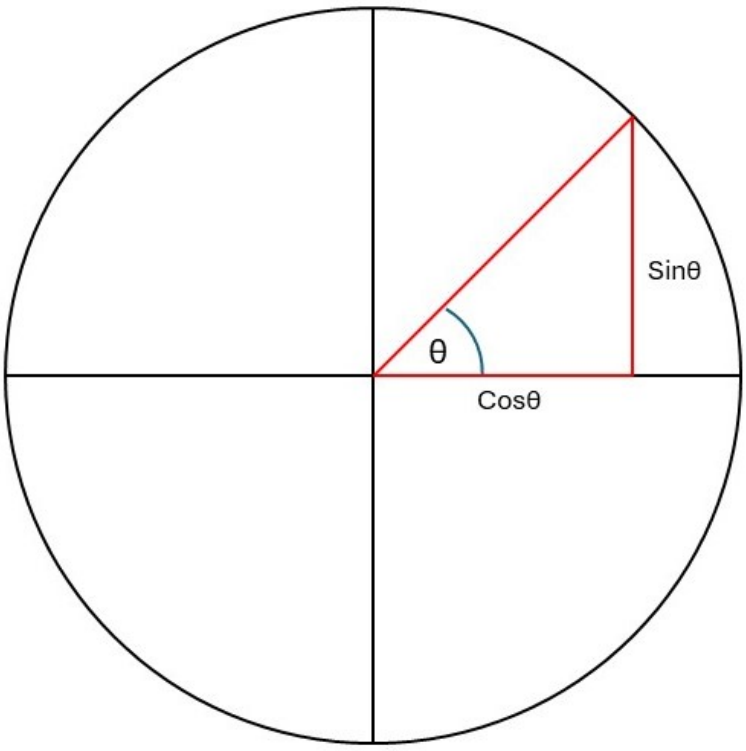


Figure 9.16: Trigonometric Relationship Between Sines and Cosines

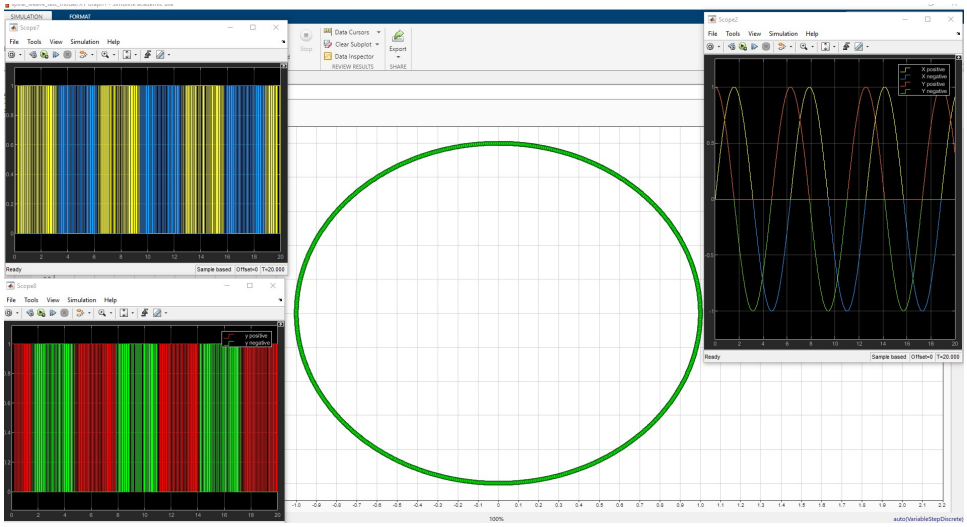


Figure 9.17: Circular Path Stationary Overhead Visualization

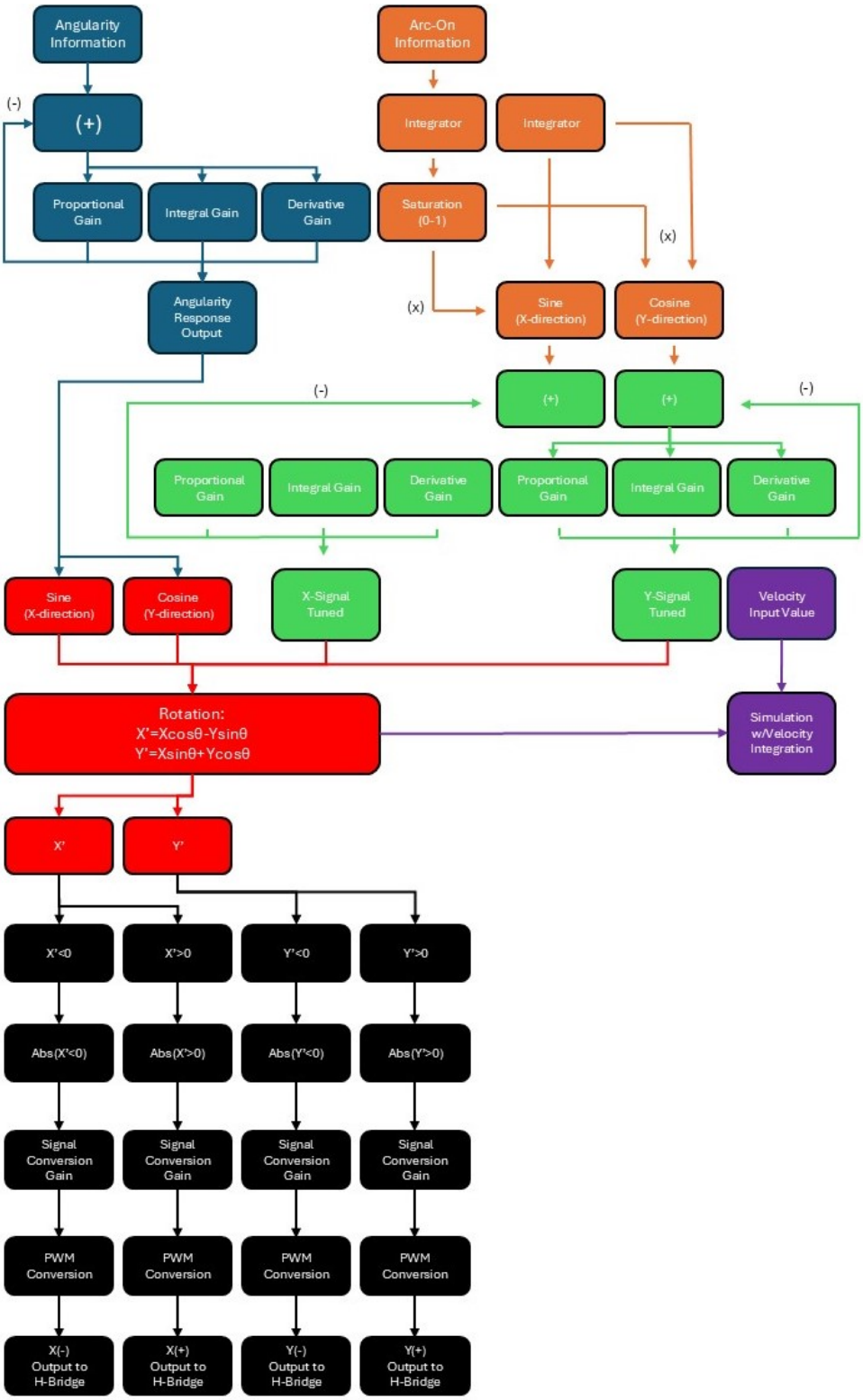


Figure 9.18: Signal Flow Chart

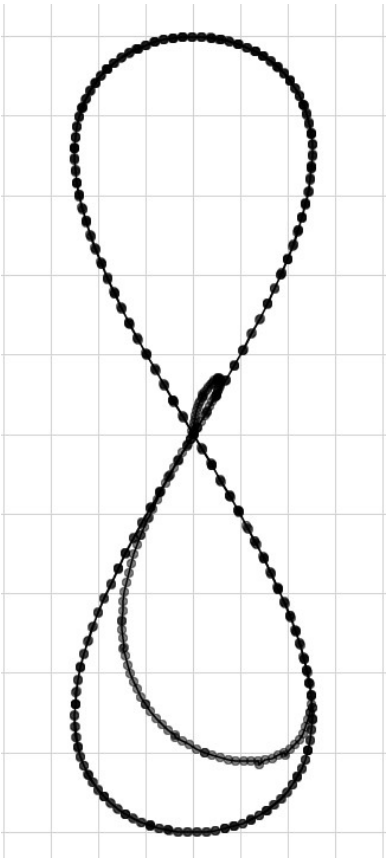


Figure 9.19: Stationary Figure 8 Weld Simulation Example

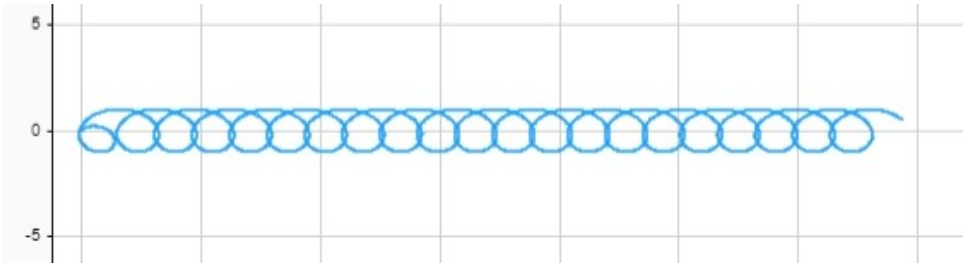


Figure 9.20: Spiral Weave Example

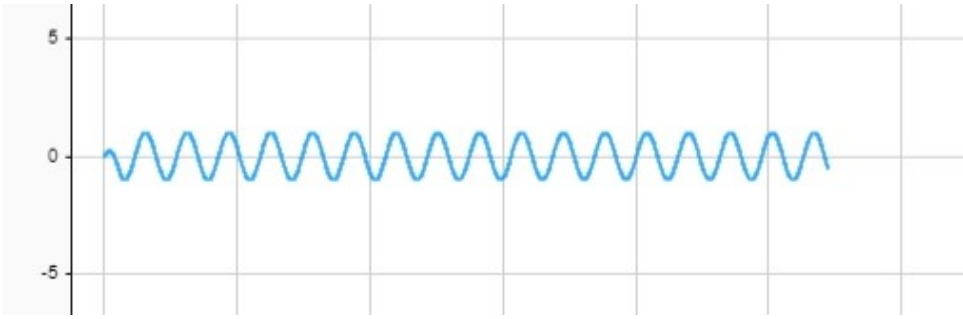


Figure 9.21: Triangular Weave Example

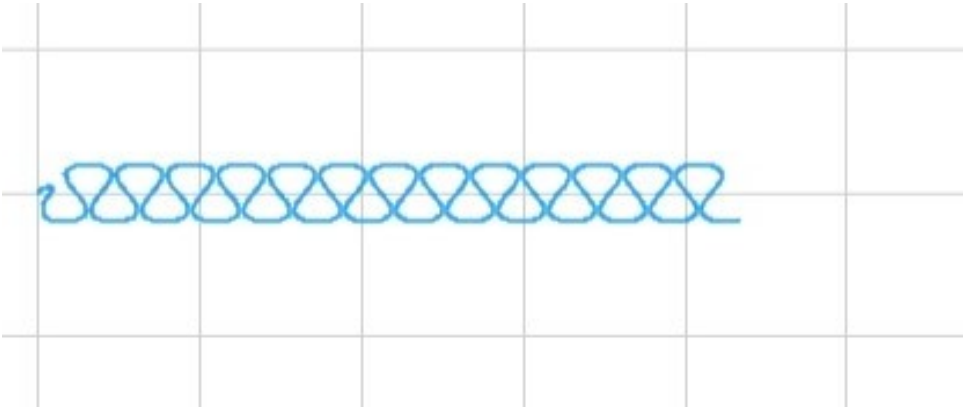


Figure 9.22: Figure-8 Weave Example

whereas the integral gain, K_i, eliminates steady state errors by summing accumulated errors over time. Finally, the derivative gain term, K_d, provides a damping effect to the controller by responding to the rate of change of the error.

$$u(t) = K_p e(t) + K_i \int_0^t e(\tau)d\tau + K_d \frac{d}{dt} e(t) \tag{9.3}$$

In this research, an initial settling time of $\sim 1s$ was chosen, which corresponds to $\sim$ 0.200" at 12 $\frac{in}{min}$ of weld travel velocity. The effectiveness of the control logic was evaluated through a multi-step process, utilizing timed step changes in angle for foundational testing, shown in Figure 9.23, and then random angle changes, shown in Figure 9.24. Finally, the Environmental Protection Agency's (EPA) US06 emissions testing drive cycle, Figure 9.25, was re-imagined to define robot travel angle, not vehicle speed, to evaluate the controller's capability to maintain system stability under varying conditions. This transition smoothing strategy was evaluated in the control logic in a single direction of travel by implementing weave transitions between three individual weaving profiles, whereby a triangular weave transitioned to a spiral weave, and, finally, a figure 8-weave. The path plan and resultant autogenous 100 A DCEN GTAW welds are seen in Figures 9.26 and 9.27, respectively.

9.3.4 Weave Rotation

Due to the nature of the fixed-torch-orientation kinematics of typical robotic weld cells, the generated weave pattern is required to rotate about the Z-axis such that, if the robot changes travel direction in the XY plane, the weave patterns can maintain the desired orientation with respect to the new robot travel direction. To do so, a counter-clockwise convention was adopted with travel in-line with the positive X-axis being the angle zero point, and a transformation matrix was employed to receive input from accelerometry-based sensing, outlined in section 9.2.2, and output a rotated weave pattern, also using the PID control-based signal smoothing demonstrated in section 9.3.3. An example can be seen in Figure 9.28, where a figure-8 weave has been rotated to a 45 degree angle, using Equations 9.4 and

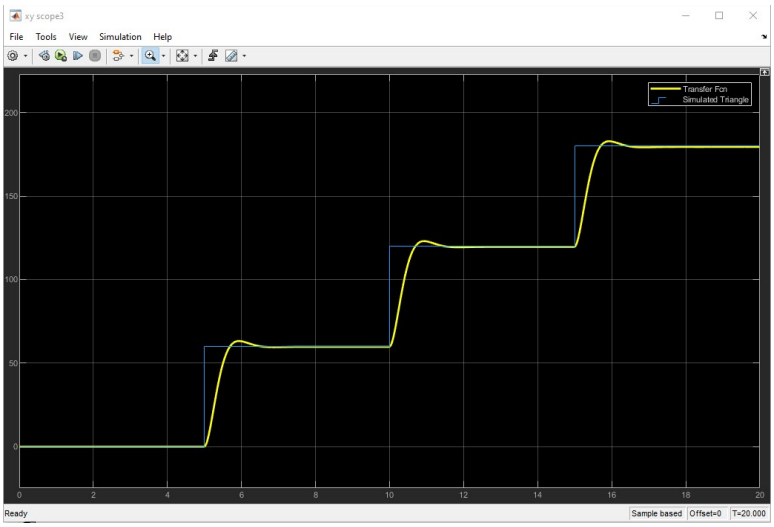


Figure 9.23: Simulated Angle Changes with PID Control

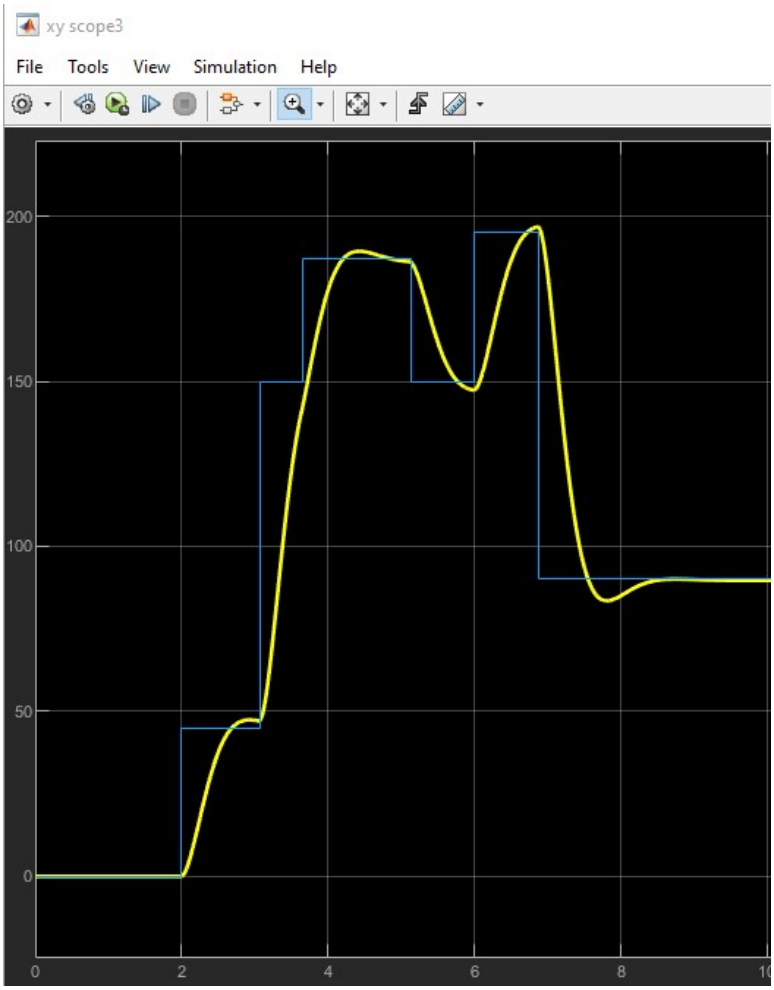


Figure 9.24: Simulated Random Angle Changes with PID Control

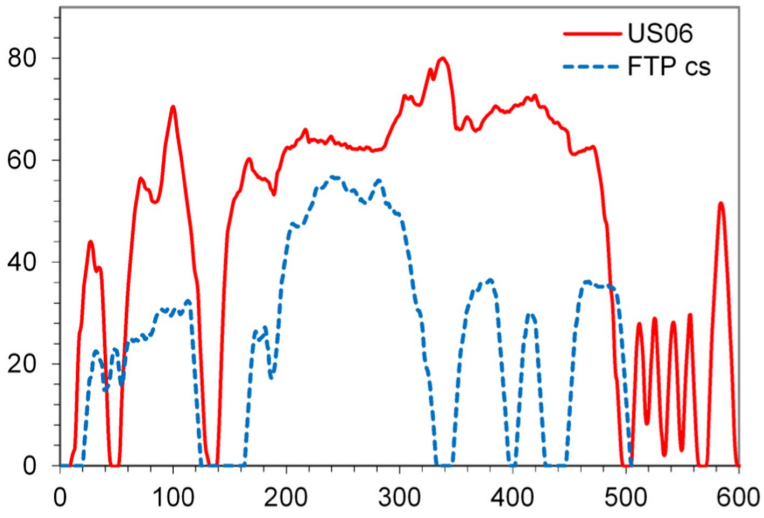


Figure 9.25: EPA US06 Emissions Drive Cycle (10)

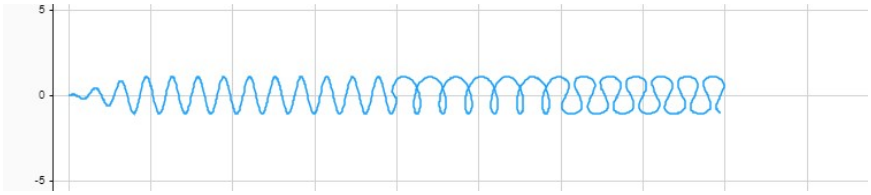


Figure 9.26: Three Weld Weave Patterns with PID Controlled Transition

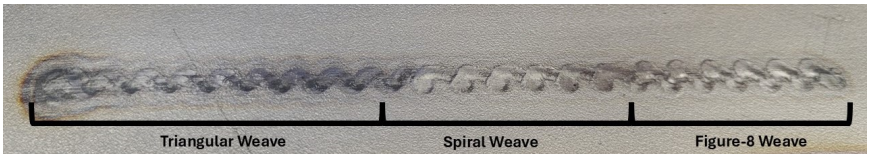


Figure 9.27: Three Weld Weave Patterns with PID Controlled Autogenous GTAW Weld

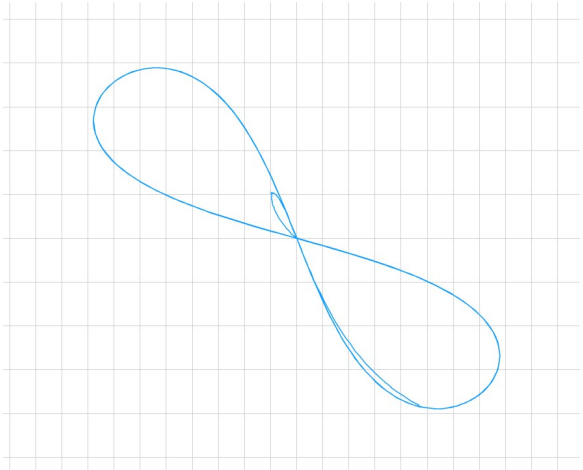


Figure 9.28: Stationary 45-Degree Rotated Figure-8 Weave Example

9.5 below. The PID control portion of this is illustrated in blue boxes on Figure 9.18, and the rotation portion is shown in red boxes.

$$X_{rotated} = X_{intial} \cos\theta - Y_{initial} \sin\theta \tag{9.4}$$

$$Y_{rotated} = X_{intial} \sin\theta + Y_{initial} \cos\theta \tag{9.5}$$

9.3.5 Weld Simulation

Shown in purple boxes on Figure 9.18, for the end user to better understand and tailor the resulting weld to the desired outcome, both a stationary path simulation and a velocity-incorporated simulation have been integrated into the control solution. In the former case, a simple stationary view of the path of deflection is able to be simulated, with resulting signal inputs and outputs monitored. In the latter case, a welding torch's travel velocity can be incorporated into the simulation to give the operator the ability to better view the resulting weave pattern prior to hardware deployment. An example of a figure 8-style weave pattern is shown in stationary configuration in Figure 9.19, as well as a velocity-incorporated figure 8 weave motion in Figure 9.29. Initial weave ramping, where its amplitude does not reach the fully-prescribed motion until a set time, can be seen in both simulations and is also a controllable input.

9.3.6 Signal Conditioning

To prepare the respective signals for output to the control hardware and with a relationship established between X and Y components of a weave pattern, the respective signals were then split into their positive (+) and negative (-) components, as shown in Figure 9.30 and illustrated in black on Figure 9.18. The absolute value of each respective signal was taken, providing four positive (+) signals. Doing so gives the ability to control the BTS7960 H-Bridge Motor Drivers, as they are optimized for a positive (+) PWM input in both the forward (conventional polarity) or reverse (inverted polarity) configurations. Splitting the

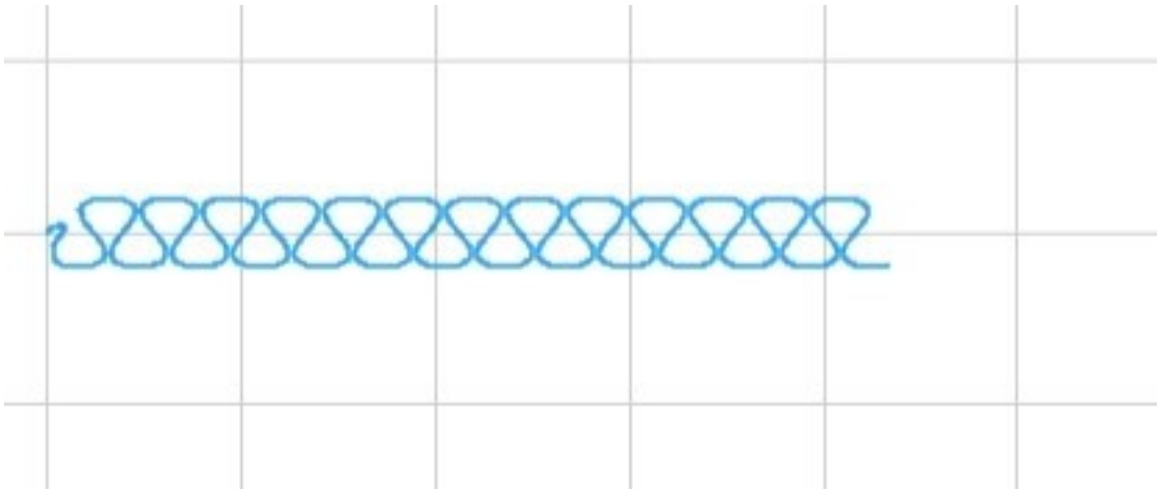


Figure 9.29: Velocity-Incorporated Figure 8 Weld Simulation Example

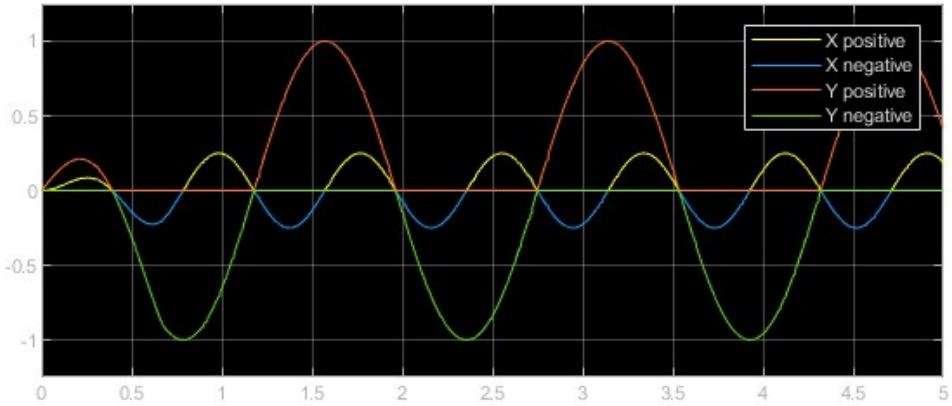


Figure 9.30: Figure 8 Weaving Profile with Split Signals

signals also ensures that the logic is not attempting to power the electromagnets in both directions simultaneously due to signal overlap.

These signals are further conditioned for output by applying a calibration constant, outlined in Section 6.2.5 to one magnet, ensuring similar magnetic field strength outputs between both axes, and, finally, the signals are converted to a PWM output for hardware deployment, Figure 9.31.

9.3.7 Programmatic Approach

Aligning with the system objective of being robot agnostic, a time-based control strategy was implemented following challenges with the accelerometry-based approach initially pursued in Section 9.2.3. In this technique, a desired geometry is outlined and distances between points are evaluated with both the weld velocity of the robot and travel direction in relation to the x-axis, as well as other factors, such as the dwell time after welding arc ignition. Within this framework, an integrator block is leveraged in lieu of using a model-borne internal clock to allow for the logic to be initiated upon recognition of arc light, outlined in Section 9.2.2, and reset following arc extinction. To evaluate this approach, a geometry consisting of right angle corners, as was the main focus of this research, was combined with 45-degree corner geometries to test the off-axis capability of the system, Figure 9.32. This geometry was evaluated and a time-based path plan was created using the counter-clockwise weave rotation convention outlined in Section 9.3.4 and shown in Figure 9.33. To further evaluate the proposed path plan prior to hardware deployment, pre-PWM conversion signal plots were examined for any deficiencies, shown in Figures 9.34 and 9.35. The result of this geometry is discussed in Section 10.2.

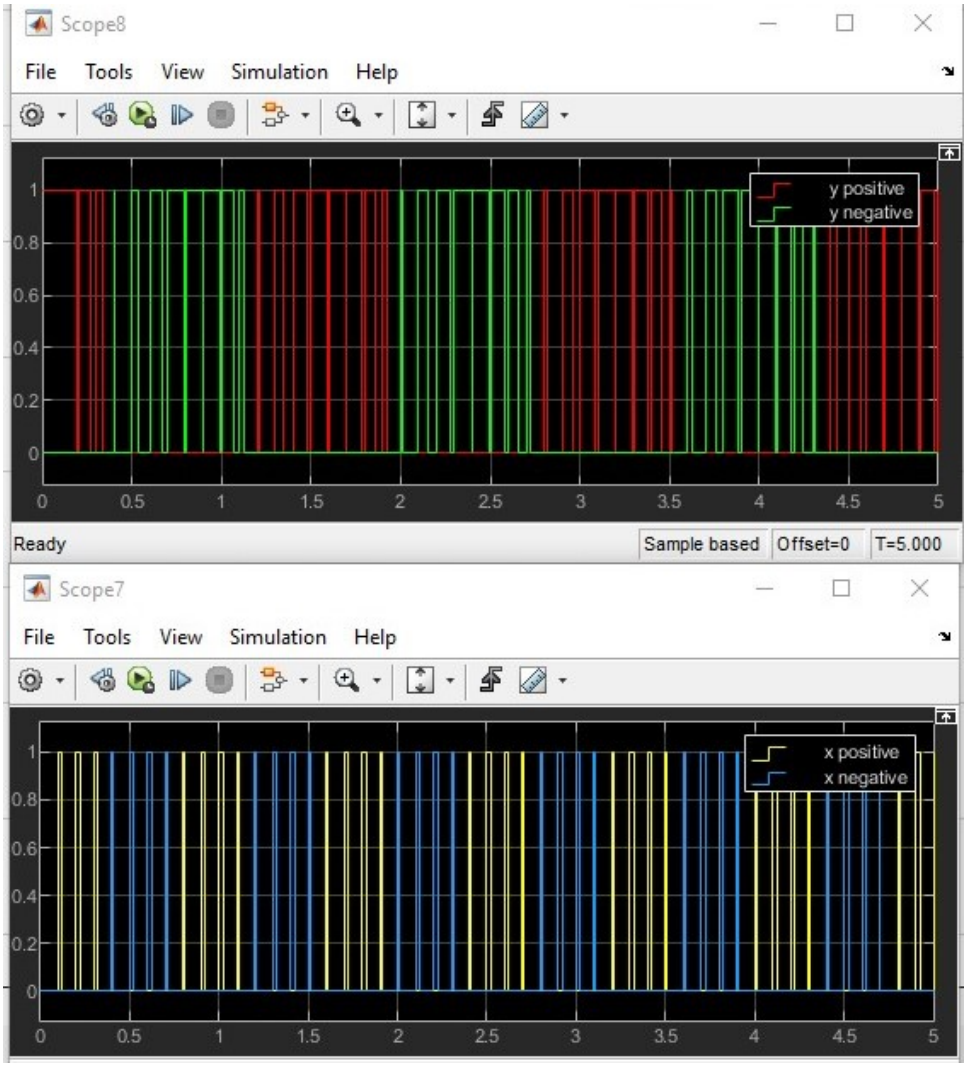


Figure 9.31: Figure 8 Weaving Profile PWM Output Signals

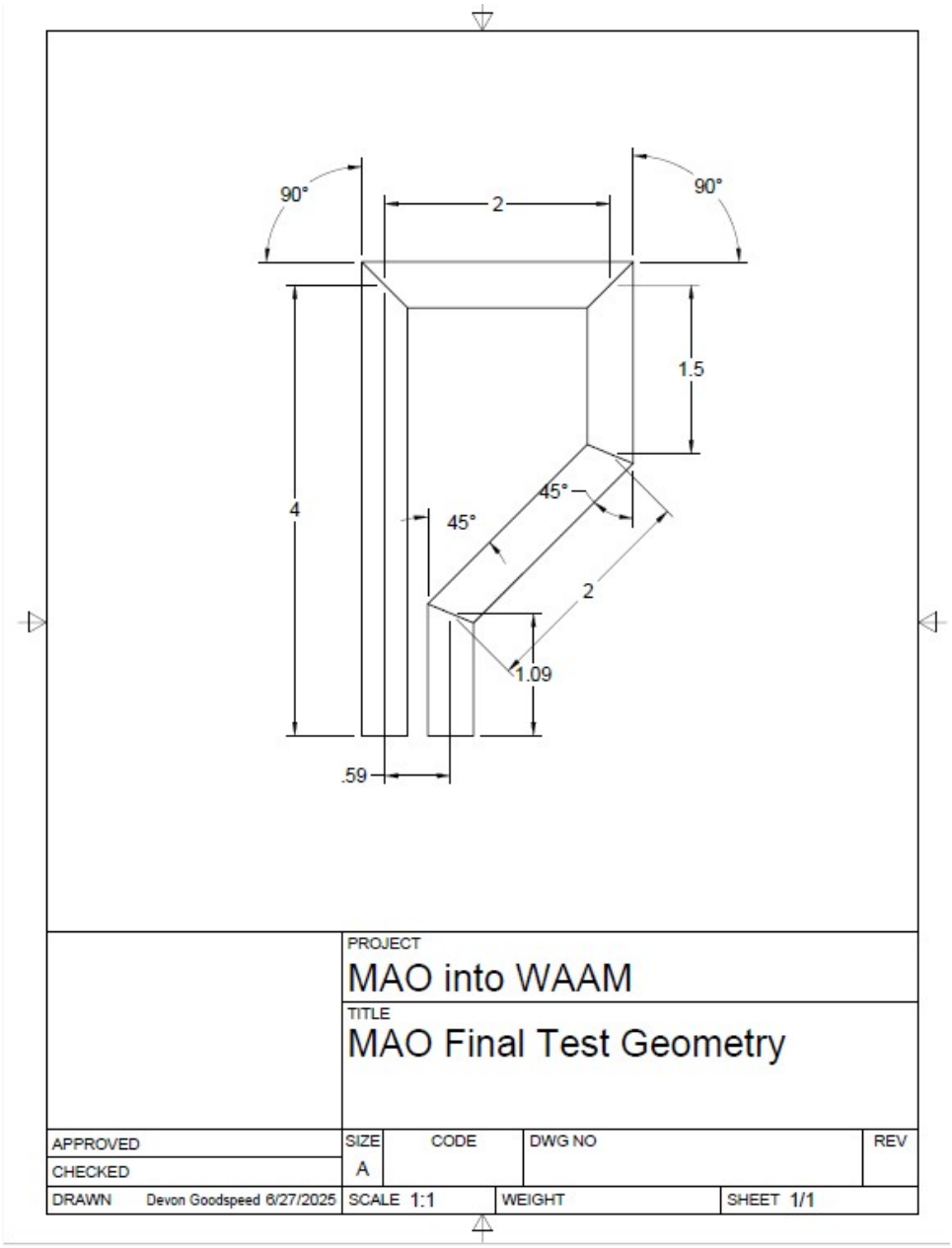


Figure 9.32: Final Geometry Layout

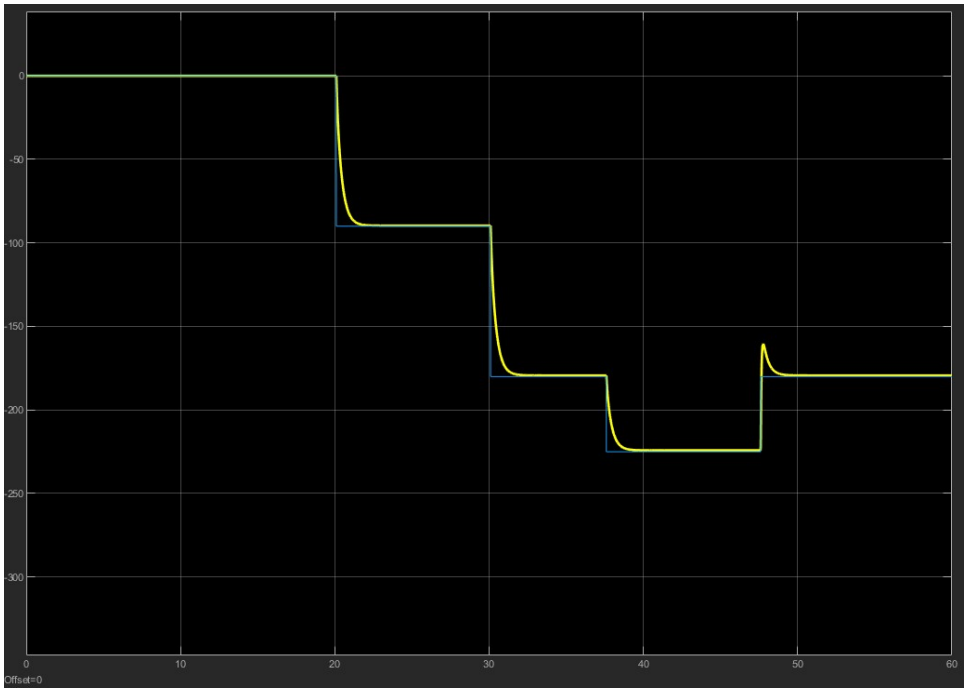


Figure 9.33: Time vs Angle Final Geometry Path Plan

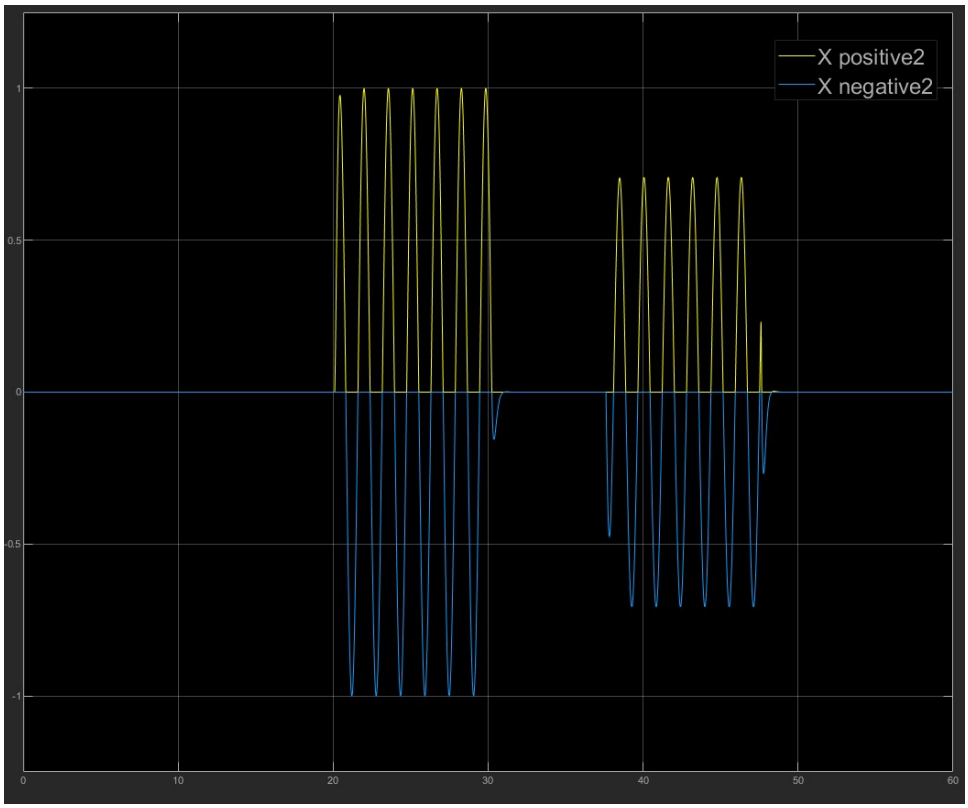


Figure 9.34: Final Geometry X-Deflection Output Pre PWM Conversion

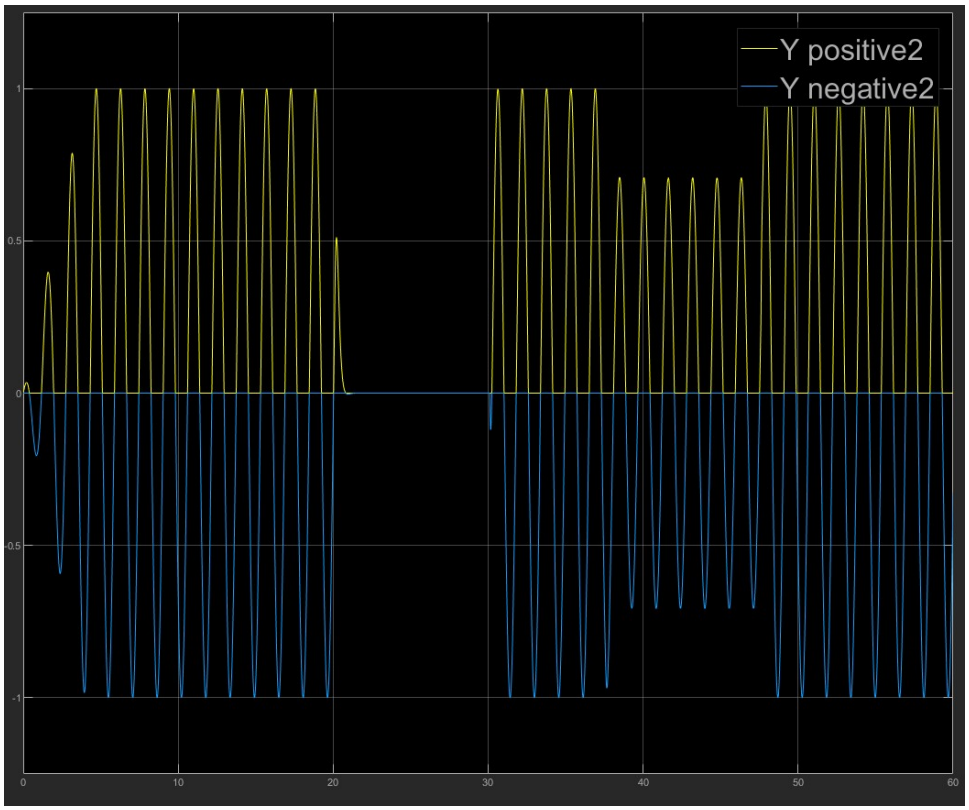


Figure 9.35: Final Geometry Y-Deflection Output Pre PWM Conversion

9.4 GTAW to GMAW Transition

9.5 Magnetic Field Strength

In electric arc welding, the internal magnetic field strength generated differs significantly between GTAW and GMAW processes. GTAW produces a more stable arc with generally lower current levels, resulting in a weaker internal magnetic field, hence its beneficial nature for precision applications and thinner materials. In contrast, the GMAW process space typically involves higher current levels and a more intense arc, leading to a stronger internal magnetic field. This increased strength can affect the weld pool dynamics and heat distribution, making GMAW typically suitable for thicker materials and faster welding speeds, but at the expense of potentially reduced arc stability when compared to GTAW. Due to this, higher magnetic field strengths will be required to deflect a GMAW arc when compared to a GTAW welding arc of the same current level.

In addition, this research has focused on stainless steel alloys that, in the case of GTAW, are typically welded in a Direct-Current-Electrode-Negative (DCEN) configuration, whereas, in the case of GMAW, a Direct-Current-Electrode-Positive (DCEP) configuration is typically employed. Due to the current flowing in opposite directions through the welding torch in these respective processes, deflection due to external magnetic field influence will also be reversed and should be considered by the operator during weld process development.

Furthermore, due to the non-consumable verses consumable electrodes involved in the GTAW and GMAW processes, respectively, the arc length produced during each respective process will differ, as illustrated in Figure 9.36. Higher external magnetic field strengths are required to influence a GMAW welding process, as shown in Figure 9.37, where maximum magnetic field strengths for the current results are highlighted. In the case of GTAW, arc length is related to the position of the tungsten electrode, whereas, in the case of GMAW, arc length is directly related to input voltage generated from the welding power supply, as well as the consumable electrode stick-out from the torch. While this could be a tunable parameter, reduced voltages, and thus reduced arc lengths, are generally employed in the

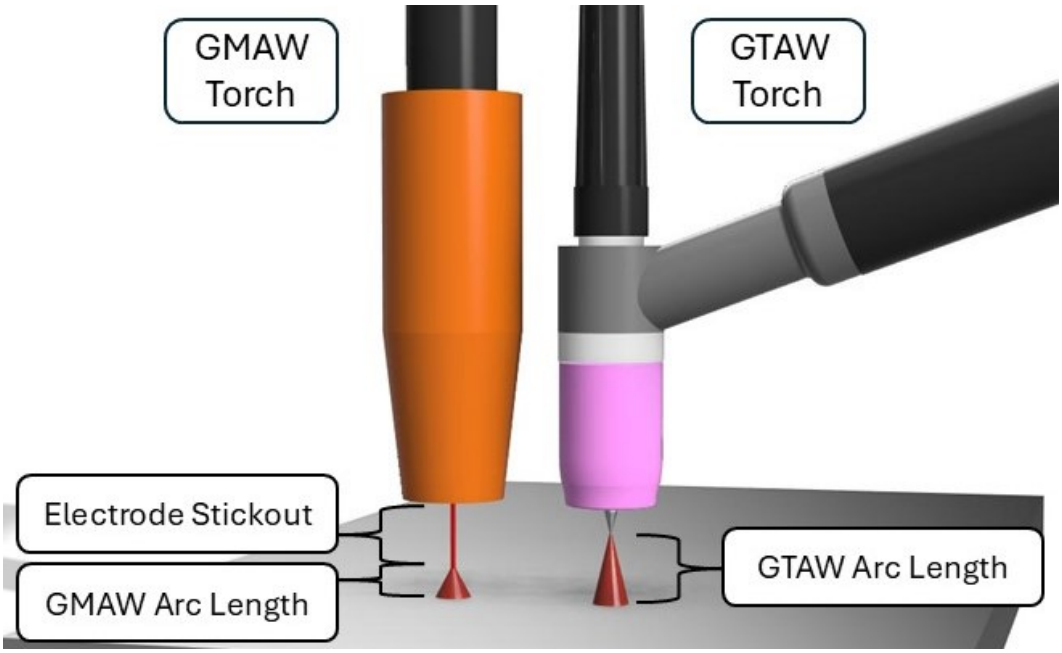


Figure 9.36: Arc Length Differences in GMAW vs GTAW

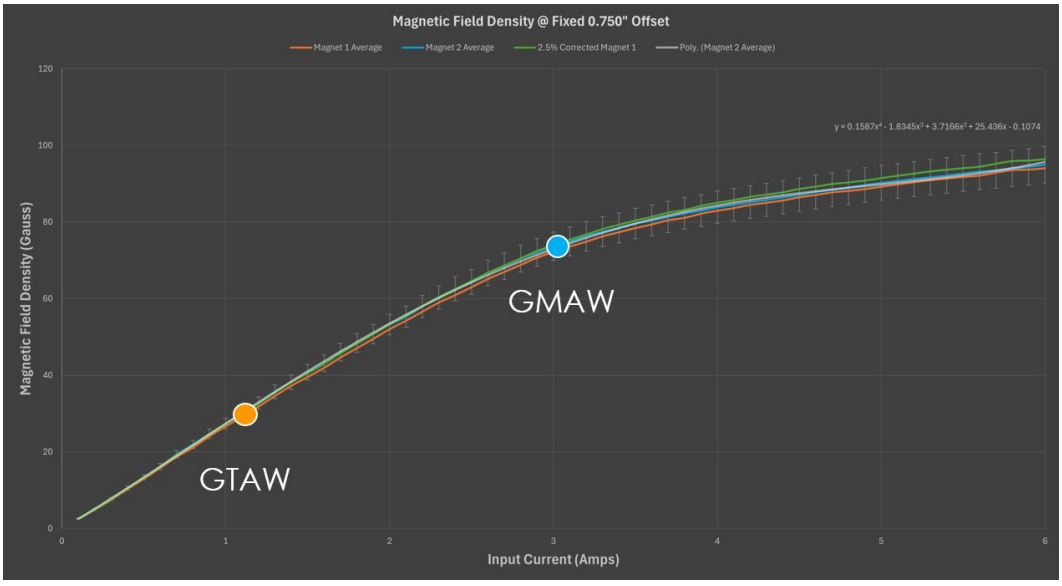


Figure 9.37: External Magnetic Field Strength Differences in GMAW vs GTAW-based MAO Experiments

WAAM process space due to reduced heat input being desired. Because of this, the external magnetic field has a smaller effective moment arm acting on the arc plasma and, thus, requires increased field strength for the same amount of deflection.

Lastly, increased magnetic field strength is also required in the GMAW process due to the increased mass and decreased velocity of a weld droplet in comparison to an arc plasma particle being manipulated in the GTAW process.

Chapter 10

Testing, Validation and Results

10.1 Procedures

To evaluate MAO actuator performance, six parameter sets were chosen. These sets align either with those found in literature (54), or with other ongoing research efforts at the University of Tennessee, and can be seen in Table 10.1. Deviations from these parameter sets had to be made in the on-robot testing configuration due to limitations in adjustability on the Fronius welding power supply used during this stage, also noted in 10.1.

10.1.1 Alignment with Standards

Where relevant, welding parameters and testing procedures were informed by the provisions of AWS D1.1 (55), D1.6 (11) and B3.0 (56), though the nature of WAAM differing from traditional joining processes did not allow for full procedural qualification under the code. ASTM E8/E8M (57) and CSWIP 3.1 (12) were also referenced where applicable.

Table 10.1: Welding Process Parameters - 316L

#	WFS (ipm)	Voltage (V)	TS (ipm)	CTWD (in)	Process Notes
1	100	18	12	0.500	*17V used on Fronius Power Supply
2	150	21	12	0.500	
3	200	22	12	0.500	*20.2V used on Fronius Power Supply
4	250	24	12	0.500	
5	300	24	12	0.500	
6	220	14.3	12	0.500	

10.1.2 +/-100 Percent Offset

To characterize the rise time of a weld at a chosen parameter set and better understand the effect of the off-axis magnet in the magnetic field, a total of five parameter sets were chosen, shown as parameter sets 1-5 in table 10.1. These parameters were combined with logic developed to move the arc from a positive Y direction (+) 100% offset to a negative Y direction (-) 100% offset, Figure 10.1, where red is the positive magnitude of deflection and green is the negative magnitude of deflection. These samples were individually measured on a Keyence VR-5200 wide-area 3D measurement system (Figure 10.2) and evaluated for symmetry and magnitude of deflection from weld centerline (Figure 10.3). The results are provided and discussed in Section 10.3.4

10.1.3 Elongated Weave

To aid in testing the GMAW-based control logic, and better measure and evaluate produced welds, beads were produced (Figure 10.4) with an elongated-weave profile in parameter sets 1, 3 and 5, respectively, on table 10.1 using the substrate and feedstock material outlined in 4.3. These were chosen to represent the lower, upper and mean of a potential parameter set focused on a wire-arc additively manufactured component. This elongated weaving profile was used to generate samples for macro etch testing, Section 10.1.5, dye penetrant testing, Section 10.31, and the final corner negotiation geometry in Section 10.2.

10.1.4 Destructive Testing

For destructive testing purposes, ∼8.5 in long, ∼1.85 in tall and ∼0.3125 in thick walls (Figure 10.5) were produced utilizing magnetically oscillated weaving techniques, as well as kinematic weaving for direct comparison between the two processes. A cut profile (Figure 10.6) was developed to maximize material usage and minimize waste, resulting in six (6) ASTM E8 subsize tensile testing specimens and one 0.187 in thick by 6 in long bend test specimen for both the kinematically woven and MAO-produced sample material.

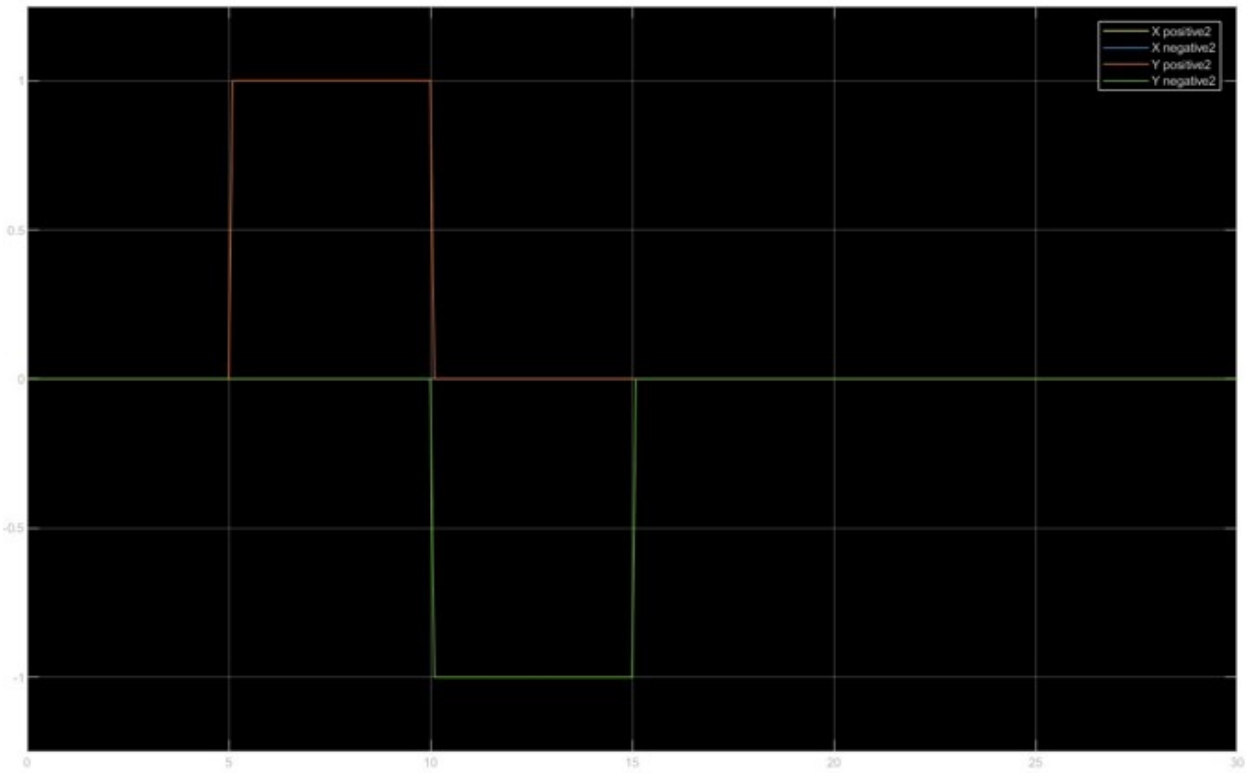


Figure 10.1: 100 Percent Offset Deflection Path

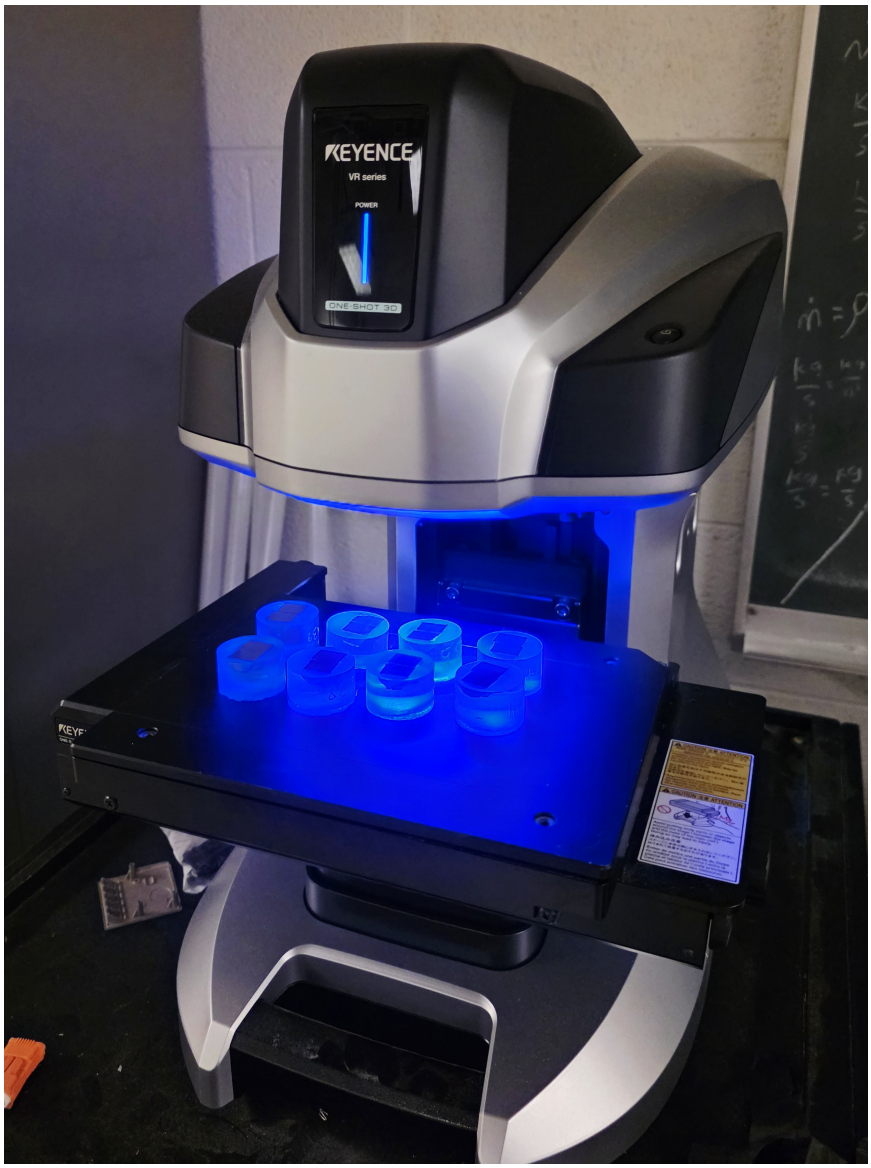


Figure 10.2: Keyence VR-5000

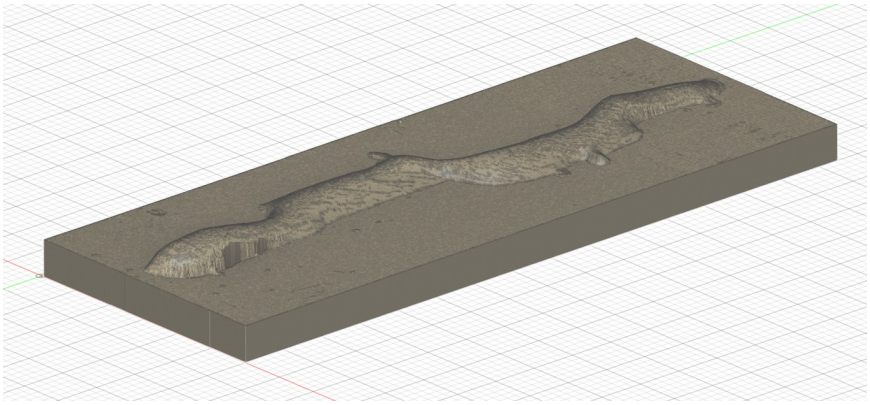


Figure 10.3: 100 Percent Offset Scanned Weld Bead

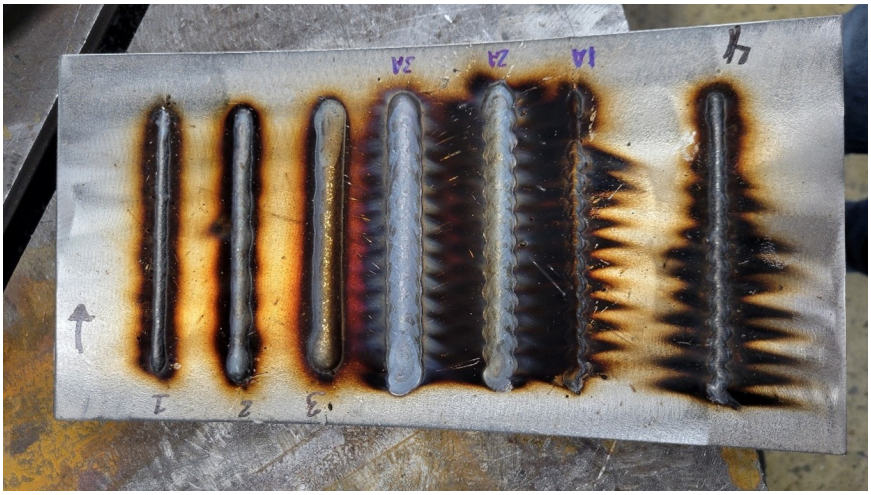


Figure 10.4: Elongated Weave Samples As Deposited



Figure 10.5: WAAM Produced 316L Destructive Testing Sample Wall

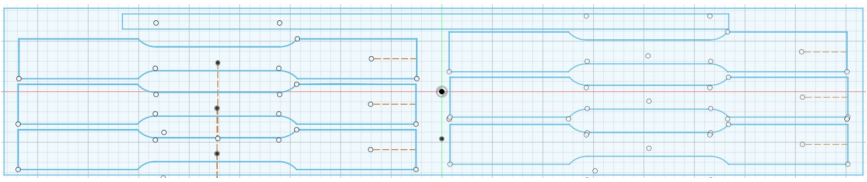


Figure 10.6: Destructive Testing Sample Wall Cut Profile

Tensile Sample Preparation

To aid in work-holding, the 304SS substrate material was sectioned around the produced wall to maximize usable material and machined (Figure 10.7) to remove high spots. These were then tack welded using a Millermatic 250 GMAW welding power supply to a 12 gauge (0.100 in) CNC plasma cut backing plate (Figures 10.8-10.9) for waterjet cutting on an OMAX 2626 JetMachining Center (Figure 10.10). The steady state region of the upper weld surface was used as a datum and positioned inline with a CNC plasma cut reference line on the backing plate for axial alignment purposes.

After waterjet cutting, the samples (Figure 10.11) were visually examined for any internal defects, then rough machined in a Kurt machining vise on an Excello 602 toolroom milling machine (Figure 10.12). For final machining to a 0.187 in thickness, purpose-built vise soft jaws (Figures 10.13-10.14) were designed and FDM additively manufactured from Acrylonitrile Styrene Acrylate (ASA) material with a 0.080 in (2 mm) recess added on one face and a 0.160 in (4 mm) recess was placed on the reverse face for machining flexibility. Utilizing these soft jaws, a 0.002 in finish pass was removed from the surface of the material with a Kennametal P/n 6767781 0.750 in diameter solid carbide four-flute end mill at 1000 rpm with 2 inch-per-minute travel speed, the result of which can be seen in Figure 10.15. The produced samples were then deburred using a ceramic fiber machining stone and polished using micro-fine jeweler's polishing compound for consistency.

Tensile Testing Procedure

After samples were prepared, a MTS Criterion Model 45 load frame equipped with a 100 kN load capability was utilized to stress the samples until failure, as shown in Figure 10.16. A total of six samples were tested to failure for each deposition type with a constant crosshead speed of 2mm/min. All tests were performed under ambient conditions on the same day, the results of which are presented and discussed in Section 10.3.1.



Figure 10.7: Substrate Removal and Machining

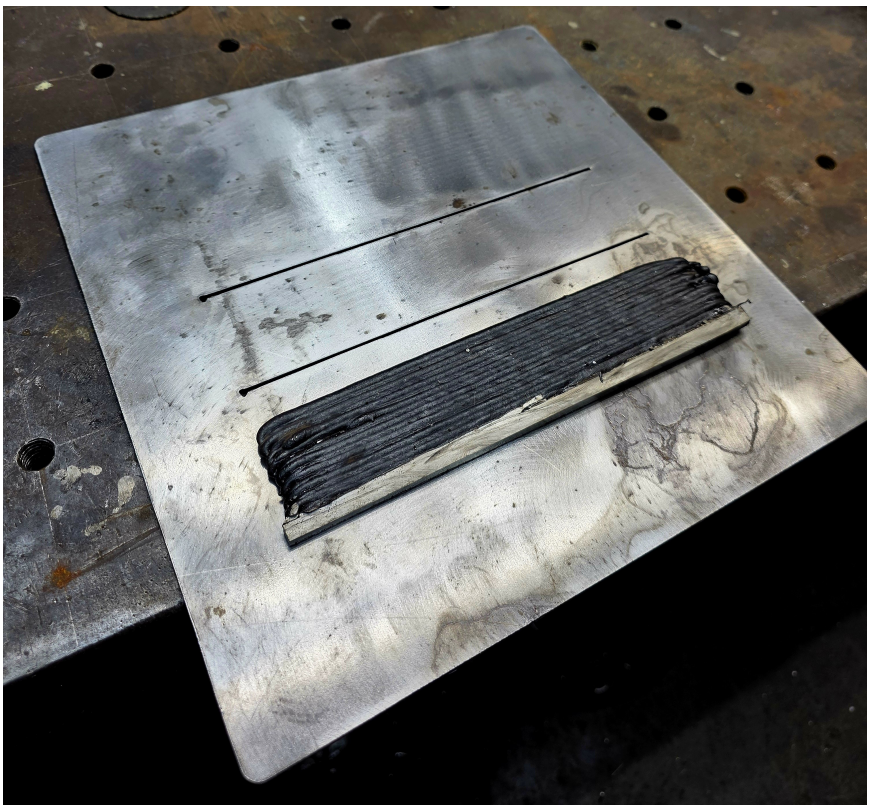


Figure 10.8: Waterjet Workholding Backing Plate

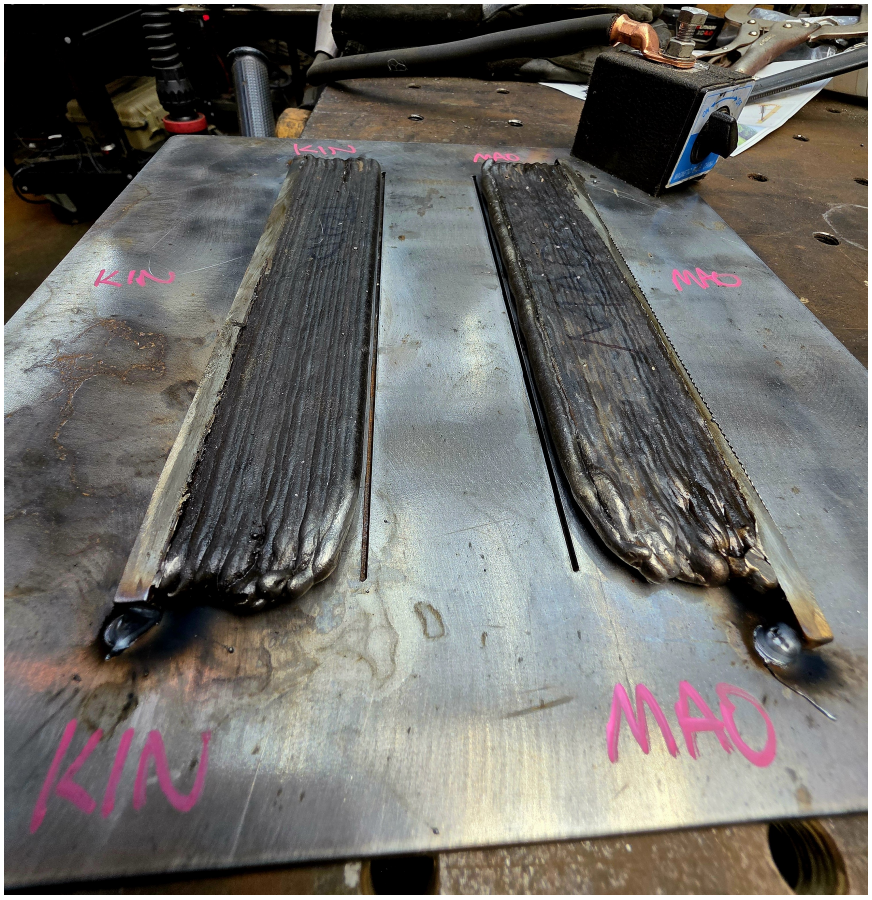


Figure 10.9: Waterjet Workholding Backing Plate with Welding Samples

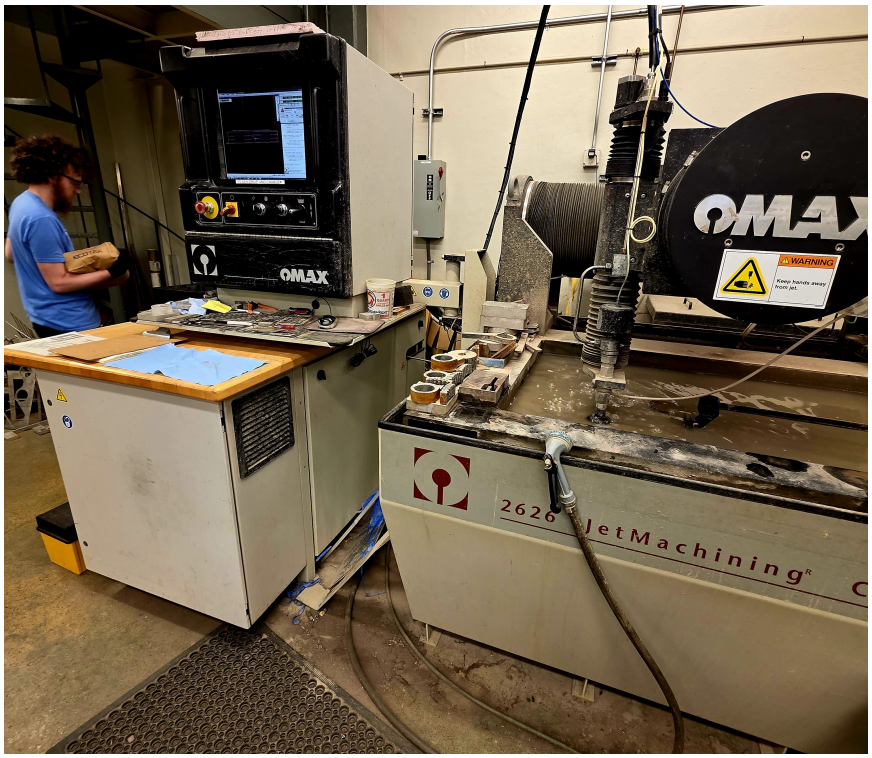


Figure 10.10: OMAX 2626 Waterjet



Figure 10.11: Waterjet Cut Tensile Test Samples Pre-Machining



Figure 10.12: Tensile Test Sample Rough Machining

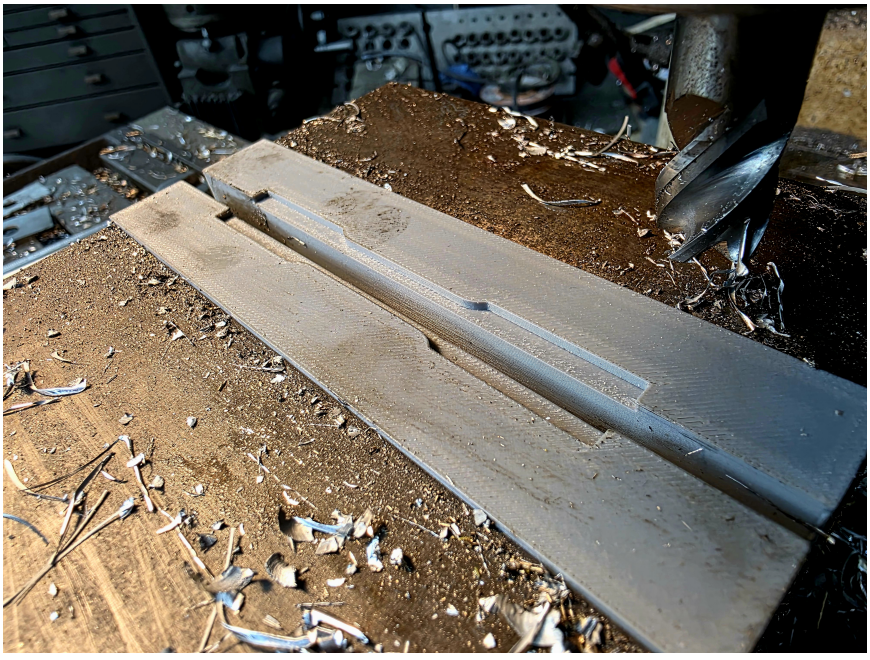


Figure 10.13: FDM Manufactured Machining Soft Vise Jaws

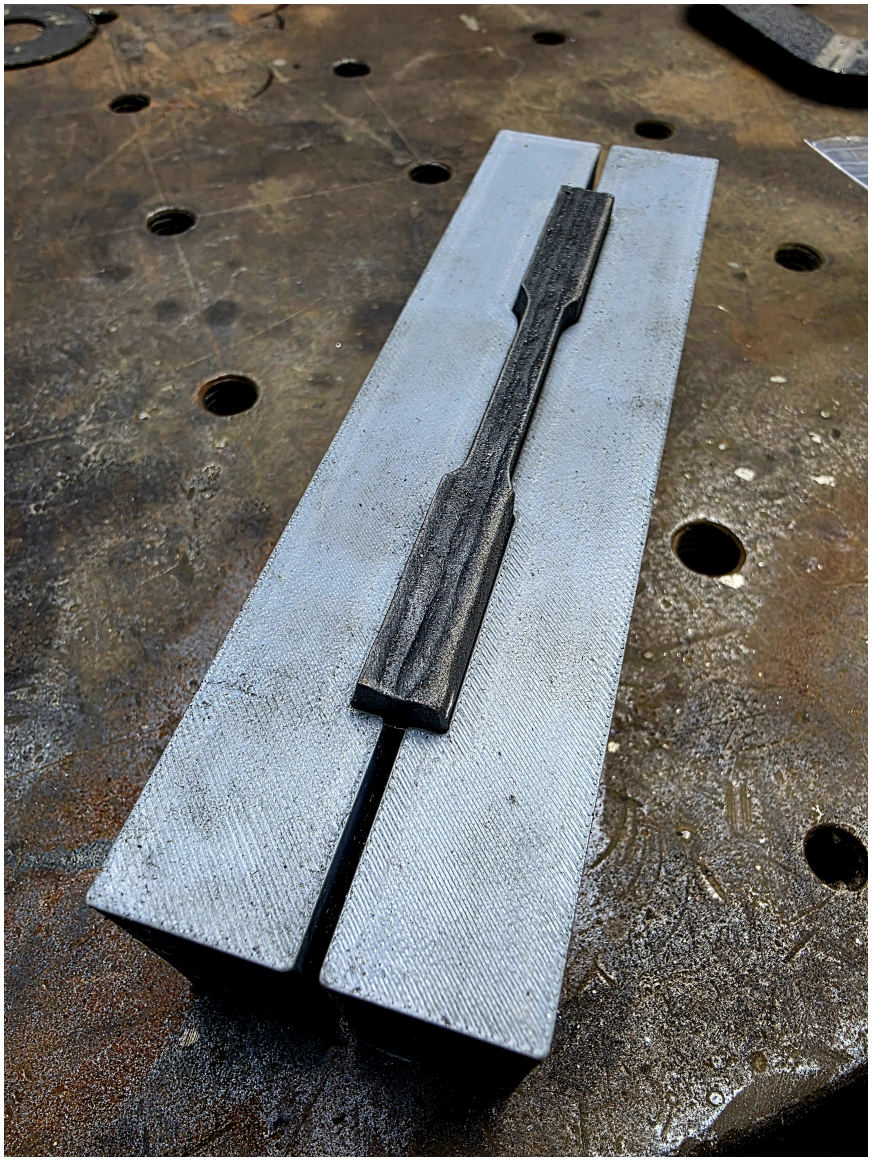


Figure 10.14: Tensile Test Sample in FDM Manufactured Vise Soft Jaw



Figure 10.15: Tensile Test Samples Pre vs Post Machining



Figure 10.16: Tensile Testing Experimental Setup

Hardness Testing Procedure

Hardness testing was carried out at the University of Tennessee's TN MADE facility, where an Insize HDT-RW160 benchtop hardness tester (Figure 10.17) was used with a 1/16" diameter hardened steel indenter to sample the material using the Rockwell B (HRB) scale. Measurements leveraged the ends of material that was later used for bend testing. A total of nine data points were recorded for each sample at both ends, shown in Figure 10.18, and on both top and bottom faces, the results of which will be discussed in Section 10.3.1.

Bend Testing Procedure

Due to the limited amount of material available due to the produced geometry and the unique nature of the WAAM process in relation to traditional joining, bend test samples were prepared using AWS D1.6/D1.6M:2007 (11) as a reference, shown in Figures 10.19-10.20, with acknowledged deviations in material sizing, specifically sample width, which was limited to the deposited bead width ($\sim$ 0.3 in). The samples pre-testing can be seen in Figure 10.21. Bend testing was accomplished in accordance with AWS D1.6/D1.6M:2007 using a bottom-guided bend testing fixture utilizing a 0.75 in radius upper plunger. N.I.G.I Grade 2 high temperature lithium grease was applied to the hardened lower die faces before testing, the experimental setup of which can be seen in Figures 10.22 and 10.23.

10.1.5 Macro-Etching

Sample Preparation

Sample material leveraged from 10.1.3 (Figure 10.24) was sectioned using Electrical Discharge Machining (EDM) at the University of Tennessee's TNMADE facility using multi-pass finishing to achieve a $\sim$20 Ra finish, shown in Figure 10.25. These samples were then mirror polished using micro-fine jeweler's polishing compound on a purpose-built buffing wheel, the results of which can be seen in Figure 10.26. Finally, samples were immersed in



Figure 10.17: Insize HDT-RW160 Hardness Tester

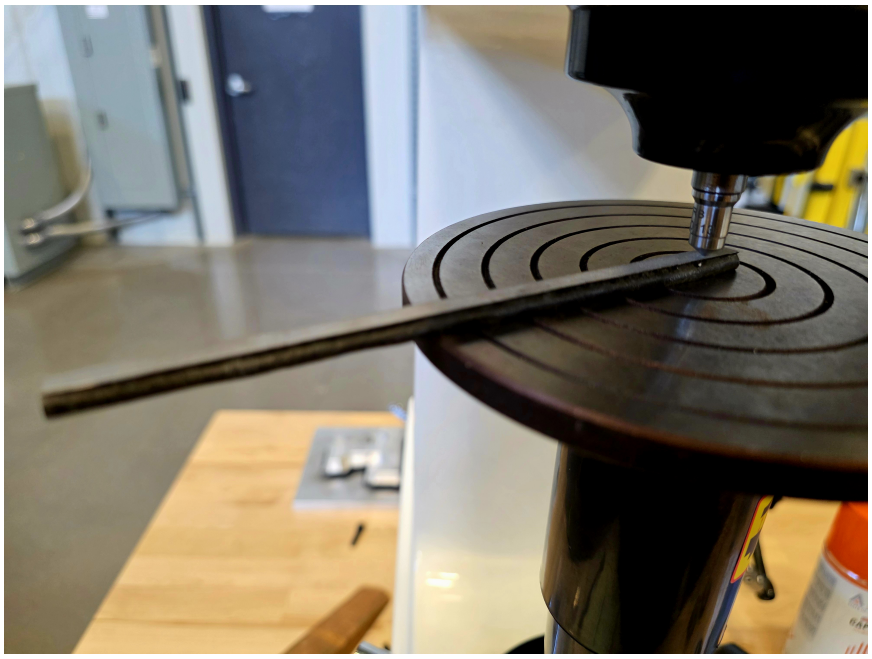
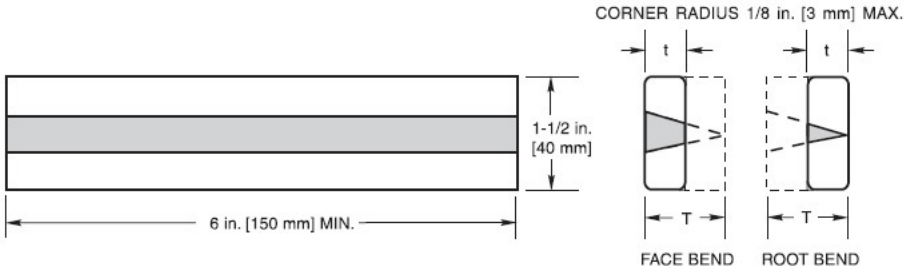


Figure 10.18: Material Being Hardness Tested



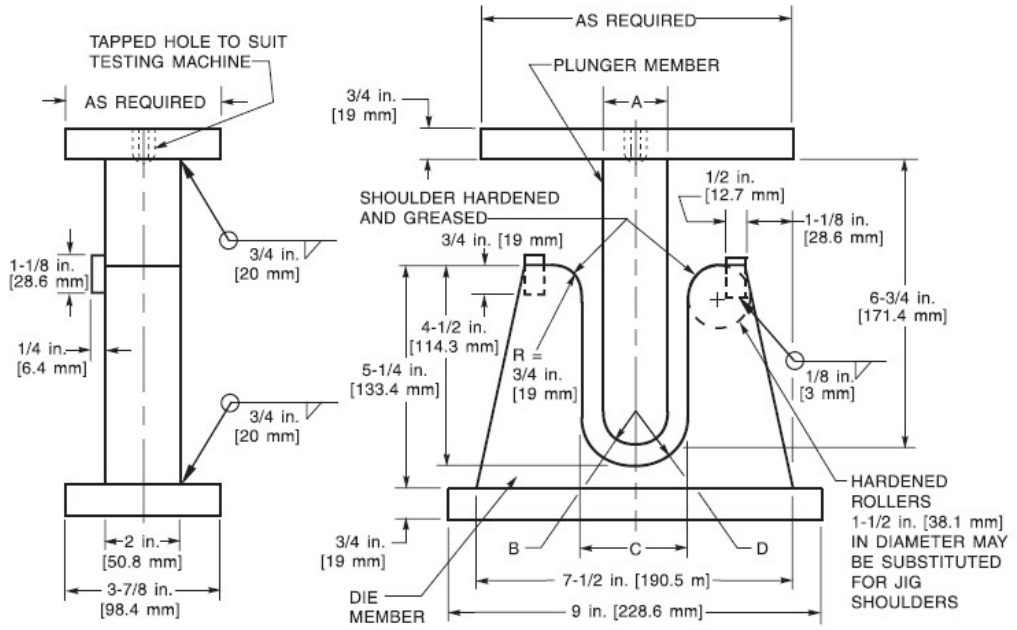
T, in.	t, in.
≤3/8	T
>3/8	3/8

T, mm	t, mm
≤10	T
>10	10

Notes:
1. The specimen may be thermally cut but, in this case, at least 1/8 in. [3 mm] of material shall be mechanically removed from the thermally cut surface.
2. If the weld joins base metals with different thicknesses, the specimen should be reduced to a constant thickness based on the thinner base metal.
3. The weld reinforcement and backing, if any, shall be mechanically removed flush with the specimen surfaces.
4. All longitudinal surfaces shall be no rougher than 125 microinches [3 µm] RMS. It is not recommended that the lay of the surface roughness be oriented parallel to the longitudinal axis of the specimen.

Figure 4.19—Longitudinal Face-Bend and Root-Bend Specimens—Plate (see 4.10.2.3)

Figure 10.19: AWS D1.6 Guidance on Bend Test Specimens (11)



Jig Dimensions for 20% Elongation					
Specimen Thickness, T		Plunger Radius, B		Die Radius, D	
in.	mm	in.	mm	in.	mm
3/8	9.5	3/4	19.0	1-3/16	30.2
T		2T		B + T + 1/16	B + T + 1.6

Figure 10.20: AWS D1.6 Guidance on Bend Test Fixture Dimensions (11)



Figure 10.21: Bend Test Samples for Kinematic and MAO Material



Figure 10.22: Bend Testing Experimental Setup (Pre-Sample Deformation)



Figure 10.23: Bend Testing Experimental Setup (Post-Sample Deformation)

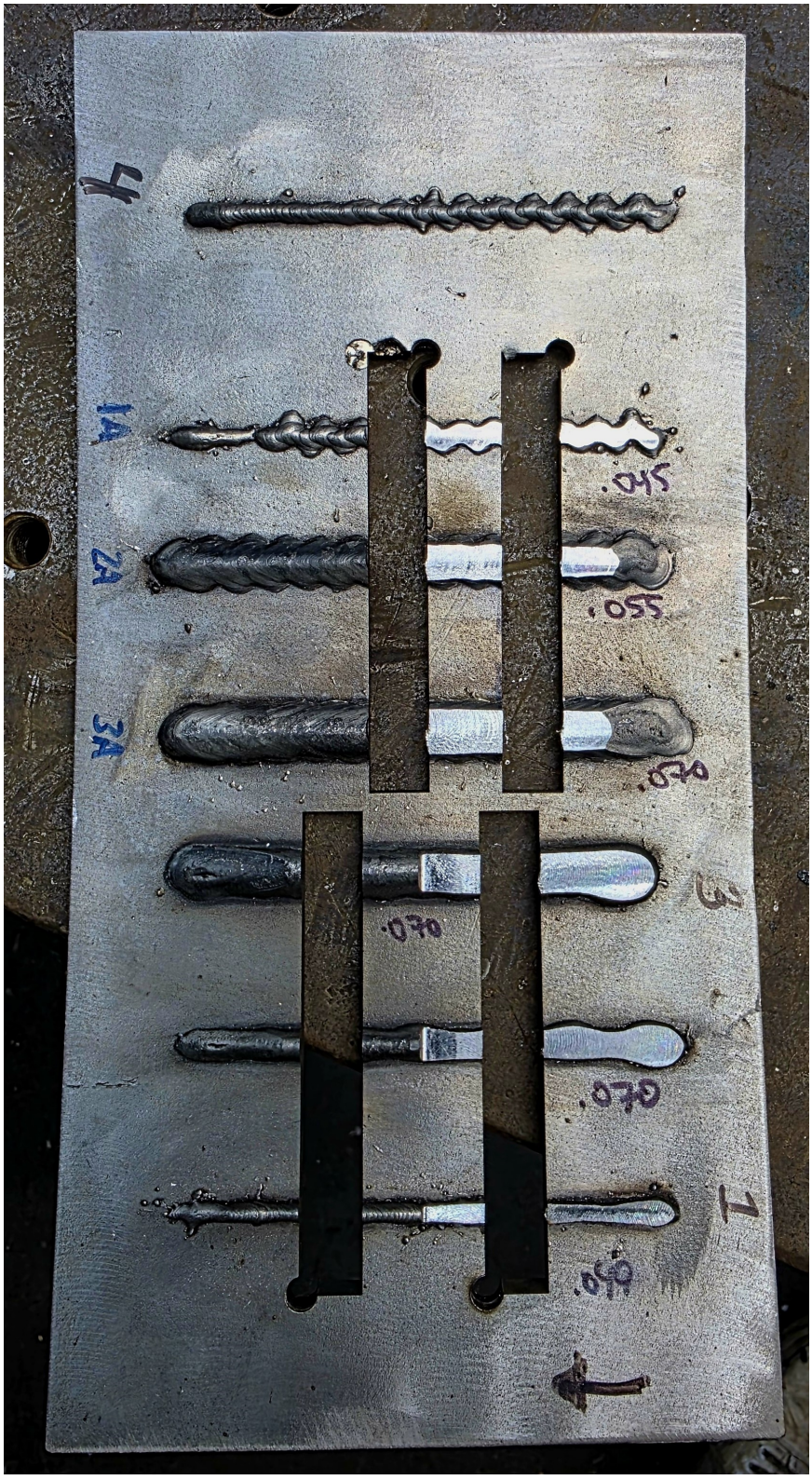


Figure 10.24: Sampled Elongated Weave Testing Material (Post Dye-Penetrant Machining)

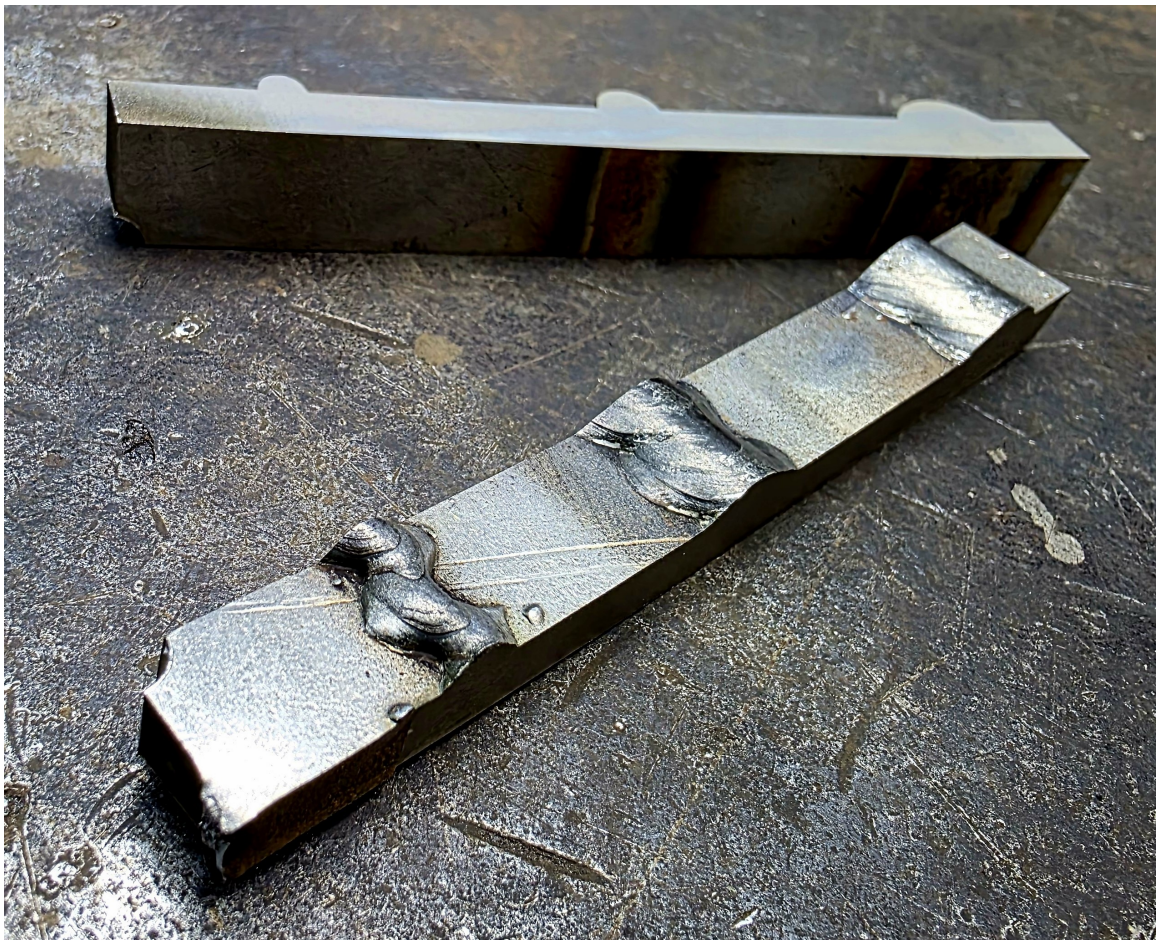


Figure 10.25: EDM-Cut Sample Sections for Macro Etching



Figure 10.26: Final Etch Sample Polish

acetone for degreasing purposes before being heat soaked in a Fisher Scientific laboratory oven at 150°F in preparation for etching.

Process

In aligning with AWS D1.6/D1.6M:2007 Annex N (11), an Aqua Regia etchant solution was produced comprising of one part 70 percent concentrated ACS grade nitric acid (HNO3) with 2 parts 37 percent concentrated ACS reagent grade hydrochloric acid. The face of the degreased samples were immersed in the solution and agitated in 30 second increments until the desired visual result was realized, the results of which can be seen in Section 10.3.3.

10.1.6 Dye Penetrant Testing

Again leveraging sample material produced in 10.1.3, the remaining material after sectioning for macro-etching was machined to 50 percent of the deposited weld height from the substrate for 50 percent of the length of the remaining material (Figures 10.27-10.28). This was done to leverage the penetrant for examination for internal, as well as surface, defects. The material was then dye penetrant tested (Figures 10.30-10.31), where a solvent, Spotcheck SKC-S, was applied, followed by Spotcheck SKL-SP2 aerosol penetrant, which was allowed to sit for 30 minutes, then wiped clean with a towel moistened with Spotcheck SKC-S cleaner before a solvent-based developer, Spotcheck SKD-S2, was applied. Because dye penetrant inspection is highly dependent on proper manual cleaning of the part prior to development, it is very sensitive to operator technique and overall cleanliness. Areas such as inside corners of the weld weaving profile, as well as the voids left from EDM sectioning were identified and excluded from examination due to the difficulty in penetrant removal from these locations, an example of which is in Figure 10.29.



Figure 10.27: Dye Penetrant Sample Machining



Figure 10.28: Machined Dye Penetrant Sample



Figure 10.29: Example Area of Concern for Dye Penetrant Removal Process



Figure 10.30: Aerosol Dye Penetrant Testing Material



Figure 10.31: Dye Penetrant Experimental Setup

10.2 Final Corner Negotiation Geometry

As discussed in Section 9.3.7, a geometry was developed to test the efficacy of both the hardware and control logic, specifically focused on the ability to negotiate historically difficult geometries, including right angles. To evaluate this, parameter set 3 in Table 10.1 was chosen, a path plan representing the desired geometry was laid out directly onto the substrate (Figure 10.32) and, using the wire electrode as a datum, programmed onto the on-robot test platform outlined in Chapter 8. Welds were then deposited following this path plan both traditionally-produced and with an MAO-based elongated weave profile, shown in Figures 10.33 and 10.34)

10.3 Paired Analysis

10.3.1 Destructive Testing Results

Tensile Results

As discussed in 10.1.4, a total of six samples were developed and destructively tested for both the MAO-based and kinematically woven samples, utilizing parameter set 6 from Table 10.1, the results of which can be seen in Figure 10.35 and Table 10.2. The results showed consistent mechanical behavior between the two groups, with a ∼40 MPa spread in ultimate tensile strength and a standard deviation of 10.92 MPa and 12.76 MPa for the kinematically woven and MAO-produced samples, respectively. Further, all samples exhibited diffuse necking behavior across the gage length, an example of which can be seen in Figure 10.36. No porosity was observed on the exterior or fracture surface of any samples.

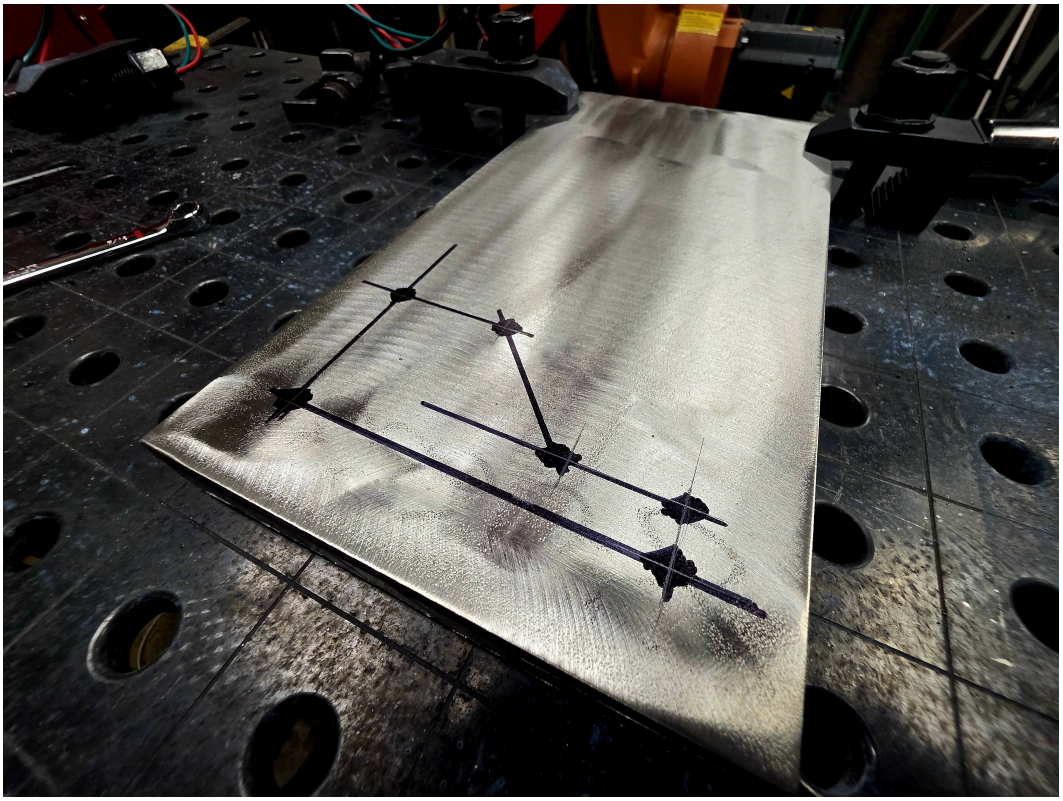


Figure 10.32: Final Geometry Path Layout



Figure 10.33: Final Geometry as Deposited

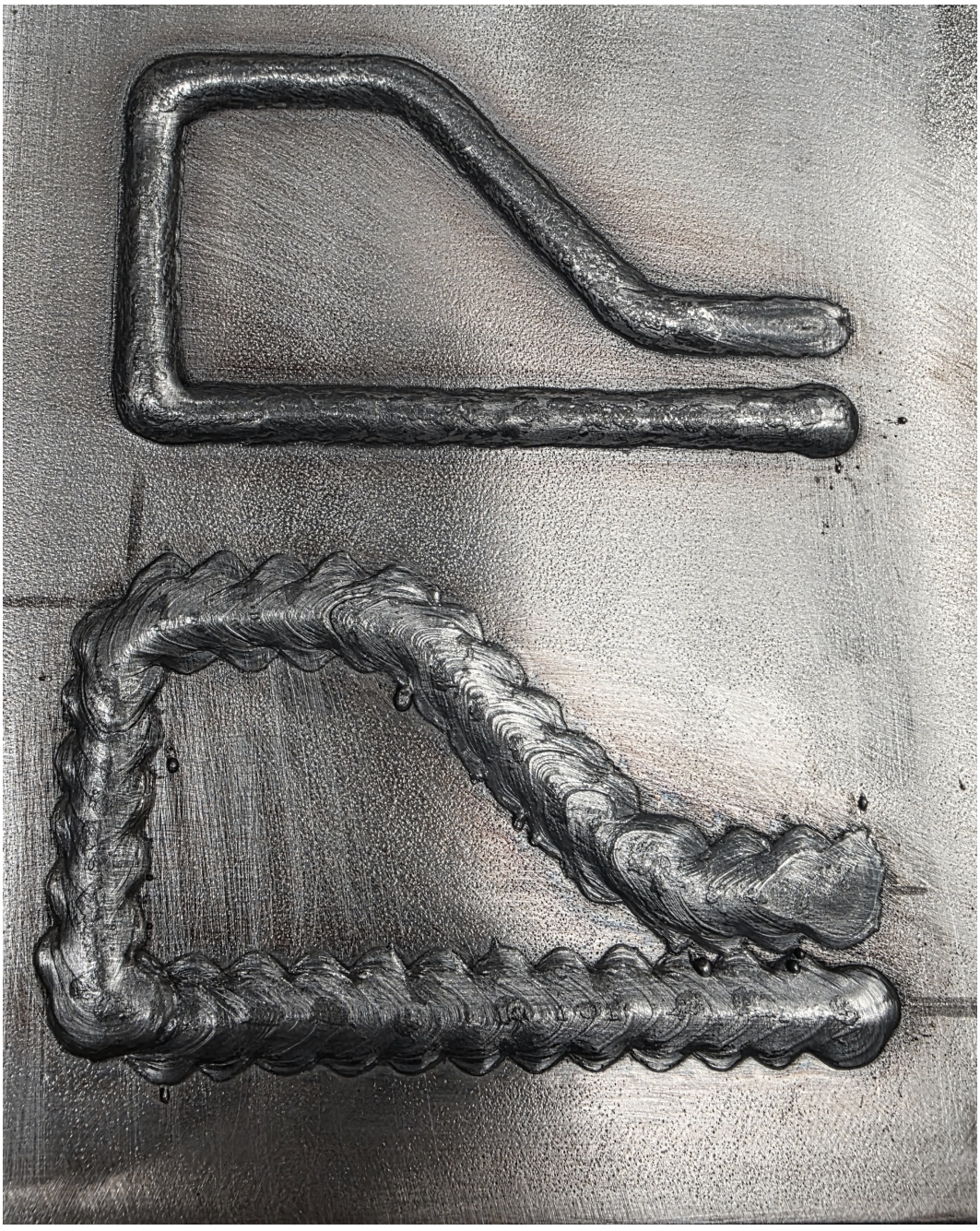


Figure 10.34: Final Geometry After Wire-brushing

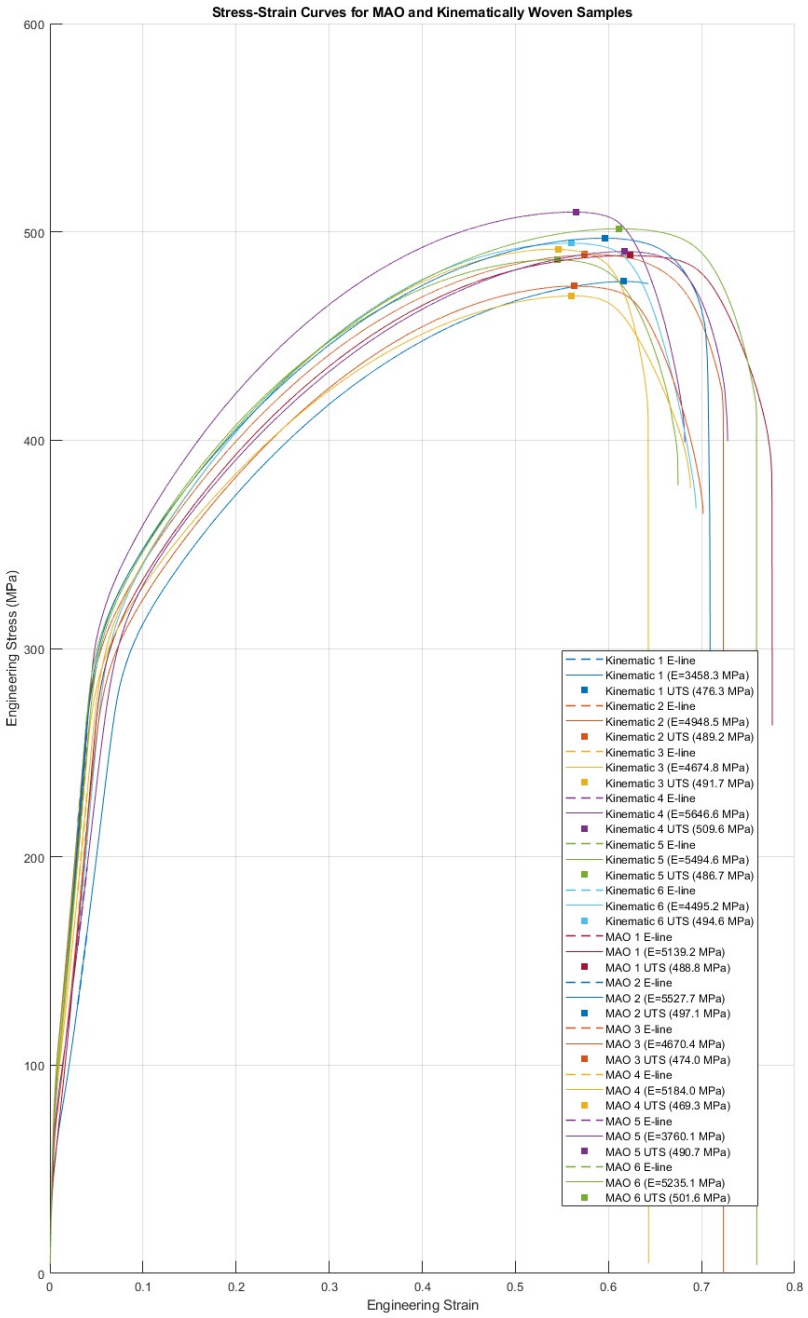


Figure 10.35: Tensile Testing Results



Figure 10.36: Diffuse Necking Along Gage Length

Table 10.2: Tensile Testing Results

Kinematic			MAO-Produced		
Kinematic #	**UTS (MPa)**	**E (MPa)**	**MAO#**	**UTS (MPa)**	**E (MPa)**
1	476.3	3458.3	1	488.8	5139.2
2	489.2	4948.5	2	497.1	5527.7
3	491.7	4674.8	3	474	4670.4
4	509.6	5646.6	4	469.3	5184
5	486.7	5494.6	5	490.7	3760.1
6	494.6	4495.2	6	501.6	5235.1
STD Dev	10.92	791.06	STD Dev	12.76	631.5

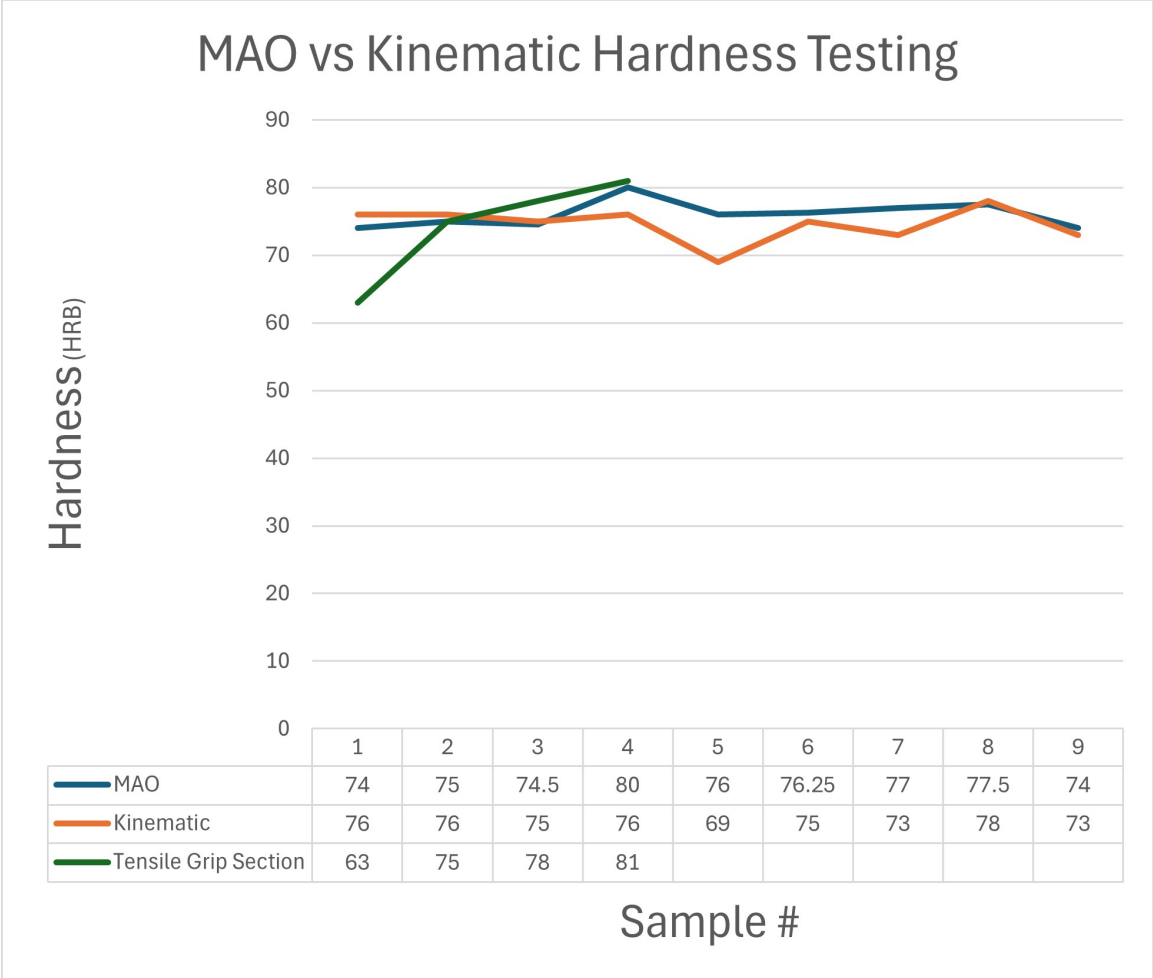
Hardness Results

Utilizing the procedure outlined in 10.1.4, both kinematically and MAO-produced samples were tested a total of nine (9) times each, the results of which can be seen in Figure 10.37, where the average hardness for a kinematically woven weld sample was 74.55 HRB, and the MAO-produced weld sample being slightly higher at 76.02 HRB. In addition, four samples were taken from the grip-section of a fractured tensile test sample, which, while having an average hardness of 74.25 HRB, showed a much larger standard deviation (∼7.89 HRB) when compared to the non-fractured samples (∼2.60 and 1.95 HRB, respectively), with the MAO-produced samples showing the least deviation.

Bend Test Results

Samples were examined and evaluated in accordance with AWS D1.6/D1.6M:2007, Section 4.6.5.1 (11), where no discontinuities shall be allowed which exceed the following dimensions:

1. 1/8 in —measured in any direction on the surface.
2. 3/8 in —the sum of the greatest dimensions of all discontinuities exceeding 1/32 in, but less than or equal to 1/8 in.
3. 1/4 in —the maximum corner crack, except when the corner crack results from visible slag inclusion or other fusion type discontinuities, then a 1/8 in maximum shall apply.



	1	2	3	4	5	6	7	8	9
MAO	74	75	74.5	80	76	76.25	77	77.5	74
Kinematic	76	76	75	76	69	75	73	78	73
Tensile Grip Section	63	75	78	81					

Figure 10.37: Hardness Testing Results

Bend test results can be seen in Figures 10.38-10.40, where no discontinuities were observed. Future work should see the inclusion of bend test samples sectioned horizontally from bulk walls, as well as vertically oriented samples from single-wall structures to better align with the dimensional guidance by AWS, outlined in Section 10.1.4.

10.3.2 Dye Penetrant Results

Shown in Figures 10.41-10.44, the elongated weave profile chosen for testing allowed penetrant to sit in interior corners, and such areas were disregarded during evaluation due to the difficulty of removing excess penetrant from these areas during application. Areas surrounding sectioned portions were also disregarded due to this. The machined portions of the sample welds showed no indications of cracks or porosity, but testing was otherwise inconclusive.

10.3.3 Macro-Etching Results

Samples from parameter sets 1, 3 and 5 from Table 10.1 were evaluated in a single bead-on-plate test, where material was deposited using the off-robot testing configuration outlined in Chapter 7, the results of which can be seen in Figure 10.45. To align with AWS D1.6 (11), three samples were etched for each parameter set. Excess material from tensile test sample production outlined in 10.1.4 was also macro-etched and evaluated, shown in Figures 10.46 and 10.47. These samples were deposited with parameter set 6 in Table 10.1 with the on-robot testing configuration outlined in Chapter 8. All samples were evaluated in accordance with AWS B3.0 (56) 4.3.3.3 and CSWIP 3.1 (12) for "complete fusion and freedom from cracks" (56) in both the weld metal and heat-affected zone (HAZ) at 1x magnification. Illustrated in Figure 10.48, measurements for penetration depth and width were taken, aligning with literature (58), for the traditional and MAO-actuated parameter sets, as well as for the kinematically and MAO-woven wall samples outlined in Figure 10.47.



Figure 10.38: MAO-based Exterior Bend Test Results



Figure 10.39: Kinematically Woven Exterior Bend Test Results



Figure 10.40: Bend Test Interior Face Results (MAO shown above)



Figure 10.41: Dye Penetrant Tested Sample



Figure 10.42: Dye Penetrant Tested Sample

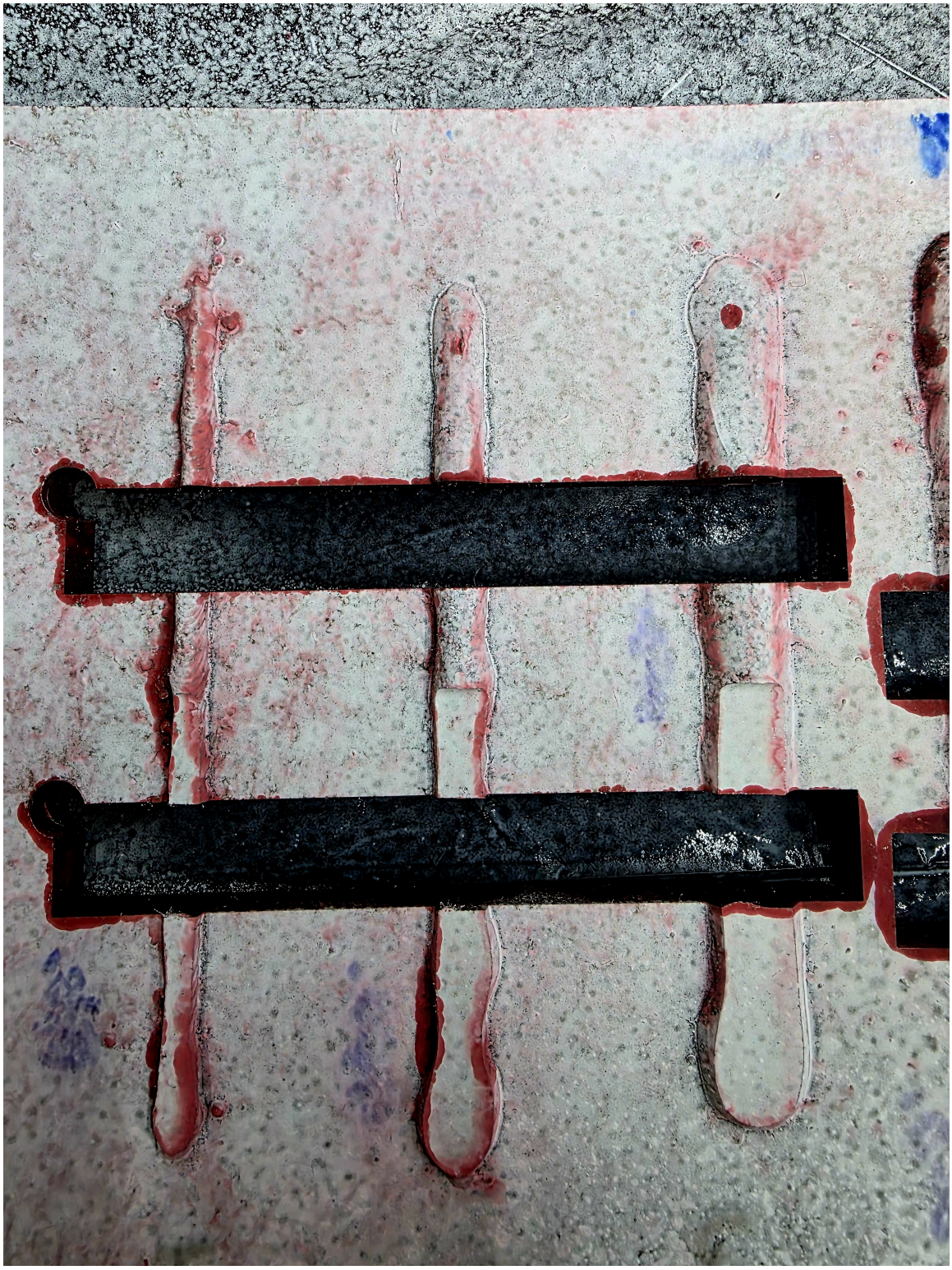


Figure 10.43: Dye Penetrant Tested Traditionally Deposited Material

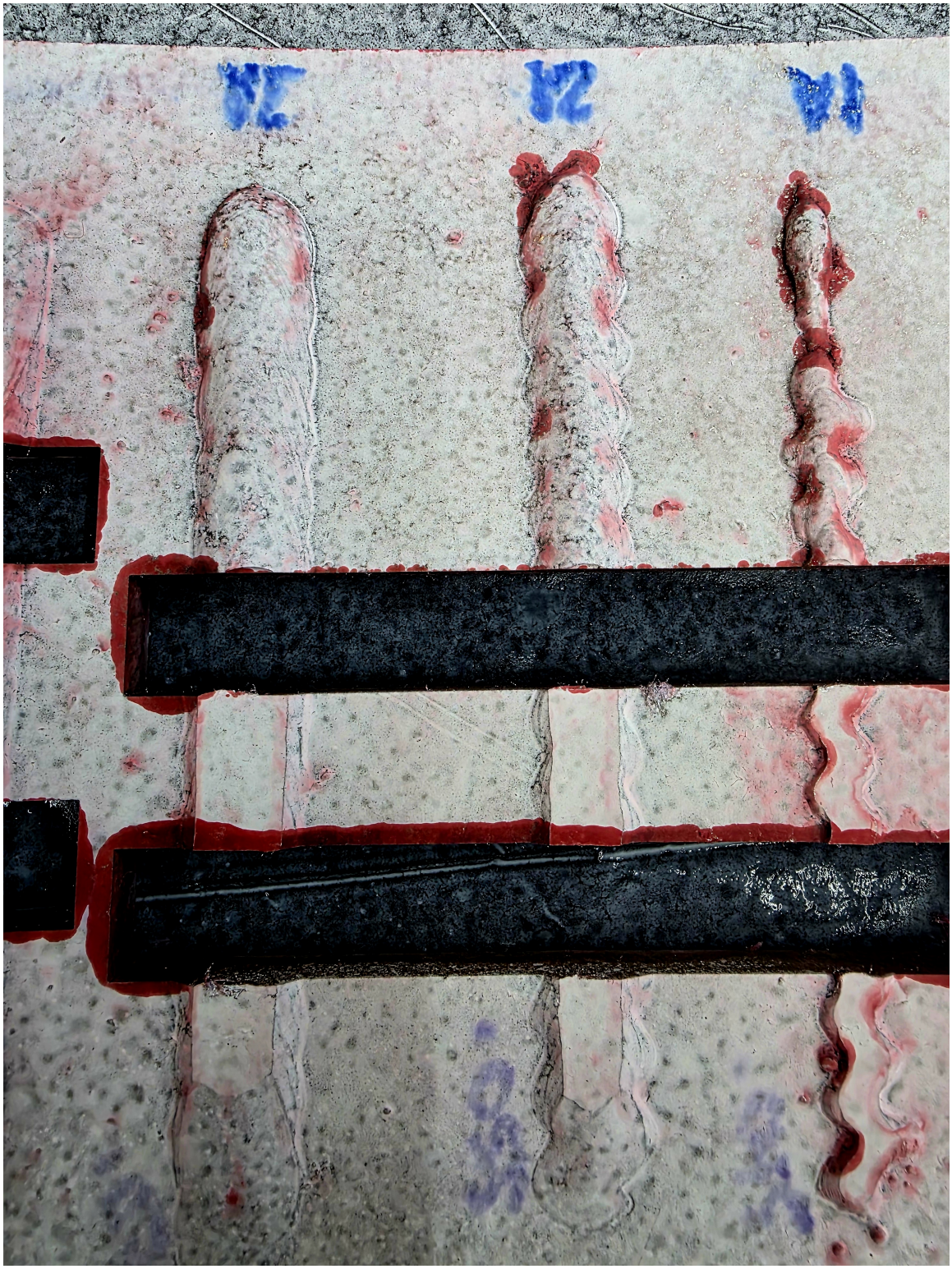
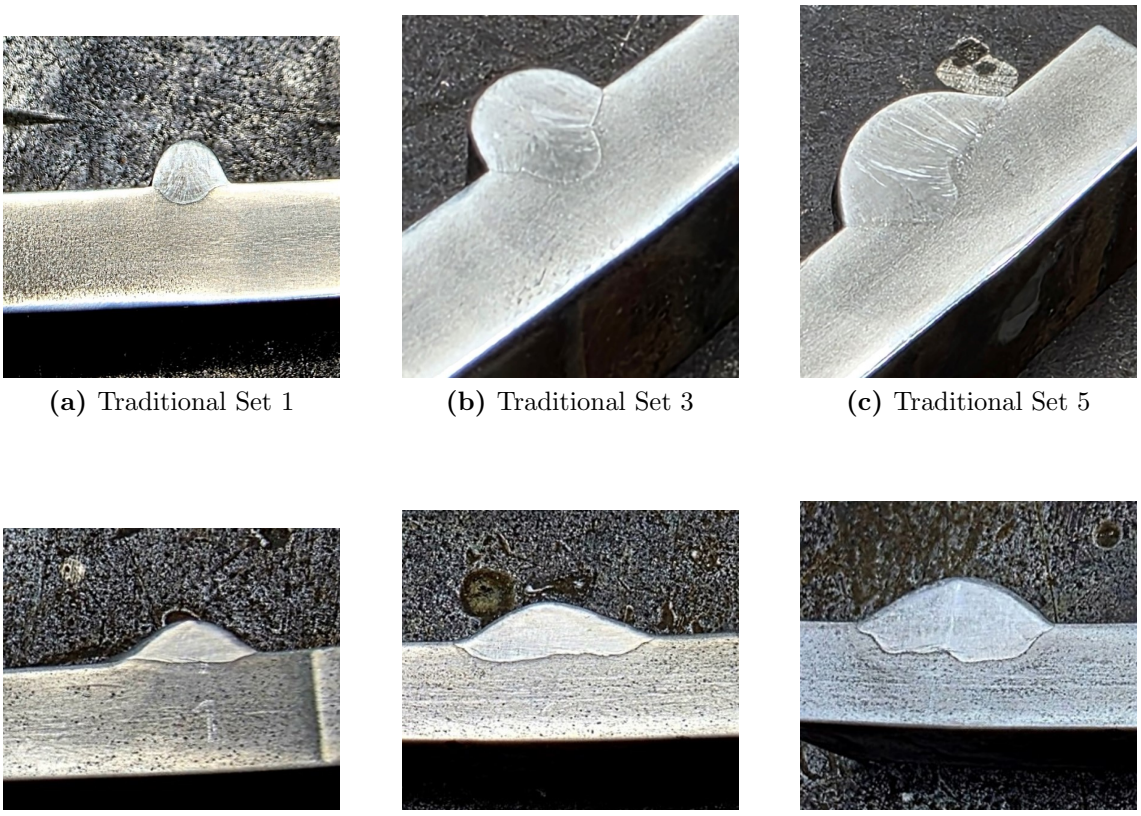


Figure 10.44: Dye Penetrant Tested MAO Deposited Material



(a) Traditional Set 1 **(b)** Traditional Set 3 **(c)** Traditional Set 5

(d) MAO Set 1 **(e)** MAO Set 3 **(f)** Mao Set 5

Figure 10.45: Macro Etching Results for Traditional and MAO Cases



Figure 10.46: Wall Samples Prior to Etching (MAO on left)



Figure 10.47: Macro Etched Wall Samples (MAO on right)

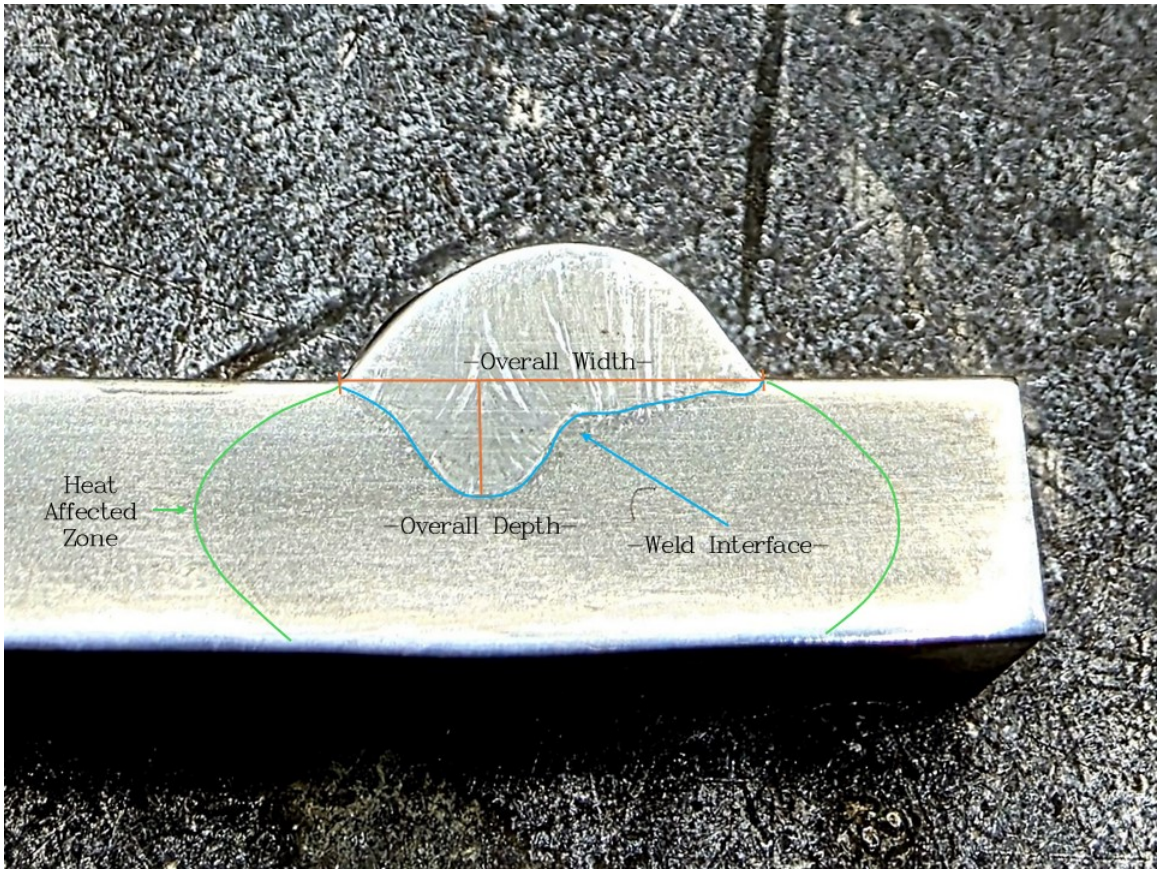


Figure 10.48: Macro Etching Example Layout

These measurements can be seen in Table 10.3. The resulting beads in both the bead-on-plate and wall-type etched samples aligned with expectations in the traditionally deposited case for bead penetration profile, illustrated in Figure 10.49, but deviated in the MAO-actuated case, where a $\leq 34\%$ deviation was seen in penetration depth, dependent on parameters, with improved uniformity throughout the cross-section.

10.3.4 Geometric Comparison

To aid in determining overall utility of produced geometries, 3D scans were taken, outlined in Section 10.1.2, and evaluated for the magnitude of deflection, symmetry of the produced profile, and deviations in both thickness of produced walls, as well as overall straightness of the resulting material.

Deflection Magnitude from Weld Centerline

Scanned weld beads were evaluated for deflection from centerline every 0.100" overall, with 0.010" evaluation intervals in areas of interest, shown in Figure 10.50. Due to MAO causing the welding arc to rotate about the wire electrode, the weld bead shape changes, as seen in Figure 10.51, causing a shorter, flatter profile when deflected. Because of this, the uppermost portion of the weld bead was chosen as a datum for evaluation. This process was repeated

Table 10.3: Measured Width and Depth of Weld Penetration

#	Welding Current (A)	Welding Voltage (V)	Width	Depth	Notes
1-T	84	18	0.176	0.595	*Unstable
1-MAO	84	18	0.246	0.039	*Unstable
3-T	164	22	0.253	0.132	
3-MAO	160	22	0.484	0.1	
5-T	216	24	0.458	0.121	
5-MAO	217	24	0.528	0.107	
Wall-T	172	14.66	0.25	0.078	
Wall-MAO	160	14.8	0.248	0.063	

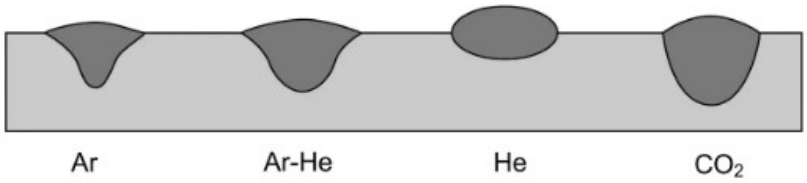


Figure 10.49: CSWIP 3.1 Guidance on Gas Composition Effect on Weld Bead Profile (12)

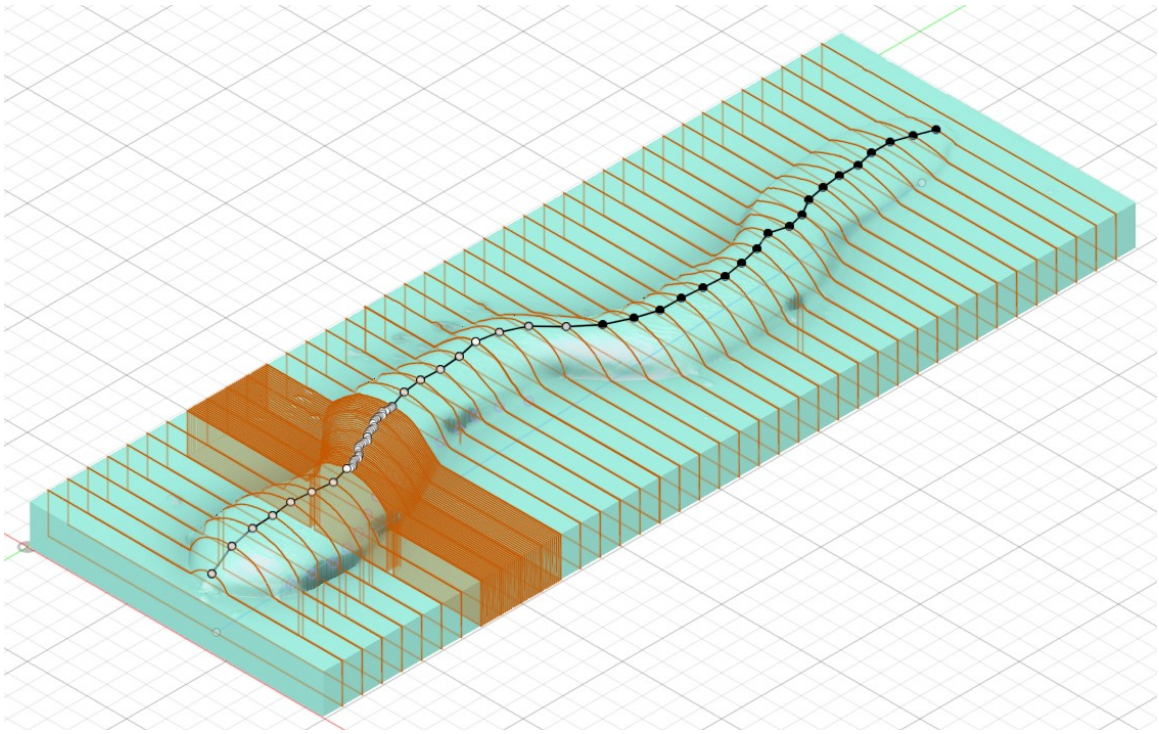


Figure 10.50: Deflection Magnitude Evaluation Method

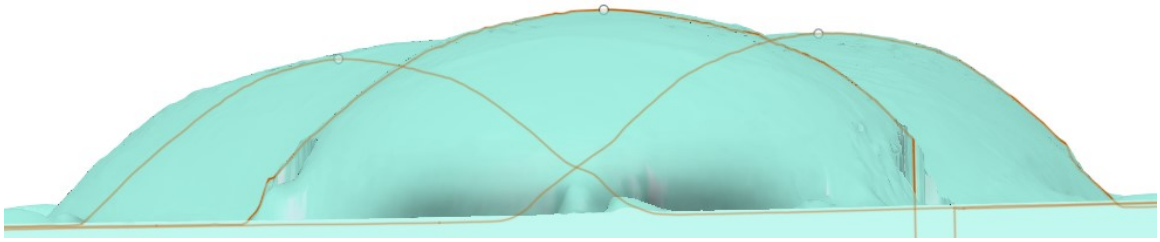


Figure 10.51: Deflected Weld Bead Profiles

for a total of five parameter sets, outlined in 10.1 and used in the development of the data-driven predictive model discussed in 5.2

Deflection Symmetry

To evaluate deflected bead profiles for symmetry in the positive (+) and negative (-) directions from travel centerline, the above produced bead centerline profiles were mirored about the X and Y axes to overlay the latter half of the bead over the former, as shown in blue on Figures 10.52 and 10.53 below. It was seen that some parameter sets exhibited a more symmetric deflection profile than others, particularly in the transition region between the positive and negative deflections, and is attributed to differences in overall process stability.

Wall Thickness Deviation

A section from the steady-state central region of material produced for tensile testing, shown in Figure 10.9, was leveraged and 3D scanned for both the kinematically produced and MAO-produced conditions (Figure 10.54). These were then evaluated in Autodesk Fusion, where sketches were developed representing the exterior perimeter of the samples, illustrated in Figure 10.55. These were then evaluated every 0.050" in deposited height and measured both in deposited width, as well as in relation to a vertical datum to aid in determining overall straightness of the material, shown in Figures 10.56 and 10.57. The results showed the MAO-produced samples having a smaller standard deviation in wall thickness than the kinematically produced material (0.0108" vs 0.0111"), but with the kinematically-produced material having a smaller deviation in straightness (0.019" vs 0.022"). Average wall thickness for the kinematically produced sample was also slightly higher at 0.294" vs 0.290" in that of the MAO-produced material.

10.3.5 Comparison with Data-Driven Model

Leveraging the analyses described in Section 10.3.4, comparison was made between the predicted results and those of deposited material from the on-robot hardware outlined in

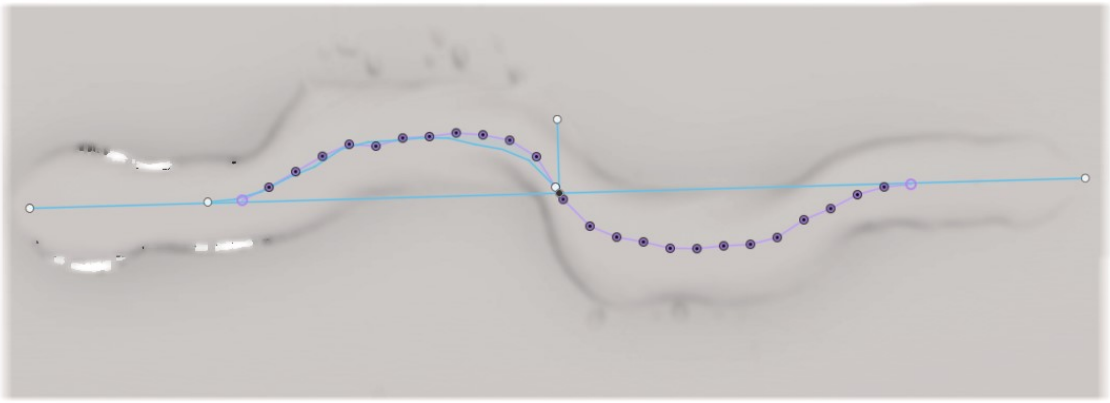


Figure 10.52: Parameter Set 4 Symmetry Evaluation

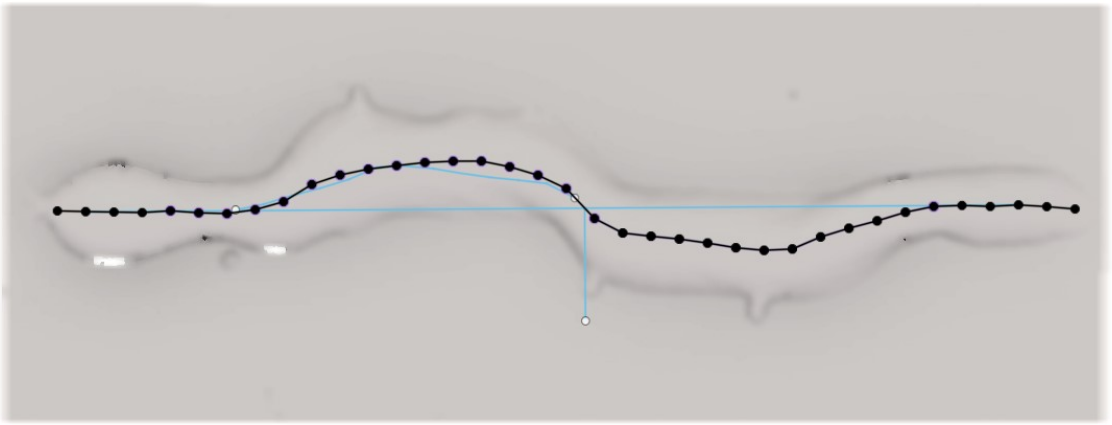


Figure 10.53: Parameter Set 3 Symmetry Evaluation



Figure 10.54: Sectioned Samples for Wall Thickness Deviation Examination

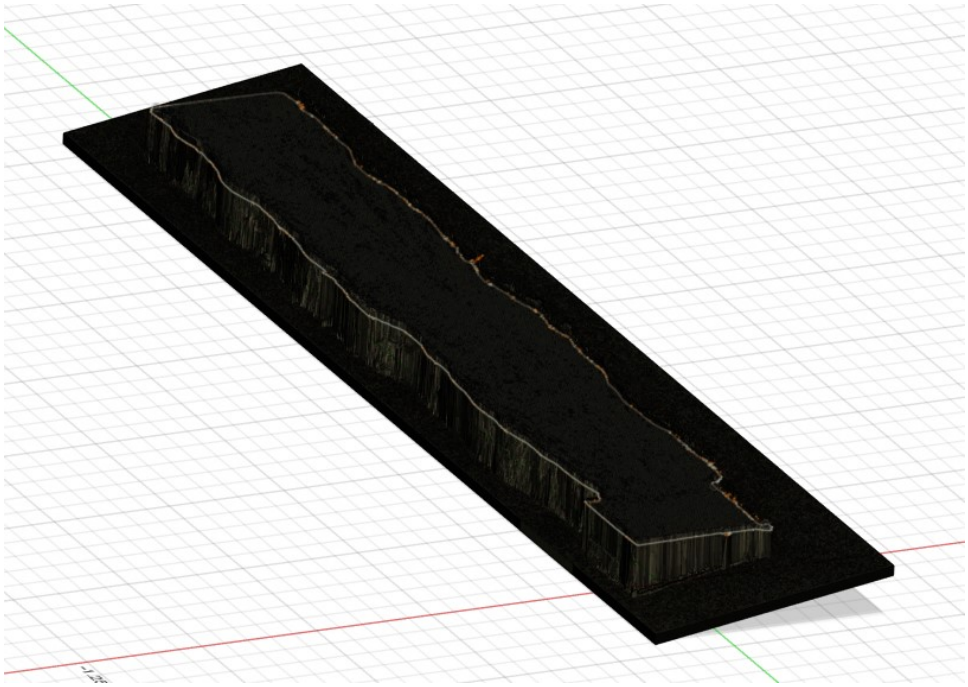


Figure 10.55: Perimeter Sketch for Wall Thickness Deviation Examination

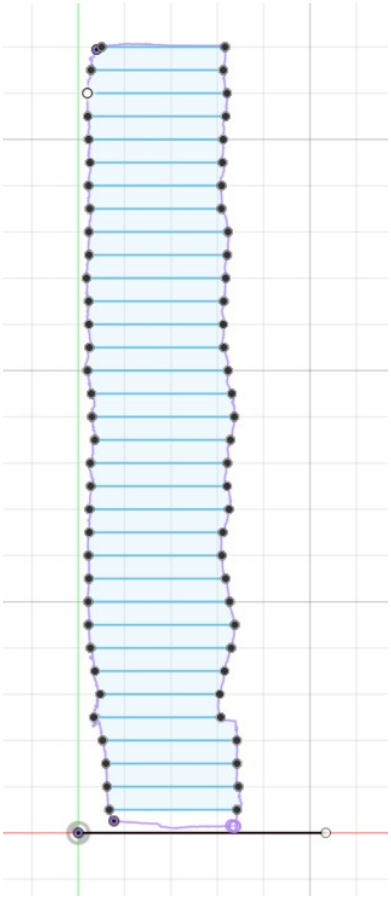


Figure 10.56: Evaluation Method for Wall Thickness Deviation (kinematic example shown)

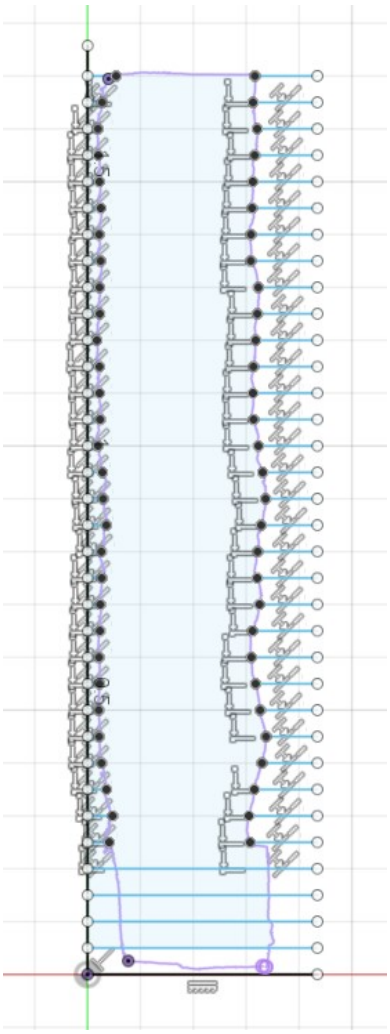


Figure 10.57: Evaluation Method for Straightness Deviation (kinematic example shown)

Chapter 8, utilizing parameter sets 1, 3, 5 and 6 from Table 10.1. Figures 10.58 and 10.59 show the calculated bead deflection magnitude and accompanying Matlab plot for welding parameter set 5 in Table 10.1, using welding power and oscillation frequency as inputs. Shown in Table 10.4, the predicted deflection from centerline had a $\sim$ 25% average error between the four sample sets when compared to deflected weld bead measurements. This was in part due to the a shift in transfer modes between the Miller and Fronius power supplies used in off-robot and on-robot testing, respectively, which is discussed in Section 11.1. An increase in bead width and decrease in bead height was also observed when measured in the steady-state regions of the traditional and MAO regions of the weld was observed across the sample range (Figures 10.60 and 10.61).

10.3.6 Waveform and Frequency Domain Analysis

Welds were made using parameters outlined in 10.1 where the MAO control logic was programmed to initiate a 4 rad/s ($\sim$0.63 Hz) triangular weave 12.5 s into the duration of the weld and data was recorded using the on-robot experimental configuration outlined in Section 8.3. A Matlab script was then developed to plot the entire data set, prompt the user to choose time intervals of interest (Figures 10.62 and 10.63), calculate the average welding current and voltage (Figure 10.64), then plot both the current and voltage of the areas of interest singularly (Figures 10.65-10.68) and overlaid with each other (Figures 10.69 and 10.70), as well as calculate the fast-Fourier-transform of both the current and voltage (Figures 10.71 and 10.72). The fast-Fourier-transform values are then overlaid with each other (Figures 10.73 and 10.74) to identify changes in deposition frequency or process stability, as well as aid in determining the deposition mode of the welding process during both the traditionally deposited and MAO-actuated case. This comparison was done for both the chosen areas of interest, as well as the full range of the two respective processes, shown in Figures 10.75-10.76. The full matlab script can be seen in Appendix B.3 along with supplementary welding waveform data plots in Appendix C. Tables 10.5 and 10.6 show the calculated average heat inputs for the Fronius power supply used in the on-robot test configuration, as well as the

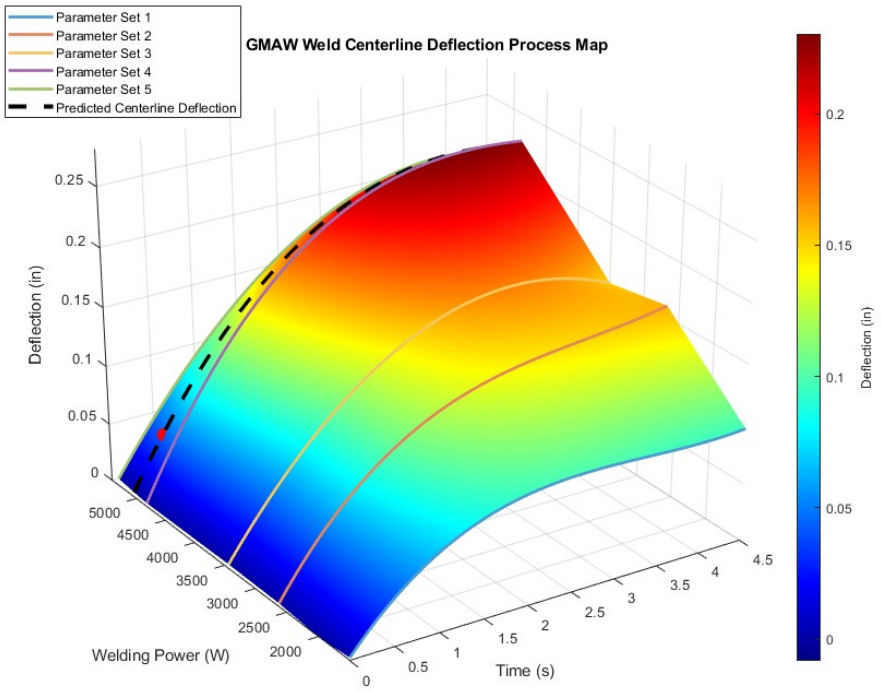


Figure 10.58: Predictive Model Output Plot for Parameter Set 5

```
Please enter the desired welding current in Amps (between 85 and 225A)  213
Please enter the desired welding voltage in Volts (between 18 and 24V)  24
Please enter the desired oscillation frequency in Hz: 0.63
The deflection at time = 0.39683 seconds is: 0.043646
```

Figure 10.59: Predictive Model Output for Parameter Set 5

Table 10.4: Predicted vs Actual Weld Deflections

#	Current/Voltage	Pred. Defl.	Actual Defl.	$Width$	$Width_{MAO}$	$Height$	$Height_{MAO}$
1	88A/18V	0.035”	0.025”	0.196”	0.22”	0.086”	0.067”
3	166A/20V	0.036”	0.050”	0.361”	0.577”	0.114”	0.095”
5	213A/24V	0.0436”	0.044”	0.499”	0.708”	0.106”	0.106”
6	150A/14.85V	0.036”	0.020”	0.268”	0.282”	0.152”	0.131”



Figure 10.60: Parameter Set 5 Width Measurement Locations

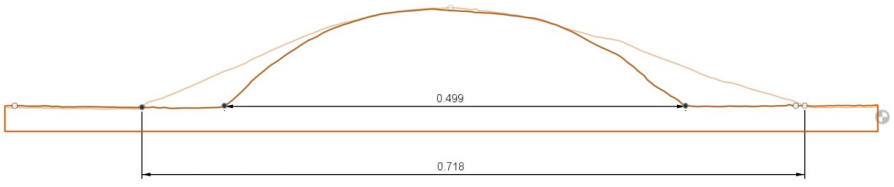


Figure 10.61: Measured Values for Parameter Set 5 Width

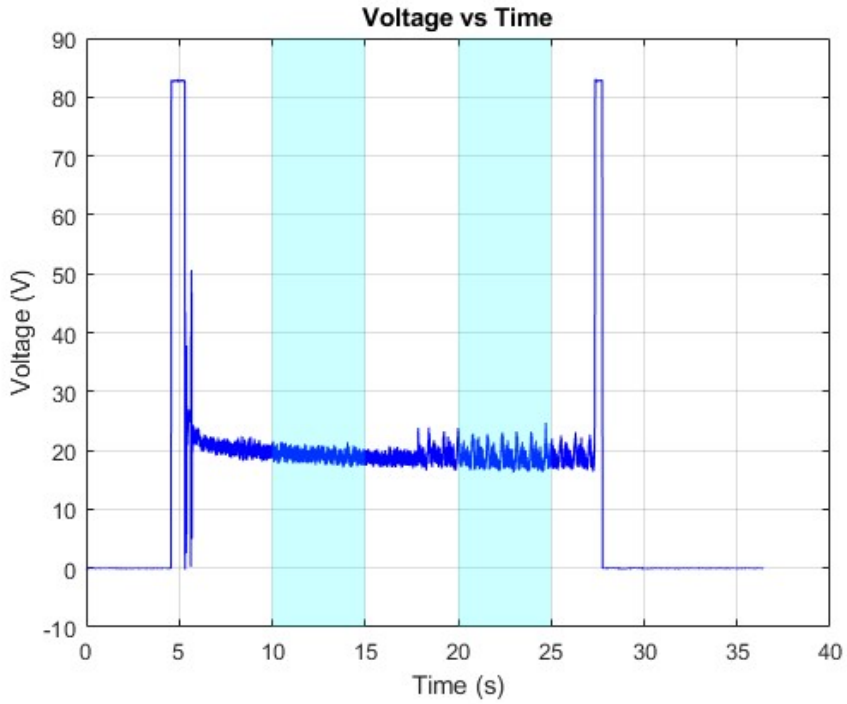


Figure 10.62: Voltage vs Time (Area of Interest Highlighted) for 200ipm/20.1V Case

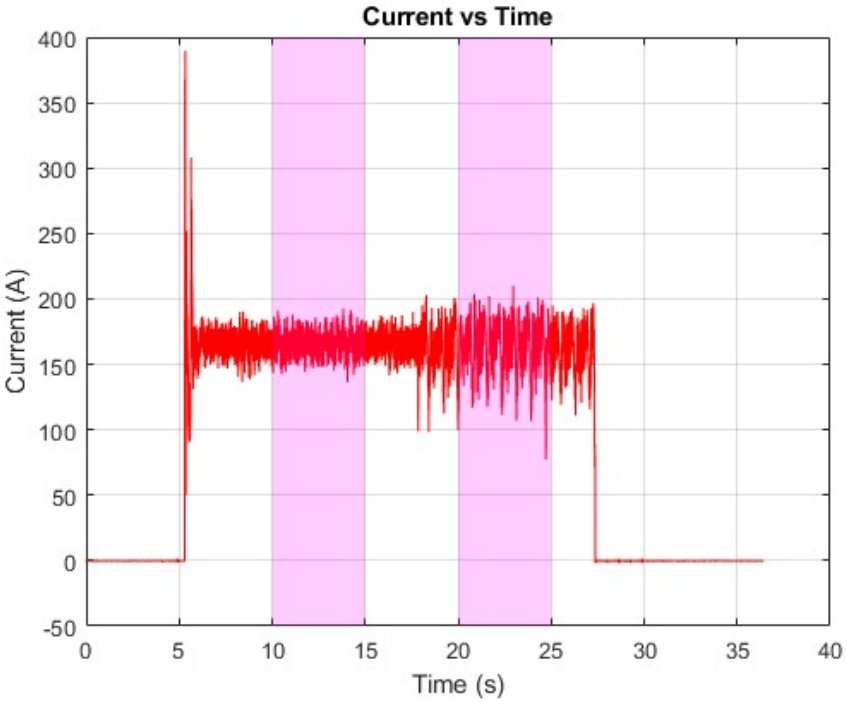


Figure 10.63: Current vs Time (Area of Interest Highlighted) for 200ipm/20.1V Case

```
Interval 1 (10.000000 s to 15.000000 s):
Mean Voltage: 19.1774 V
Mean Current: 166.2940 A

Interval 2 (20.000000 s to 25.000000 s):
Mean Voltage: 18.8822 V
Mean Current: 163.1249 A
```

Figure 10.64: MATLAB Average Current and Voltage Output for 200ipm/20.1V Case

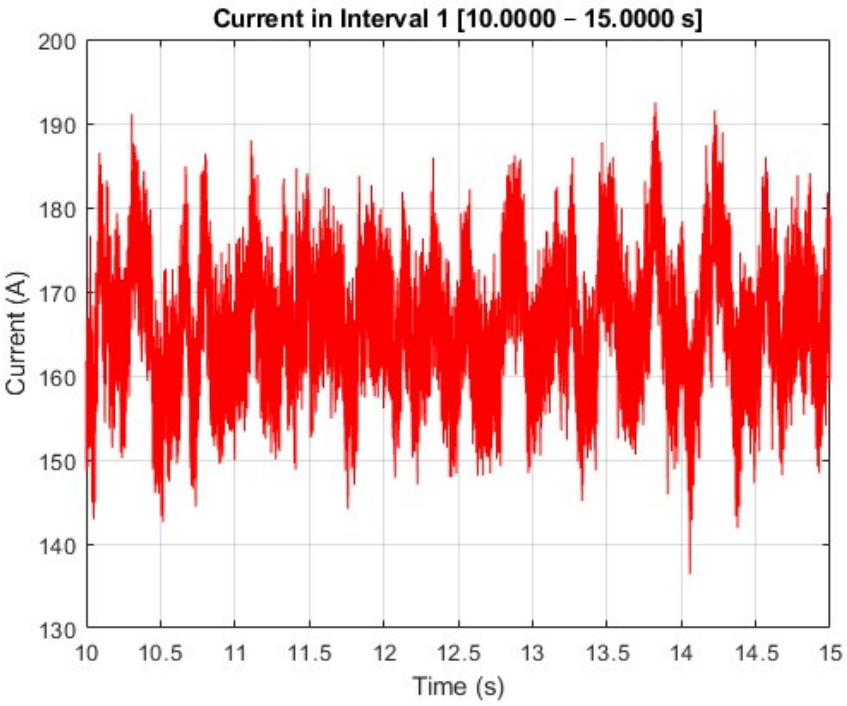


Figure 10.65: MATLAB Current Output for 200ipm/20.1V Case in Interval 1

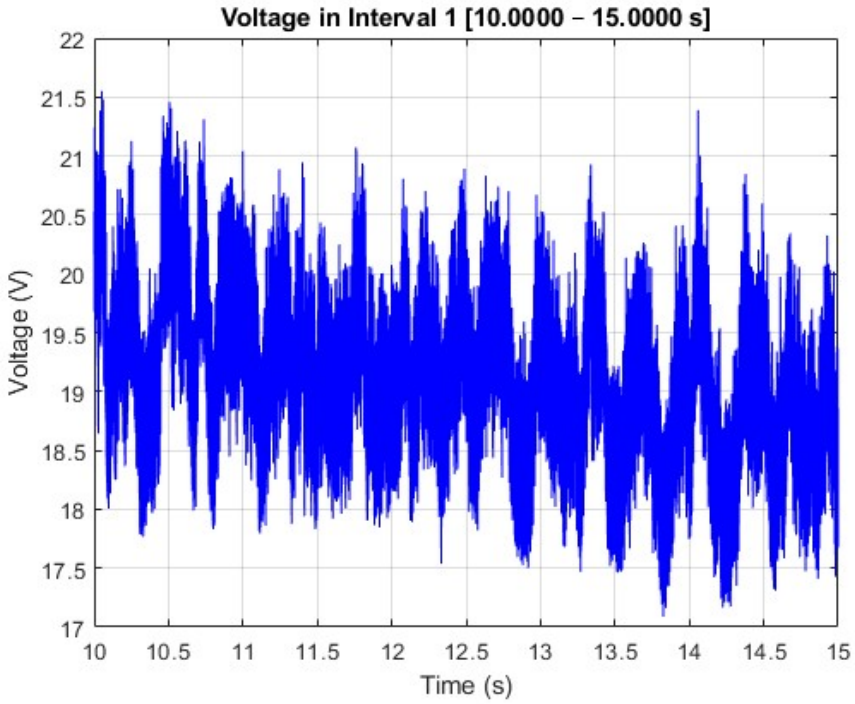


Figure 10.66: MATLAB Voltage Output for 200ipm/20.1V Case in Interval 1

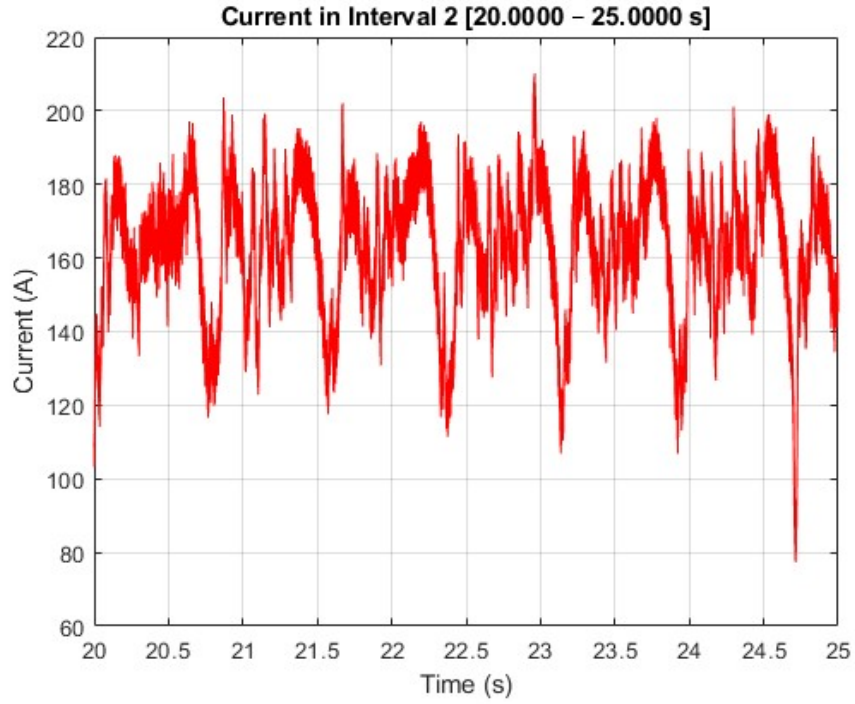


Figure 10.67: MATLAB Current Output for 200ipm/20.1V Case in Interval 2

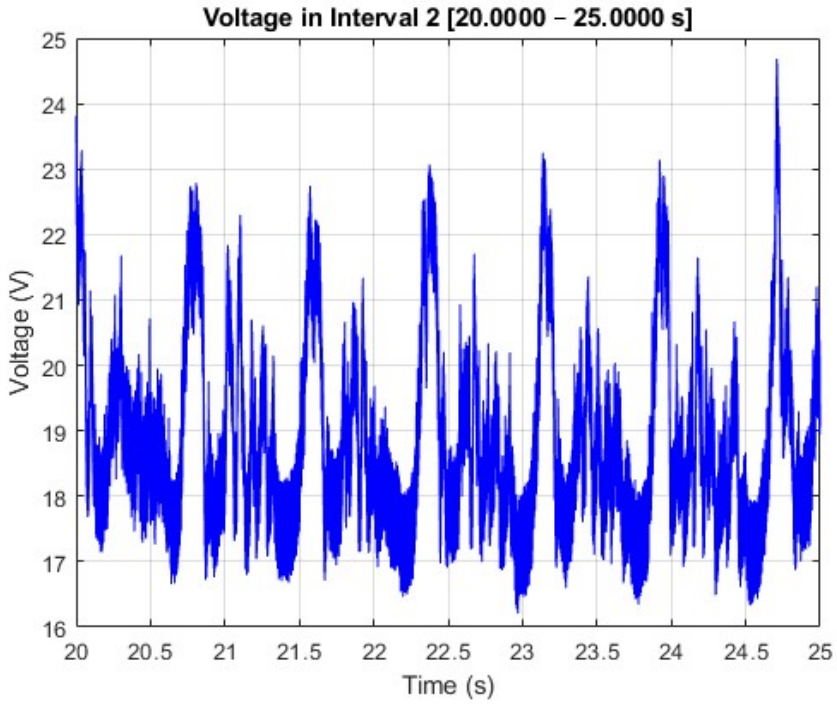


Figure 10.68: MATLAB Voltage Output for 200ipm/20.1V Case in Interval 2

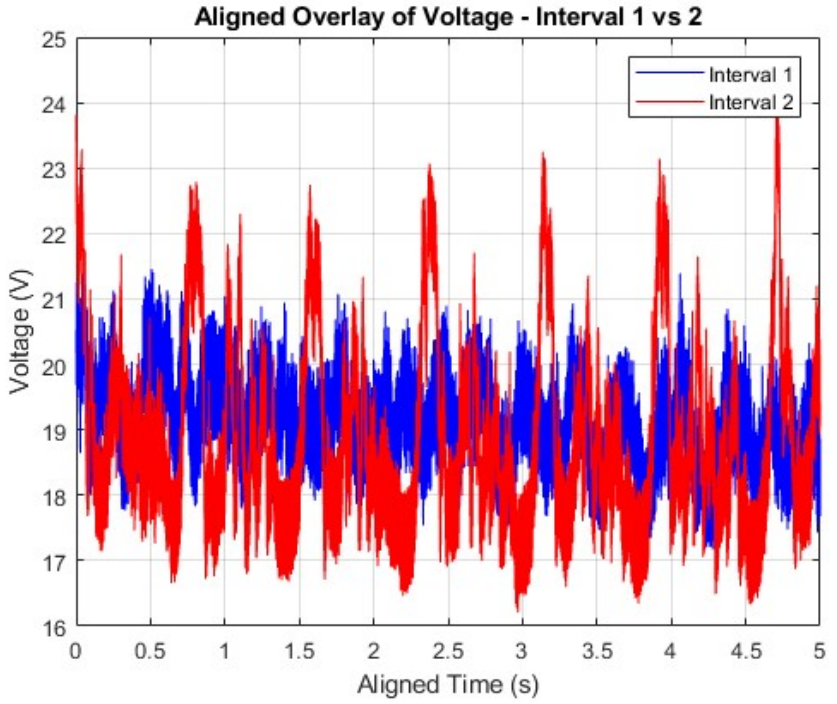


Figure 10.69: MATLAB Overlaid Voltage Output for 200ipm/20.1V Case

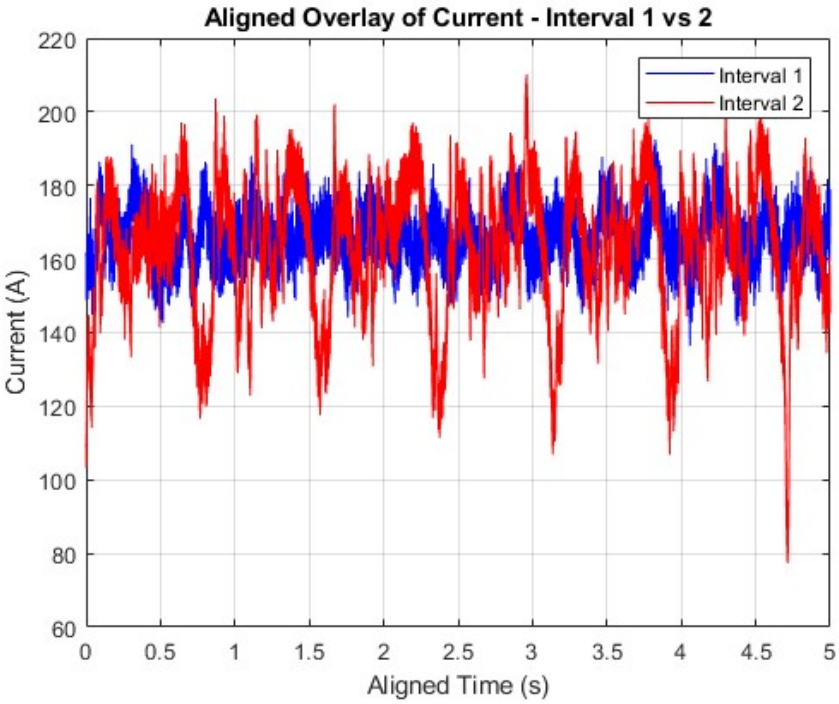


Figure 10.70: MATLAB Overlaid Current Output for 200ipm/20.1V Case

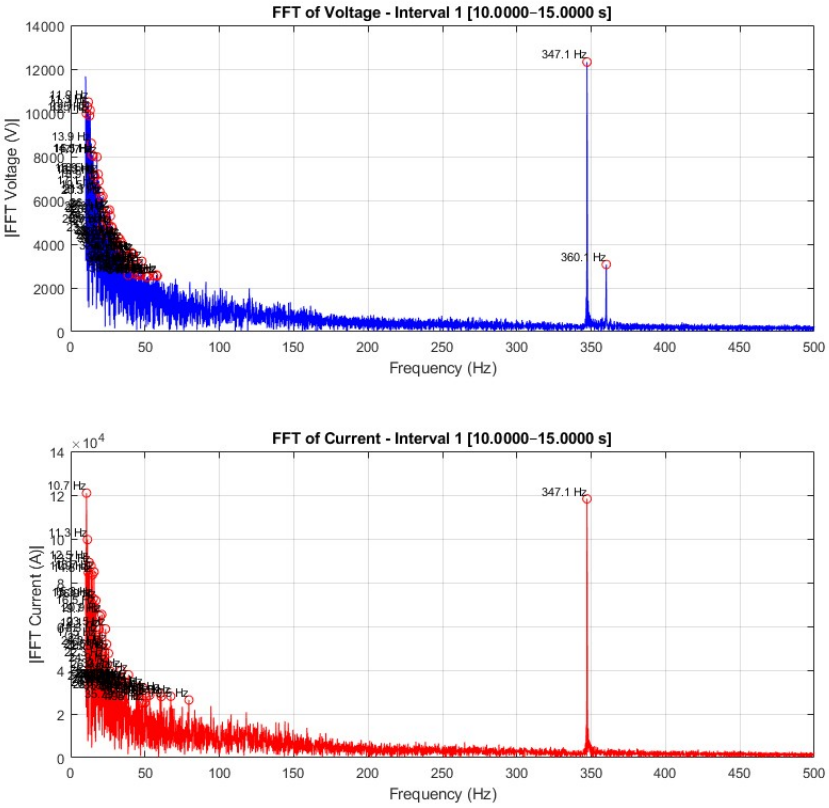


Figure 10.71: MATLAB FFT Plot for Interval 1 in 200ipm/20.1V Case

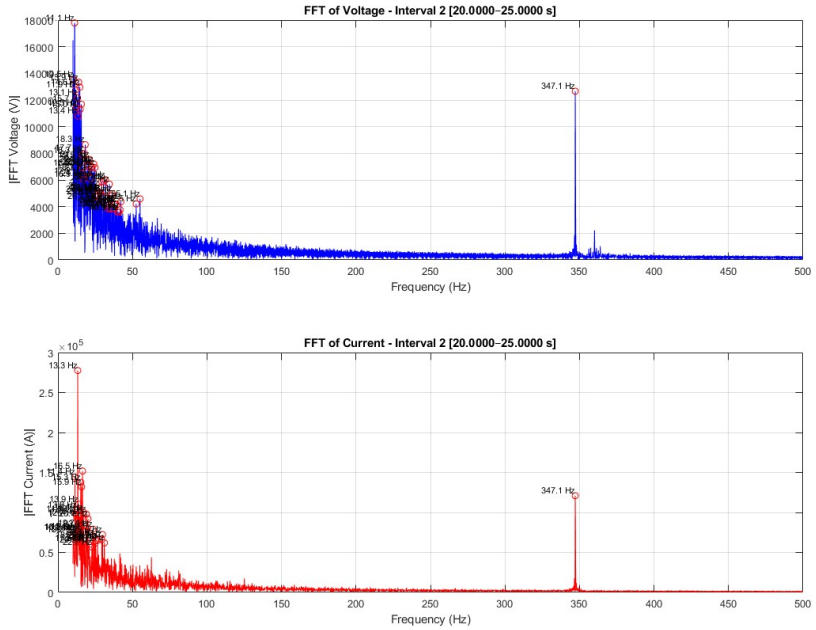


Figure 10.72: MATLAB FFT Plot for Interval 2 in 200ipm/20.1V Case

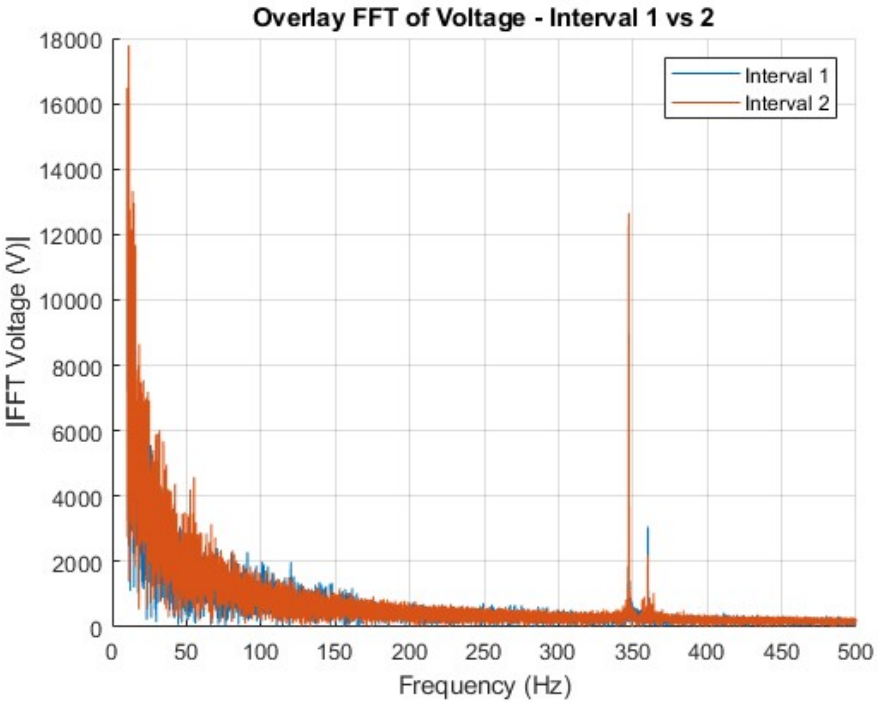


Figure 10.73: MATLAB Voltage FFT Overlaid for 200ipm/20.1V Case

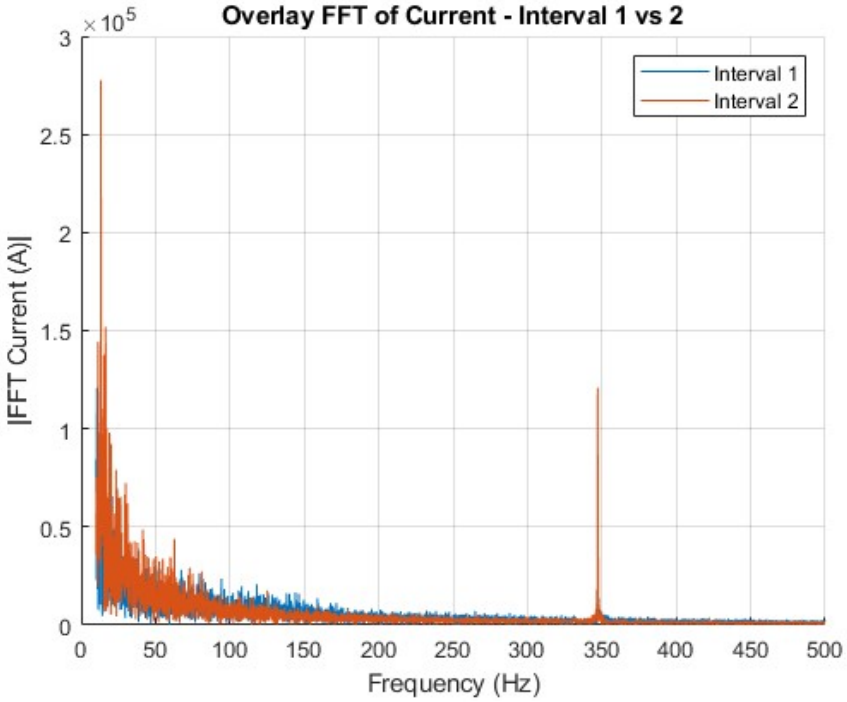


Figure 10.74: MATLAB Current FFT Overlaid for 200ipm/20.1V Case

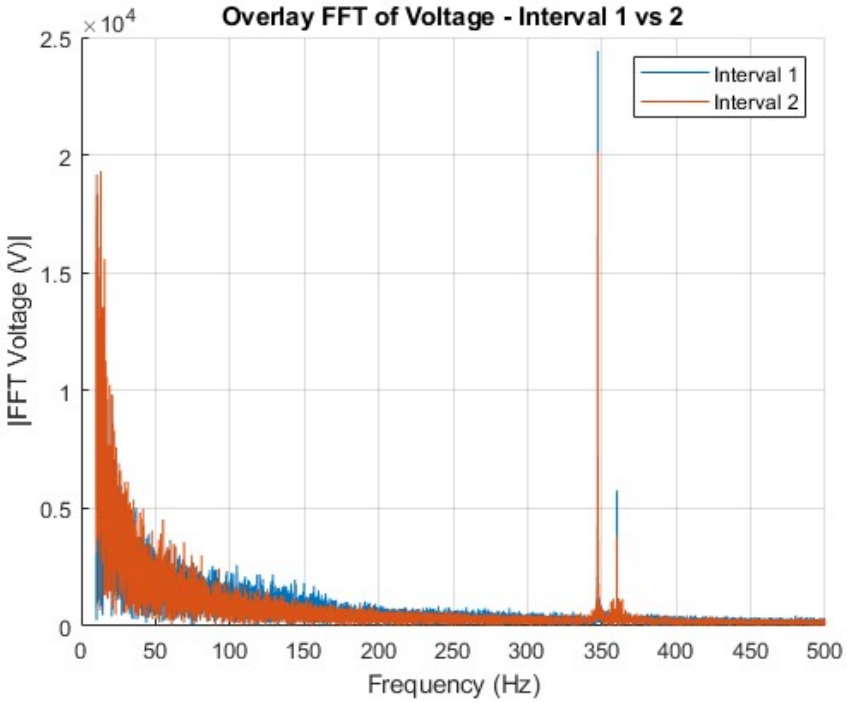


Figure 10.75: MATLAB Voltage FFT Overlaid for Entire Range of 200ipm/20.1V Case

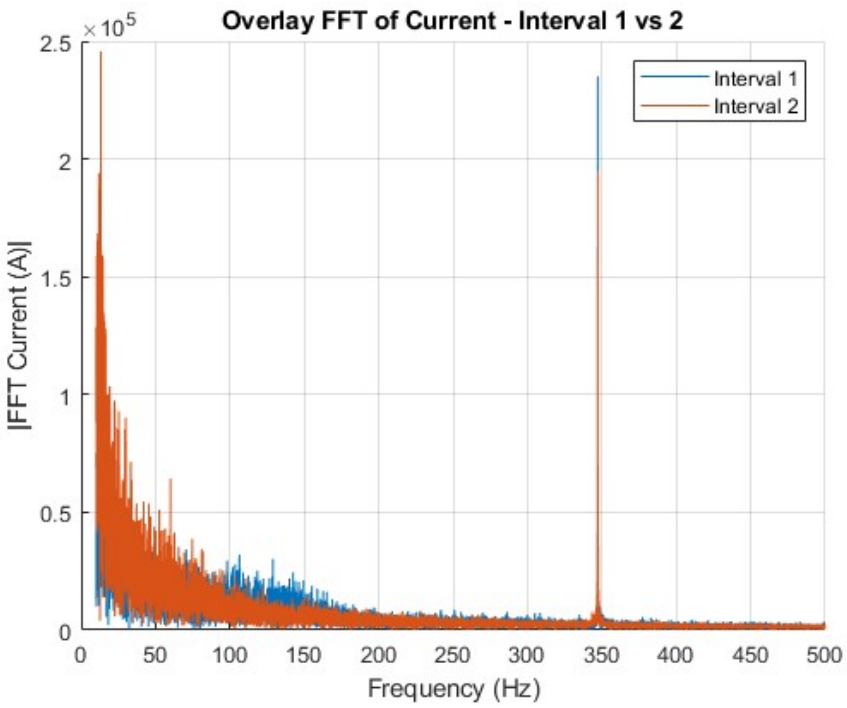


Figure 10.76: MATLAB Current FFT Overlaid for Entire Range of 200ipm/20.1V Case

Miller Pipeworx 400 used in off-robot testing, respectively. These values assume a 12 in/min travel velocity, as well as an industry accepted efficiency value of 0.8 (59) (2) in Equation 2.1 from Chapter 2.

10.3.7 Exploration of Out-of-Scope Processes

While this research was limited to 3XX series stainless steel materials, an exploration was made into the efficacy of this process involving ferromagnetic and aluminum substrates and feedstocks, as well as an inquiry into the functionality of the developed hardware in a traditional spray transfer ($> 25V$) process window.

Traditional Spray Transfer Process Parameters

A brief assessment of $>$ 25 V process parameter sets, shown in Table 10.7, was made in an effort to determine the mechanism causing weld deflection in a free-fall welding transfer mode. During this assessment, static welds were made in a full-deflection electromagnetic field condition and welds were imaged using the technique outlined in Section 7.6 then compared to those of a short-circuit transfer process to identify differences in deflection characteristics, illustrated in Figures 10.77-10.78. It was observed that larger deflection magnitudes were possible due to increased arc lengths and reduced droplet sizes associated with spray transfer at the expense of a decrease in deflection symmetry presumably due to the pole of the off-axis magnet being present in the field. Work should be done to explore the possible benefits of a mirrored arrangement of electromagnetic poles in future design iterations.

Ferromagnetic Substrates

Limited evaluation of the potential use of MAO on ferromagnetic substrates was conducted in both the GTAW and GMAW processes. With the GTAW process, welds were deflected during early control logic development in a 100 Amp direct-current-electrode-negative (DCEN) configuration with suboptimal results (Figure 10.79), likely due to interaction

Table 10.5: Recorded Heat Inputs - 316L Fronius Power Supply

#	WFS (ipm)	Volt (V)	Avg Voltage (V)	Avg Current (A)	Heat Input (J/mm)
1-T	100	17	n/a	n/a	*Unstable
1-MAO	100	17	n/a	n/a	*Unstable
3-T	200	20.2	19.1774	166	507
3-MAO	200	20.2	18.88	163.12	491
5-T	300	24	27.01	264	1136
5-MAO	300	24	27.46	252.25	1104
6-T	220	14.3	14.66	172.3	402
6-MAO	220	14.3	14.8	160.1	377

Table 10.6: Welding Process Parameters - 316L Miller Pipeworx 400 Power Supply

#	WFS (ipm)	Volt (V)	Avg Current (A)	Avg Voltage (V)	Heat Input (J/mm)
3-Miller	200	20.2	20.47	165.7	540
5-Miller	300	24	24	215.7	825
6-Miller	220	14.3	14.6849	145.2	340

Table 10.7: Welding Process Parameters - 316L - Spray Transfer

#	WFS (ipm)	Volt (V)	TS (ipm)	CTWD (in)	Process Notes
1	300	36	n/a	0.500	*25cfh 98/2 Ar/o2 shielding gas throughout
2	350	36	n/a	0.500	
3	400	36	n/a	0.500	
4	450	36	n/a	0.500	
5	500	36	n/a	0.500	

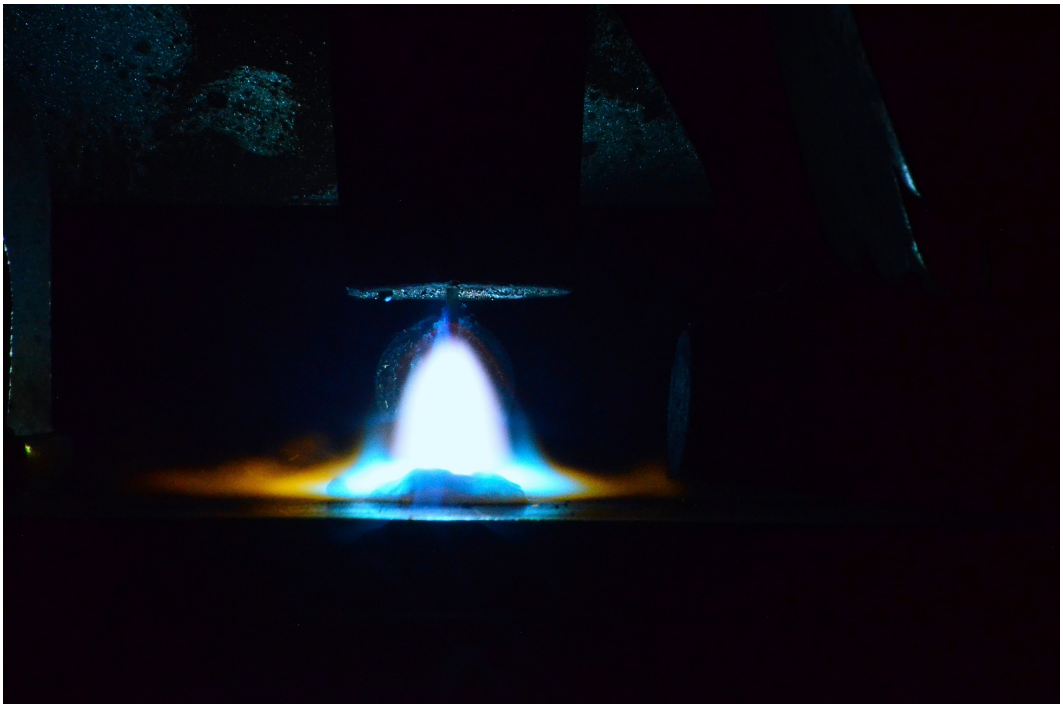


Figure 10.77: Stationary Spray Transfer Welding Arc

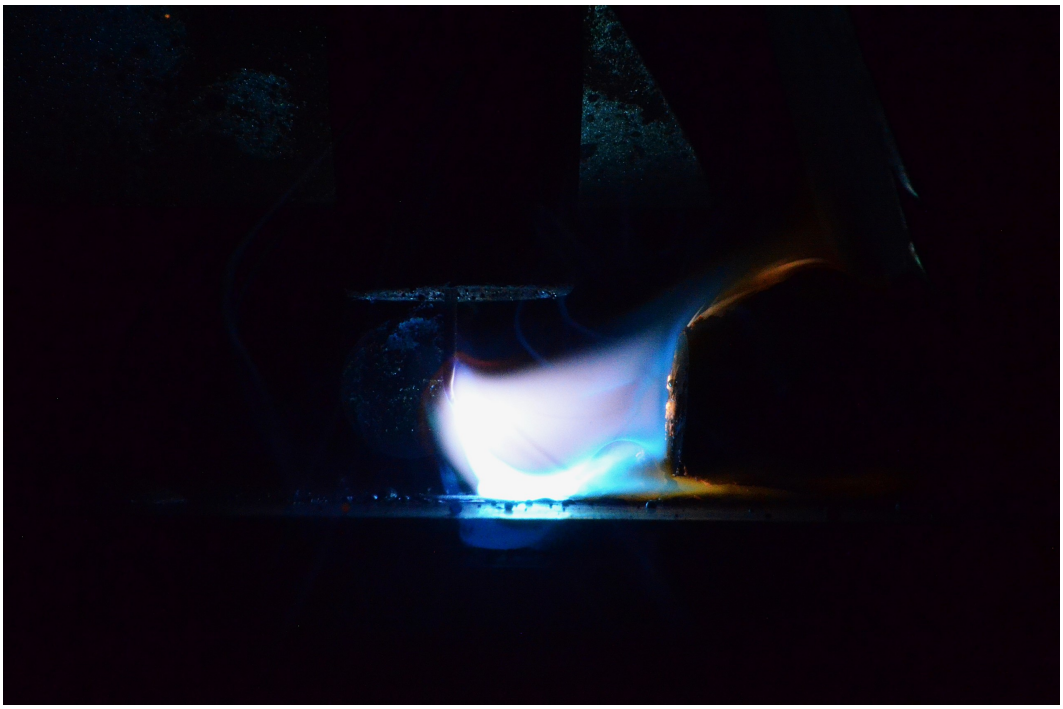


Figure 10.78: Deflected Spray Transfer Welding Arc



Figure 10.79: Test GTAW-MAO Weld (left) vs Traditional Weld (right) on A36/1018 Substrate

between the electromagnetic hardware and the substrate causing a greatly reduced deflection. In the GMAW-case, welds were made using spray transfer process parameters outlined in Section 10.3.7, with no observed deflection in weld path. In Figure 10.80, it can be seen that, while the arc plasma is deflected, the material deposition remains below the wire electrode. While this could potentially be combated with increased magnetic fields, the adverse effects of magnetic remanence would also increase, severely limiting the practicality of this technology in such an application.

Aluminum Substrates

Exploratory study into the utility of MAO-based weaving techniques using aluminum substrates was limited to 2319 alloy wire electrode material deposited onto 6061 substrates shielded with 100% industrial grade argon, shown in Figure 10.81. Welds were made using the same experimental techniques outlined in 10.3.6 with pulsed transfer, cold metal transfer (CMT), short-circuit GMAW, and spray transfer processes. During this, it was observed that the CMT process did not show any response to external magnetic field influence visually or in collected data. This is presumably due to the arc extinguishing briefly during each deposition cycle, causing the arc-light initiation logic to reset with each short circuit, and has potential for future development. Collected current, voltage and frequency data can be seen in Appendix E.



Figure 10.80: Spray Transfer Test Weld on A36/1018 Substrate

Table 10.8: Welding Process Parameters - 2319AL

Wire Feed Speed (ipm)	Voltage (V)	Travel Speed (ipm)	Process Notes
360	20.9	12	GMAW-P
360	10.4	12	CMT
360	18.3	12	GMAW
360	21	12	Spray Transfer



Figure 10.81: 2319Al Test Welds (Left to right: Spray Transfer, GMAW, CMT, GMAW-P shown)

Chapter 11

Discussion

11.1 Interpretation of Test Results

As outlined in Chapter 10, extensive testing was conducted, including destructive testing in the macro etch, tensile, hardness, dye penetrant and bend testing spaces, aligning with AWS, ASTM or CSWIP standards when applicable, with the primary motivation being a paired analysis of MAO-produced samples when compared to that of traditionally-produced material. In addition, geometric comparisons were made, focused on wall thickness deviation, straightness, magnitude of deviation from weld centerline and deviation symmetry. Lastly, waveform and frequency domain data was analyzed in both traditionally and MAO-produced processes for 316L wire electrode material, as well as brief exploration into out-of-scope processes, such as 2319 aluminum deposition.

By aligning with values found in literature (60) (61) (62) (63) and guidance from weld standards (56) (11) (12), mechanical equivalence to traditionally manufactured material was observed within this new process window, with noted deviations below.

Average Current

While largely dependent on the area of interest, a reduction in average welding current ($\leq 10A$) was observed across all sampled values, resulting in a reduction in average heat input of $\sim 6\%$ in the worst recorded case.

Process Modes

Particularly in parameter set 3 in Table 10.1, it was observed that, while these values aligned with the middle of the short-circuit parameter range outlined in the proposed research, as well as those found in literature (54), the chosen combination of wire feed speed and current produced a short-circuit transfer mode with the Miller Pipeworx 400 welding power supply used in the off-robot test configuration with a detachment frequency of $\sim 100Hz$, but a spray-transfer mode was observed in the on-robot test configuration utilizing a Fronius CMT Advanced 4000 power supply at a detachment frequency of $\sim 350Hz$. These values were recorded using the same feedstock and substrate material, shielding gas configuration and data collection techniques multiple times with the same outcome. While the introduction of oxygen into the shielding gas mixture was recommended by the electrode manufacturer (64) and will reduce the spray-transfer transition point in the GMAW process (65), this is well below expectations, indicating distinct differences in waveform generation and/or control strategies employed by the two power supply manufacturers. Supporting plots can be found in Appendices C, D.

11.2 Performance Related To Design Goals

This research successfully achieved its primary goal of the utilization of external magnetic field influence to maintain weaving profiles while negotiating historically difficult geometries within the wire arc additive manufacturing space, although some trade-offs in process parameters suggest further refinement is needed to develop parameter sets that more effectively leverage the additional control that this technology could provide.

11.3 Performance Related to Proposed Challenges and Risks

As discussed in Section 3.4, multiple challenges and risks were outlined and were segregated into hardware, controls and process-focused areas.

11.3.1 Hardware-Focused

Thermal Effects

In this research, thermal effects were largely mitigated by the utilization of aluminum heat shielding integrated into the mounting solutions for the electromagnets, as well as the design decision to use oversized magnet wire in the winding process. Future iterations could reduce the diameter of the magnet wire to a size suitable for the total input current ($\sim 3A$) and either reduce the overall footprint or integrate additional coil windings, resulting in potentially stronger magnetic fields. To date, the only failure directly attributed to thermal effects can be seen in Section 8.1.2, where the heat generated from the welding arc caused the FDM-manufactured accelerometer mount to deform.

Weld Spatter

Given that the electromagnet core material is both in close proximity to the melt pool and of a material that bonds well with the weld material, weld spatter continues to be a nuisance, and effort should be made in future iterations to shield the electromagnetic poles from the spatter, potentially by means of a non-ferrous cap. Current methods utilize polyamide high-temperature tape with limited success.

Packaging

Discussed in 11.4.1, packaging is a continuing concern, specifically around the integration of both MAO hardware and trailing gas support. Future iterations will realize a combined configuration of electromagnet and trailing gas systems into an integrated system.

11.3.2 Controls-Focused

Model Fidelity

Model fidelity continued to be a concern throughout this research, most notably due to the change in transfer modes of certain parameter sets when transitioning between different welding power supply manufacturers, discussed in 11.1. Due to the differences in welding characteristics between these transfer modes, model accuracy suffered. Future work will see increased data sets to better train the predictive modeling efforts in such a way that integrates different transfer modes and/or power supply manufacturers.

Magnet Control

While initial iterations used electromagnetic relay-type solutions, magnet control was ultimately handled by the utilization of off-the-shelf components geared towards the do-it-yourself CNC community and pulse-width-modulation, which proved to be a robust and serviceable solution.

Processor Speed

Processor speed proved to be more than adequate post transition from Arduino to RaspberryPi-based control logic, although updating control logic continued to be problematic and should be transitioned to an executable-based solution.

Signal Sensitivity

Outlined in 9.2.2 and 7.4, accelerometry signal sensitivity suffered both due to robot-related factors, such as system stiffness, as well as electrical noise generated by the welding hardware. Efforts should be made to identify the fundamental frequency of the robotic manipulator through "tap" testing or other efforts.

11.3.3 Process-Focused

Ferrous and Non-Ferrous Materials

To mitigate the effects of magnetic interaction with the hardware, nonferrous materials were used in components in close proximity to the magnetic hardware, particularly in heat shielding and mounting bracketry. In addition, aluminum riser material was used in weld tests to provide an additional level of isolation between the electromagnets and the steel welding fixture table in the on-robot experimental test configuration.

Process Transition

The transition from the GTAW welding process to the GMAW one brought with it unique challenges. While the expectation was that increased magnetic field strength would be required to deflect a welding arc in the GMAW space, a $\sim 300\%$ increase in field strength was needed to achieve meaningful deflection, also marking the saturation point of the electromagnets, albeit at a $\sim$ 50% lower input current than initially planned for. A combination of reduced wire diameter and an increased number of turns would more effectively use the overall footprint of the electromagnets and provide additional design margin in magnetic field density.

11.4 Limitations of Current Design

In engineering design, the first iteration of a potential solution is a critical step toward realizing a robust final implementation, but it is typically constrained by incomplete data, assumptions, and simplifications that later versions address. In this research, limitations can be categorized into the hardware, materials and modeling/controls spaces.

11.4.1 Hardware Limitations

Access Restrictions

Due to the increase in hardware footprint from the addition of the MAO hardware, access for both material deposition, as well as support hardware, such as trailing gas nozzles, is greatly hindered. In addition, the current design allows for minimal vertical clearance between the workpiece and the core of the electromagnets, demonstrated in Figure 11.1, further limiting effectiveness.

An iterated design could realize parallel electromagnets on either side of the welding electrode with a reduced winding wire diameter and improved clearance characteristics, and/or a monolithic design that incorporates programmatic trailing gas control hardware within it. Improved electromagnet pole geometry could be a short term solution to more desirable clearance between the substrate and electromagnetic hardware, illustrated in Figure 11.2.

Alignment Procedure

The current prototype mounting hardware design allows for multiple axes of linear and rotational adjustment for research and development purposes. Due to this, alignment of the individual components, outlined in Section 8.2, is a very time consuming and iterative process. A monolithic mounting solution could potentially reduce this significantly as well, at the expense of process and hardware flexibility.

11.4.2 Materials Limitations

As discussed in 10.3.7, this process is restricted to feedstocks and substrates that have limited magnetic permeability. While the scope of this research was limited to austenitic stainless steel materials, this process could be applied to bronze or aluminum deposition and is a potential area of future research, the efficacy of which has also been demonstrated in 10.3.7.



Figure 11.1: Demonstration of Substrate to Magnetic Pole Clearance

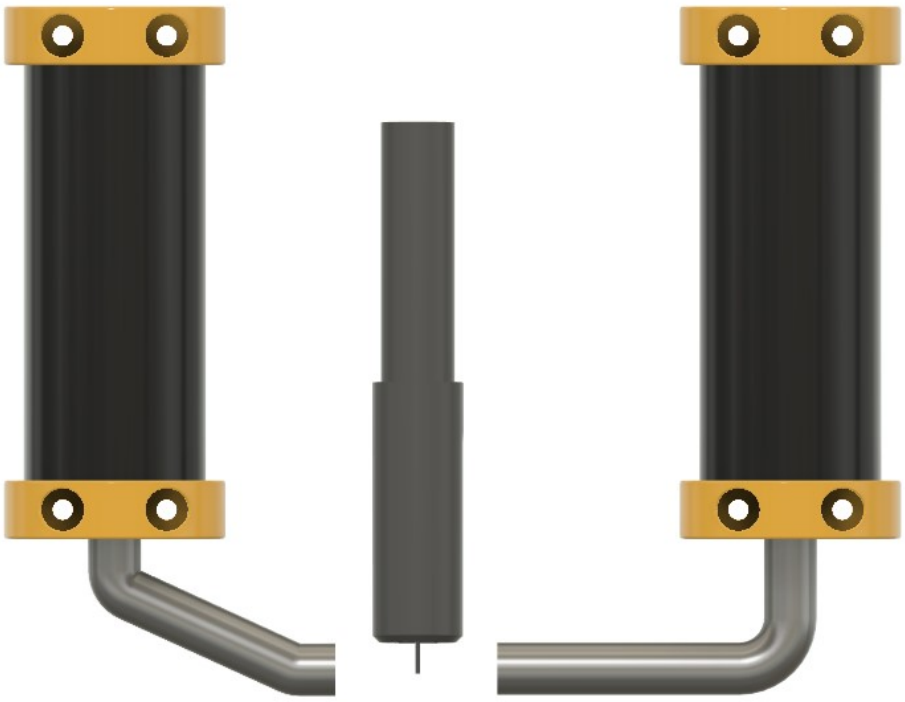


Figure 11.2: Comparison of Potential Magnetic Pole Redesign (Left) vs Current Geometry (Right) for Improved Substrate Clearance

11.4.3 Model and Controls Limitations

Model Limitations

While the predictive bead deflection model outlined in Section 5.2 was within design expectations for a first iteration, it is limited to short circuit transfer modes at 0.500" contact-tip-to-workpiece distance and fixed to 12 in/min weld velocity. Further refinement with increased parameter sets tailored to a desired welding power supply is necessary to better train the model. As outlined in Section 11.1, the control strategies and welding efficiencies of various power supplies have an effect on the transfer mode, and, thus, the characteristics of the welding arc. This leads to reduced prediction accuracy and should be an area of focus for future research by incorporating various transfer modes.

Control Limitations

While the Simulink simulation environment has proven invaluable for research and development by reducing time to implementation for control logic improvements and allowing for the simulation of a parameter set prior to hardware deployment, work should be done to transition the control strategy into a real-time executable format using languages such as C++ or Python. Doing so would aim to resolve issues faced when logic is deployed to the stand-alone control hardware and also potentially give the operator adjustability at the hardware level post-deployment.

11.5 Best Practices for MAO in WAAM

While positive results were seen throughout the course of this research, certain hardware and process limitations exist within the MAO-WAAM space and should be taken into consideration with future efforts.

11.5.1 Substrates and Feedstocks

As outlined throughout this research, as well as in Section 10.3.7, positive results were seen with both austenitic stainless steel materials, as well as aluminum substrates and feedstocks. Poor results, however, were observed with mild steel substrates, as seen in Section 10.3.7 and this technique would not be well-suited towards such processes.

11.5.2 Hardware

As seen in both the off-robot test configuration (Chapter 7), as well as the on-robot configuration (Chapter 8), non-ferrous assembly materials were utilized to limit magnetic interactions within the hardware and should be considered with future research endeavors. Furthermore, as seen in Section 8.1.2, polymer-based additively manufactured components should be limited in their use and heat shielding should be employed to increase the longevity of such parts. In addition, components should be monitored for heat accumulation throughout the build process.

11.5.3 Process

While measurable deflection was achieved with the short-circuit transfer mode, increased deflection was seen in the spray-transfer mode, outlined in Section 10.3.7. These parameters, however, are not well-suited to the WAAM process due to their increased heat input, therefore it is recommended to develop process parameters that both leverage the MAO technology within the WAAM space, as well as cater to the WAAM process, rather than act as additional hardware on top of existing process parameters. To this point, additional efforts should include solutions to control the position of trailing gas hardware in such a way that it can be reoriented throughout the changes in robot travel direction as it negotiates corner geometries.

Chapter 12

Conclusions and Future Work

This work saw the development of a Magnetic Arc Oscillation system within the Wire Arc Additive Manufacturing space. During this research, electromagnets were modeled, custom hardware was developed to manufacture them, modular hardware mounting solutions were adopted, test fixturing was designed and implemented, data acquisition systems were leveraged to better understand the process, weaving patterns and control logic were applied using PID and PWM control strategies, and material testing and analysis was performed, culminating in a final geometry that realized the initial goal of developing the ability to negotiate right-angles while performing an MAO-actuated weaved weld.

12.1 Contributions to Field

This research aided in setting the groundwork for integrating magnetic arc oscillation into the wire arc additive manufacturing space. By demonstrating the variation in bead geometry, heat inputs and overall process stability that can be expected from the introduction of external magnetic fields as an additional level of control, as well as the proven capability of the technology to negotiate historically difficult geometries in the space, future efforts can leverage this work to develop tailored parameter sets aimed towards better harnessing this utility.

12.2 Recommendations for Future Development

As outlined in 11.4, improvements could be made in the hardware, controls and modeling spaces. In particular, a monothithic design with integrated trailing gas directional control should be implemented, along with the migration of control logic to an executable platform, such as Python, for increased robustness in the model calibration and updating spaces. In addition, parameter sets should be optimized for the material, welding power supply and be tailored to the process.

Bibliography

[1] Z. Wang, G. Lu, C. Hu, S. Lin, X. Ren, J. Wu, and J. Tian, "A review on fast-frequency pulse tig welding technology," *Welding International*, vol. 36, pp. 510–521, 9 2022. doi: 10.1080/09507116.2022.2109448. xiii, 5

[2] S. Kou, *Welding Metallurgy*. Hoboken, NJ: Wiley-Interscience, 2003. xiii, 7, 9, 201

[3] H. Hong, Y. Han, M. Du, *et al.*, "Investigation on droplet momentum in vppa-gmaw hybrid welding of aluminum alloys," *International Journal of Advanced Manufacturing Technology*, vol. 86, pp. 2301–2308, 2016. xiii, 8, 39, 43

[4] M. Gupta and J. Davim, *Advanced Welding and Deforming*. Springer, 2011. xiii, 9, 10, 12, 13

[5] T. Kumar, D. V. Kiran, N. Arora, and P. S. Kumar, "Study of steel-aluminium joining under the influence of current waveforms using advanced cmt process variants," *Materials and Manufacturing Processes*, vol. 37, pp. 1578–1595, 10 2022. doi: 10.1080/10426914.2022.2030879. xiii, 13

[6] X. Wang, A. Wang, K. Wang, and Y. Li, "Process stability for gtaw-based additive manufacturing," *Rapid Prototyping Journal*, vol. 25, pp. 809–819, 8 2019. xiii, 1, 2, 6, 14, 15

[7] T. R. Larquer and R. P. Reis, *Gas Tungsten Arc Welding with Synchronized Magnetic Oscillation*. IntechOpen, 2016. xiii, 17, 18, 19, 20, 21

[8] X. Jian and H. Wu, "Influence of the longitudinal magnetic field on the formation of the bead in narrow gap gas tungsten arc welding," *Metals*, vol. 10, 2020. xiii, 17, 20, 21

[9] Y. Kang and S. NA, "Characteristics of welding and arc signal in narrow groove gas metal arc welding using electromagnetic arc oscillation," *Welding Journal*, vol. May, pp. 93–99, 2003. xiii, 20, 22

[10] M. M. Maricq, J. J. Szente, A. L. Harwell, and M. J. Loos, "Impact of aggressive drive cycles on motor vehicle exhaust pm emissions," *Journal of Aerosol Science*, vol. 113, pp. 1–11, 2017. xvi, 119

[11] American Welding Society, "AWS D1.6/D1.6M:2007 Structural Welding Code – Stainless Steel," Standard D1.6/D1.6M:2007, American Welding Society, Miami, FL, 2007. xviii, 130, 147, 149, 150, 157, 168, 170, 208

[12] The Welding Institute (TWI), "CSWIP 3.1: Welding Inspector – Certification Scheme for Welding and Inspection Personnel," 2023. Available at: https://www.cswip.com [Accessed: July 3, 2025]. xix, 130, 170, 182, 208

[13] L. P. Raut and R. V. Taiwade, "Wire arc additive manufacturing: A comprehensive review and research directions," *Journal of Materials Engineering and Performance*, vol. 30, pp. 4768–4791, 2021. 1, 2, 14

[14] R. Meredith, "Welding torch," 1941. 4

[15] C. Coffin, "Method of electric welding," 1 1890. 4

[16] J. F. Lancaster, *The Physics of Welding*. Oxford: Pergamon Press, 2nd ed., 1986. 5

[17] M. Goodarzi, R. Choo, T. Takasu, and J. Toguri, "The effect of the cathode tip angle on the gas tungsten arc welding arc and weld pool: Ii. the mathematical model for the weld pool," *Journal of Physics D: Applied Physics*, vol. 31, p. 569, 1 1999. 6

[18] W. Zhou, Q. Le, L. Ren, Y. Shi, Y. Jiang, and Q. Liao, "Effect of welding current and laves phase on the microstructures and mechanical properties of gtaw joints for zc63 magnesium alloy," *Materials Science and Engineering: A*, vol. 872, p. 144954, 2023. 6

[19] B.J., G. Seidu, S.O. Eghabor, and A. K. Ibitoye, "Review of gtaw welding parameters," *Journal of Minerals and Materials Characterization and Engineering*, vol. 6, pp. 541–554, 9 2018. 6

[20] L. Quintino, O. Liskevich, L. Vilarinho, and A. Scotti, "Heat input in full penetration welds in gas metal arc welding (gmaw)," *International Journal of Advanced Manufacturing Technology*, vol. 68, pp. 2833–2840, 10 2013. 6

[21] P. G. Jönsson, T. W. Eagar, and J. Szekely, "Heat and metal transfer in gas metal arc welding using argon and helium," *Metallurgical and Materials Transactions B*, vol. 26, pp. 383–395, Apr. 1995. 9

[22] G. Xu, J. Hu, and H. L. Tsai, "Three-dimensional modeling of the plasma arc in arc welding," *Journal of Applied Physics*, vol. 104, p. 103301, 11 2008. 12, 20

[23] H. Jahns, J. Unglaub, J. Müller, J. Hensel, and K. Thiele, "Material behavior of high-strength low-alloy steel (hsla) waam walls in construction," *Metals*, vol. 13, 2023. 12

[24] Z. Pan, D. Ding, B. Wu, D. Cuiuri, H. Li, and J. Norrish, "Arc welding processes for additive manufacturing: A review," 2018. 14

[25] J. Z. Li, M. R. Alkahari, N. A. B. Rosli, R. Hasan, M. N. Sudin, and F. R. Ramli, "Review of wire arc additive manufacturing for 3d metal printing," *International Journal of Automation Technology*, vol. 13, pp. 346–353, 2019. 14

[26] B. Wu, Z. Pan, D. Ding, D. Cuiuri, H. Li, J. Xu, and J. Norrish, "A review of the wire arc additive manufacturing of metals: properties, defects and quality improvement," *Journal of Manufacturing Processes*, vol. 35, pp. 127–139, 2018. 14

[27] Y. Li, C. Su, and J. Zhu, "Comprehensive review of wire arc additive manufacturing: Hardware system, physical process, monitoring, property characterization, application and future prospects," *Results in Engineering*, vol. 13, p. 100330, 2022. 14

[28] P. Sharma, S. Chattopadhyaya, N. K. Singh, A. Kumar, S. Sharma, C. Li, V. Kumar, S. Wojciechowski, G. Krolczyk, and S. M. Eldin, "Recent developments in the design, development, and analysis of the influence of external magnetic-field on gas-metal arc welding of non-ferrous alloys: review on optimization of arc-structure to enhance the morphology, and mechanical properties of welded joints for automotive applications," *Heliyon*, vol. 8, 12 2022. 17

[29] C. S. Wu, M. A. Chen, Y. F. Lu, L. A. Jones, T. W. Eagar, and J. H. Lang, "Magnetic forces acting on molten drops in gas metal arc welding," *Journal of Physics D: Applied Physics J. Phys. D: Appl. Phys*, vol. 31, pp. 93–106, 1998. 17

[30] Z. Qiu, B. Dong, B. Wu, Z. Wang, K. Carpenter, T. Wu, J. Zhang, D. Wexler, H. Zhu, and H. Li, "Tailoring the surface finish, dendritic microstructure and mechanical properties of wire arc additively manufactured hastelloy c276 alloy by magnetic arc oscillation," *Additive Manufacturing*, vol. 48, p. 102397, 2021. 17, 20

[31] H. Wu, Y. L. Chang, A. Babkin, and B. Lee, "The behavior of tig welding arc in a high-frequency axial magnetic field," *Welding in the World*, vol. 65, pp. 95–104, 2021. 17

[32] X. Yu, Y. C. Lim, R. Smith, S. S. Babu, D. F. Farson, J. C. Lippold, and S. McCracken, "Reducing hot cracking tendency of dissimilar weld overlay by magnetic arc oscillation," *Materials Science and Technology*, vol. 30, pp. 930–937, 7 2014. doi: 10.1179/1743284713Y.0000000358. 17, 20

[33] M. Electric, "Miller cyclomatic® magnetic oscillator," 2023. 20

[34] L. Electric, "Lincoln directarc™ magnetic arc control systems," 2023. 20

[35] K. INDUSTRY, "Magnetic oscillator om type," 6 2004. 20

[36] S. Sundaresan and G. D. J. Ram, "Use of magnetic arc oscillation for grain refinement of gas tungsten arc welds in – titanium alloys," *Science and Technology of Welding and Joining*, vol. 4, pp. 151–160, 6 1999. doi: 10.1179/136217199101537699. 20

[37] B. Wu, Z. Qiu, B. Dong, D. Wexler, Z. Pan, K. Carpenter, D. R. Corradi, and H. Li, "Effects of synchronized magnetic arc oscillation on microstructure, texture, grain boundary and mechanical properties of wire arc additively manufactured ti6al4v alloy," *Additive Manufacturing*, vol. 54, p. 102723, 2022. 20

[38] Y. C. Lim, X. Yu, J. H. Cho, J. Sosa, D. F. Farson, S. S. Babu, S. McCracken, and B. Flesner, "Effect of magnetic stirring on grain structure refinement part 2 – nickel alloy weld overlays," *Science and Technology of Welding and Joining*, vol. 15, pp. 400–406, 7 2010. doi: 10.1179/136217110X12720264008231. 20

[39] M. McCracken, X. Yu, Y. C. Lim, D. Farson, and S. Babu, "Grain structure refinement in nickel alloy welds by magnetic arc stirring," in *American Society of Mechanical Engineers, Pressure Vessels and Piping Division (Publication) PVP*, vol. 6, 4 2011. 20

[40] A. Kumar, P. Shailesh, and S. Sundarrajan, "Optimization of magnetic arc oscillation process parameters on mechanical properties of aa 5456 aluminum alloy weldments," *Materials Design*, vol. 29, pp. 1904–1913, 2008. 20

[41] L. Juliani, A. Bracarense, and P. Modenesi, "Study of the behavior of the electric arc in pulsed gmaw influenced by magnetic oscillation using shielding gas mixtures with different co2 content," *J Braz. Soc. Mech. Sci. Eng.*, vol. 43, p. 325, 2021. 20

[42] Y. Chang, X. Che, J. Li, *et al.*, "Effect of external magnetic field on droplet transfer mode and weld microstructure and properties of mig welding," *Welding*, vol. 10, pp. 25–28, 2008. 23

[43] S. Y. Jiang *et al.*, "The impact of adscititious longitudinal magnetic field on co2 welding process," *Advanced Materials Research*, vol. 538–541, pp. 1447–1450, 2012. 23

[44] C. Wu, F. Yang, and J. Gao, "Effect of external magnetic field on weld pool flow conditions in high-speed gas metal arc welding," *Proceedings of the Institution of Mechanical Engineers, Part B: Journal of Engineering Manufacture*, vol. 230, no. 1, pp. 188–193, 2014. 23

[45] L. Wang, Y. Ma, J. Xu, *et al.*, "Improving spread ability of molten metal in mig welding-brazing of aluminum to steel by external magnetic field," *Journal of Manufacturing Processes*, vol. 81, pp. 35–47, 2022. 23

[46] X. Wang, A. Harrison, Y. Chang, *et al.*, "Pinching arc plasmas by high-frequency alternating longitudinal magnetic field," *Physics of Plasmas*, vol. 29, no. 7, p. 73506, 2022. 23

[47] L. Cao, Q. Zhou, H. Liu, *et al.*, "Mechanism investigation of the influence of the magnetic field on the molten pool behavior during laser welding of aluminum alloy," *International Journal of Heat and Mass Transfer*, vol. 162, p. 120390, 2020. 23

[48] J. Yu, B. Wang, H. Zhang, *et al.*, "Characteristics of magnetic field assisting plasma gmaw-p," *Welding Journal*, vol. 99, no. 1, pp. 25–38, 2020. 23

[49] J. Yu, H. Zhang, X. Yang, *et al.*, "Arc characteristics and welding process of magnetic field assisting plasmagmaw-p," *Welding Journal*, vol. 100, no. 1, pp. 1S–12S, 2021. 23

[50] D. Lee, J. Silva, and M. C. et al, "A review on the prediction of droplet behavior in gas metal arc welding," *Science and Technology of Welding and Joining*, vol. 24, no. 1, pp. 2–10, 2019. 39

[51] Y. S. Kim, T. Eagar, *et al.*, "Analysis of metal transfer in gas metal arc welding," *WELDING JOURNAL-NEW YORK-*, vol. 72, pp. 269–s, 1993. 43

[52] Z. Zhu, W. Wu, and Q. Chen, "Random nature of droplet size and its origins in short circuit co2 arc welding," *Science and Technology of Welding and Joining*, vol. 10, no. 6, pp. 636–642, 2005. 43

[53] M. Mousavi Anzehaee and M. Haeri, "Estimation and control of droplet size and frequency in projected spray mode of a gas metal arc welding (gmaw) process," *ISA Transactions*, vol. 50, no. 3, pp. 409–418, 2011. 43

[54] D. B. Hoyos-Arango, O. L. Mejía-López, and J. E. Giraldo-Barrada, "Construction of a short circuit frequency map to define gmaw-s parameters during wpss development," *DYNA*, vol. 85, pp. 240–248, June 2018. 130, 209

[55] American Welding Society, "AWS D1.1/D1.1M:2020 – Structural Welding Code – Steel," 2020. ISBN: 978-1-64322-111-2. 130

[56] American Welding Society, "AWS B3.0: Welding Procedure and Performance Qualification," 1977. Historical standard; 44 pages. Originally published April 1, 1977. 130, 170, 208

[57] ASTM International, "ASTM E8/E8M-23: Standard Test Methods for Tension Testing of Metallic Materials," 2023. DOI: https://doi.org/10.1520/E0008_E0008M-23. 130

[58] H. Tasalloti, P. Kah, and J. Martikainen, "Effects of welding wire and torch weaving on gmaw of s355mc and aisi 304l dissimilar welds," *The International Journal of Advanced Manufacturing Technology*, vol. 71, no. 1–4, pp. 197–205, 2014. 170

[59] L. Andersen, "Heat input & interpass temperature during welding." https://teandersen.com/uploads/rDh63ZFc/technical_update_heat_input_and_interpass_temperature_during_welding.pdf, n.d. TE Andersen Consulting, accessed July 2025. 201

[60] X. Zhao, S. Li, M. Zhang, Y. Liu, T. Sercombe, S. Wang, and Y. Hao, "Research on mechanical properties and microstructure by selective laser melting of 316l stainless steel," *Materials Research Express*, vol. 6, no. 12, p. 1265a5, 2019. 208

[61] B. Barkia, P. Aubry, P. Haghi-Ashtiani, T. Auger, L. Gosmain, F. Schuster, and H. Maskrot, "On the origin of the high tensile strength and ductility of additively manufactured 316l stainless steel: Multiscale investigation," *Journal of Materials Science & Technology*, vol. 41, pp. 209–218, 2020. 208

[62] X. Zhang, Y. Chen, and F. W. Liou, "Fabrication of ss316l–in625 functionally graded materials by powder-fed directed energy deposition," *Science and Technology of Welding & Joining*, vol. 24, no. 5, pp. 504–516, 2019. 208

[63] C. Wang, T. G. Liu, P. Zhu, Y. H. Lu, and T. Shoji, "Study on microstructure and tensile properties of 316l stainless steel fabricated by cmt wire and arc additive manufacturing," *Materials Science and Engineering A*, vol. 796, p. 140006, 2020. 208

[64] Lincoln Electric, "Blue max 316l mig welding wire (er316/316l)." https://ch-delivery.lincolnelectric.com/api/public/content/4f1b2b39fcc84d1fbf24c691c148ce4a?v=63c841c3, n.d. Datasheet accessed July 2025. 209

[65] Lincoln Electric, "Gas metal arc welding: Carbon, low alloy, and stainless steels and aluminum." https://static.gasandsupply.com/docs/LIN_c4200.pdf, n.d. Accessed July 2025. 209

Appendix A

Block Diagrams

The following block diagrams were produced using Matlab Simulink software intended for deployment to system control hardware. The system consists of multiple subsystems in which signals are bussed from subsystem to subsystem for cleanliness and ease of calibration. A flow chart of signal development can be seen in Figure 9.18.

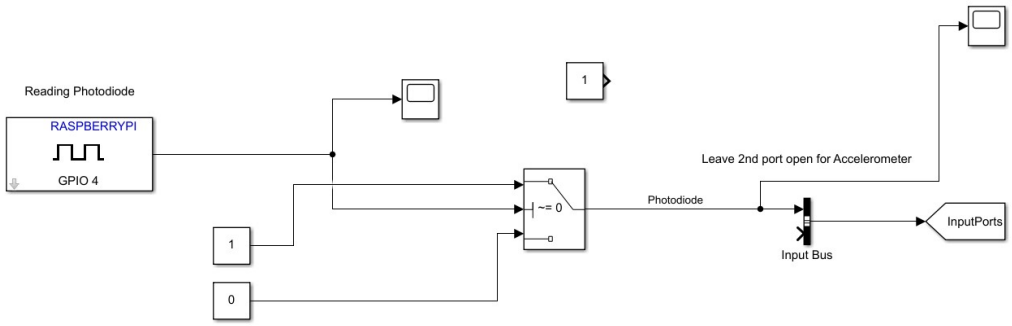


Figure A.1: Simulink Signal Input Block Diagrams

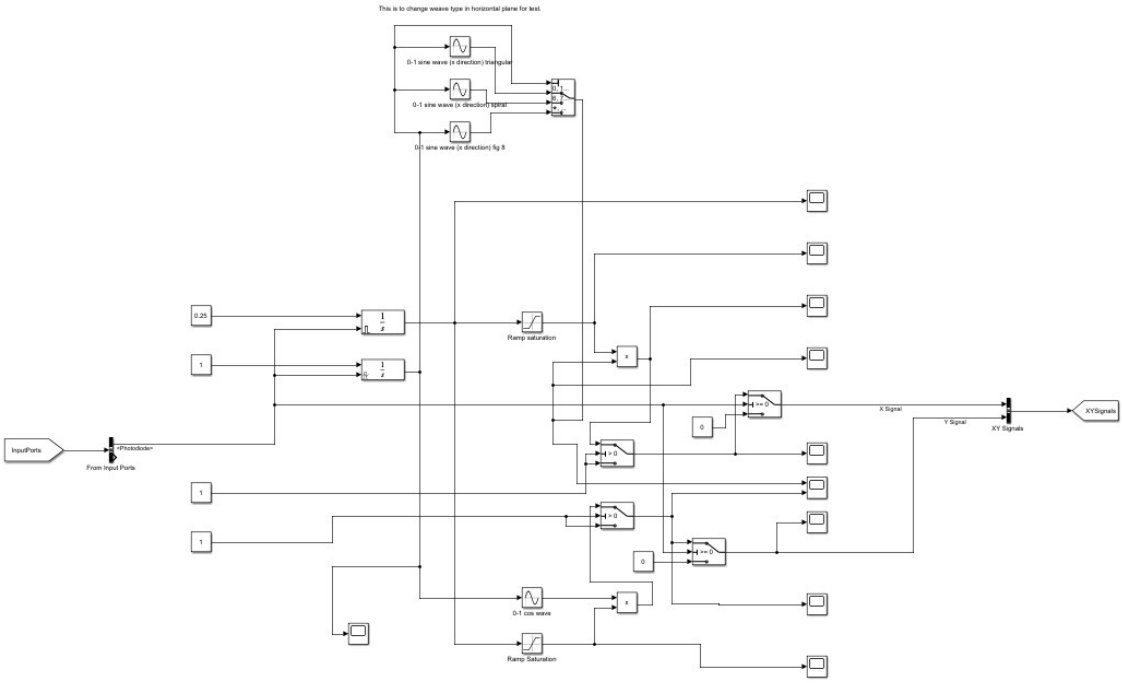


Figure A.2: X and Y Signal Development Block Diagram

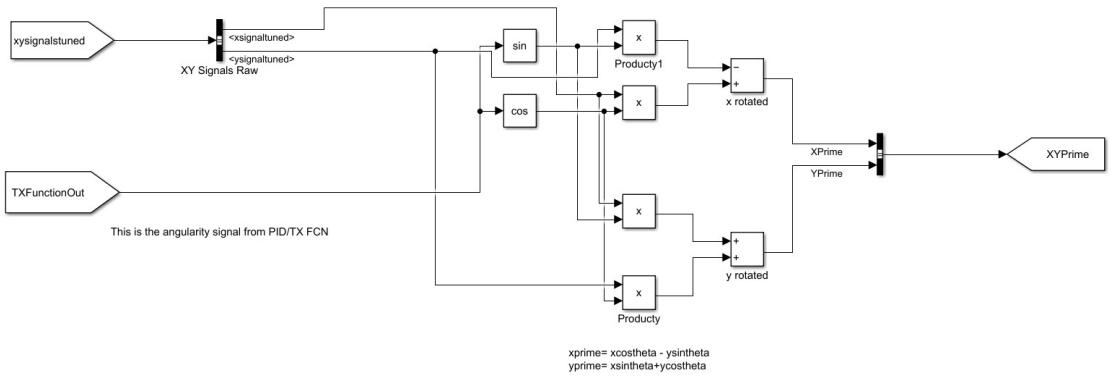


Figure A.3: Travel Direction Adaptation Block Diagram

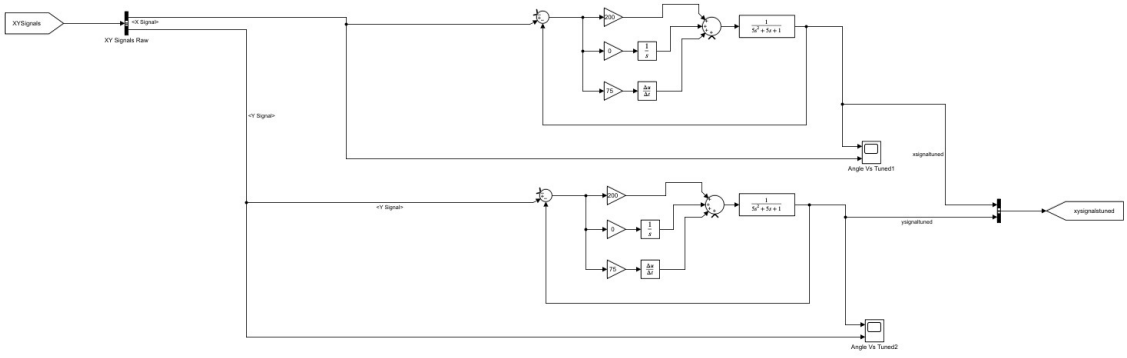


Figure A.4: Response Tuning Block Diagram

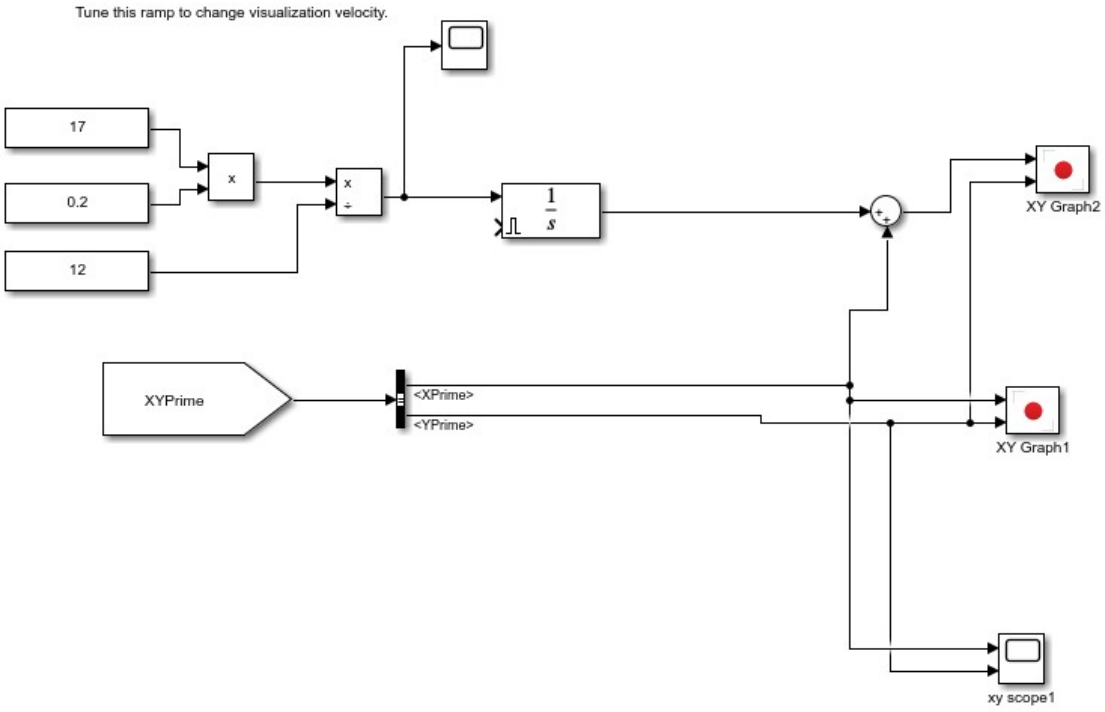


Figure A.5: Signal Visualization Block Diagram

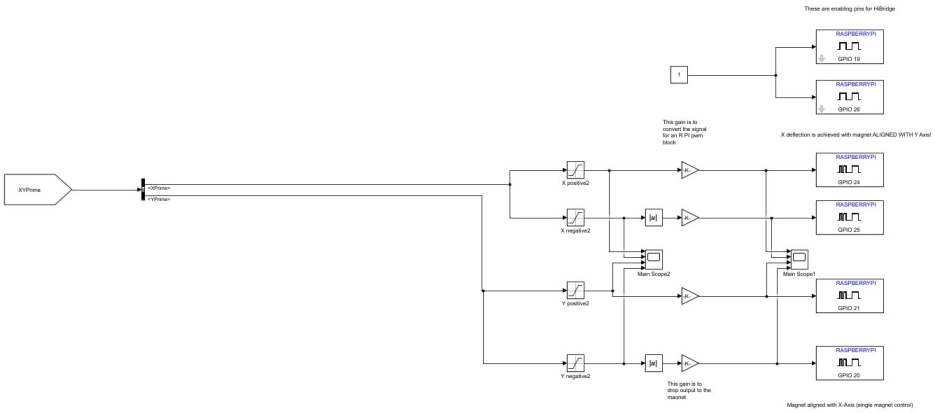


Figure A.6: Simulink Signal Output Block Diagram

Appendix B

Matlab Scripts

B.1 Predictive Bead Deflection Model

The following script was produced in MATLAB R2022a:

```
clear; clc; close all;

x_fit = [0, 0.5, 1, 1.5, 2, 2.5, 3, 3.5, 4, 4.5];

x_dense = linspace(min(x_fit), max(x_fit), 100);

y_sets = {
    [0, 0.044, 0.078, 0.073, 0.095, 0.102, 0.098, 0.095, 0.097,
       0.095],
    [0, 0.036, 0.087, 0.112, 0.13, 0.139, 0.142, 0.148, 0.155,
       0.159],
    [0, 0.031, 0.091, 0.124, 0.144, 0.155, 0.165, 0.169, 0.169,
       0.148],
    [0, 0.053, 0.108, 0.163, 0.205, 0.195, 0.222, 0.225, 0.236,
       0.226],
    [0, 0.031, 0.085, 0.134, 0.152, 0.187, 0.2, 0.196, 0.197, 0.21]
```

```
};

% Polynomial degree
degree = 3;

% Offsets for each curve (along y-axis)
weldingpower = [84*18, 127*21, 159*22, 203*24, 226*24];

if length(weldingpower) ~= length(y_sets)
    error('Offsets length must match y_sets');
end

desiredweldingcurrent = input('Please enter the desired welding
   current in Amps (between 85 and 225A)  ');
desiredweldingvoltage = input('Please enter the desired welding
   voltage in Volts (between 18 and 24V)  ');

desiredweldingpower = desiredweldingcurrent*desiredweldingvoltage;

if desiredweldingpower < 1550 || desiredweldingpower > 5400
    error('Welding Parameter Mismatch! Desired welding power must be
       between 1550 and 5400 Watts. Please check desired parameter
       set!');
end

desiredtime = input('Please enter the desired oscillation frequency
   in Hz: ');
desiredtime = (1/desiredtime)/4;

if desiredtime < min(x_dense) || desiredtime > max(x_dense)
```

```
38      error('Desired time must be between %.2f and %.2f seconds', min(
            x_dense), max(x_dense));
39  end
40
41  [X, Y] = meshgrid(x_dense, weldingpower);  % X: x-axis, Y: offset (
        curve index)
42
43  Z = zeros(size(Y));
44
45  figure;
46  hold on;
47  grid on;
48  view(-33, 30);
49  camproj('perspective');
50  colors = lines(length(y_sets));
51
52  for i = 1:length(y_sets)
53      y = y_sets{i};
54      [p, S, mu] = polyfit(x_fit, y, degree);
55      y_fit_dense = polyval(p, x_dense, S, mu);
56      Z(i, :) = y_fit_dense;
57
58
59      alpha_val = 0.7;
60      bg_color = [1 1 1];
61      line_color = (1 - alpha_val) * bg_color + alpha_val * colors(i
            ,:);
62      plot3(x_dense, weldingpower(i) * ones(size(x_dense)),
            y_fit_dense, ...
63      'Color', line_color, 'LineWidth', 2);
```

```
end

y_interp = zeros(size(x_dense));
for j = 1:length(x_dense)
    y_interp(j) = interp1(weldingpower, Z(:, j), desiredweldingpower
        , 'linear');
end


plot3(x_dense, desiredweldingpower * ones(size(x_dense)), y_interp,
    ...
    'k--', 'LineWidth', 3);


surf(X, Y, Z, 'EdgeColor', 'none', 'FaceAlpha', 1.0);
shading interp;  % Interpolate colors across faces

colormap(jet);

Z_min = min(Z, [], 'all');
Z_max = max(Z, [], 'all');
caxis([min(Z(:)), max(Z(:))]);


cb = colorbar;
ylabel(cb, 'Deflection␣(in)');

[~, time_idx] = min(abs(x_dense - desiredtime));
highlight_x = x_dense(time_idx);
highlight_y = desiredweldingpower;
```

```
highlight_z = y_interp(time_idx);

plot3(highlight_x, highlight_y, highlight_z, 'ro', 'MarkerFaceColor'
    , 'r', 'MarkerSize', 8);

disp(['The deflection at time = ' num2str(desiredtime) ' seconds is:
    ' num2str(highlight_z)]);

total_deflection = 2 * highlight_z;
disp(['The total predicted centerline deflection is: ' num2str(
    total_deflection)]);

xlabel('Time (s)');
ylabel('Welding Power (W)');
zlabel('Deflection (in)');
title('GMAW Weld Centerline Deflection Process Map');

xlim([min(x_dense), 4.5]);
ylim([min(weldingpower), max(weldingpower)]);
zlim([0, max(Z, [], 'all') + 0.05]);

legend('Parameter Set 1','Parameter Set 2','Parameter Set 3','
    Parameter Set 4','Parameter Set 5','Predicted Centerline
    Deflection', ...
        'Location', 'northwest');
```

Listing B.1: Predicted Bead Deflection Model Script

B.2 Wire Turn Estimation Script

```
1
2 % used to calculate the number of turns and OD given a specific
     length of
3 % core. Based on using an iron core.
4
5 clc
6 clear all
7
8 %% define variables
9
10 mu= 2.5*10^-1; %for iron
11 muzero= 4*pi*10^-7; %for air
12 corelength= 6; %in
13 gaplength= 0.25; %in
14 I= 5.2; %Amps. = Ampacity rating for 16 awg wire
15 Fstrength= 150*10^-4; %field strength in gauss converted to Tesla
16
17 %% Calculate number of turns needed in 6" core length
18
19 Nturns=(Fstrength*((corelength/mu)+(gaplength/muzero))/I)
20
21 % core length doesn't have much effect on number of turns (<1 turn
22 % difference)
23
24 %% Calculate field strength based on 662 turns of wire seen from 1.5
     lbs of magnet wire
25
26 I_662_turns=(Fstrength*((corelength/mu)+(gaplength/muzero))/662)
27
28 %% Approximate dimensions of spool given weight of copper wire used.
```

```
% Copper supplied in 1.5lb spool, so using this as starting point.
   Will need to relate this to number of turns in the future.

Dcopper = 0.324 %density of copper in lb/in^3
ID = 0.625 %in
Spoollength= 4 %in
Wcopper = 1.5 %lbs

%% calculate dimensions of copper as a solid
ODsolid= 2*sqrt(((((Dcopper^-1)*Wcopper)/Spoollength)+(pi*(ID/2)^2))
   /pi)

Douter= 2*(sqrt((Wcopper/(Dcopper*pi*Spoollength)+(ID/2)^2)))


%% calculate dimensions based on packing density of 0.48

packingdensity= 0.48


odcorrected= ODsolid*(1/packingdensity)

%% "practical method" from spooling company

TotalLengthofWeight= ((Dcopper^-1*Wcopper)/(pi*(0.051/2)^2))/12 %in
   feet

D=0.051; %in
ODpractical=1.3654;

```

```
56
57 n= (0.95*Spoollength)/D;
58 p=(ODpractical-ID-0.2*D)/(1.8*D);
59
60 TotalLength= (pi*p*n*(ID+D+(0.9*D*p)))/12 %in feet
61
62 %% relating number of turns to wire length if assuming total
      diameter (for checking)
63
64 Turnlength= (Nturns*(pi*1.45))/12
```

Listing B.2: Wire Turn Calculation Script for Magnetic Bobbin

B.3 Data Plotting

```
1
2 % MATLAB script to read a CSV file and create separate subplots
3 %D. Goodspeed 01.23.2025
4 clc
5 clear all
6
7 [file, path] = uigetfile('*.csv', 'Select a CSV file');
8
9 if isequal(file, 0)
10     disp('No file selected. Exiting script.');
11     return;
12 end
13
14 filePath = fullfile(path, file);
15
```

```
data = readtable(filePath);

if width(data) < 3
    disp('The CSV file must have at least three columns.');
    return;
end

x = data{:, 1};  % First column (x-axis values in ms)
y2 = data{:, 2}; % Second column (Voltage)
y3 = data{:, 3}; % Third column (Current)



y2 = (((4.84/1024) * y2) * 21)-2.3408;
y3 = y3 %* (3/20);

rmsVoltage = sqrt(mean(y2.^2));
disp(['RMS Voltage: ', num2str(rmsVoltage), ' V']);

rmsCurrent = sqrt(mean(y3.^2));
disp(['RMS Current: ', num2str(rmsCurrent), ' A']);

figure;

subplot(5, 1, 1);
plot(x, y2, '-r', 'DisplayName', 'Voltage');
xlabel('Time (ms)');
ylabel('Voltage');
title('Voltage vs Time');
grid on;
```

```
46 legend;
47
48 subplot(5, 1, 2);
49 plot(x, y3, '-b', 'DisplayName', 'Current');
50 xlabel('Time (ms)');
51 ylabel('Current (Amps)');
52 title('Current vs Time');
53 grid on;
54 legend;
55
56 % Plot the Fast Fourier Transform (FFT) of y2 in the third subplot
57 subplot(5, 1, 3);
58
59 N = length(y2);
60 x_seconds = x / 1000;
61
62 Y2 = fft(y2);  % FFT of Voltage
63 Y3 = fft(y3);  % FFT of Current
64
65 Y2 = Y2 / N;
66 Y3 = Y3 / N;
67
68 Fs = 1 / (x_seconds(2) - x_seconds(1));
69 f = (0:N-1) * (Fs / N);
70
71 f_max = 1000;
72 f_limit = f(f <= f_max);
73
74 subplot(5, 1, 3);
```

```
plot(f_limit, abs(Y2(1:length(f_limit))), '-r', 'DisplayName', 'FFT of Voltage');
xlabel('Frequency (Hz)');
ylabel('Magnitude');
title('FFT of Voltage (0-1000 Hz)');
xlim([0 f_max]);
grid on;
legend;

subplot(5, 1, 4);

plot(f_limit, abs(Y3(1:length(f_limit))), '-b', 'DisplayName', 'FFT of Current');
xlabel('Frequency (Hz)');
ylabel('Magnitude');
title('FFT of Current (0-1000 Hz)');
xlim([0 f_max]);
grid on;
legend;

power = y2 .* y3;

subplot(5, 1, 5);
plot(x, power, '-g', 'DisplayName', 'Power');
xlabel('Time (ms)');
ylabel('Power (W)');
title('Power vs Time');
grid on;
legend;

```

```
currentDateTime = datetime('now', 'Format', 'yyyy-MM-dd HH:mm:ss');
sgtitle([file ' - ' char(currentDateTime)]);
```

Listing B.3: CSV Plotting Matlab Script

```

%D.Goodspeed 2025
% Used to interpret Miller LEM data and plot values. Will ask user
    for
% desired time intervals

[filename, pathname] = uigetfile('*.csv', 'Select a CSV file');
if isequal(filename, 0)
    error('No file selected.');
end

filePath = fullfile(pathname, filename);
data = readmatrix(filePath);

if size(data, 2) < 7
    error('CSV must have at least 7 columns.');
end

data(:, 5) = data(:, 5) * 10;
data(:, 7) = data(:, 7) * 100;

numRows = size(data, 1);
dt = 5e-5;
t = (0:numRows-1)' * dt;

figure(1);
```

```
plot(t, data(:,5), 'b');
xlabel('Time (s)');
ylabel('Voltage (V)');
title('Voltage vs Time');
grid on;
hold on;

figure(2);
plot(t, data(:,7), 'r');
xlabel('Time (s)');
ylabel('Current (A)');
title('Current vs Time');
grid on;
hold on;

disp('Review the plots, then enter two time ranges for analysis.');
pause(0.5);

range1 = input('Enter FIRST time range as [start end] in seconds (e.
    g., [0.01 0.05]): ');
range2 = input('Enter SECOND time range as [start end] in seconds (e
    .g., [0.10 0.15]): ');
intervals = [range1; range2];

for i = 1:2
    t_start = intervals(i,1);
    t_end = intervals(i,2);

    figure(1);
    yLimits = ylim;
```

```
54      fill([t_start t_end t_end t_start], [yLimits(1) yLimits(1)
            yLimits(2) yLimits(2)], ...
55          'cyan', 'FaceAlpha', 0.2, 'EdgeColor', 'none');
56
57      figure(2);
58      yLimits = ylim;
59      fill([t_start t_end t_end t_start], [yLimits(1) yLimits(1)
            yLimits(2) yLimits(2)], ...
60          'magenta', 'FaceAlpha', 0.2, 'EdgeColor', 'none');
61  end
62
63  fft_f = cell(2, 1);
64  fft_mag_voltage = cell(2, 1);
65  fft_mag_current = cell(2, 1);
66  seg_t = cell(2,1);
67  seg_voltage = cell(2,1);
68  seg_current = cell(2,1);
69
70  for i = 1:2
71      t_start = intervals(i,1);
72      t_end = intervals(i,2);
73      idx = find(t >= t_start & t <= t_end);
74
75      seg_t{i} = t(idx);
76      seg_voltage{i} = data(idx, 5);
77      seg_current{i} = data(idx, 7);
78
79      figure;
80      plot(seg_t{i}, seg_voltage{i}, 'b');
81      xlabel('Time␣(s)');
```

```
    ylabel('Voltage (V)');
    title(sprintf('Voltage in Interval %d [%.4f    %.4f s]', i,
        t_start, t_end));
    grid on;

    figure;
    plot(seg_t{i}, seg_current{i}, 'r');
    xlabel('Time (s)');
    ylabel('Current (A)');
    title(sprintf('Current in Interval %d [%.4f    %.4f s]', i,
        t_start, t_end));
    grid on;

    mean_voltage = mean(seg_voltage{i});
    mean_current = mean(seg_current{i});

    N = length(idx);
    Nfft = 2^nextpow2(N);
    Fs = 1 / dt;

    fft_voltage = fft(seg_voltage{i}, Nfft);
    fft_current = fft(seg_current{i}, Nfft);
    f = Fs * (0:Nfft/2-1) / Nfft;

    mag_voltage = abs(fft_voltage(1:Nfft/2));
    mag_current = abs(fft_current(1:Nfft/2));

    fft_f{i} = f;
    fft_mag_voltage{i} = mag_voltage;
    fft_mag_current{i} = mag_current;
```

```
110
111     freq_mask = (f >= 2 & f <= 500);
112
113     figure;
114     subplot(2,1,1);
115     plot(f(freq_mask), mag_voltage(freq_mask), 'b');
116     xlabel('Frequency (Hz)');
117     ylabel('|FFT Voltage (V)|');
118     title(sprintf('FFT of Voltage - Interval %d [%.4 f  %.4f s]', i,
            t_start, t_end));
119     grid on;
120
121     subplot(2,1,2);
122     plot(f(freq_mask), mag_current(freq_mask), 'r');
123     xlabel('Frequency (Hz)');
124     ylabel('|FFT Current (A)|');
125     title(sprintf('FFT of Current - Interval %d [%.4 f  %.4f s]', i,
            t_start, t_end));
126     grid on;
127
128     fprintf('\nInterval %d (%.6f s to %.6f s):\n', i, t_start, t_end
          );
129     fprintf('Mean Voltage: %.4f V\n', mean_voltage);
130     fprintf('Mean Current: %.4f A\n', mean_current);
131 end
132
133 figure;
134 hold on;
135 for i = 1:2
136     freq_mask = (fft_f{i} >= 2 & fft_f{i} <= 500);
```

```
    plot(fft_f{i}(freq_mask), fft_mag_voltage{i}(freq_mask), ...
        'DisplayName', sprintf('Interval %d', i));
end
xlabel('Frequency (Hz)');
ylabel('|FFT Voltage (V)|');
title('Overlay FFT of Voltage - Interval 1 vs 2');
legend;
grid on;

figure;
hold on;
for i = 1:2
    freq_mask = (fft_f{i} >= 2 & fft_f{i} <= 500);
    plot(fft_f{i}(freq_mask), fft_mag_current{i}(freq_mask), ...
        'DisplayName', sprintf('Interval %d', i));
end
xlabel('Frequency (Hz)');
ylabel('|FFT Current (A)|');
title('Overlay FFT of Current - Interval 1 vs 2');
legend;
grid on;

aligned_t1 = seg_t{1} - seg_t{1}(1);
aligned_t2 = seg_t{2} - seg_t{2}(1);

figure;
plot(aligned_t1, seg_voltage{1}, 'b', 'DisplayName', 'Interval 1');
hold on;
plot(aligned_t2, seg_voltage{2}, 'r', 'DisplayName', 'Interval 2');
xlabel('Aligned Time (s)');
```

```
ylabel('Voltage (V)');
title('Aligned Overlay of Voltage - Interval 1 vs 2');
legend;
grid on;

figure;
plot(aligned_t1, seg_current{1}, 'b', 'DisplayName', 'Interval 1');
hold on;
plot(aligned_t2, seg_current{2}, 'r', 'DisplayName', 'Interval 2');
xlabel('Aligned Time (s)');
ylabel('Current (A)');
title('Aligned Overlay of Current - Interval 1 vs 2');
legend;
grid on;
```

Listing B.4: Frequency Analysis Matlab Script

Appendix C

Supplementary 316L Welding Waveform Data - Fronius CMT4000 Power Supply

C.1 220ipm 14.3V case

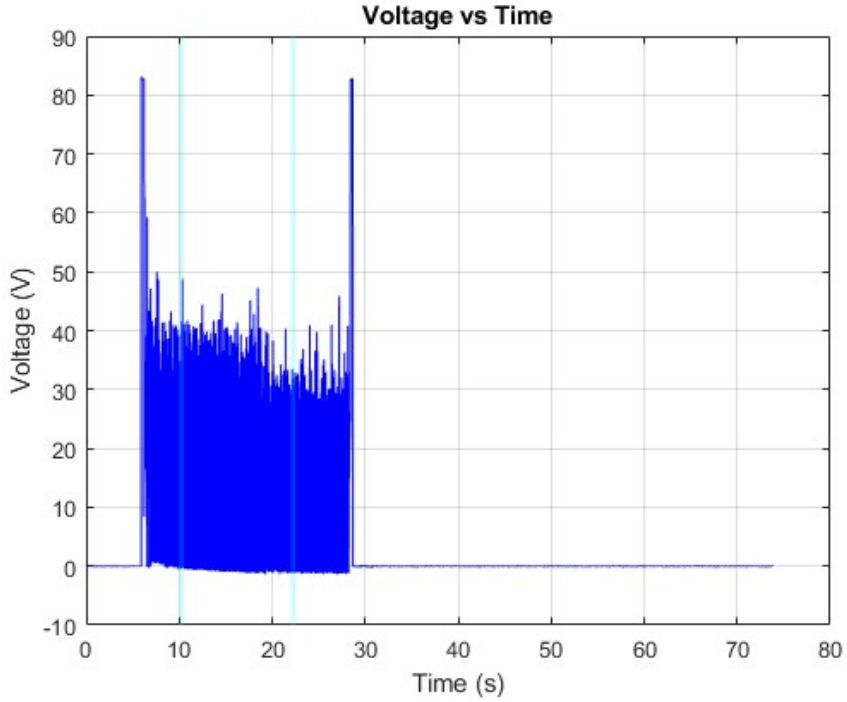


Figure C.1: Voltage vs Time (Area of Interest Highlighted) for 220ipm/14.3V Case

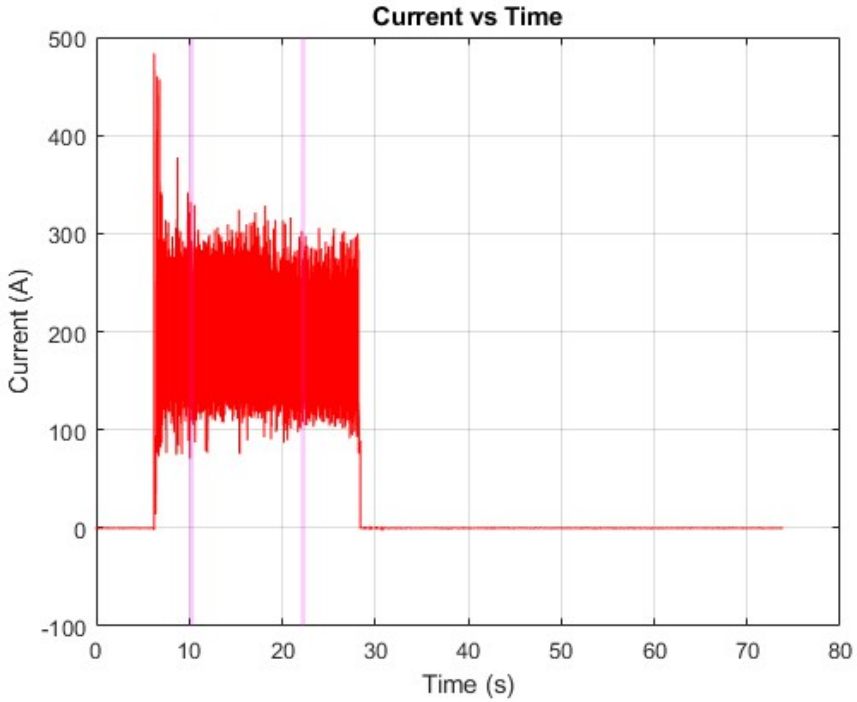


Figure C.2: Current vs Time (Area of Interest Highlighted) for 220ipm/14.3V Case

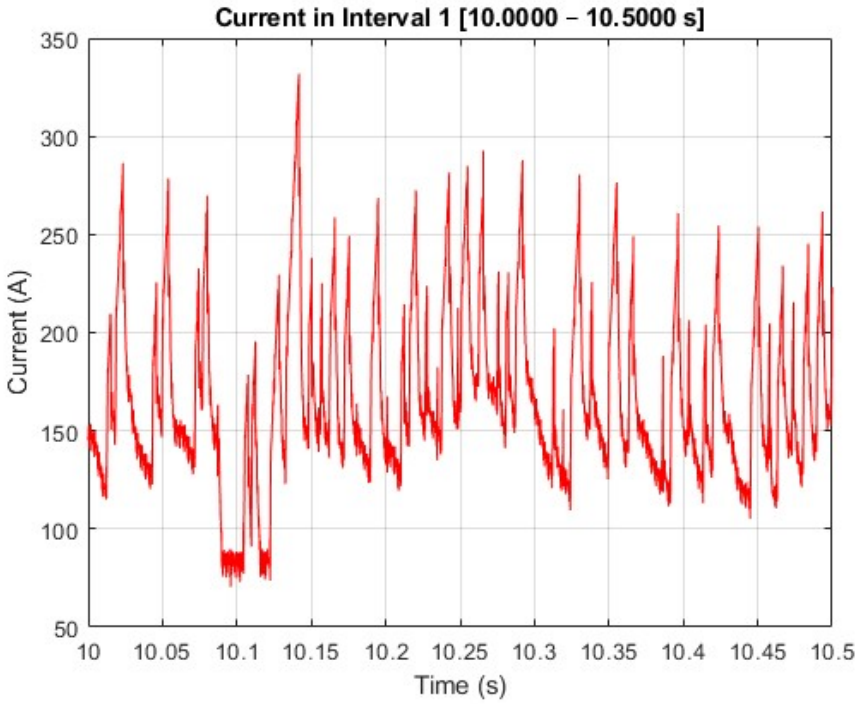


Figure C.3: MATLAB Current Output for 220ipm/14.3V Case in Interval 1

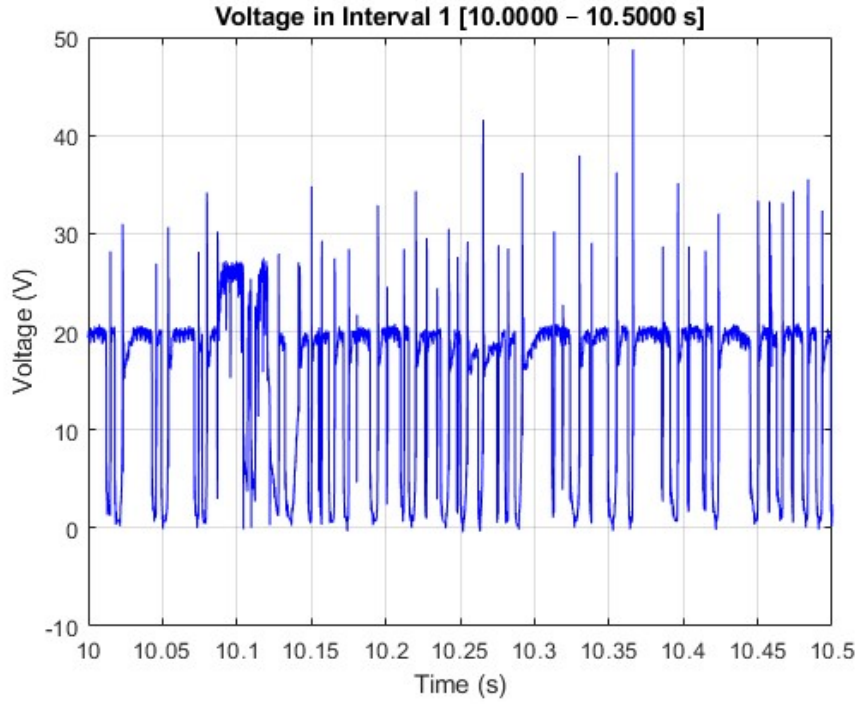


Figure C.4: MATLAB Voltage Output for 220ipm/14.3V Case in Interval 1

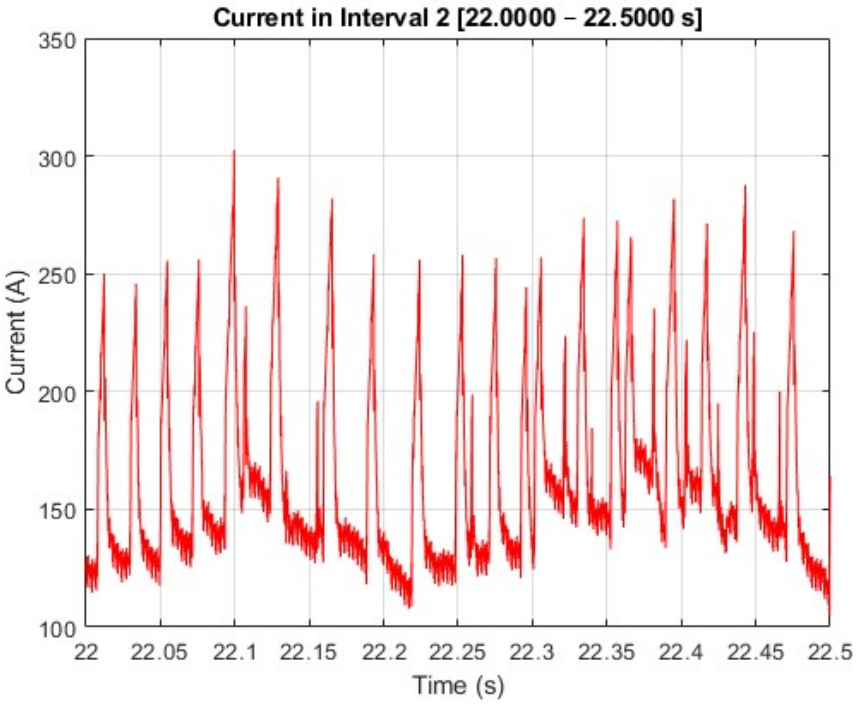


Figure C.5: MATLAB Current Output for 220ipm/14.3V Case in Interval 2

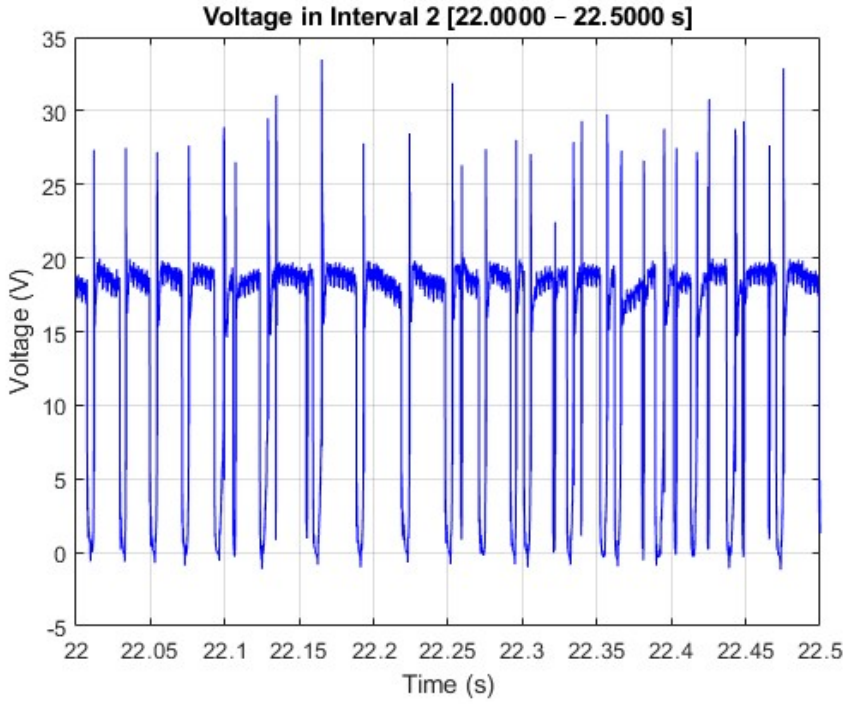


Figure C.6: MATLAB Voltage Output for 220ipm/14.3V Case in Interval 2

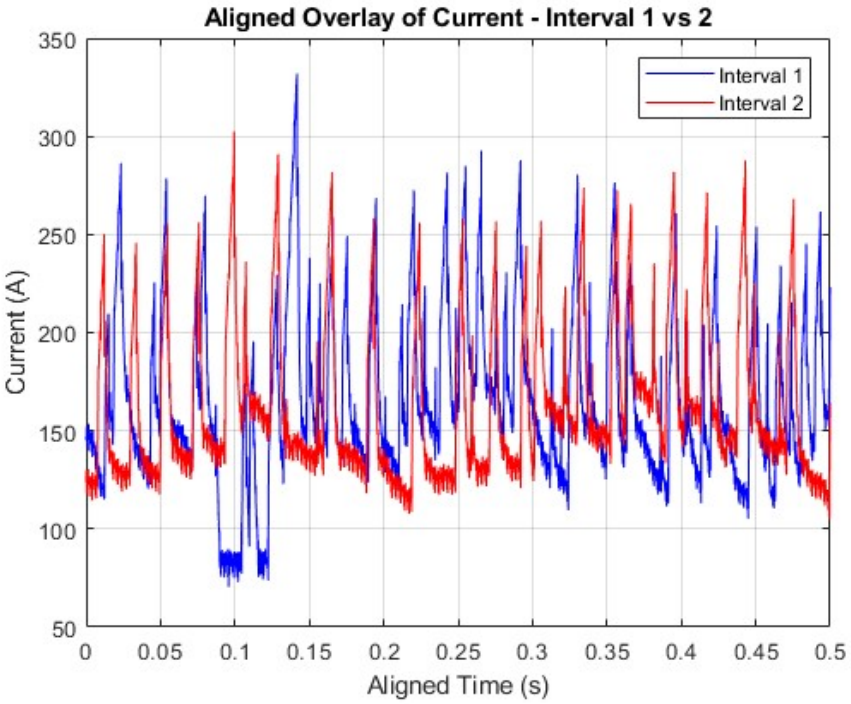


Figure C.7: MATLAB Overlaid Current Output for 220ipm/14.3V Case

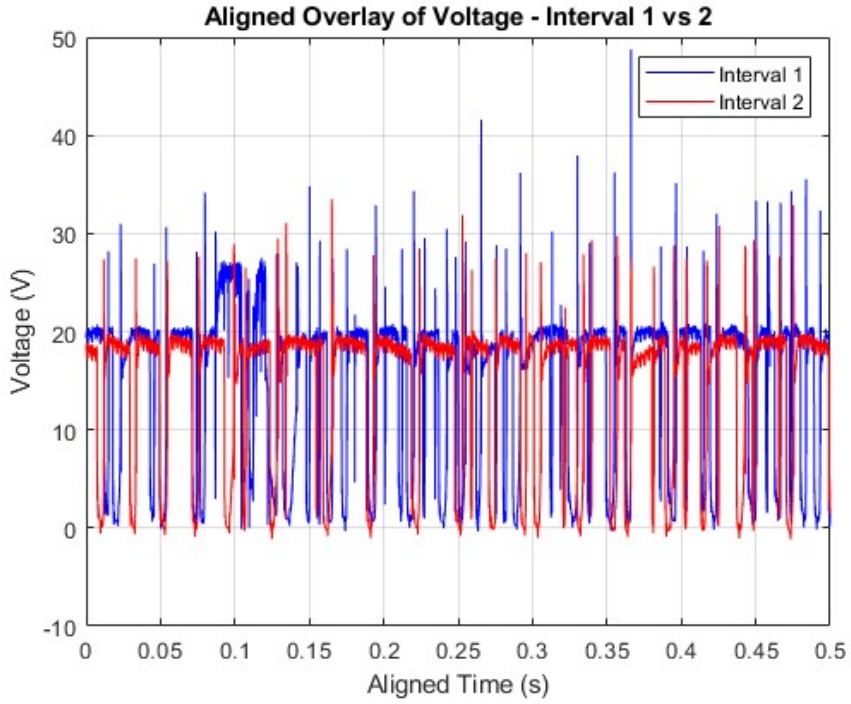


Figure C.8: MATLAB Overlaid Voltage Output for 220ipm/14.3V Case

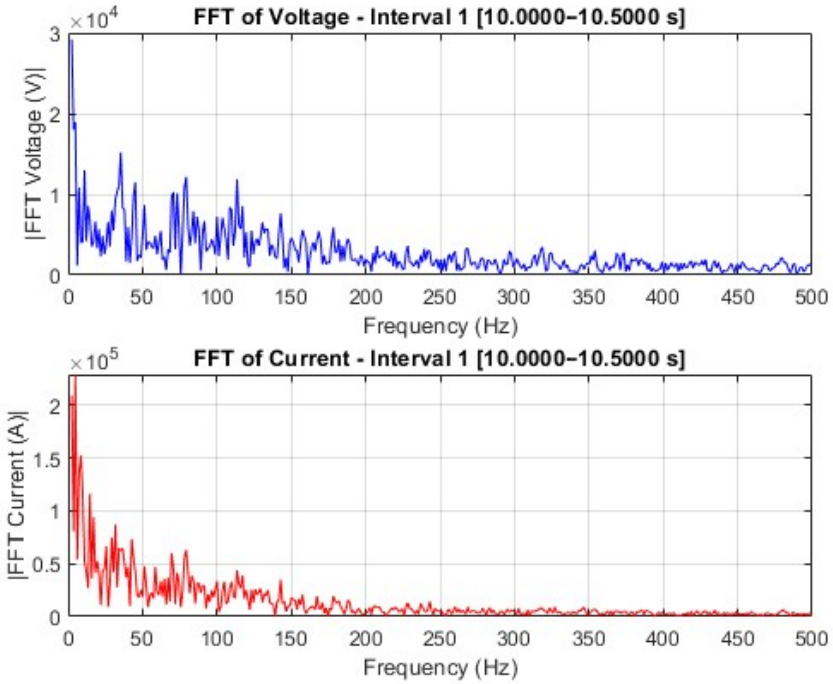


Figure C.9: MATLAB FFT Plot for Interval 1 in 220ipm/14.3V Case

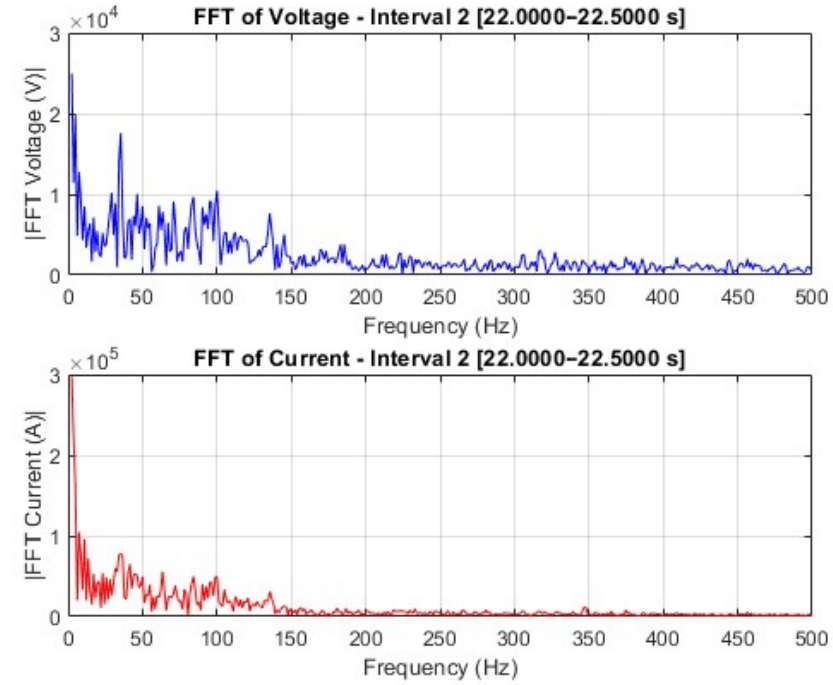


Figure C.10: MATLAB FFT Plot for Interval 2 in 220ipm/14.3V Case

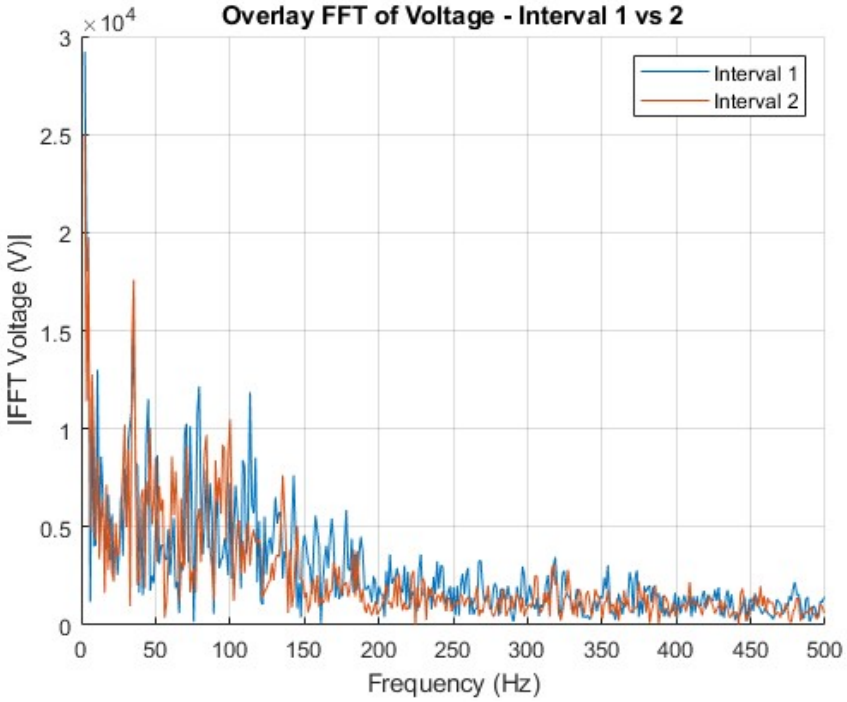


Figure C.11: MATLAB Voltage FFT Overlaid for 220ipm/14.3V Case

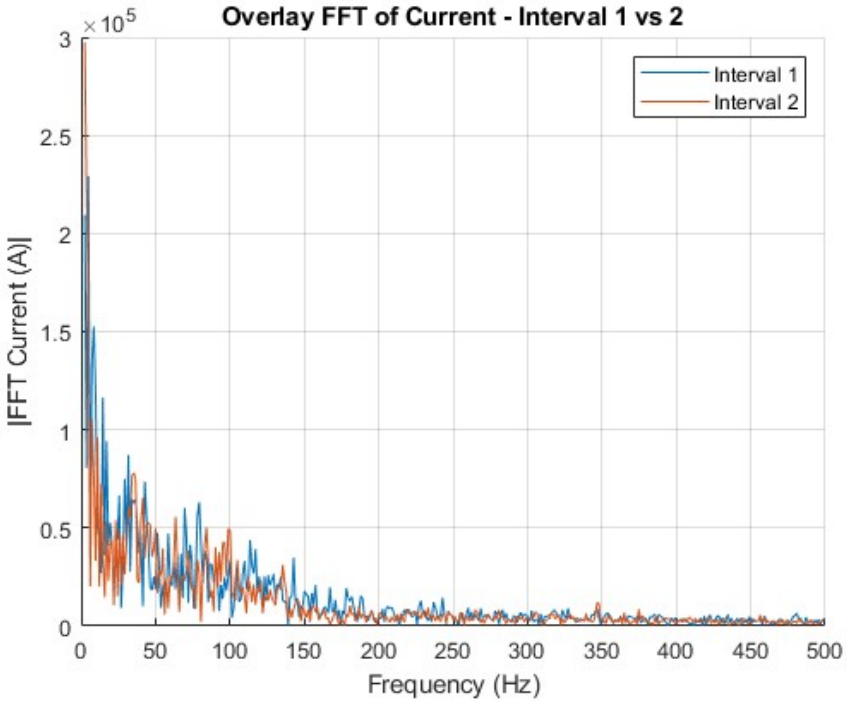


Figure C.12: MATLAB Current FFT Overlaid for 220ipm/14.3V Case

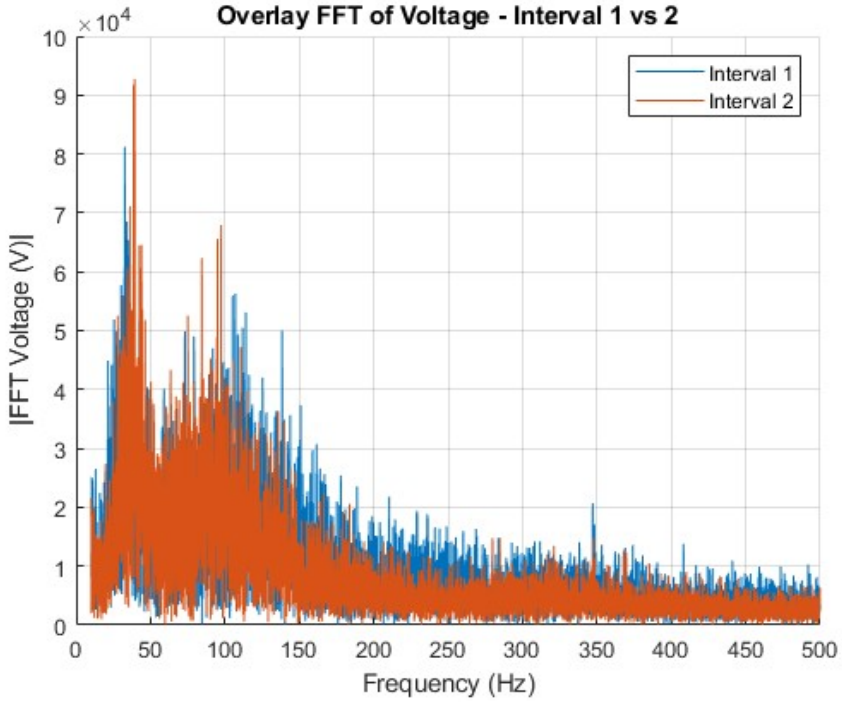


Figure C.13: MATLAB Voltage FFT Overlaid for Entire Range of 220ipm/14.3V Case

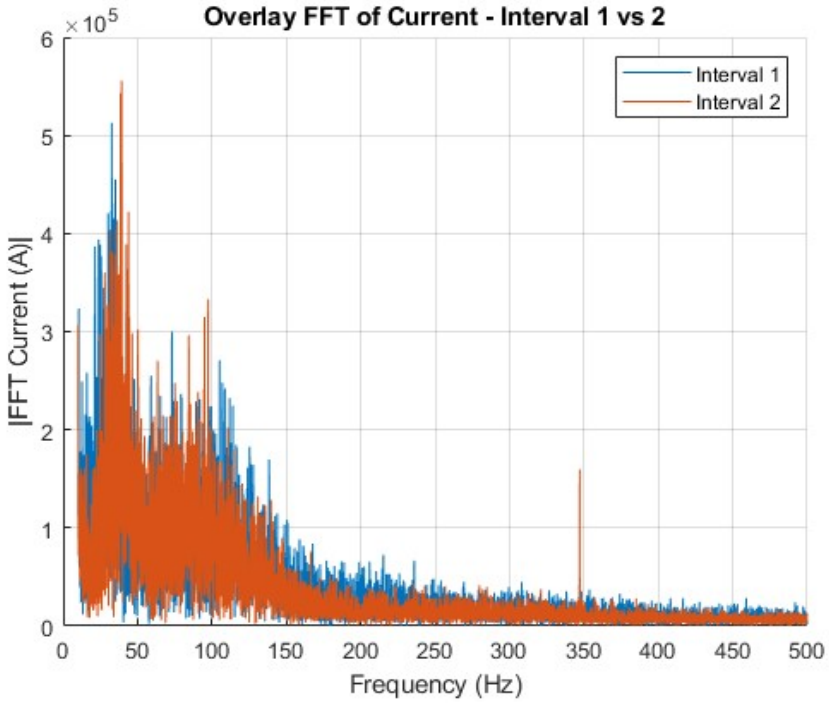


Figure C.14: MATLAB Current FFT Overlaid for Entire Range of 220ipm/14.3V Case

C.2 300ipm 24V case

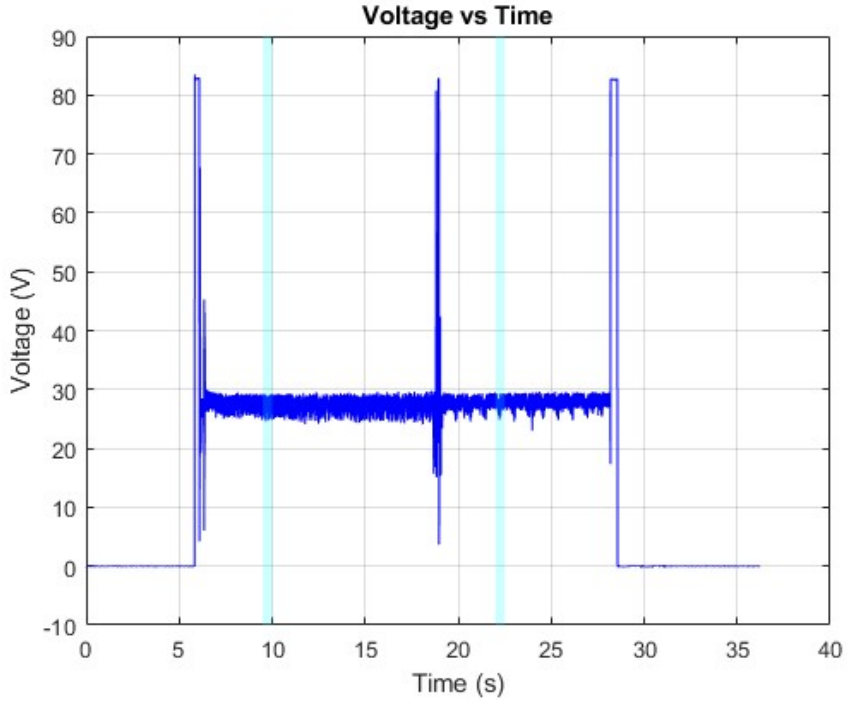


Figure C.15: Voltage vs Time (Area of Interest Highlighted) for 300ipm/24V Case

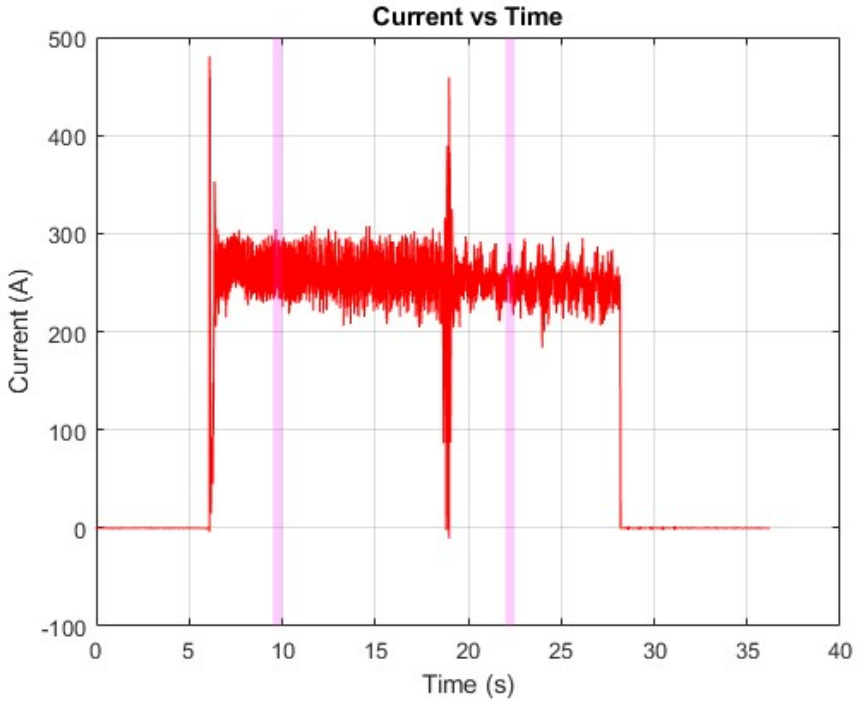


Figure C.16: Current vs Time (Area of Interest Highlighted) for 300ipm/24V Case

```
Interval 1 (9.500000 s to 10.000000 s):
Mean Voltage: 27.0184 V
Mean Current: 264.0514 A

Interval 2 (22.000000 s to 22.500000 s):
Mean Voltage: 27.4627 V
Mean Current: 252.2514 A
```

Figure C.17: Average Current and Voltage for Areas of Interest for 300ipm/24V Case

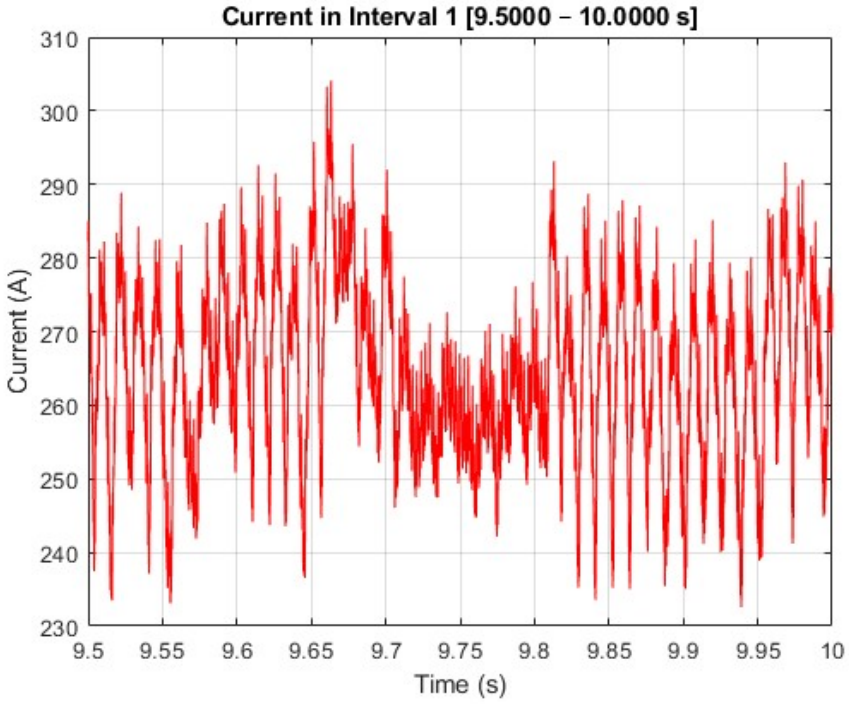


Figure C.18: MATLAB Current Output for 300ipm/24V Case in Interval 1

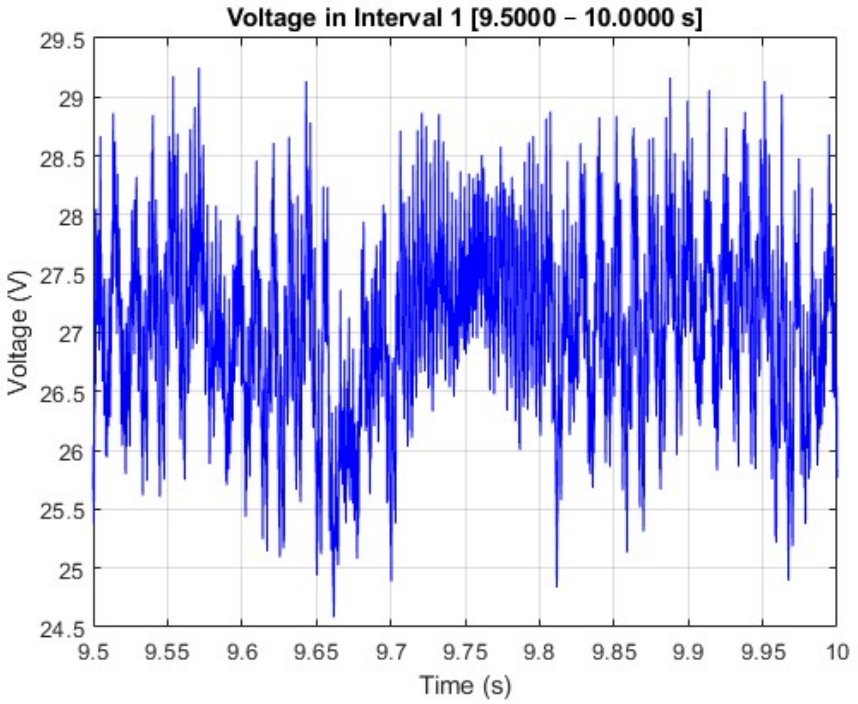


Figure C.19: MATLAB Voltage Output for 300ipm/24V Case in Interval 1

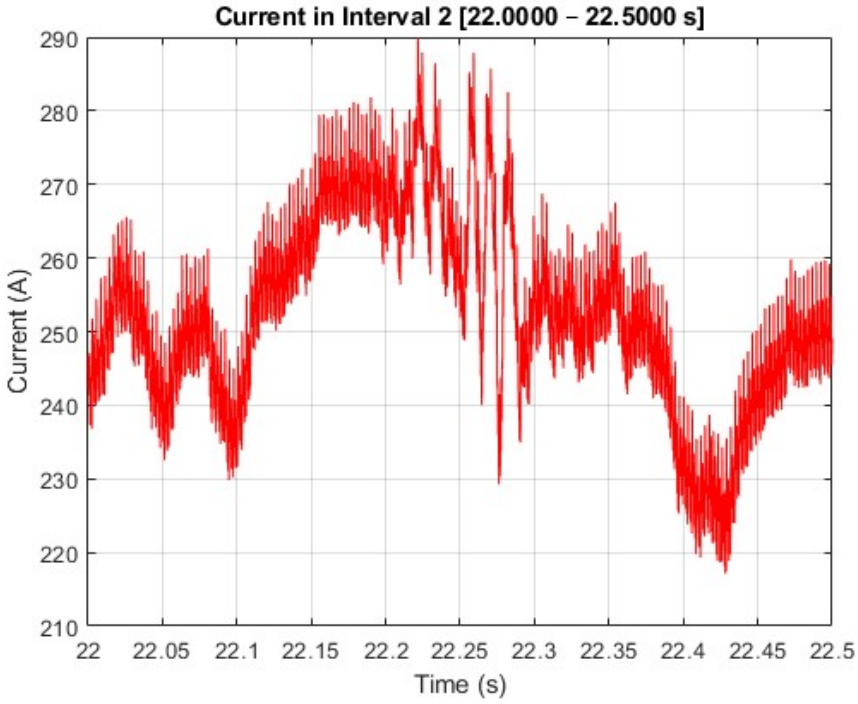


Figure C.20: MATLAB Current Output for 300ipm/24V Case in Interval 2

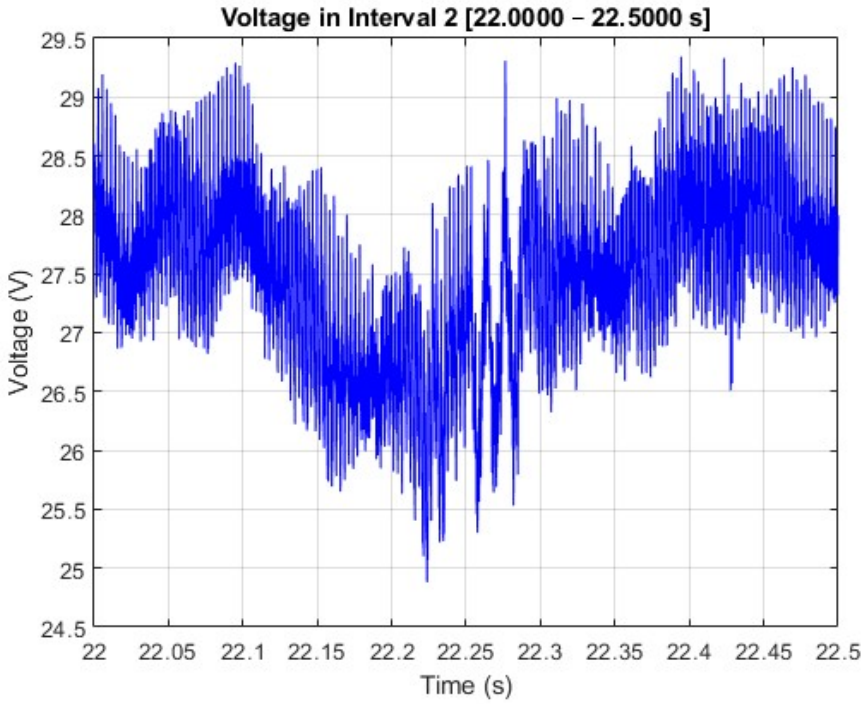


Figure C.21: MATLAB Voltage Output for 300ipm/24V Case in Interval 2

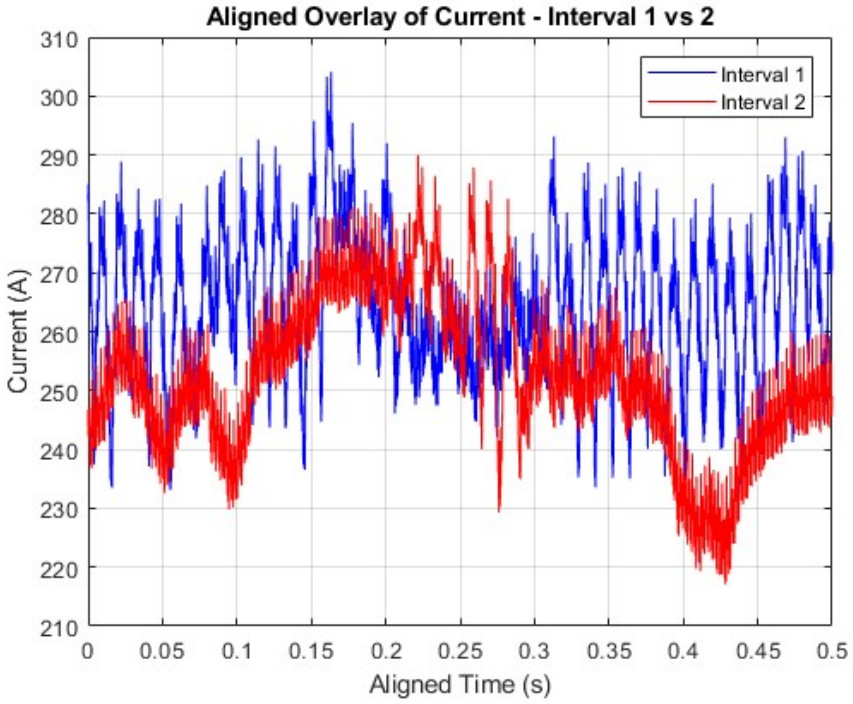


Figure C.22: MATLAB Overlaid Current Output for 300ipm/24V Case

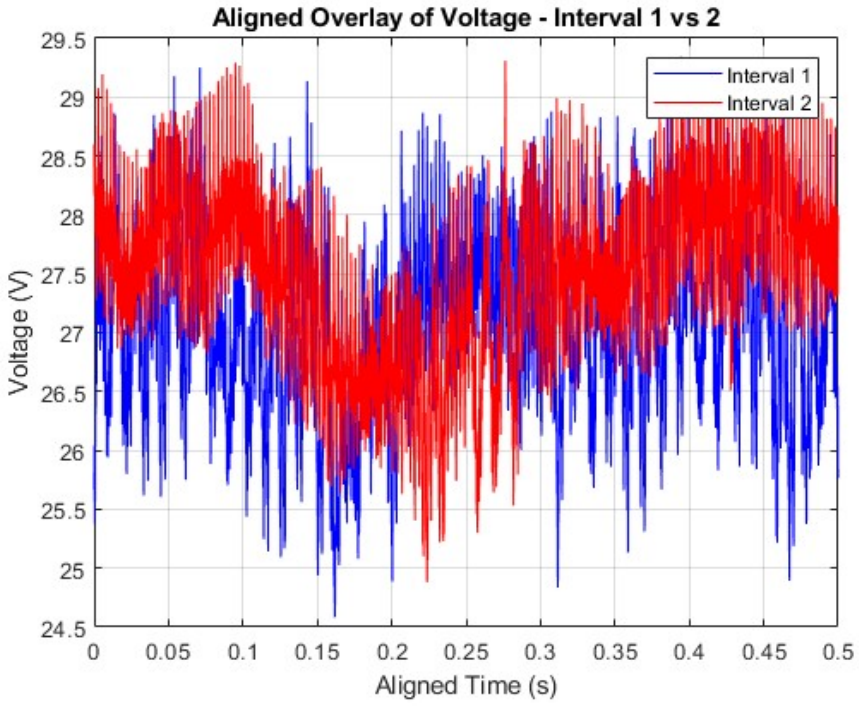


Figure C.23: MATLAB Overlaid Voltage Output for 300ipm/24V Case

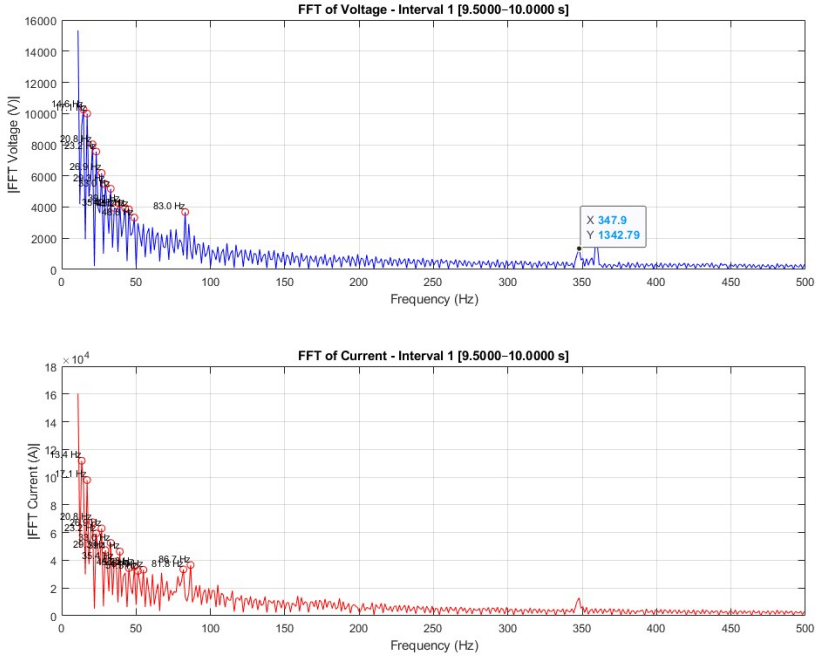


Figure C.24: MATLAB FFT Plot for Interval 1 in 300ipm/24V Case

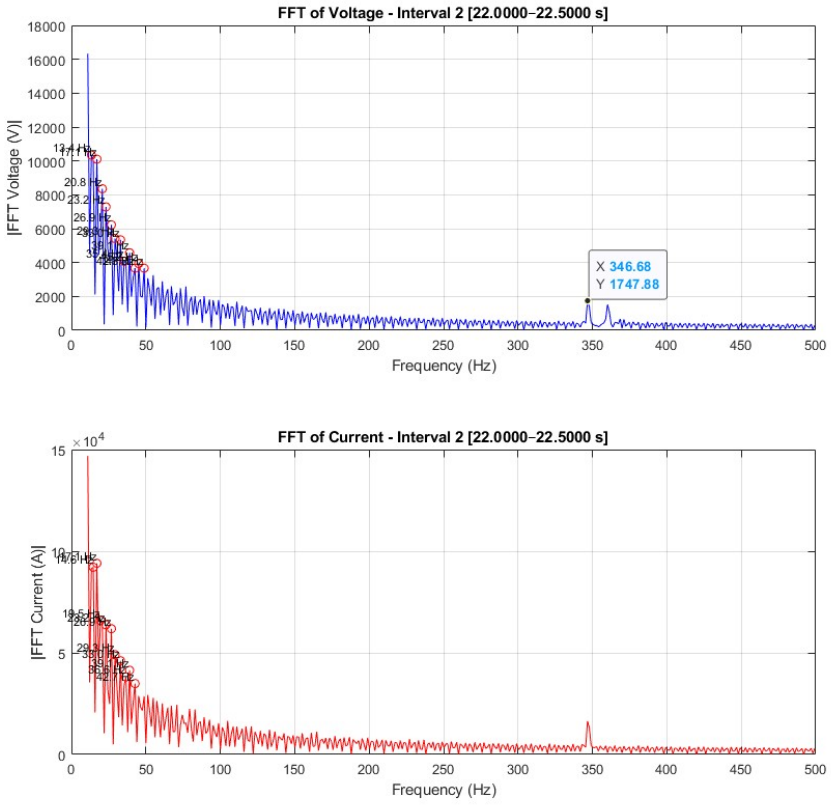


Figure C.25: MATLAB FFT Plot for Interval 2 in 300ipm/24V Case

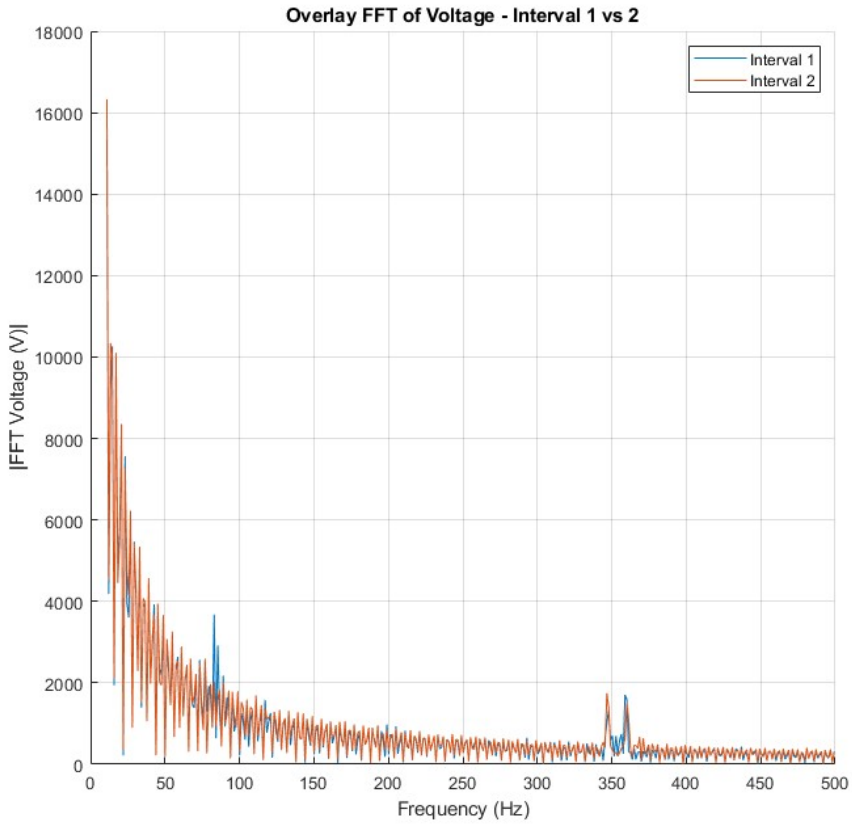


Figure C.26: MATLAB Voltage FFT Overlaid for 300ipm/24V Case

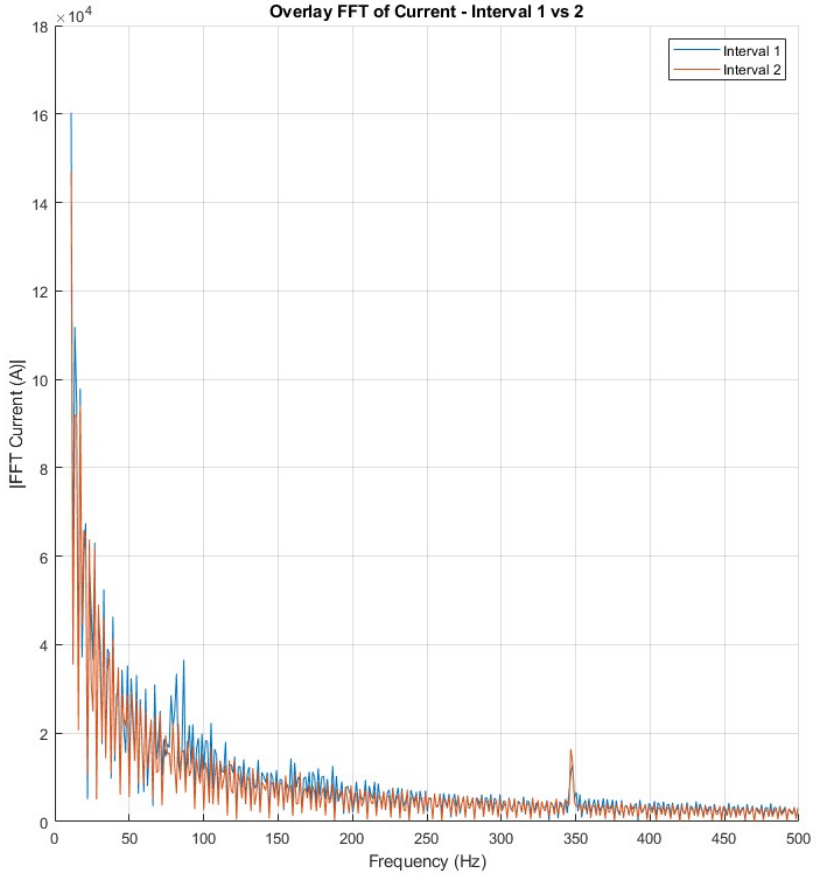


Figure C.27: MATLAB Current FFT Overlaid for 300ipm/24V Case

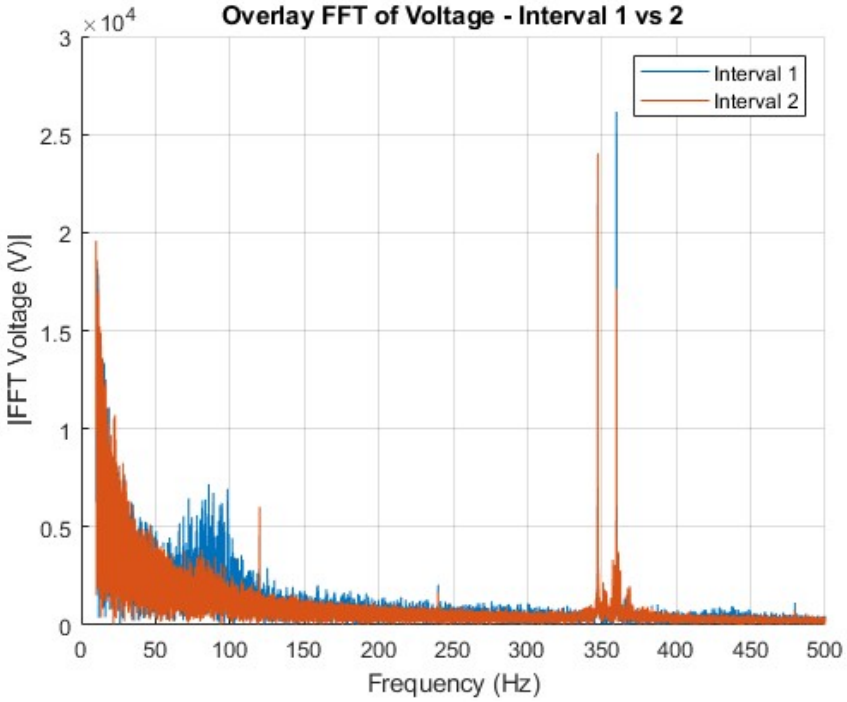


Figure C.28: MATLAB Voltage FFT Overlaid for Entire Range of 300ipm/24V Case

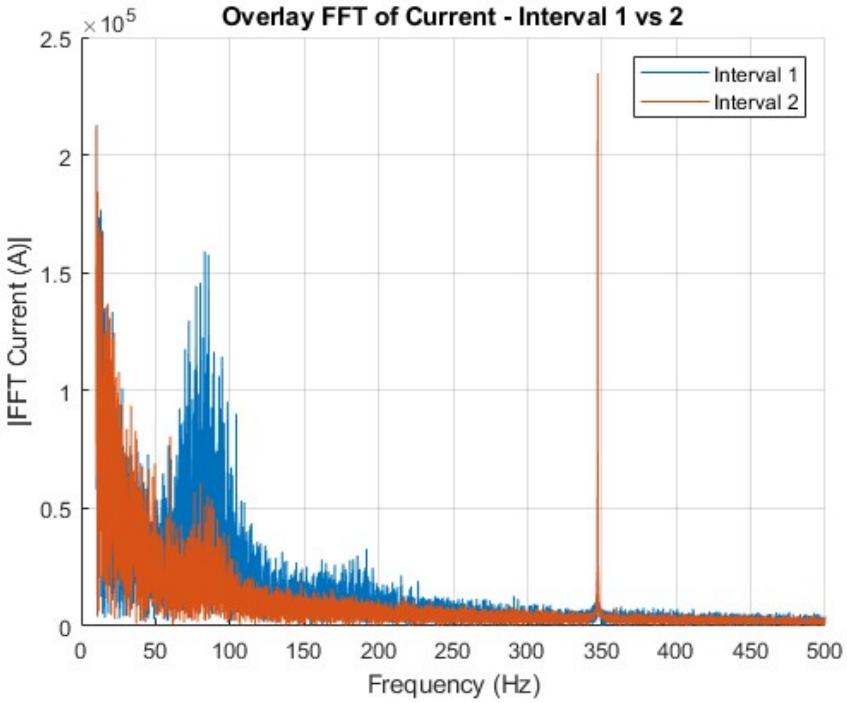


Figure C.29: MATLAB Current FFT Overlaid for Entire Range of 300ipm/24V Case

Appendix D

Supplementary 316L Welding Waveform Data - Miller Pipeworx 400

D.1 200ipm 20.2V Case on Miller Pipeworx400 Power Supply

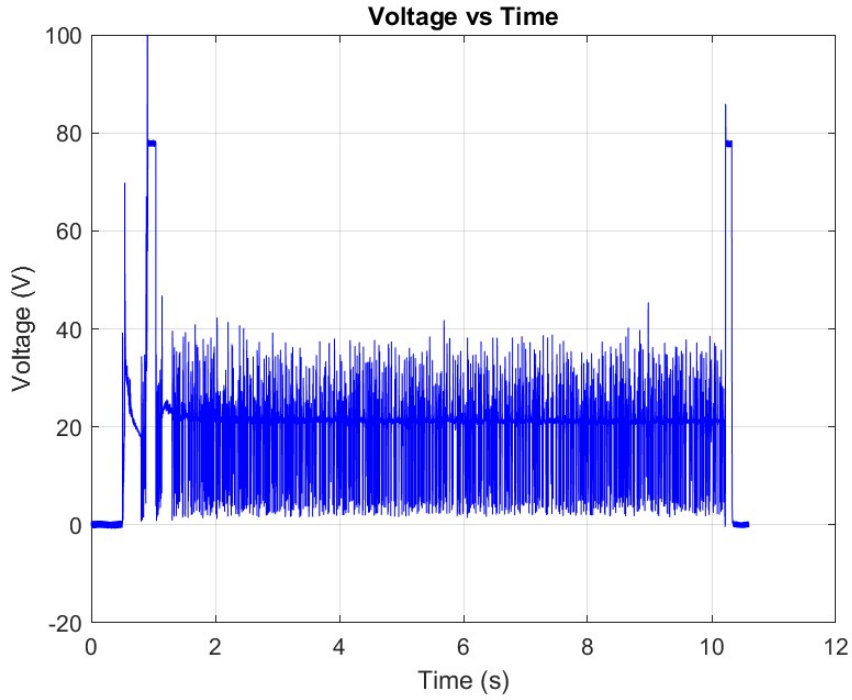


Figure D.1: Voltage vs Time for 200ipm/20.2V Case on Miller Pipeworx400 Power Supply

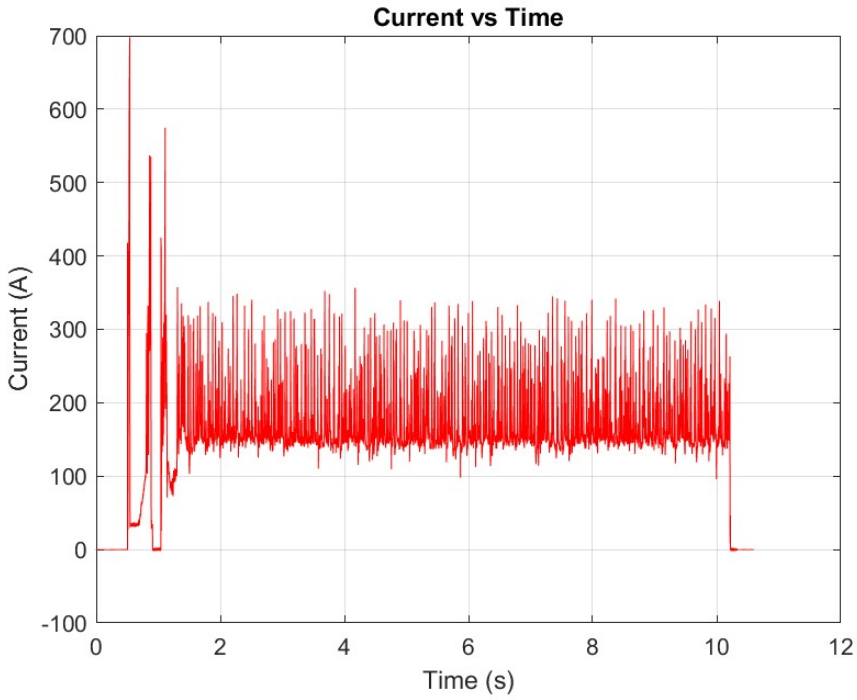


Figure D.2: Current vs Time for 200ipm/20.2V Case on Miller Pipeworx400 Power Supply

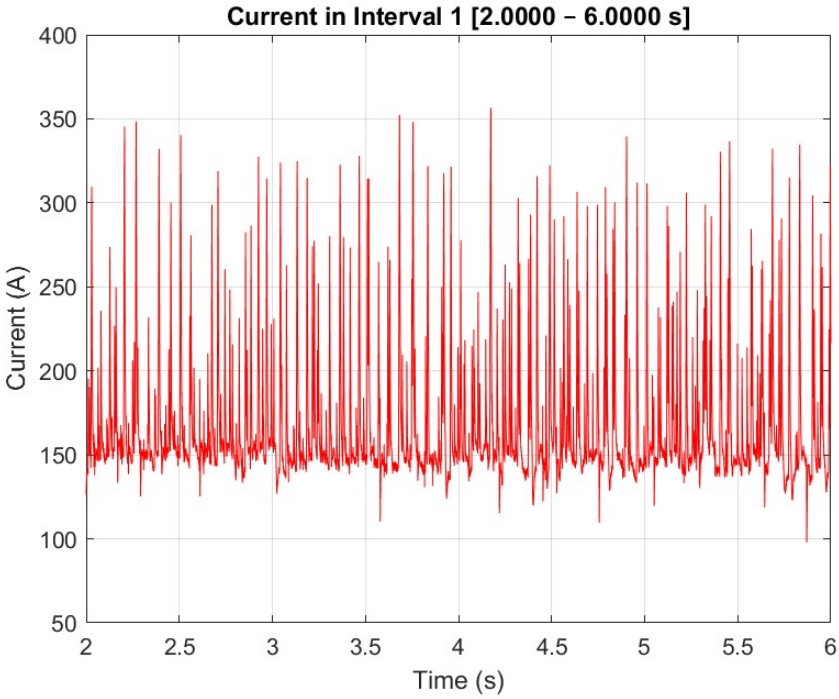


Figure D.3: MATLAB Current Output for 200ipm/20.2V Case on Miller Pipeworx400 Power Supply

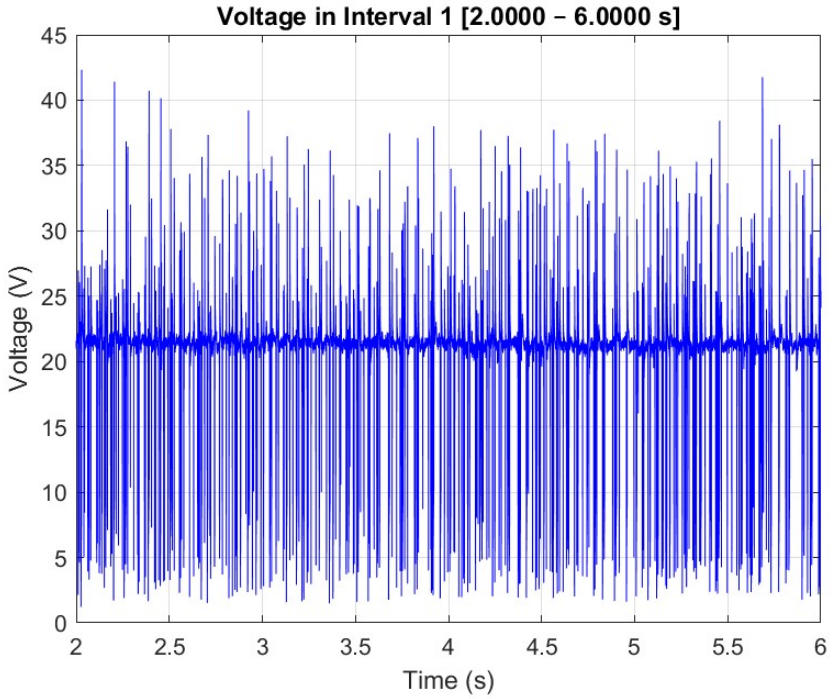


Figure D.4: MATLAB Voltage Output for 200ipm/20.2V Case on Miller Pipeworx400 Power Supply

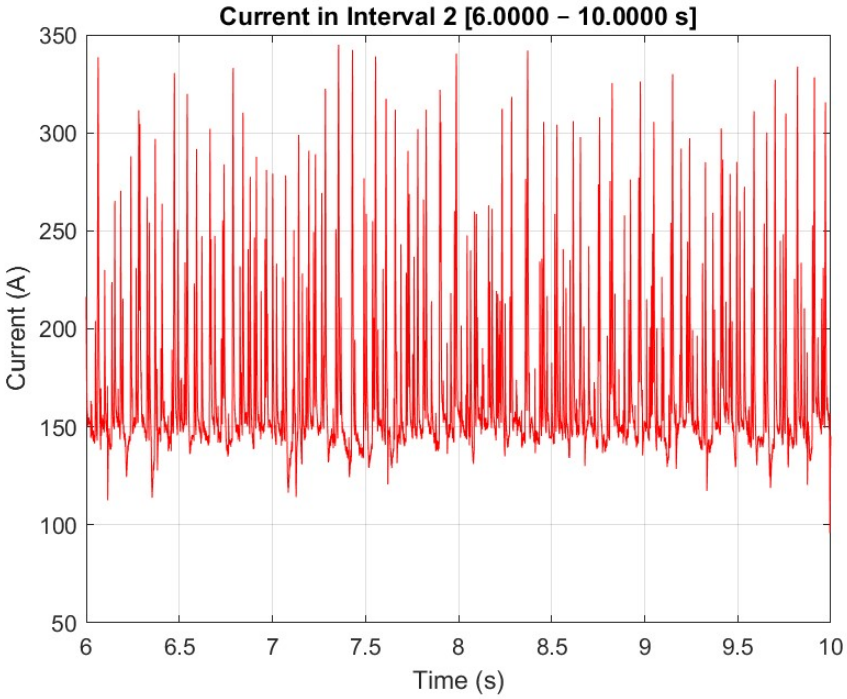


Figure D.5: MATLAB Current Output for 200ipm/20.2V Case on Miller Pipeworx400 Power Supply

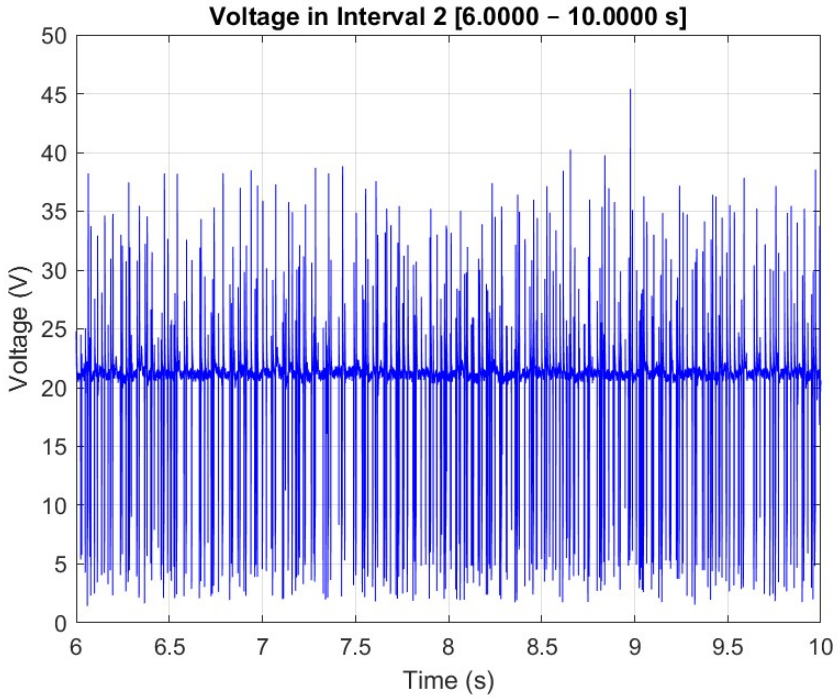


Figure D.6: MATLAB Voltage Output for 200ipm/20.2V Case on Miller Pipeworx400 Power Supply

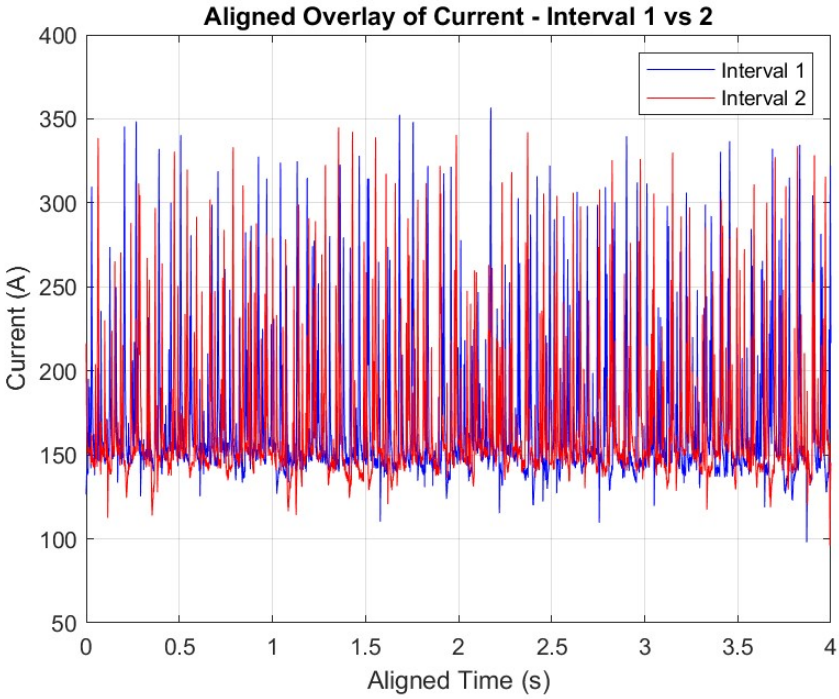


Figure D.7: MATLAB Overlaid Current Output for 200ipm/20.2V Case on Miller Pipeworx400 Power Supply

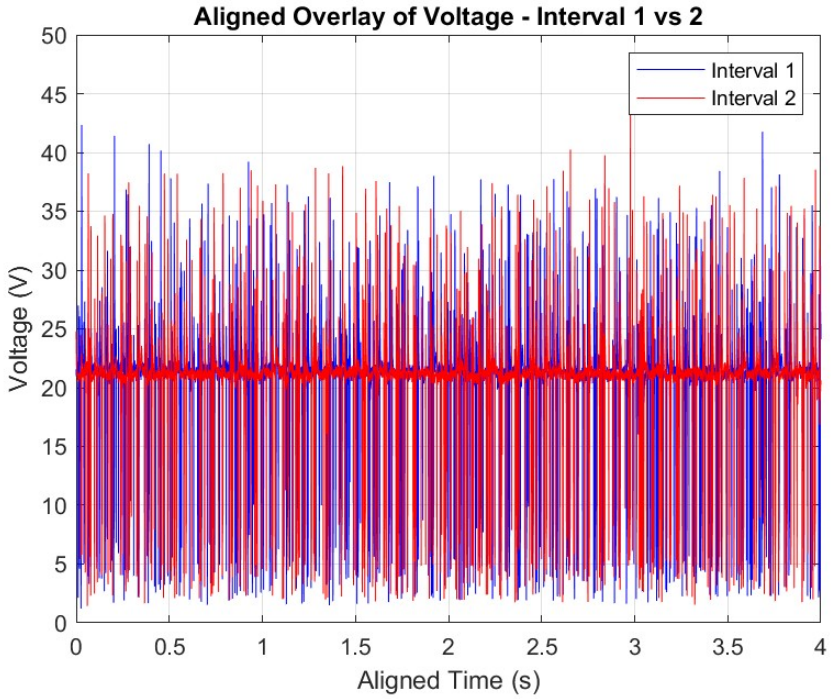


Figure D.8: MATLAB Overlaid Voltage Output for 200ipm/20.2V Case on Miller Pipeworx400 Power Supply

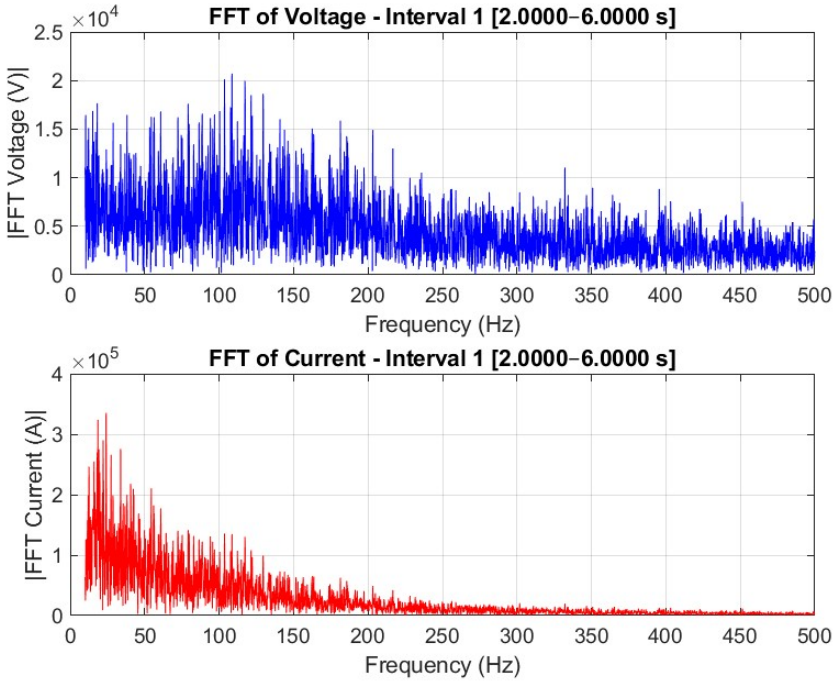


Figure D.9: MATLAB FFT Plot for Interval 1 in 200ipm/20.2V Case on Miller Pipeworx400 Power Supply

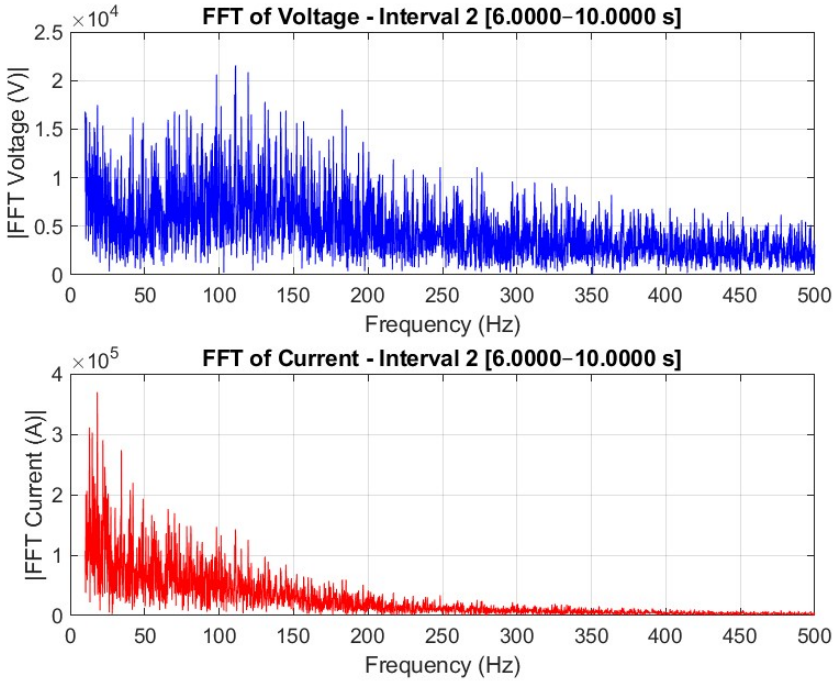


Figure D.10: MATLAB FFT Plot for Interval 2 in 200ipm/20.2V Case on Miller Pipeworx400 Power Supply

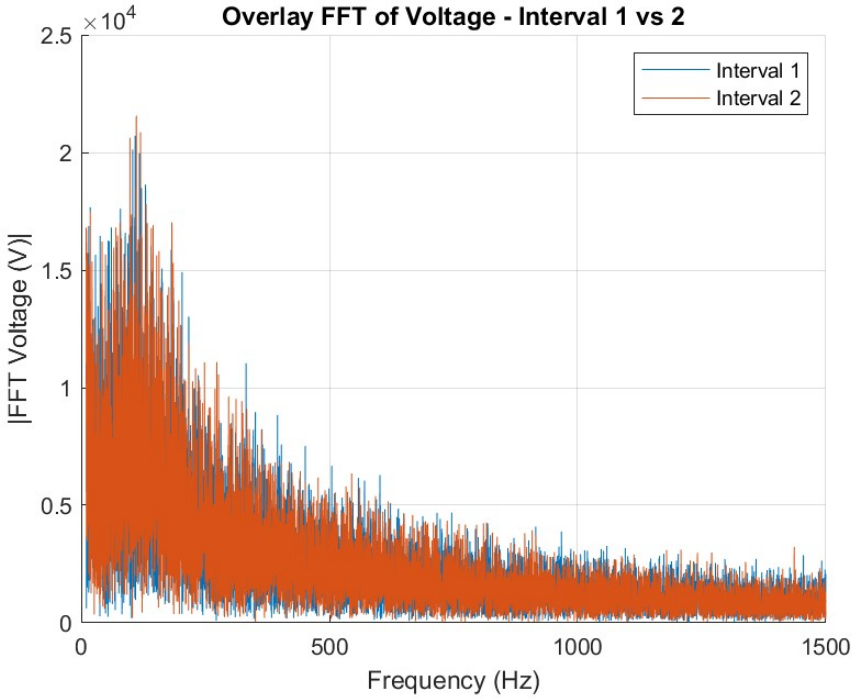


Figure D.11: MATLAB Voltage FFT Overlaid for 200ipm/20.2V Case on Miller Pipeworx400 Power Supply

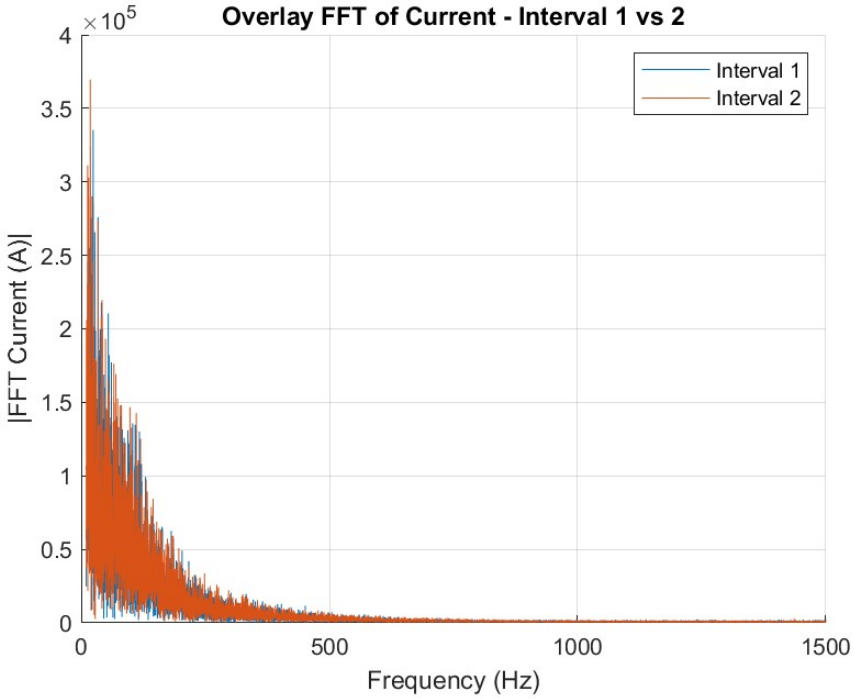


Figure D.12: MATLAB Current FFT Overlaid for 200ipm/20.2V Case on Miller Pipeworx400 Power Supply

D.2 220ipm 14.3V Case on Miller Pipeworx400 Power Supply

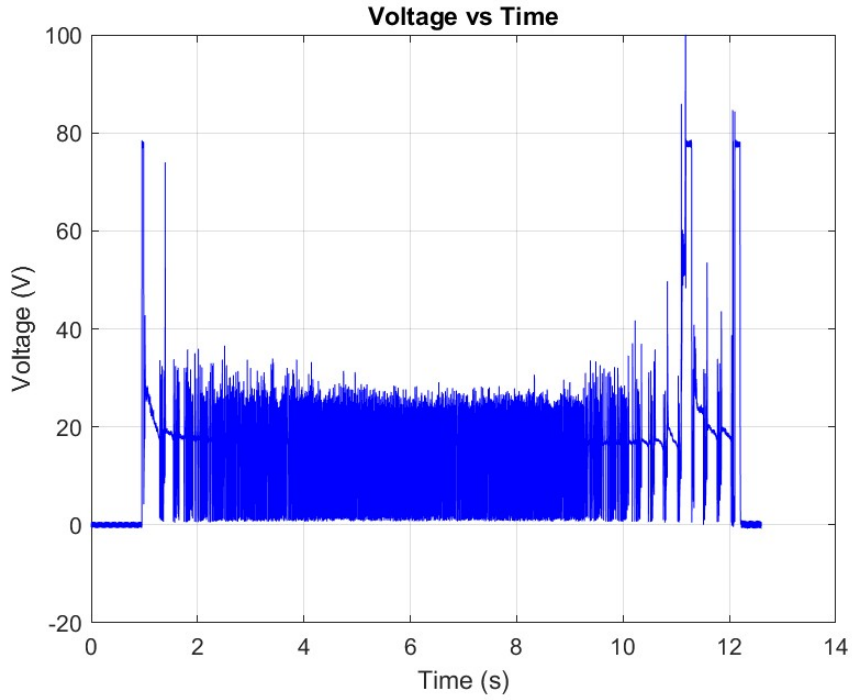


Figure D.13: Voltage vs Time for 220ipm/14.3V Case on Miller Pipeworx400 Power Supply

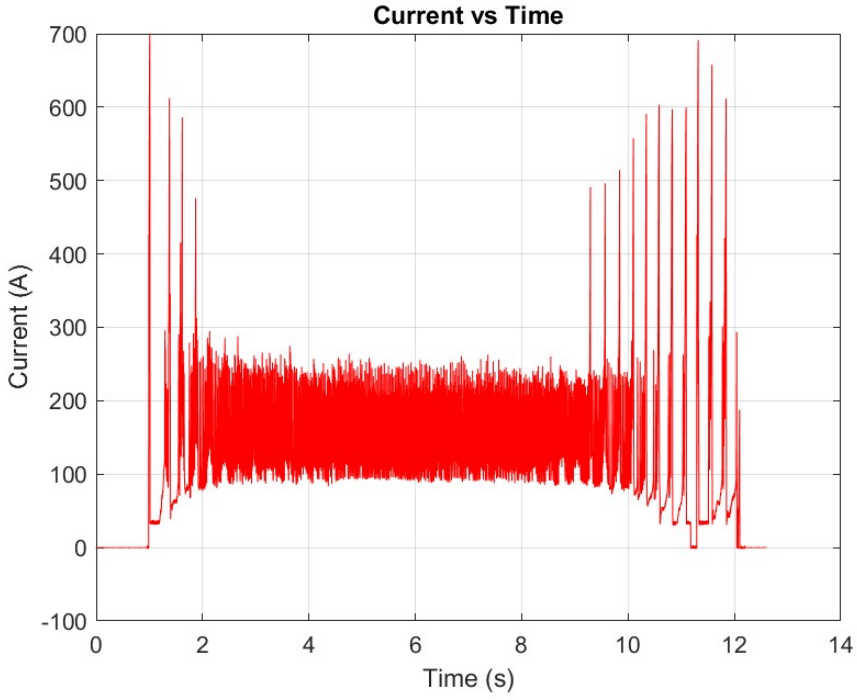


Figure D.14: Current vs Time for 220ipm/14.3V Case on Miller Pipeworx400 Power Supply

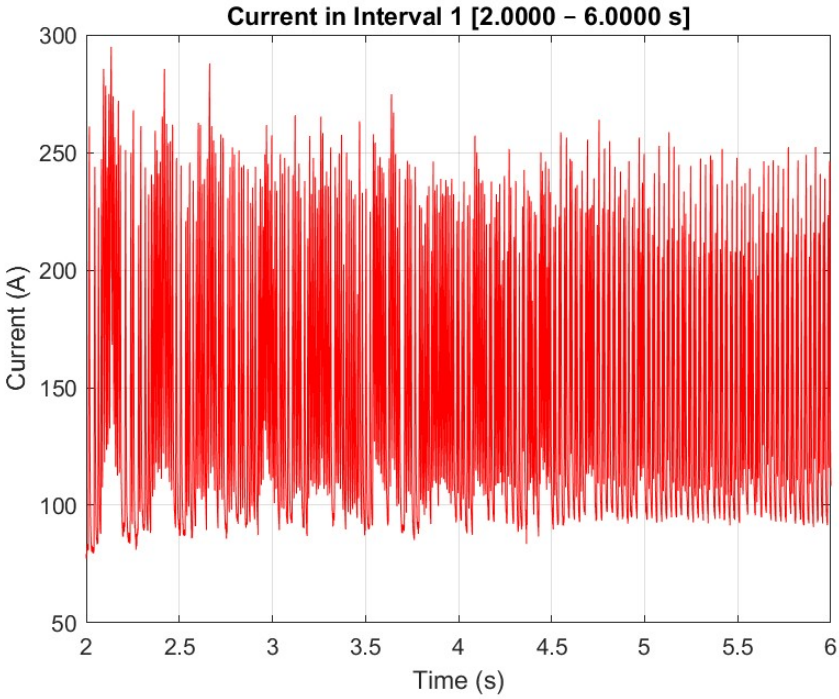


Figure D.15: MATLAB Current Output for 220ipm/14.3V Case on Miller Pipeworx400 Power Supply

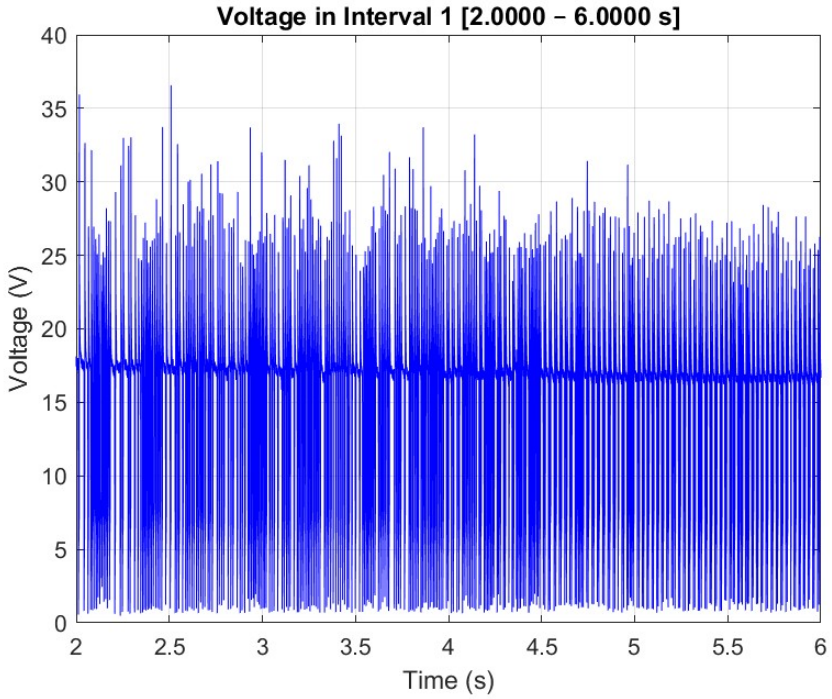


Figure D.16: MATLAB Voltage Output for 220ipm/14.3V Case on Miller Pipeworx400 Power Supply

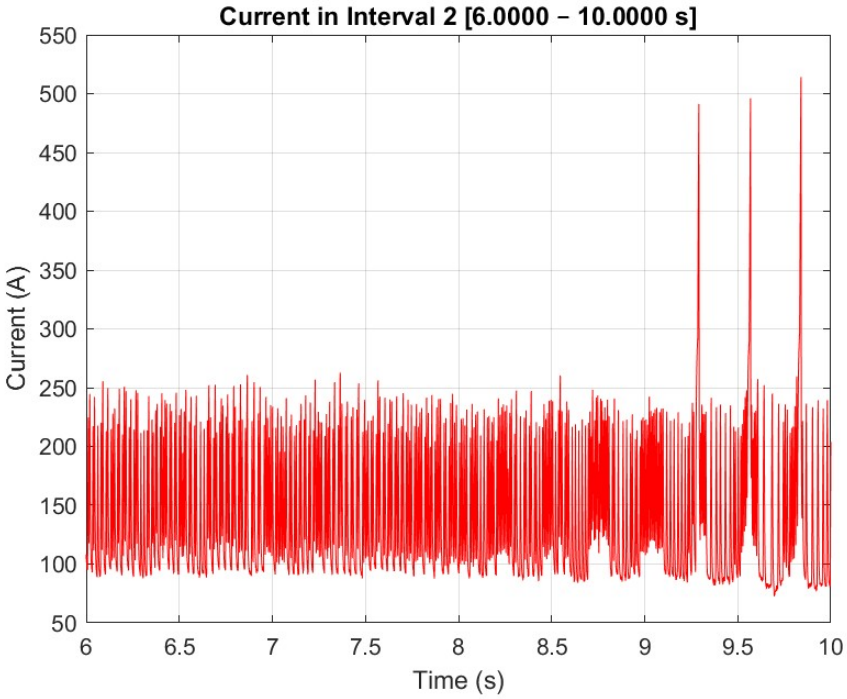


Figure D.17: MATLAB Current Output for 220ipm/14.3V Case on Miller Pipeworx400 Power Supply

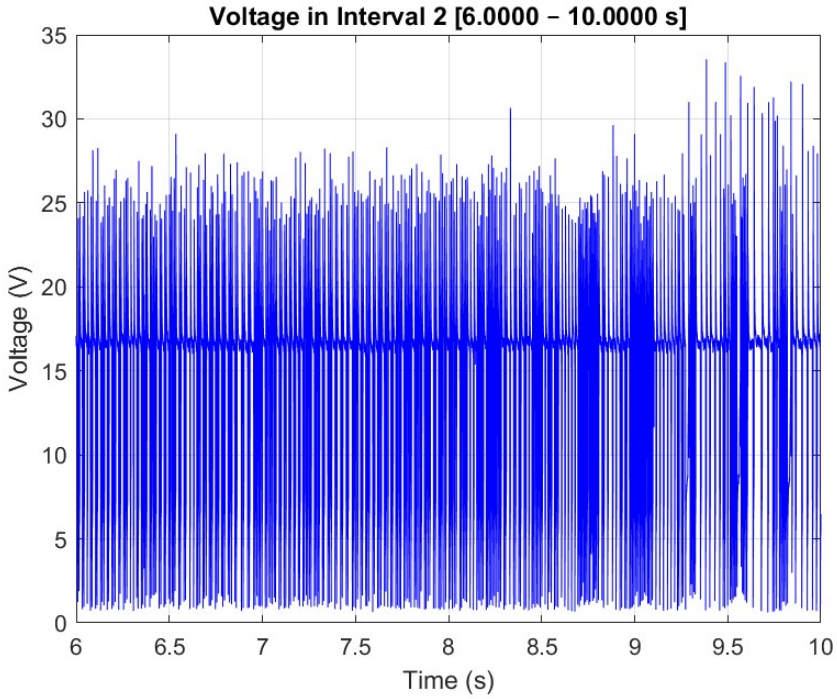


Figure D.18: MATLAB Voltage Output for 220ipm/14.3V Case on Miller Pipeworx400 Power Supply

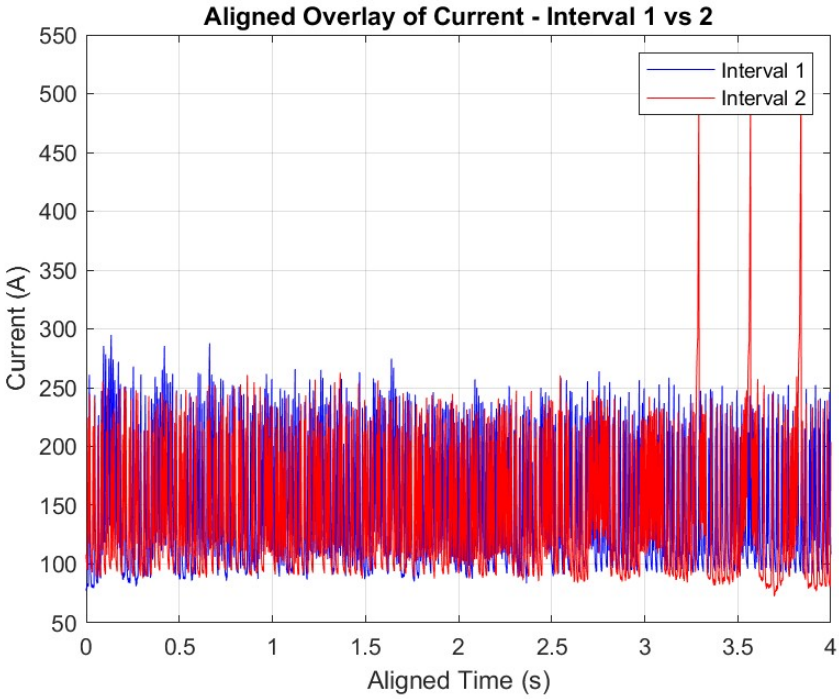


Figure D.19: MATLAB Overlaid Current Output for 220ipm/14.3V Case on Miller Pipeworx400 Power Supply

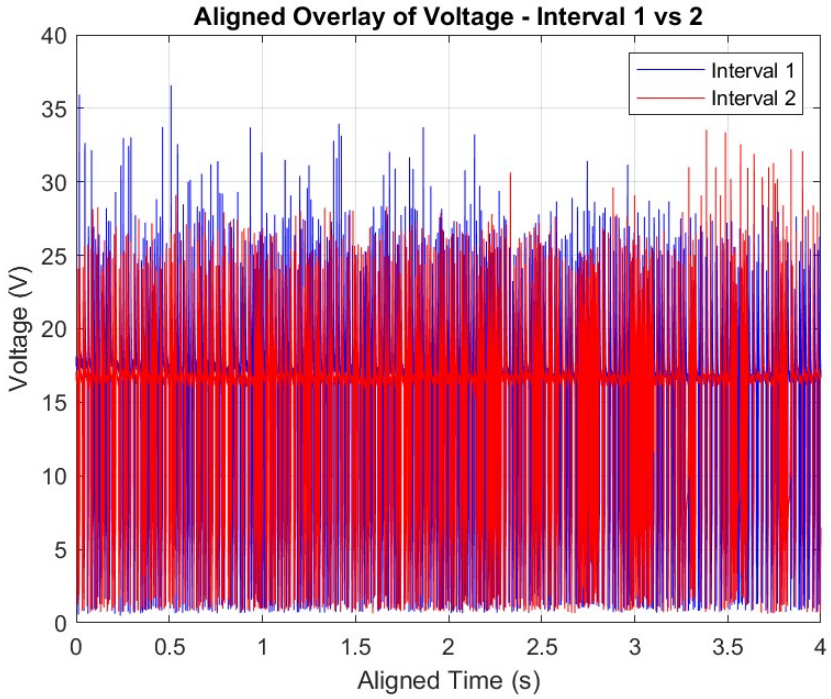


Figure D.20: MATLAB Overlaid Voltage Output for 220ipm/14.3V Case on Miller Pipeworx400 Power Supply

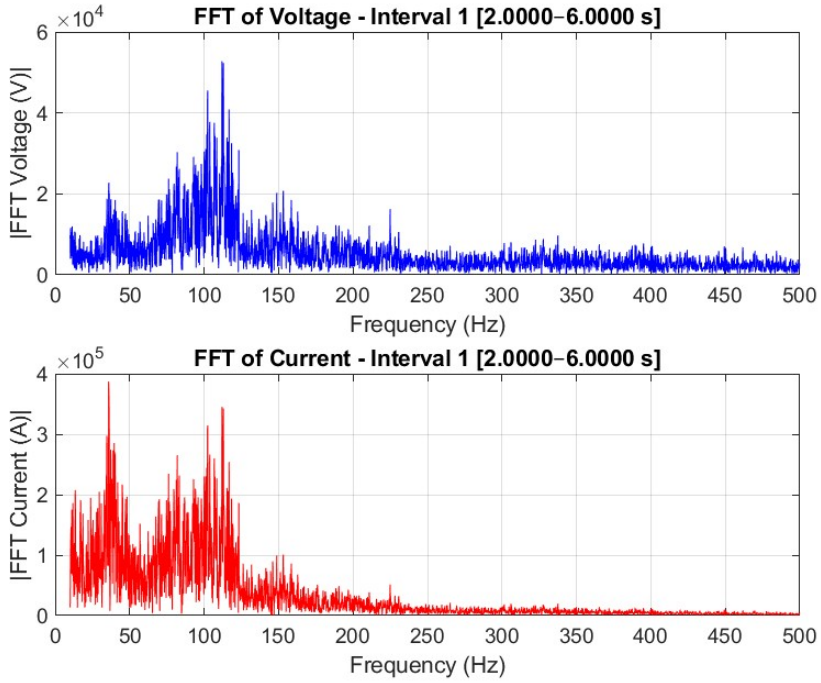


Figure D.21: MATLAB FFT Plot for Interval 1 in 220ipm/14.3V Case on Miller Pipeworx400 Power Supply

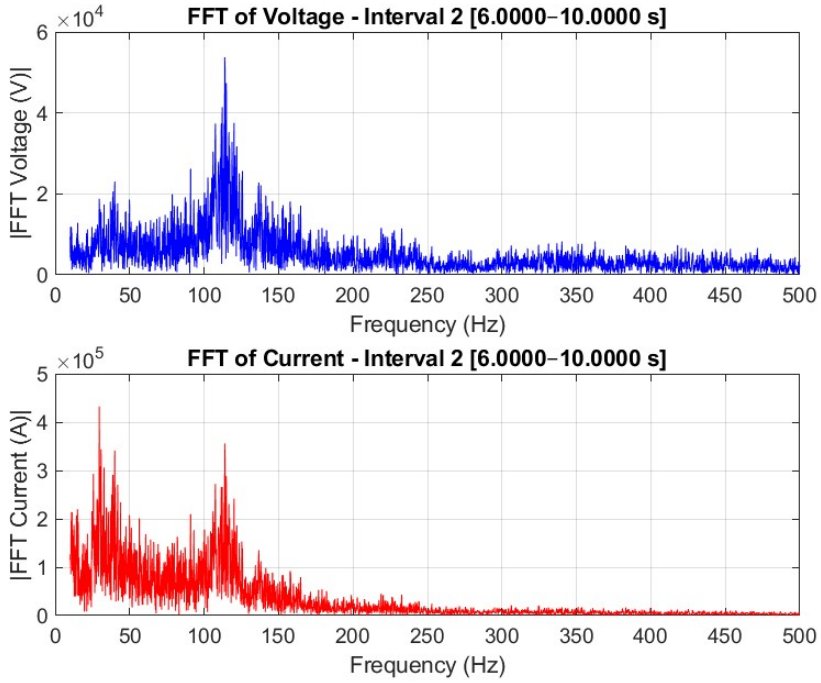


Figure D.22: MATLAB FFT Plot for Interval 2 in 220ipm/14.3V Case on Miller Pipeworx400 Power Supply

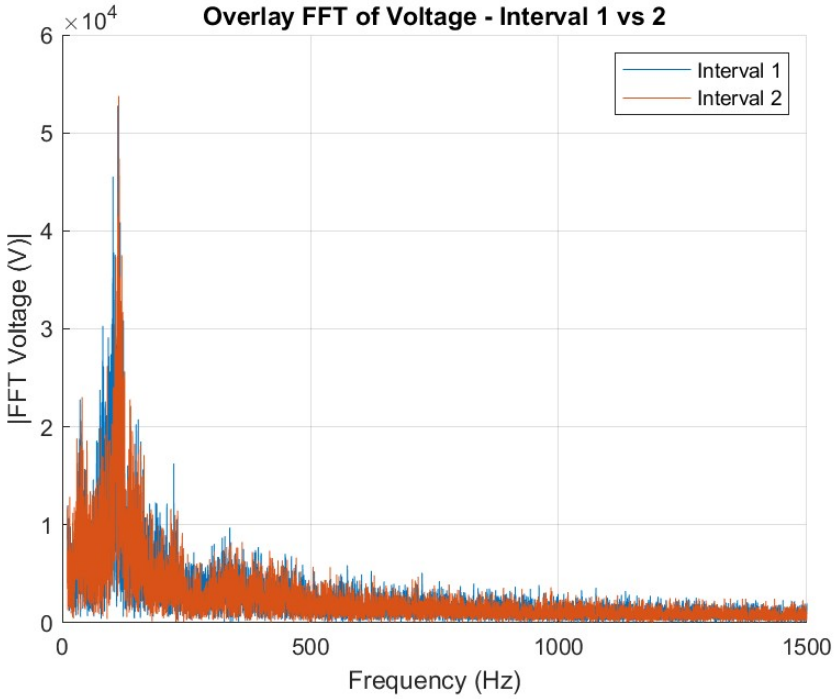


Figure D.23: MATLAB Voltage FFT Overlaid for 220ipm/14.3V Case on Miller Pipeworx400 Power Supply

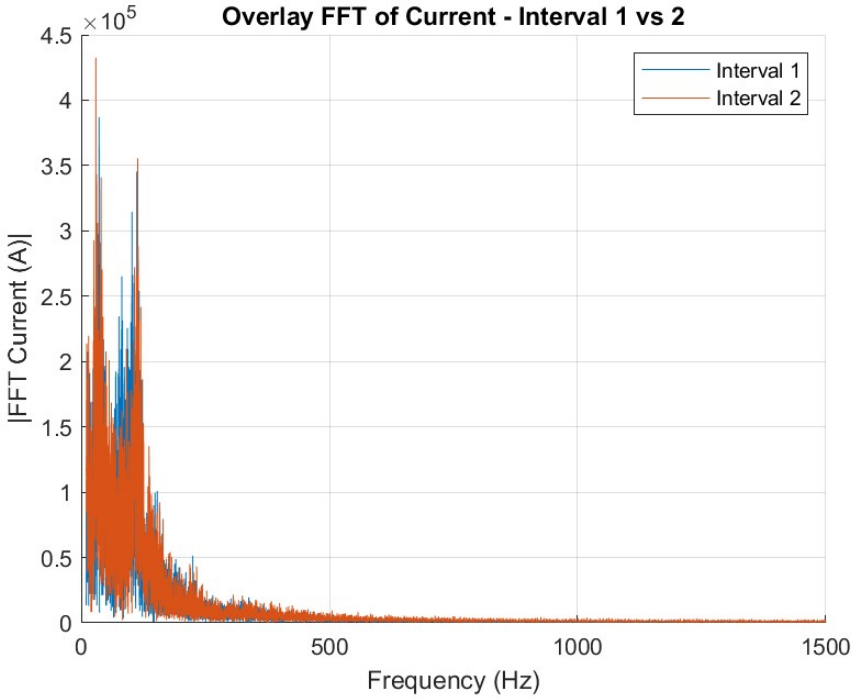


Figure D.24: MATLAB Current FFT Overlaid for 220ipm/14.3V Case on Miller Pipeworx400 Power Supply

D.3 300ipm 24V Case on Miller Pipeworx400 Power Supply

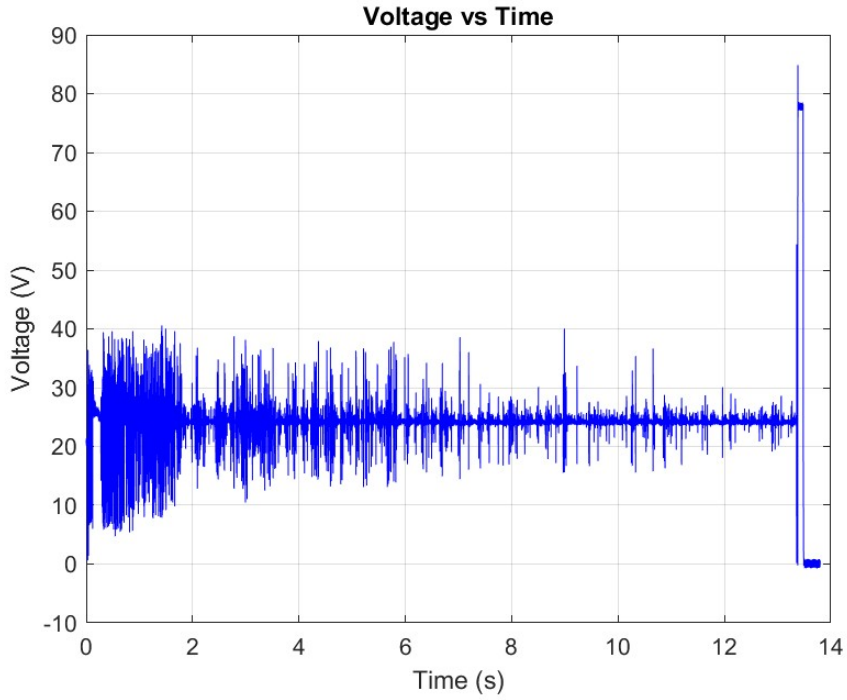


Figure D.25: Voltage vs Time for 300ipm/24V Case on Miller Pipeworx400 Power Supply

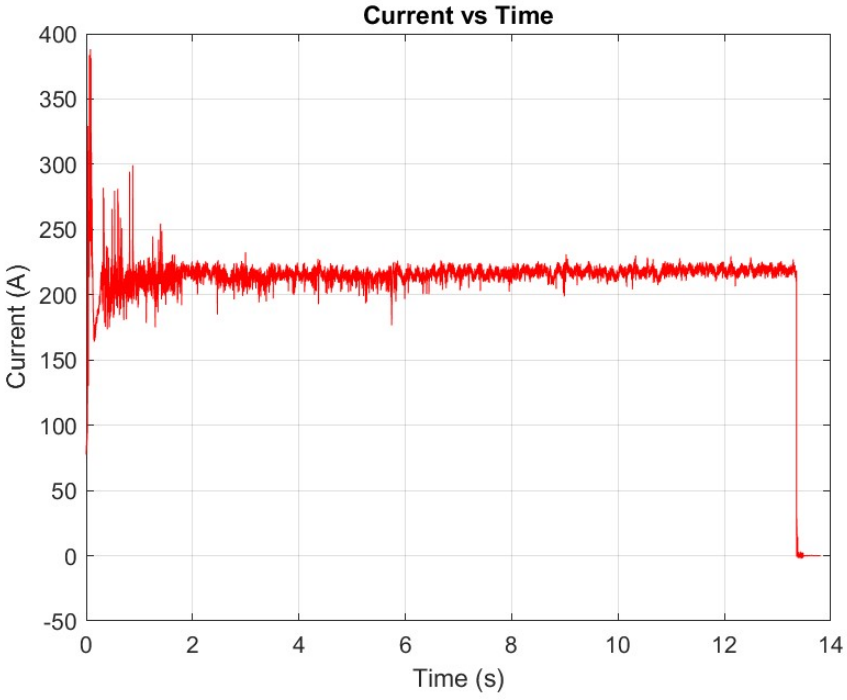


Figure D.26: Current vs Time for 300ipm/24V Case on Miller Pipeworx400 Power Supply

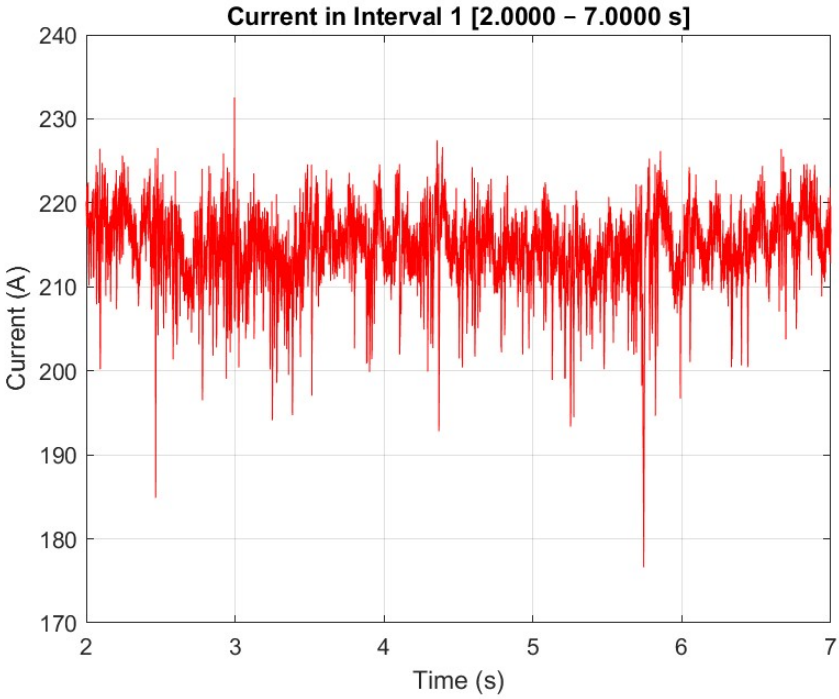


Figure D.27: MATLAB Current Output for 300ipm/24V Case on Miller Pipeworx400 Power Supply

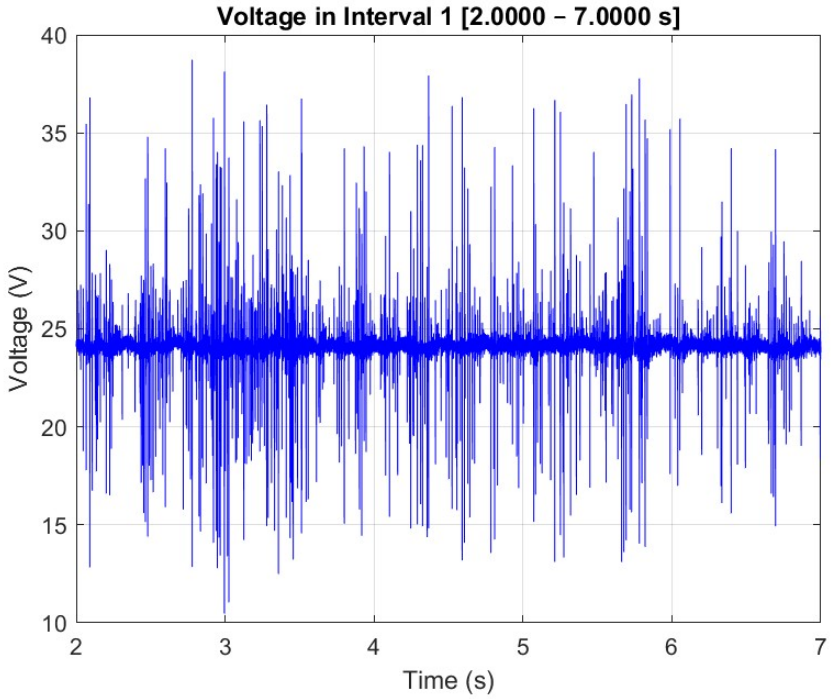


Figure D.28: MATLAB Voltage Output for 300ipm/24V Case on Miller Pipeworx400 Power Supply

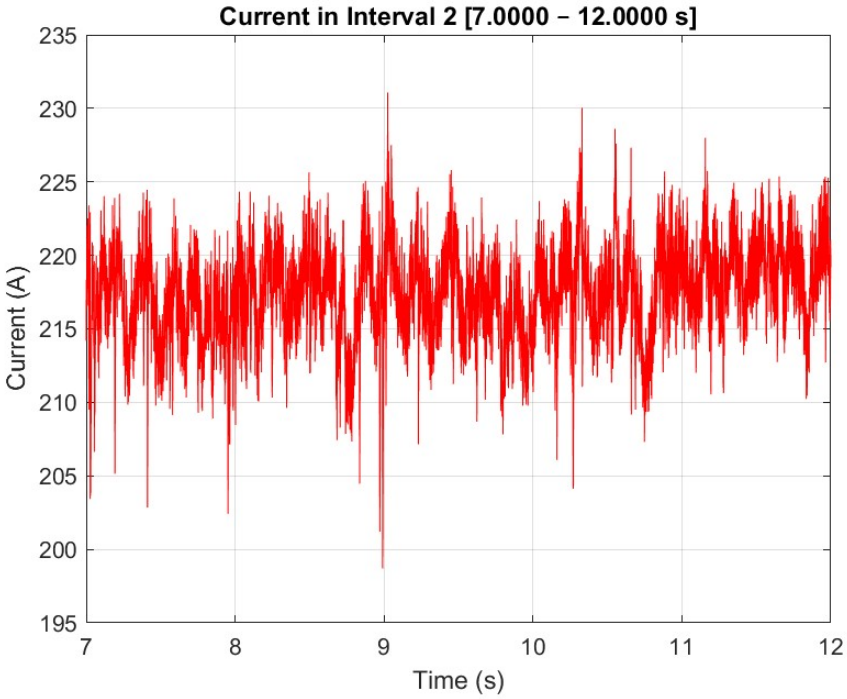


Figure D.29: MATLAB Current Output for 300ipm/24V Case on Miller Pipeworx400 Power Supply

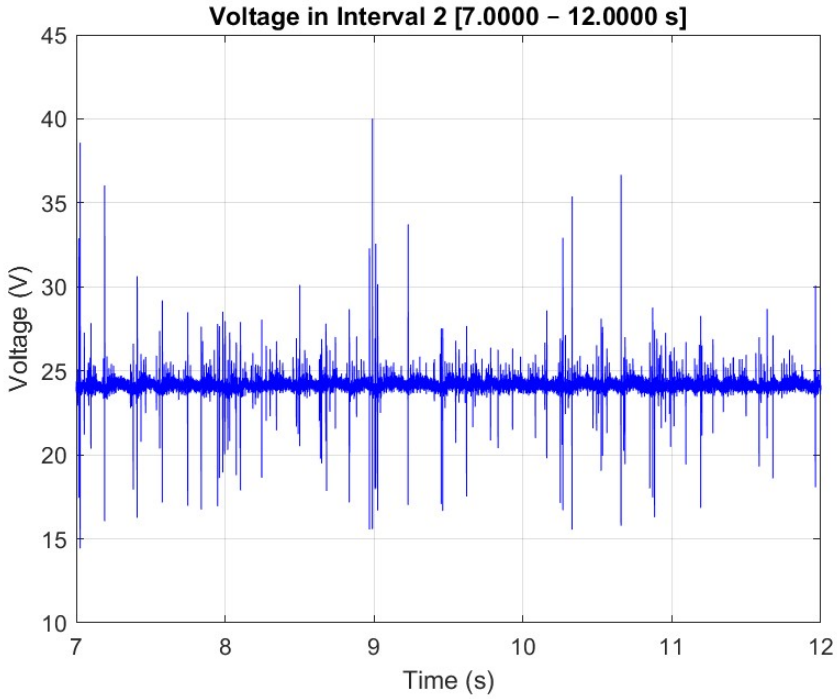


Figure D.30: MATLAB Voltage Output for 300ipm/24V Case on Miller Pipeworx400 Power Supply

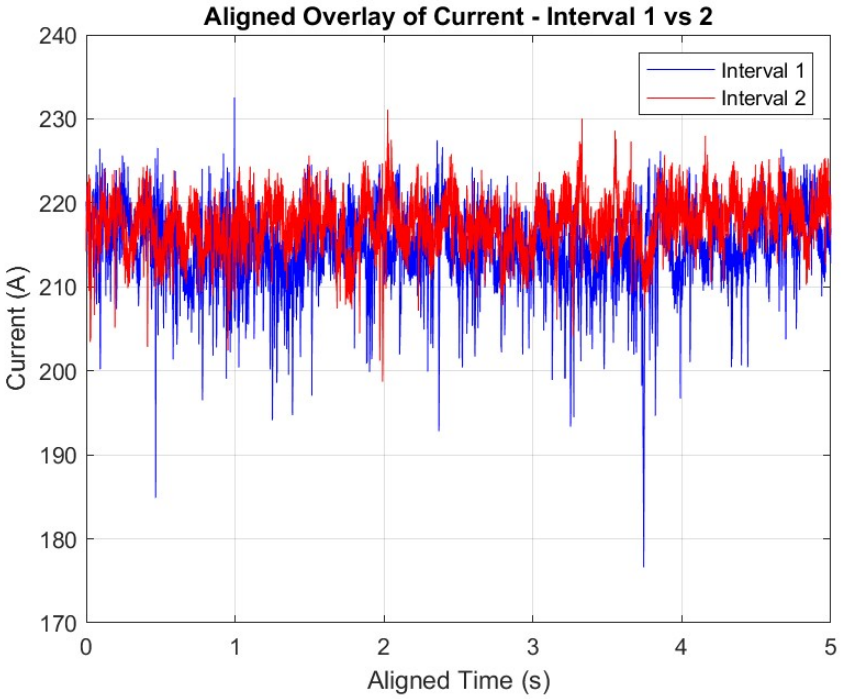


Figure D.31: MATLAB Overlaid Current Output for 300ipm/24V Case on Miller Pipeworx400 Power Supply

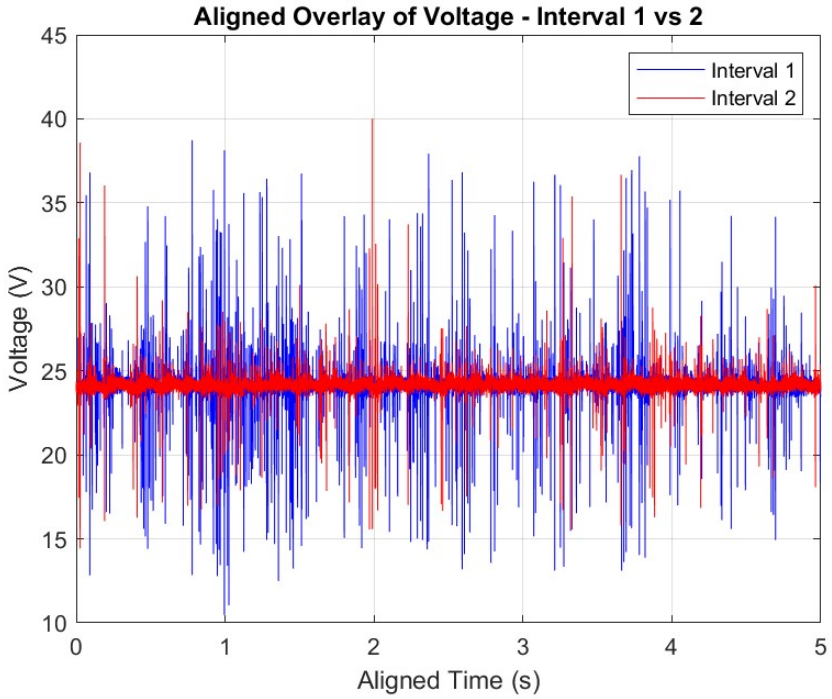


Figure D.32: MATLAB Overlaid Voltage Output for 300ipm/24V Case on Miller Pipeworx400 Power Supply

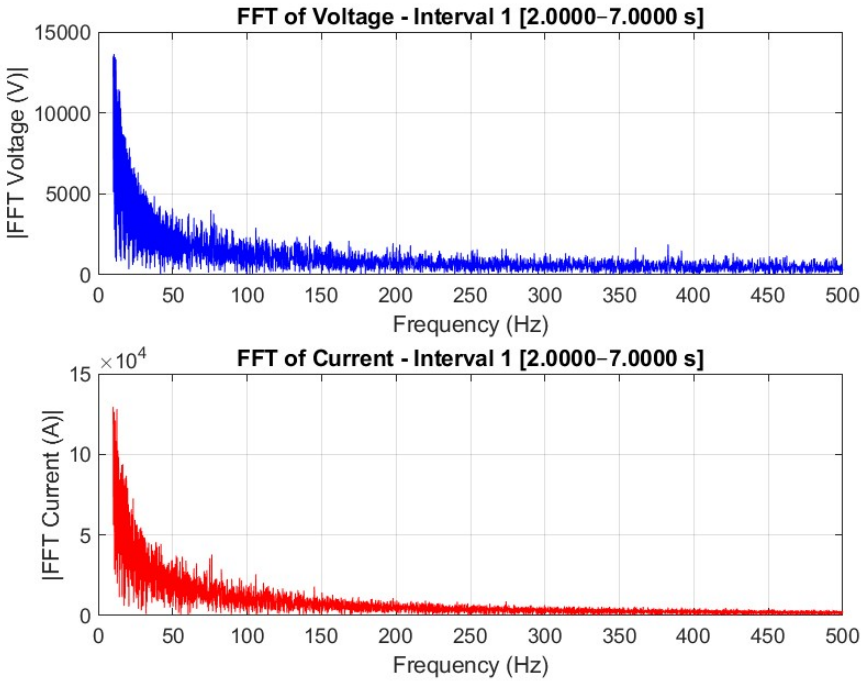


Figure D.33: MATLAB FFT Plot for Interval 1 in 300ipm/24V Case on Miller Pipeworx400 Power Supply

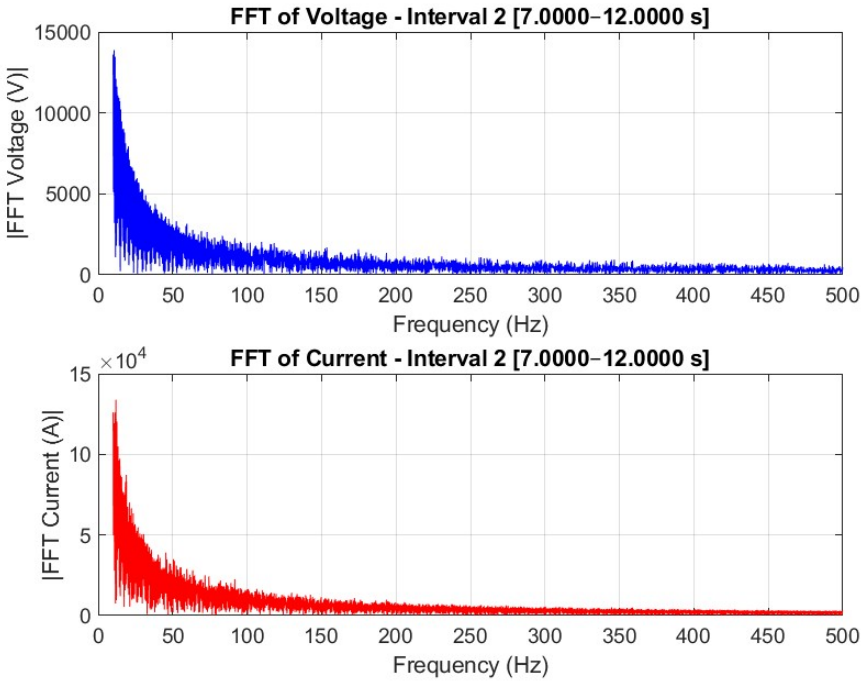


Figure D.34: MATLAB FFT Plot for Interval 2 in 300ipm/24V Case on Miller Pipeworx400 Power Supply

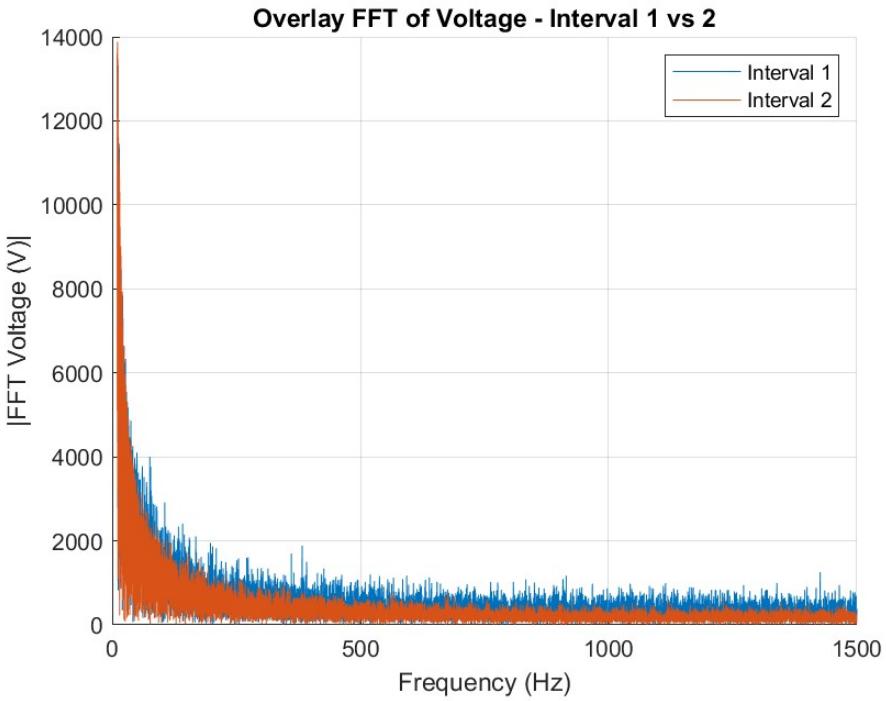


Figure D.35: MATLAB Voltage FFT Overlaid for 300ipm/24V Case on Miller Pipeworx400 Power Supply

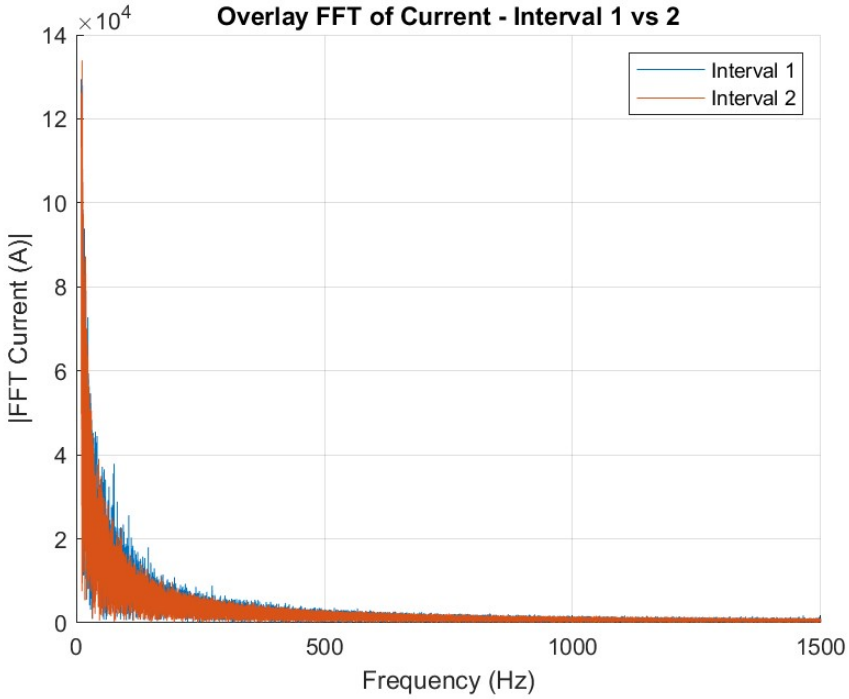


Figure D.36: MATLAB Current FFT Overlaid for 300ipm/24V Case on Miller Pipeworx400 Power Supply

Appendix E

Supplementary 2319AL Welding Waveform Data

E.1 360ipm 20.9V Pulse 2319AL

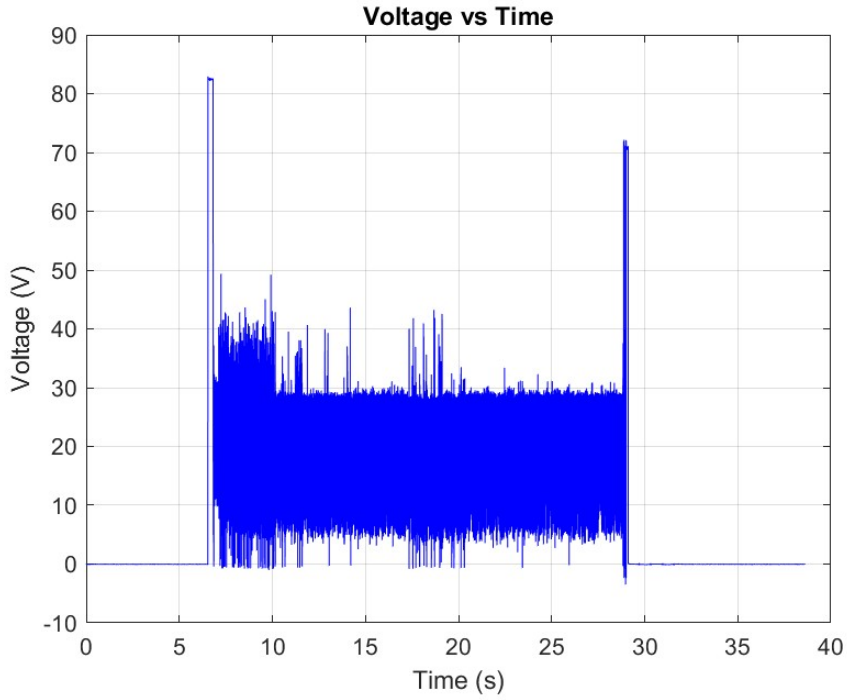


Figure E.1: Voltage vs Time for 360ipm/20.9V Pulsed Transfer Case

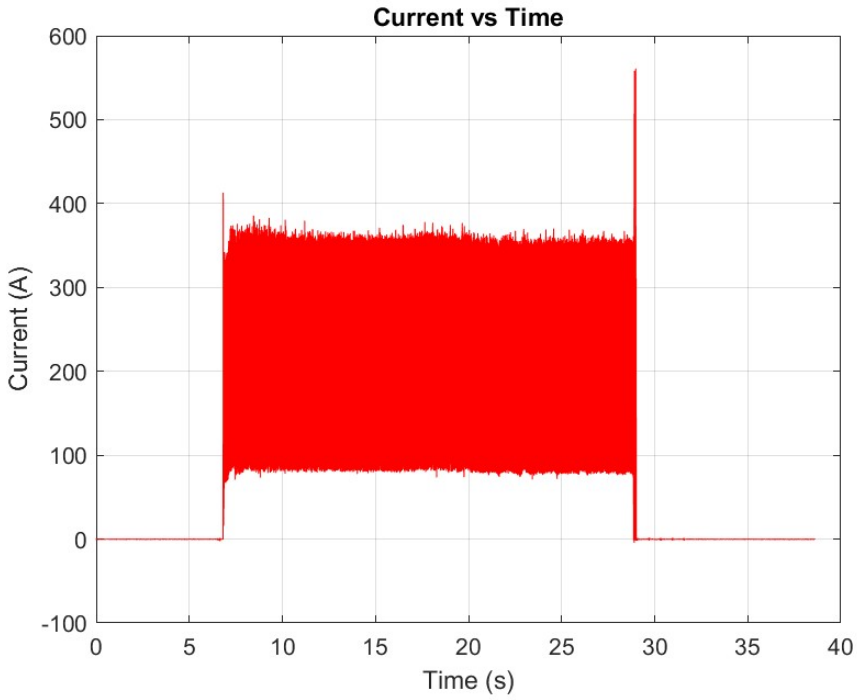


Figure E.2: Current vs Time for 360ipm/20.9V Pulsed Transfer Case

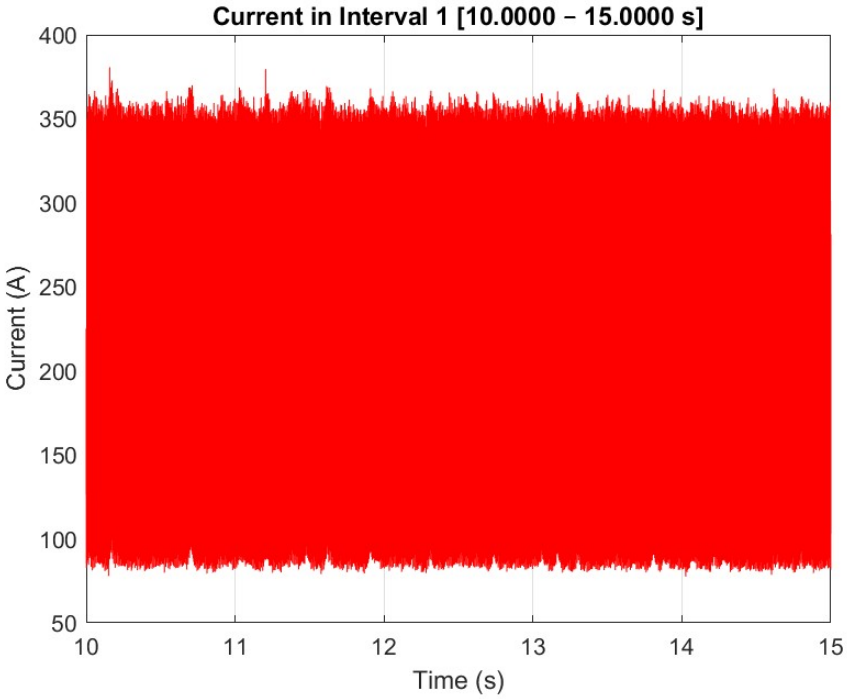


Figure E.3: MATLAB Current Output for 360ipm/20.9V Pulsed Transfer Case in Interval 1

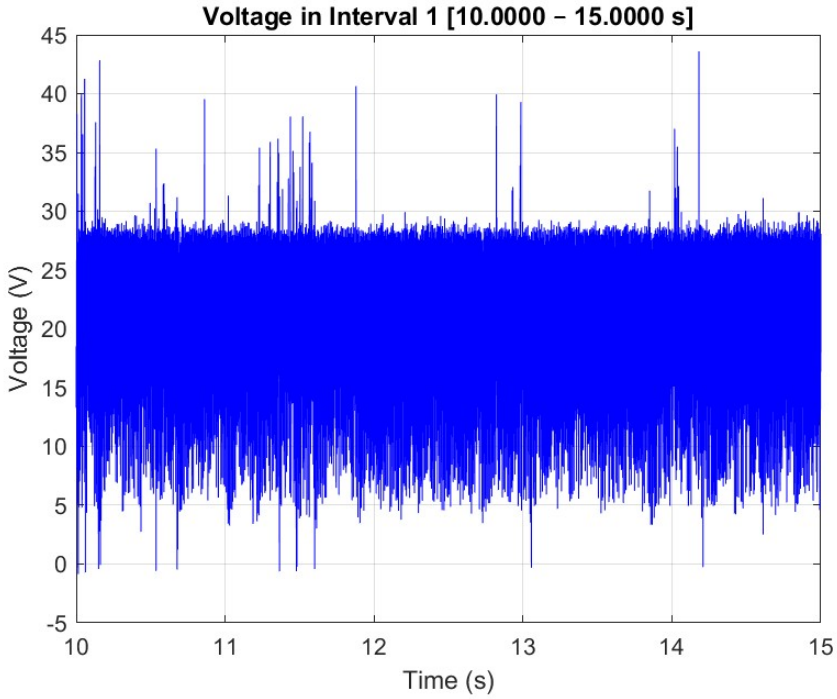


Figure E.4: MATLAB Voltage Output for 360ipm/20.9V Pulsed Transfer Case in Interval 1

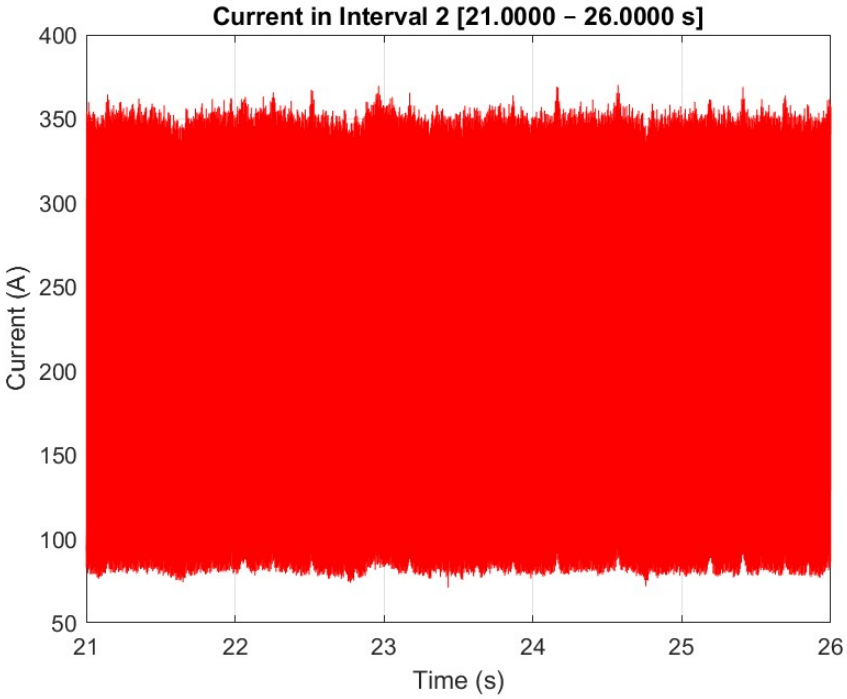


Figure E.5: MATLAB Current Output for 360ipm/20.9V Pulsed Transfer Case in Interval 2

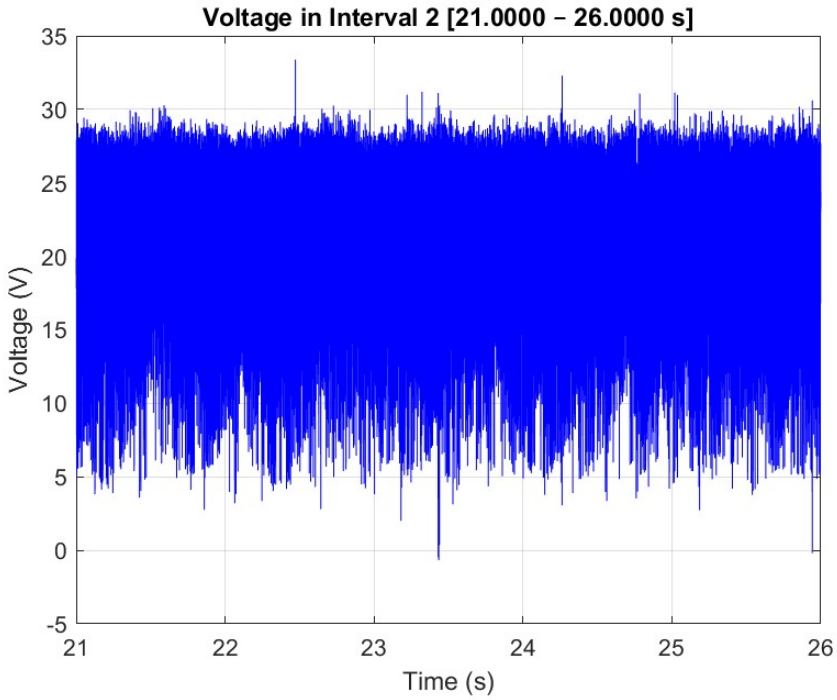


Figure E.6: MATLAB Voltage Output for 360ipm/20.9V Pulsed Transfer Case in Interval 2

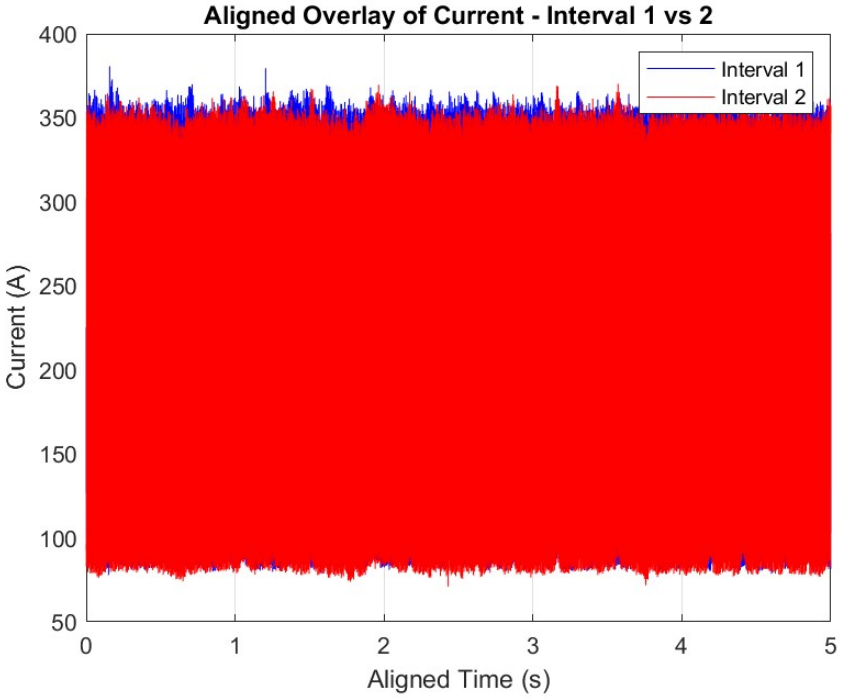


Figure E.7: MATLAB Overlaid Current Output for 360ipm/20.9V Pulsed Transfer Case

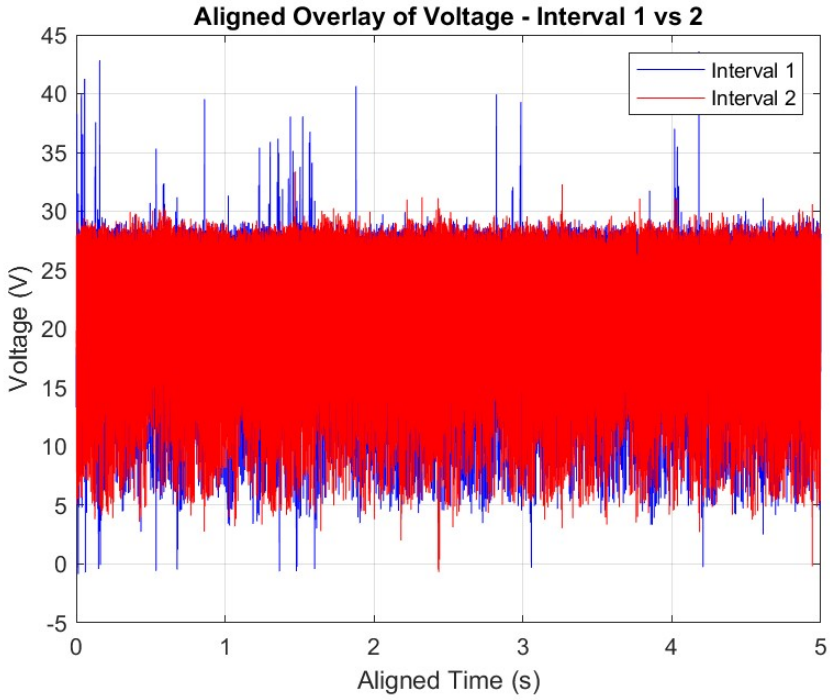


Figure E.8: MATLAB Overlaid Voltage Output for 360ipm/20.9V Pulsed Transfer Case

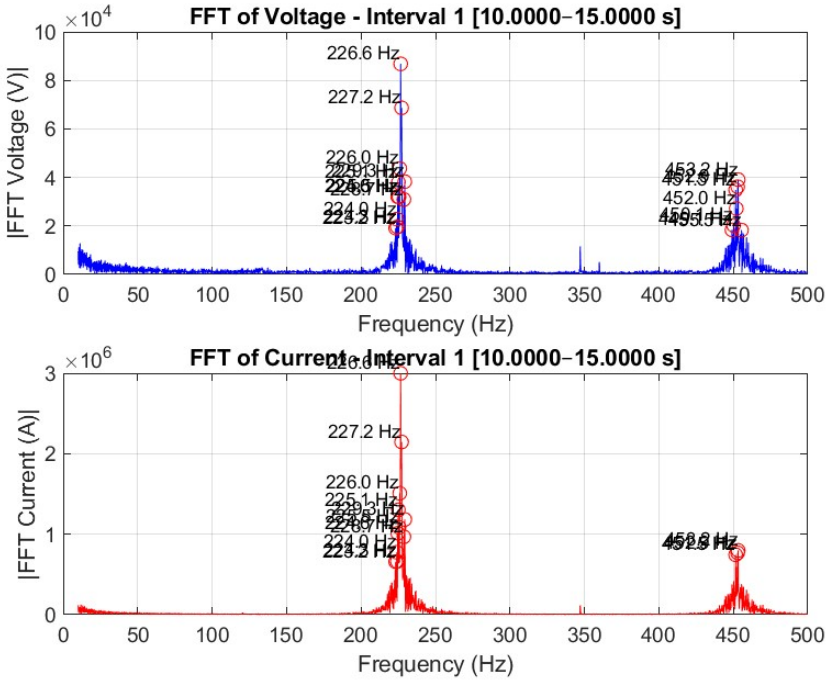


Figure E.9: MATLAB FFT Plot for Interval 1 in 360ipm/20.9V Pulsed Transfer Case

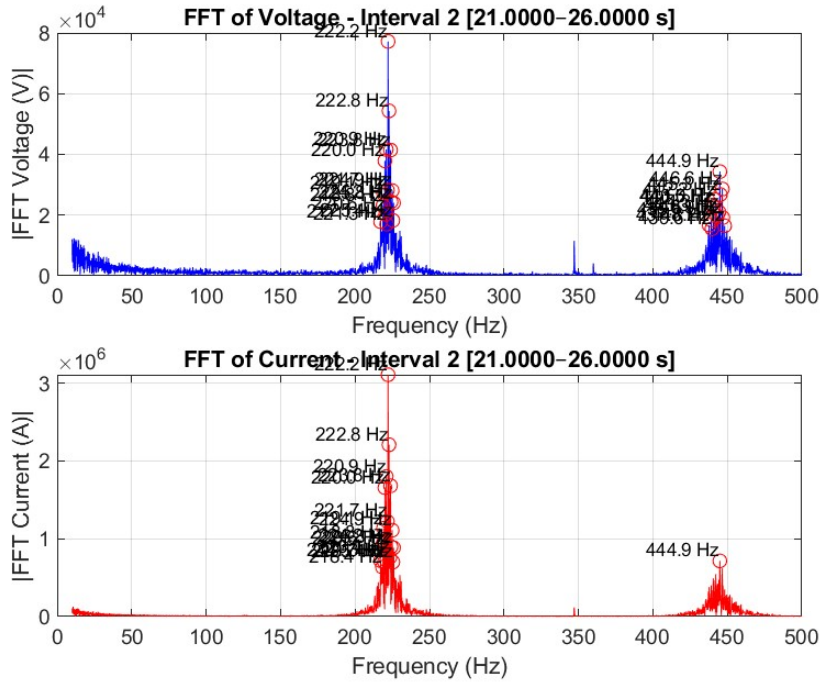


Figure E.10: MATLAB FFT Plot for Interval 2 in 360ipm/20.9V Pulsed Transfer Case

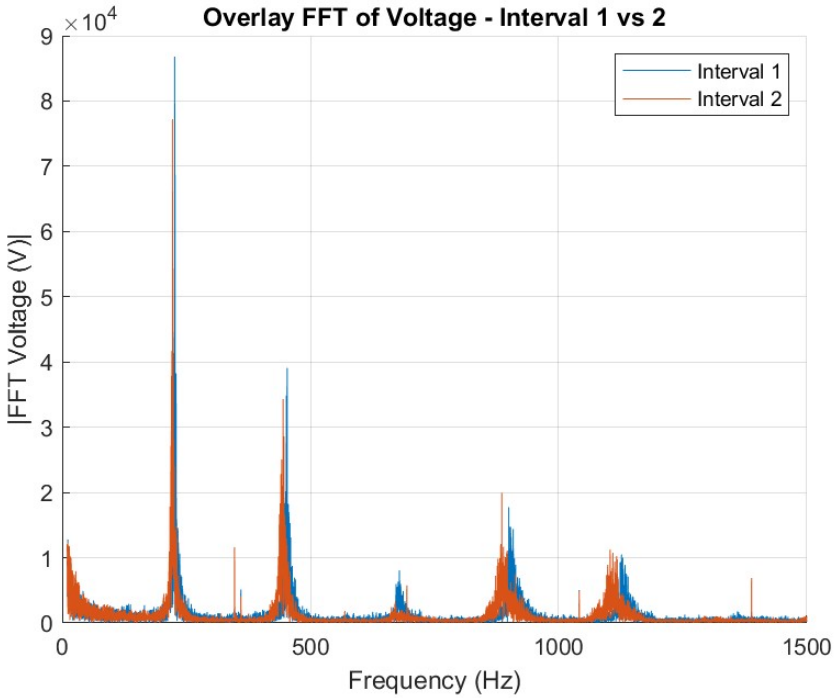


Figure E.11: MATLAB Voltage FFT Overlaid for 360ipm/20.9V Pulsed Transfer Case

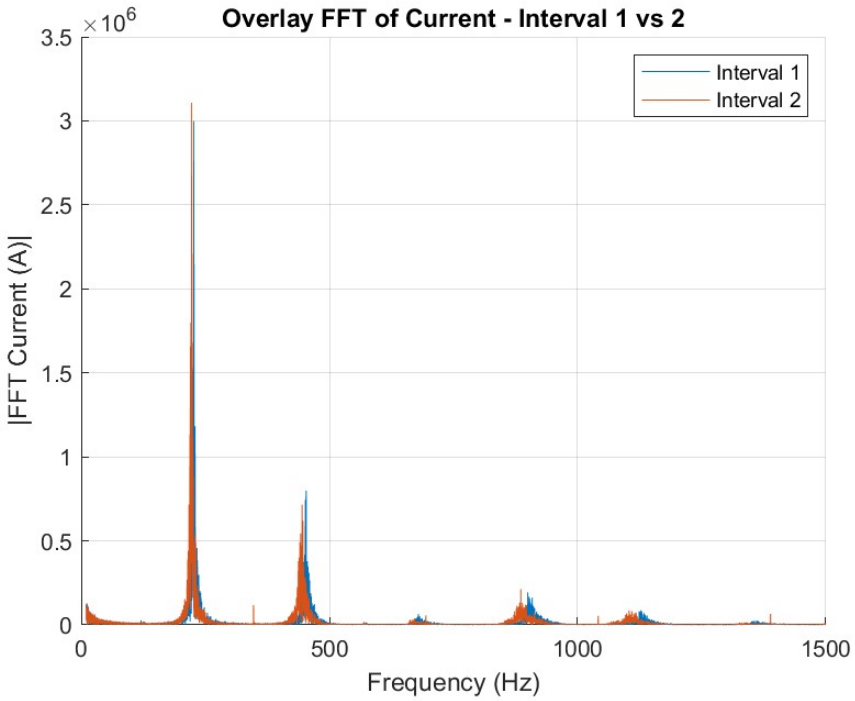


Figure E.12: MATLAB Current FFT Overlaid for 360ipm/20.9V Pulsed Transfer Case

E.2 360ipm 18.3V GMAW 2319AL

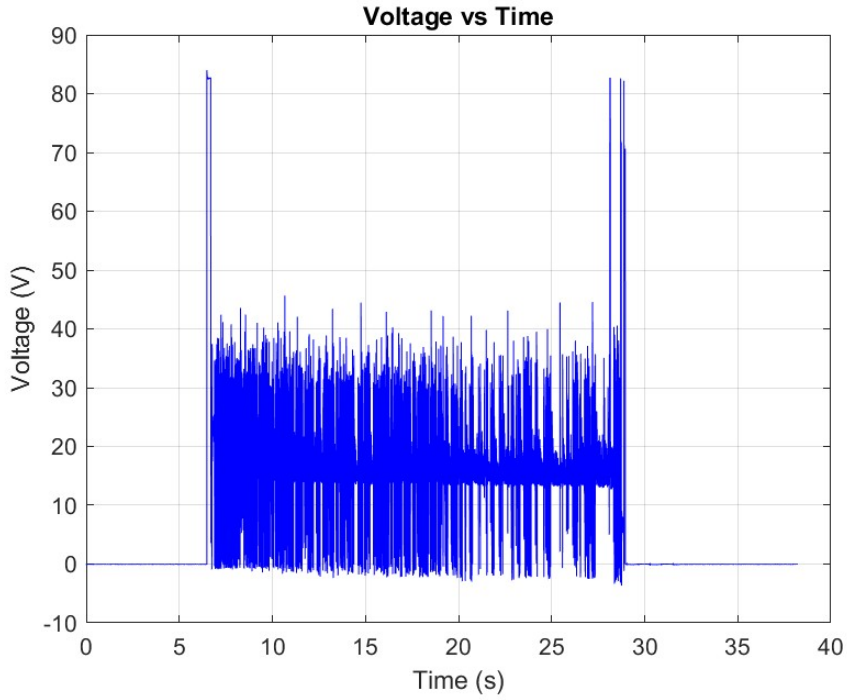


Figure E.13: Voltage vs Time for 360ipm/18.3V GMAW Case

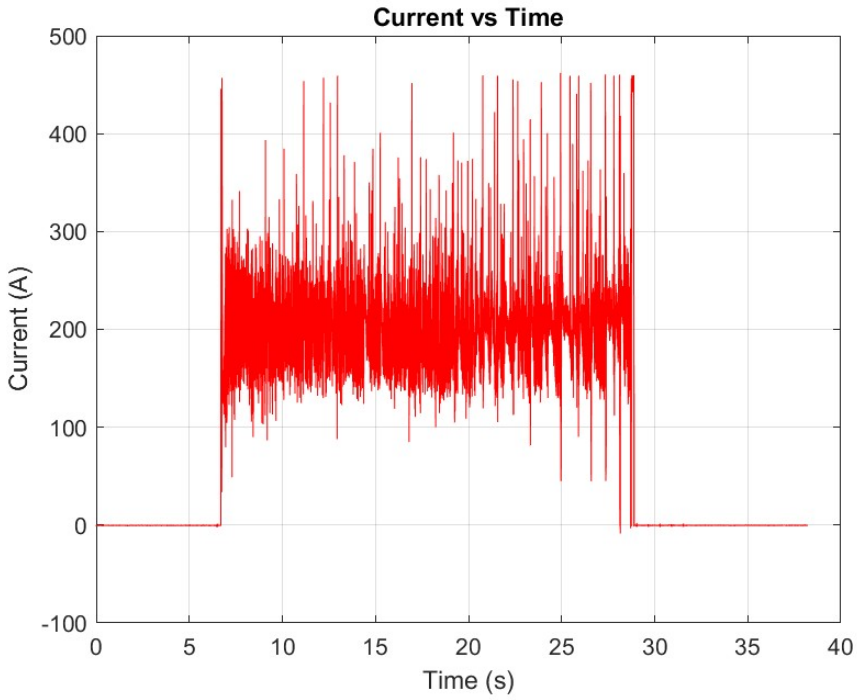


Figure E.14: Current vs Time for 360ipm/18.3V GMAW Case

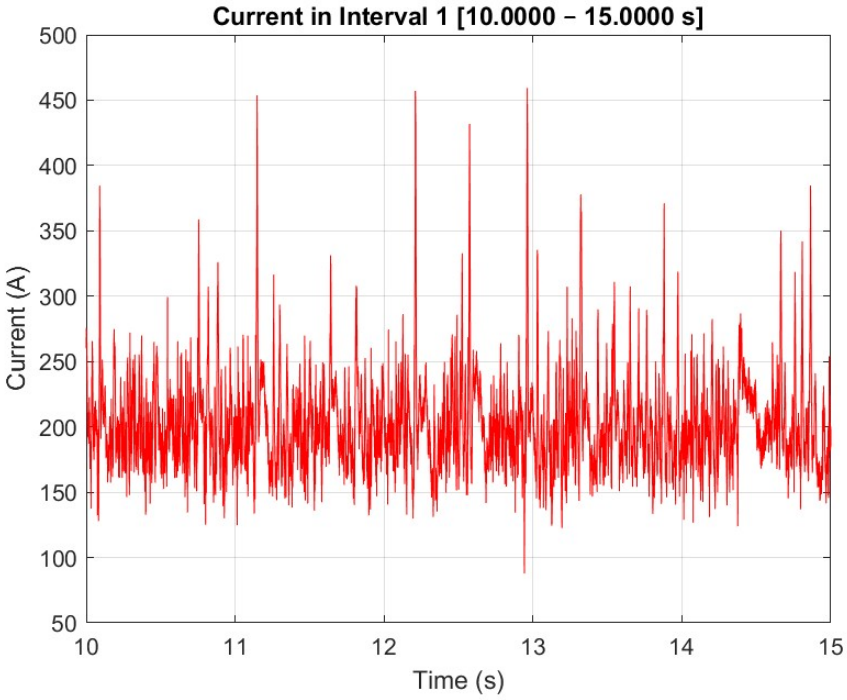


Figure E.15: MATLAB Current Output for 360ipm/18.3V GMAW Case in Interval 1

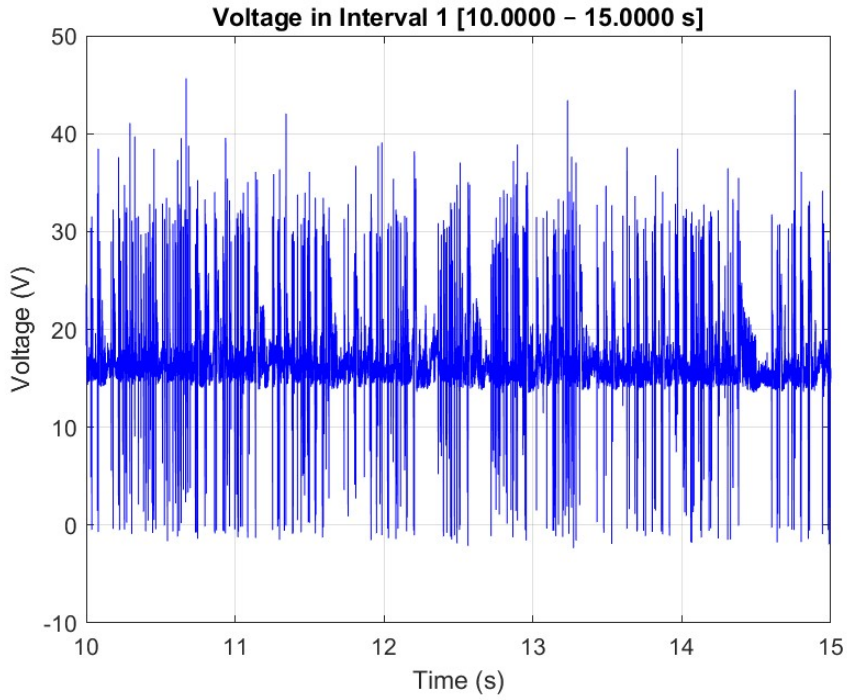


Figure E.16: MATLAB Voltage Output for 360ipm/18.3V GMAW Case in Interval 1

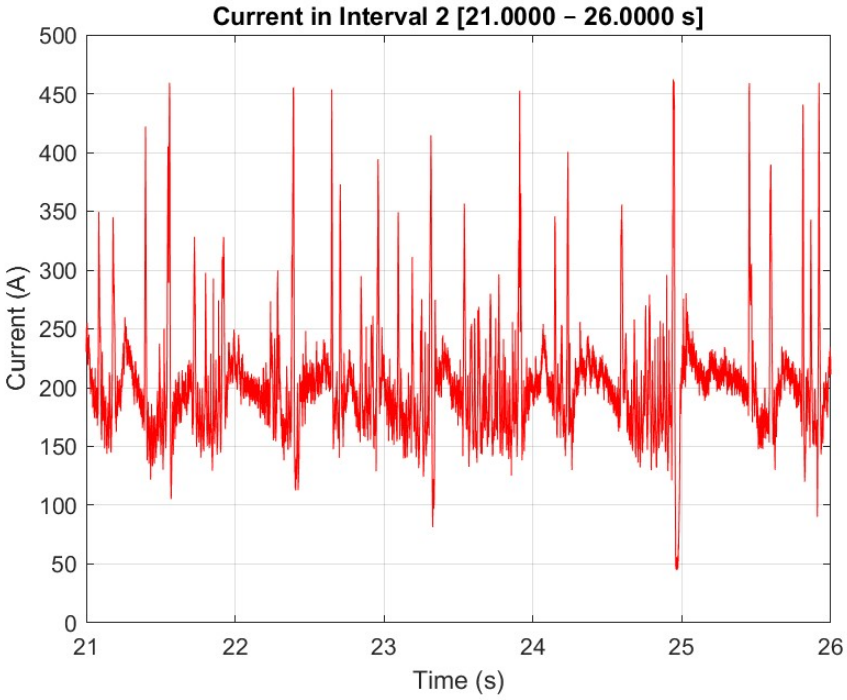


Figure E.17: MATLAB Current Output for 360ipm/18.3V GMAW Case in Interval 2

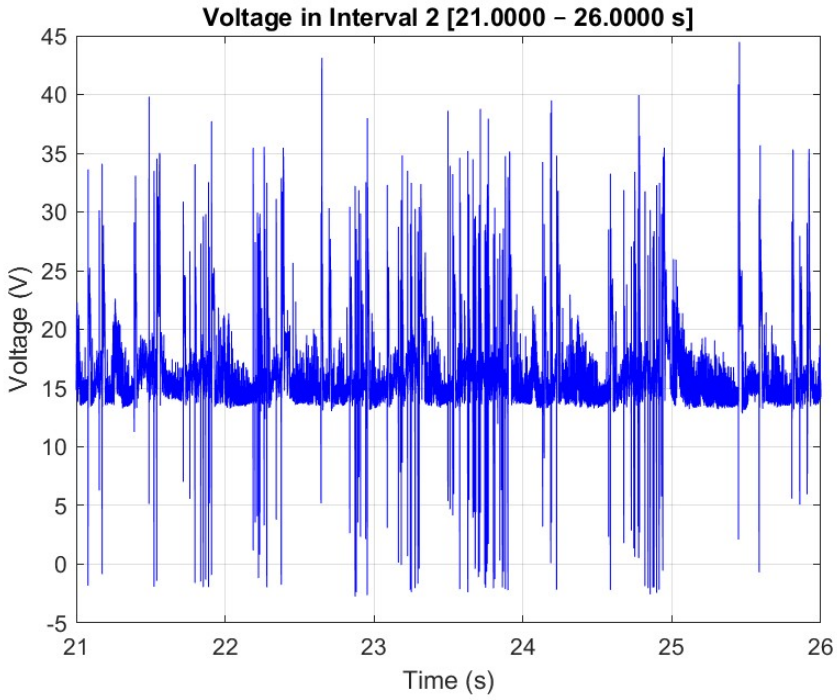


Figure E.18: MATLAB Voltage Output for 360ipm/18.3V GMAW Case in Interval 2

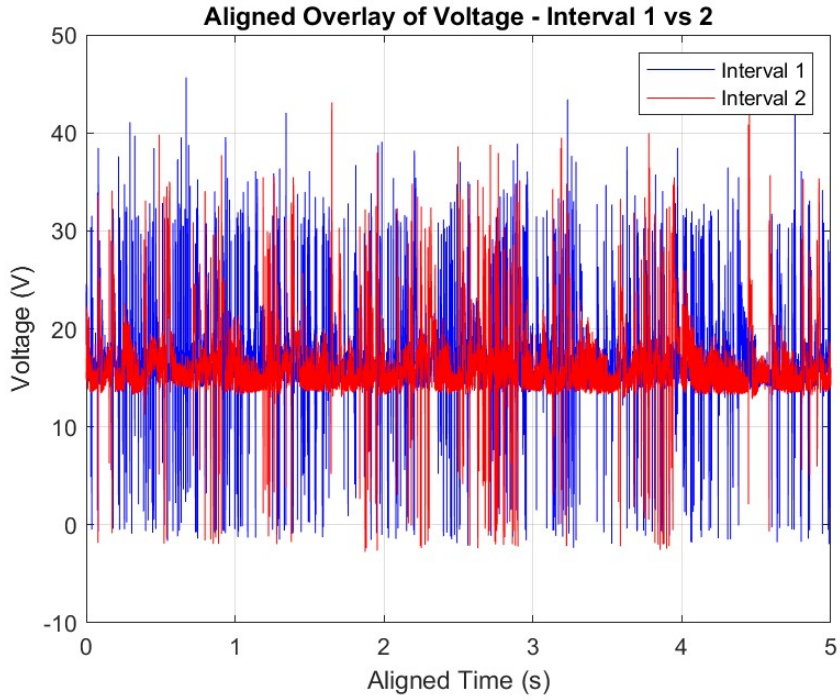


Figure E.19: MATLAB Overlaid Voltage Output for 360ipm/18.3V GMAW Case

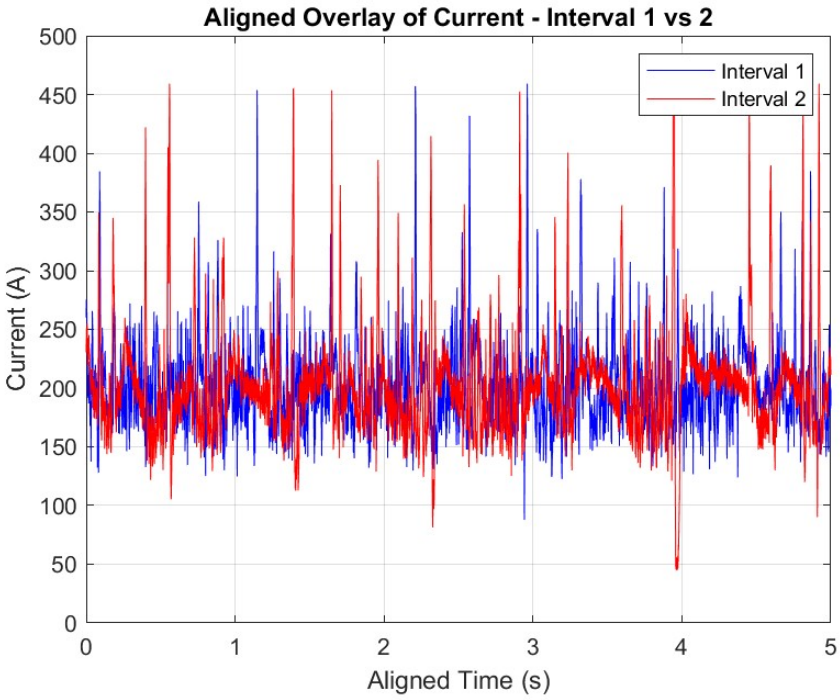


Figure E.20: MATLAB Overlaid Current Output for 360ipm/18.3V GMAW Case

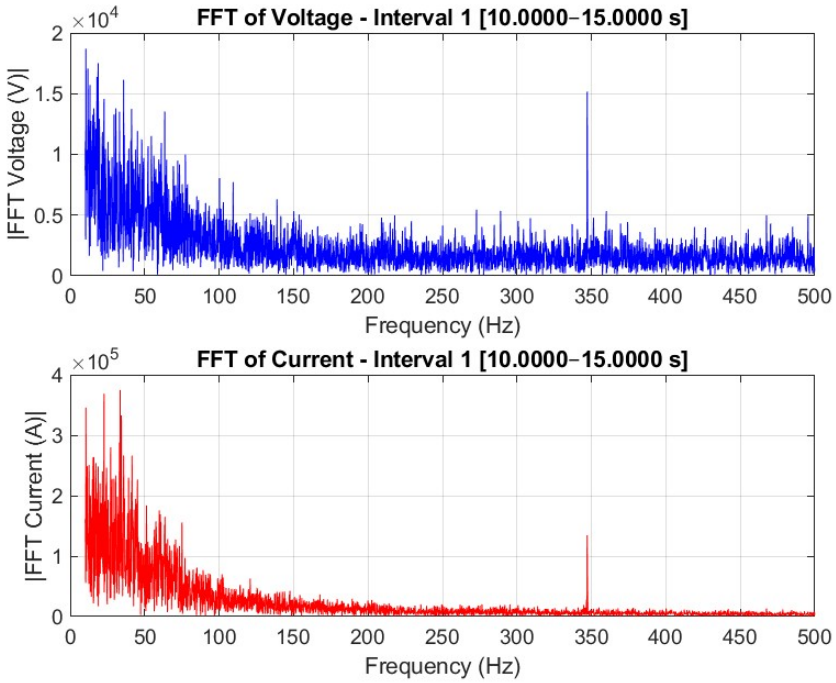


Figure E.21: MATLAB FFT Plot for Interval 1 in 360ipm/18.3V GMAW Case

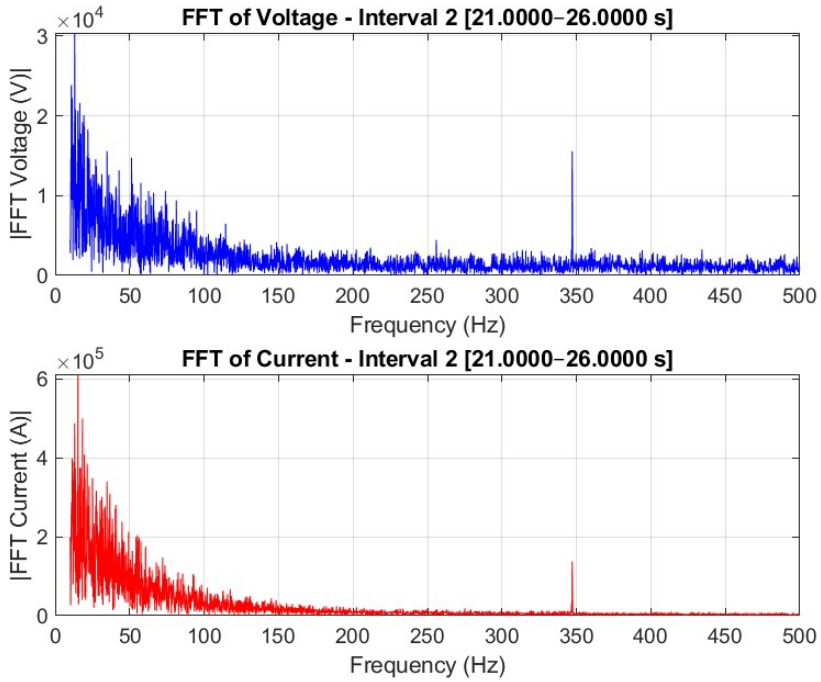


Figure E.22: MATLAB FFT Plot for Interval 2 in 360ipm/18.3V GMAW Case

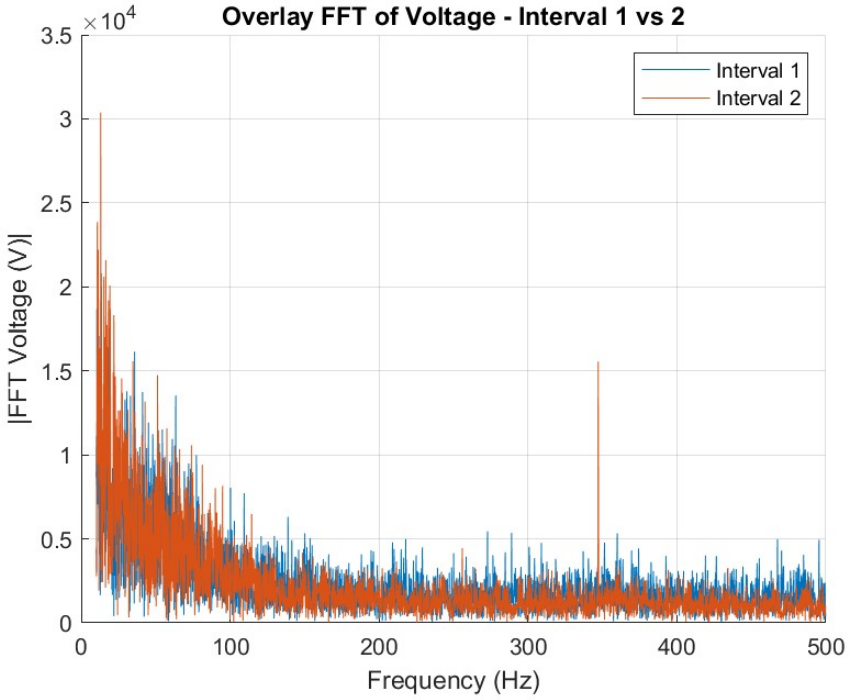


Figure E.23: MATLAB Voltage FFT Overlaid for 360ipm/18.3V GMAW Case

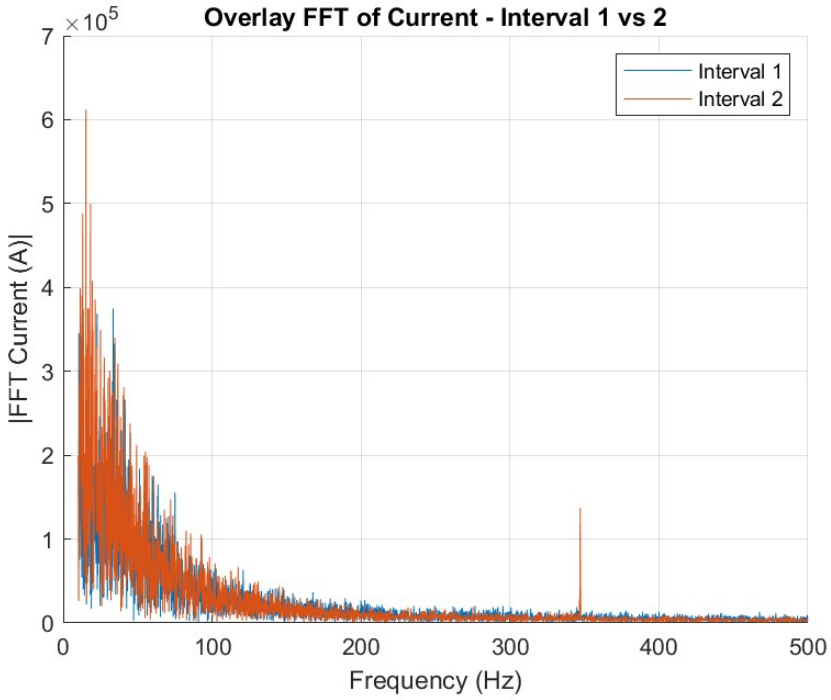


Figure E.24: MATLAB Current FFT Overlaid for 360ipm/18.3V GMAW Case

E.3 360ipm 21V Spray Transfer 2319AL

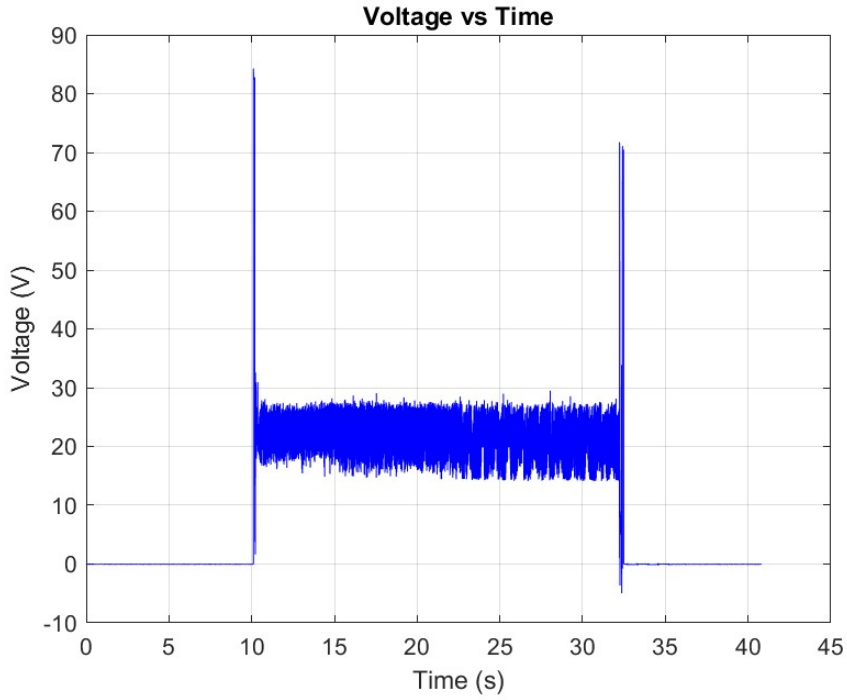


Figure E.25: Voltage vs Time for 360ipm/21V Spray Transfer Case

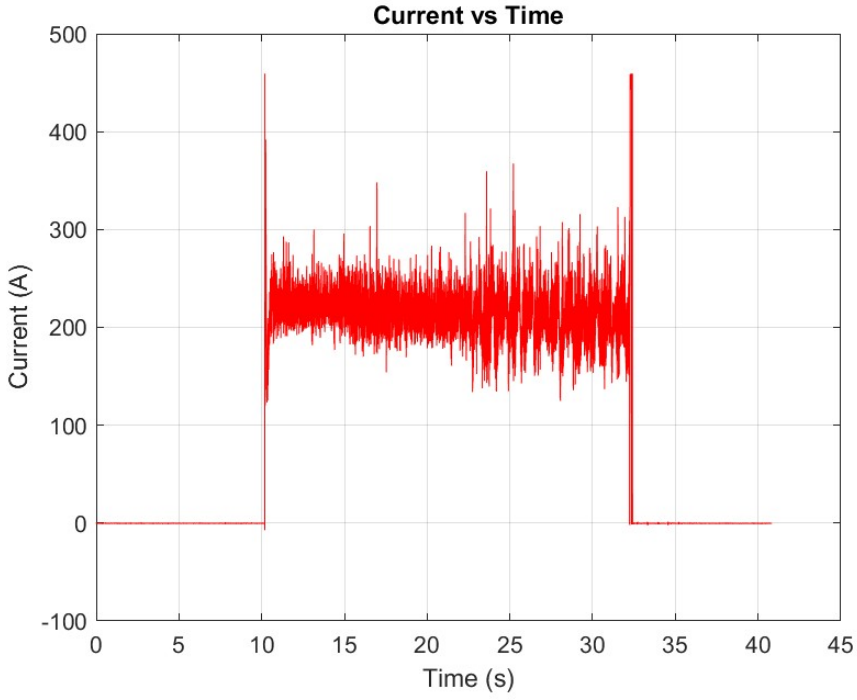


Figure E.26: Current vs Time for 360ipm/21V Spray Transfer Case

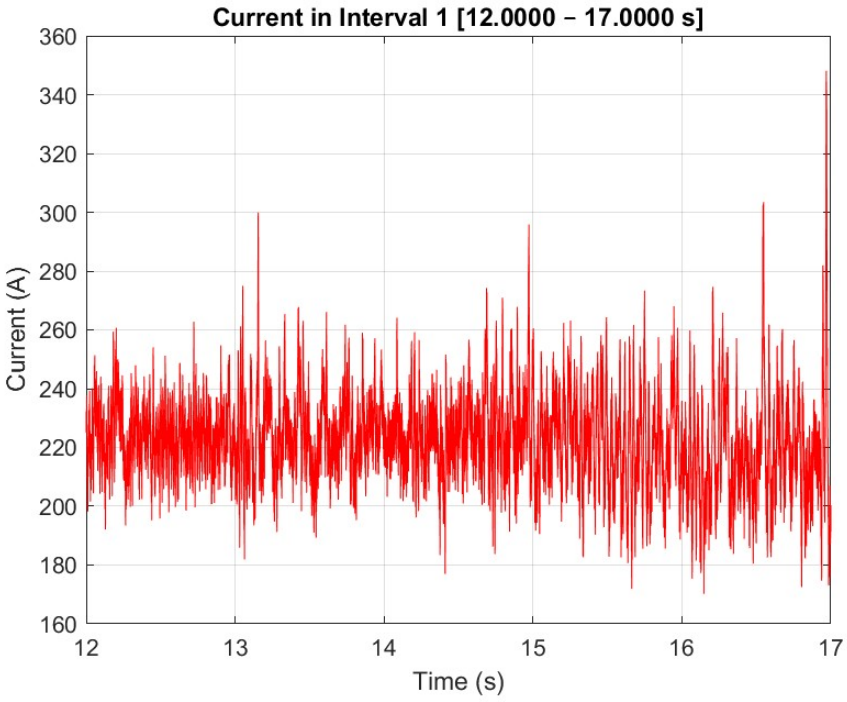


Figure E.27: MATLAB Current Output for 360ipm/21V Spray Transfer Case in Interval 1

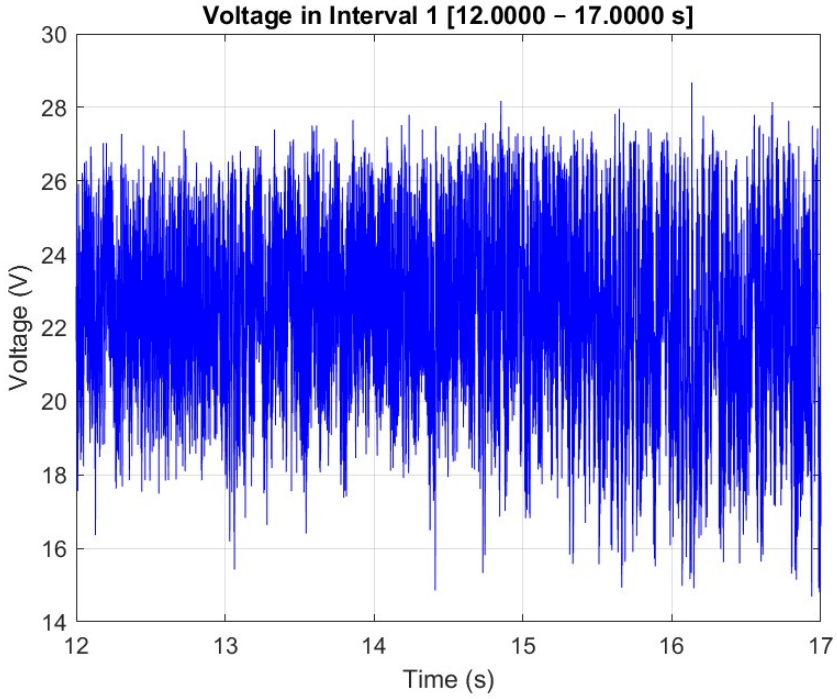


Figure E.28: MATLAB Voltage Output for 360ipm/21V Spray Transfer Case in Interval 1

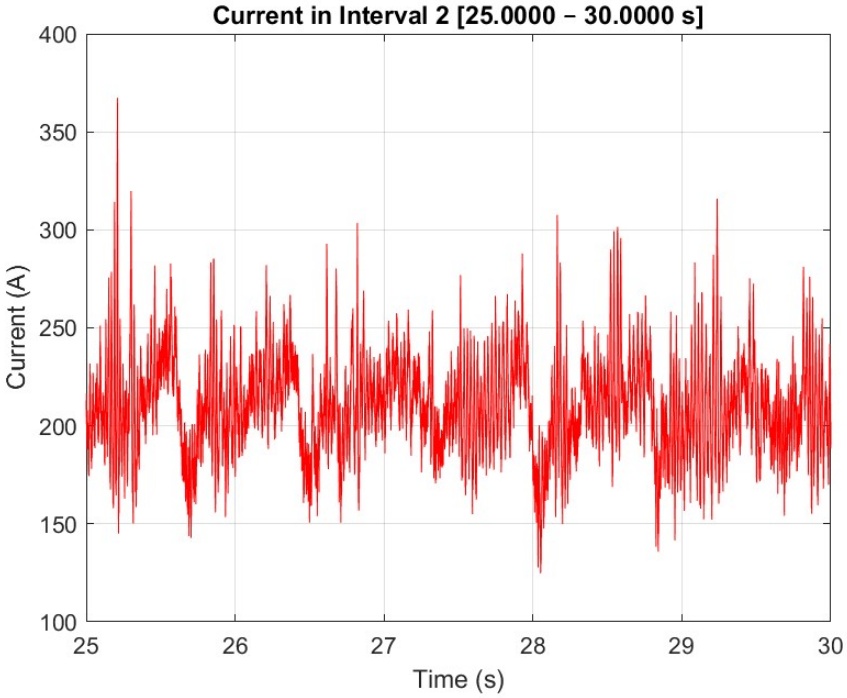


Figure E.29: MATLAB Current Output for 360ipm/21V Spray Transfer Case in Interval 2

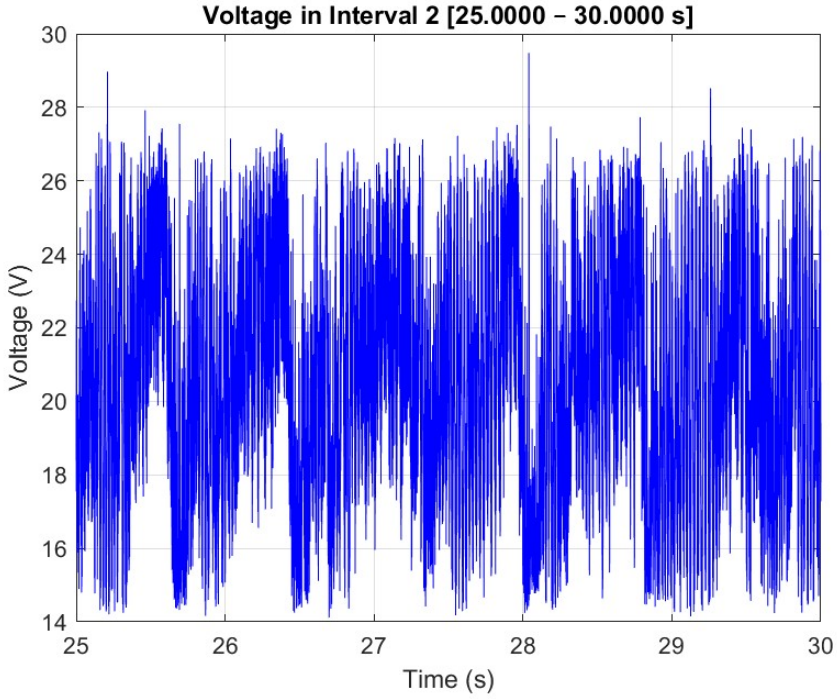


Figure E.30: MATLAB Voltage Output for 360ipm/21V Spray Transfer Case in Interval 2

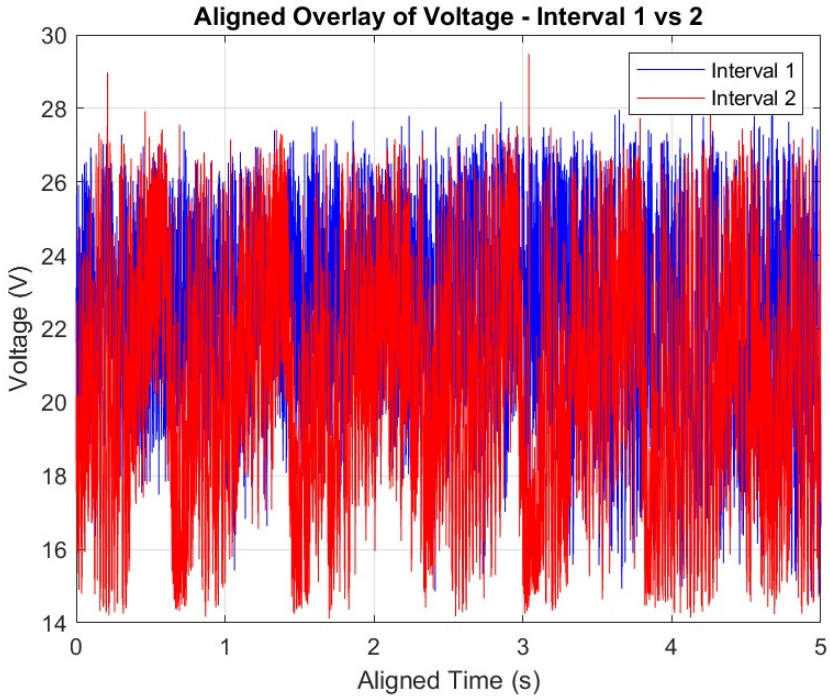


Figure E.31: MATLAB Overlaid Voltage Output for 360ipm/21V Spray Transfer Case

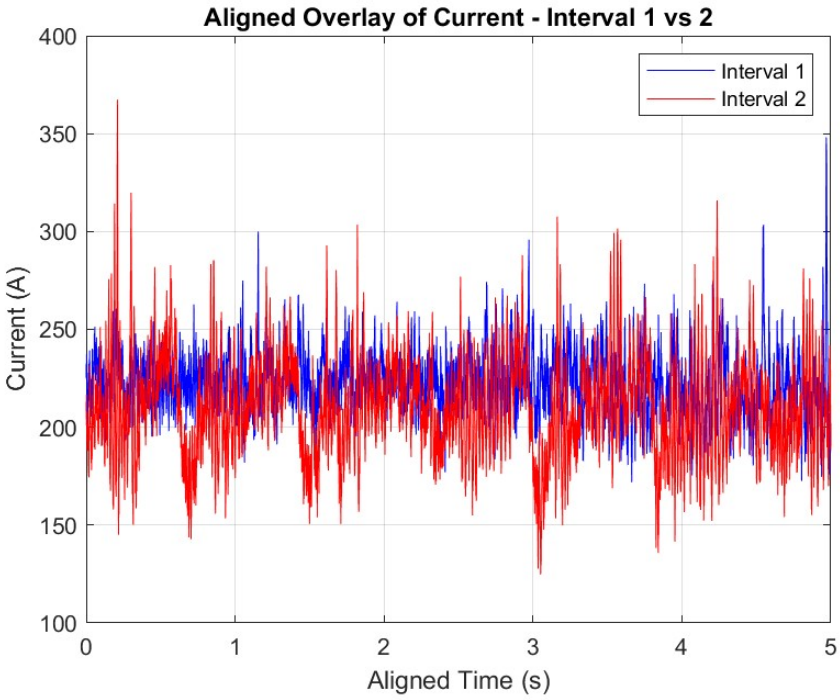


Figure E.32: MATLAB Overlaid Current Output for 360ipm/21V Spray Transfer Case

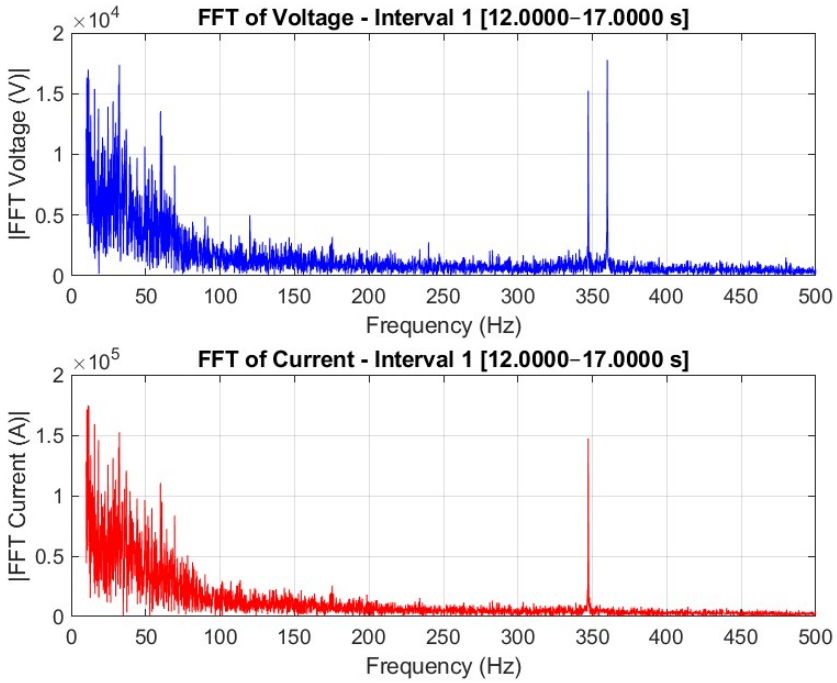


Figure E.33: MATLAB FFT Plot for Interval 1 in 360ipm/21V Spray Transfer Case

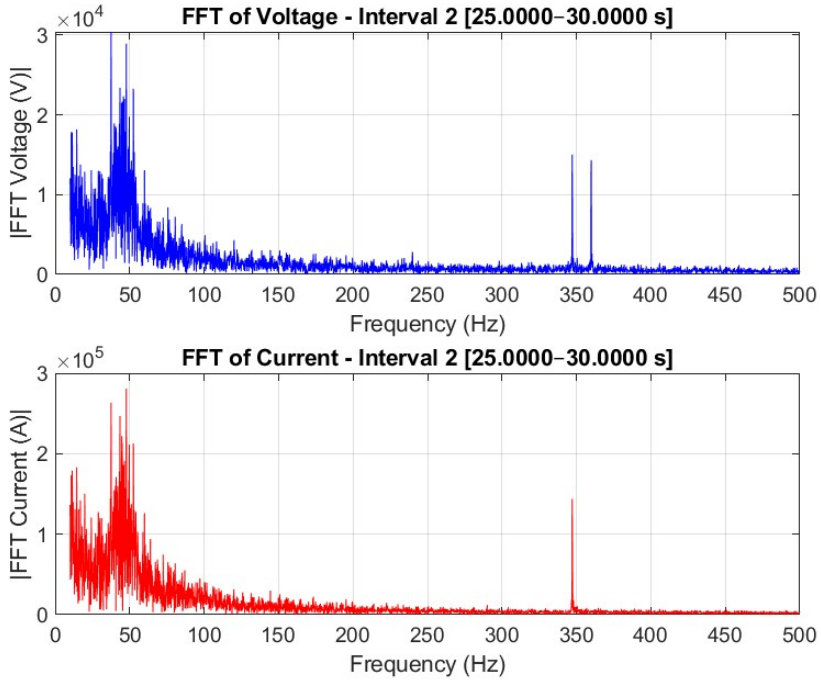


Figure E.34: MATLAB FFT Plot for Interval 2 in 360ipm/21V Spray Transfer Case

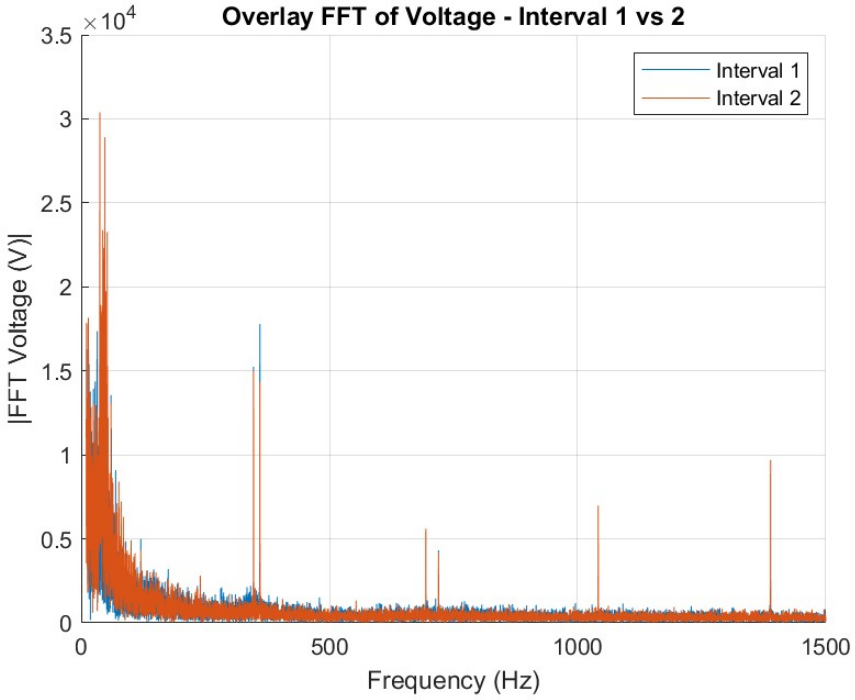


Figure E.35: MATLAB Voltage FFT Overlaid for 360ipm/21V Spray Transfer Case

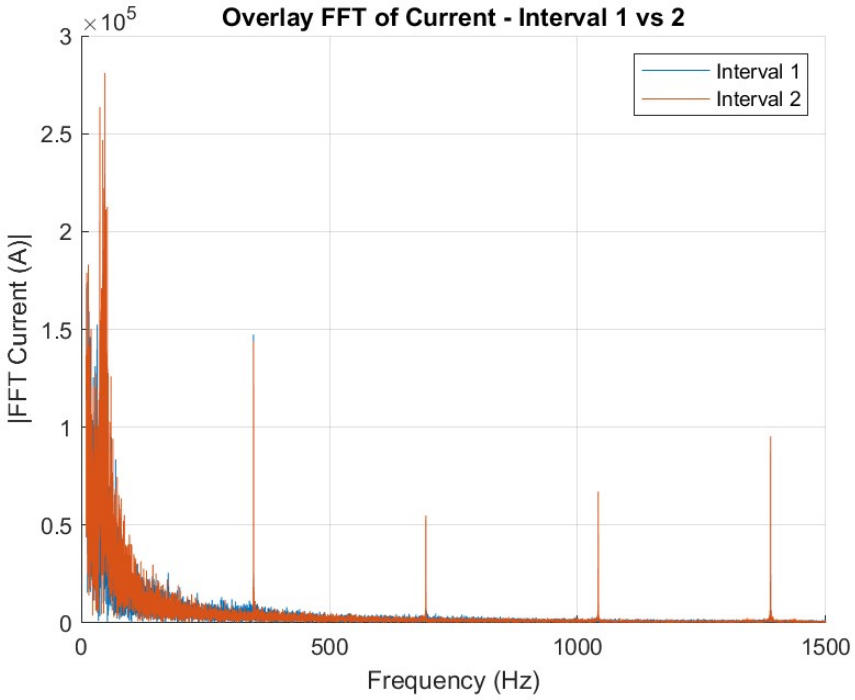


Figure E.36: MATLAB Current FFT Overlaid for 360ipm/21V Spray Transfer Case

Vita

Being a non-traditional student, Devon Goodspeed spent the first decade of his career in machining, welding and heavy fabrication, primarily for the power generation industry, before pivoting to engineering. He graduated magna cum laude with his BS in Mechanical Engineering from the University of Tennessee in 2021 after working on hybrid-electric vehicle controls research for General Motors' Ecocar Mobility Project and acting as an assistant instructor for the UTK SCUBA program. Following this, he began additive manufacturing research under Dr. Bradley Jared, participating in projects ranging from powder-based additive manufacturing defect detection research to wire-arc-additive-manufacturing (WAAM) work for NASA, the Office of Naval Research, and General Electric, among others. He earned his Master of Science in Mechanical Engineering in 2024 as a member of the Manufacturing Automation and Process Lab, where his primary focus has been the manipulation of welding arcs through the influence of external magnetic fields. During this time, Devon acted as instructor for graduate level weld process modeling and wire arc additive manufacturing courses at UTK. He is a member of Tau Beta Pi national engineering honor society and volunteers as a licensed emergency medical technician, rescue diver, high-angle rescue, swift-water rescue and vehicle extrication technician for the Jefferson County Rescue Squad.